Engineering genetically encoded indicators for neurotransmission

by

Rochelin R. S. Dalangin

A thesis submitted in partial fulfillment of the requirements for the degree of

Doctor of Philosophy

Department of Chemistry
University of Alberta

Abstract

Information is transmitted between neurons through the flow of different ions and the release of neurotransmitters at speeds on the order of milliseconds. The advent of genetically encoded fluorescent protein (FP)-based optical indicators for neuronal activity, which can be precisely targeted towards desired populations of cells and enabled non-invasive imaging of both single neurons and populations of neurons, revolutionized our understanding of neurotransmission. In this thesis, we detail our efforts to expand the repertoire of genetically encoded indicators for neurotransmission by combining directed evolution and rational design.

First, we expand the pool of analytes for which genetically encoded indicators are available by engineering a new series of green FP-based aspartate indicators, which we call "ODIN1", from a new aspartate/glutamate periplasmic binding protein. By analyzing the protein's solvent accessibility, we were able to identify the optimal insertion point for a circularly permutated (cp) green FP and engineer bright prototypes with large dynamic ranges. Further optimization efforts to introduce specificity for aspartate over glutamate led to variants with different and well-separated affinities for aspartate and glutamate. By tethering the ODIN1 variants on the surface of cells using the SpyTag and SpyCatcher system, we were able to show that ODIN1 had good response towards aspartate that is comparable to other first-generation indicators for amino acids.

Second, we capitalized on our efforts from engineering ODIN1 by engineering the first single FP-based glutamine indicator using a glutamine binding protein that is homologous to our aspartate/glutamate binding protein. By careful optimization of the linkers, we engineered a highly specific variant, which we refer to as "Qigon1", with relatively high affinity and modest response. Using SpyTag and SpyCatcher, we demonstrated that Qigon1 is functional on the cell surface.

Next, we describe the development of a new red genetically encoded calcium ion (Ca^{2+}) indicator (GECI), RCaMP3.0, using mRuby3, one of the brightest red FPs to date. RCaMP3.0 shows a significantly larger dynamic range than its predecessor but still has low brightness and affinity for Ca^{2+}. As a result, its performance in cells is limited.

Last, we expand the spectral palette of available GECIs by engineering a new series of far-red Ca^{2+} indicators, the FR-GECO series, based on a new monomeric far-red FP. The FR-GECOs have high affinity and large dynamic ranges, are bright under one-photon and two-photon illumination *in vitro* and offer fast and sensitive detection of single action potentials in neurons.

Preface

A version of Chapter 1 has been published as: Dalangin, R.; Kim, A.; Campbell R.E, The role of amino acids in neurotransmission and fluorescent tools for their detection. *Int. J. Mol. Sci.* **2020**, *21* (17), 6197.

For the aspartate indicators in Chapter 2, the experimental work was performed by Matthew D. Wiens, Anna Kim, and myself. Matthew D. Wiens and Anna Kim contributed to the engineering performed on the GltI-based indicator. For the PEB1a-based design, I designed the initial construct, performed the engineering, *in vitro* characterization and experiments in cells. A.K. contributed to the engineering and *in vitro* characterization. Robert E. Campbell supervised the project and edited the chapter.

For the glutamine indicators in Chapter 3, Abhi Aggarwal and I performed the experimental work. Abhi Aggarwal built the initial constructs with the glutamine binding protein from *E. coli*, optimized its linkers, and provided figures. I performed further optimization on this design and all experimental work with the second glutamine binding protein from *B. pseudomallei*. Robert E. Campbell directed the project and edited the chapter.

I carried out all the work in Chapter 4. Robert E. Campbell supervised the research and edited the chapter.

A version of Chapter 5 is being prepared for publication as: R. Dalangin, M. Drobizhev, R. S. Molina, Y. Zhao, J. Wu, T. E. Hughes, Y. Shen, R. E. Campbell, Far-red fluorescent genetically encoded calcium ion indicators. Yi Shen, Jiahui Wu and I performed protein engineering. Yi Shen and I performed the 1P *in vitro* characterization, while Mikhail Drobizhev and Rosana S. Molina performed 2P *in vitro* characterization. Yi Shen and Yufeng Zhao performed

cultured cell imaging. Yi Shen, Thomas E. Hughes and Robert E. Campbell directed the project. Yi Shen, Mikhail Drobizhev, Robert E. Campbell and I wrote the manuscript.

To my sister.

For reminding me I was human, even when I didn't want to remember.

"It was the secrets of heaven and earth that I desired to learn; and whether it was the outward substance of things, or the inner spirit of nature and the mysterious soul of man that occupied me, still my enquiries were directed to the metaphysical, or in its highest sense, the physical secrets of the world."

— Mary Shelley, *Frankenstein*

Acknowledgments

This would not have been possible without the support and guidance of those around me. While I am, by far, more eloquent with ink and pixels, I am under no illusion that my best words do justice to these individuals.

First, I would like to offer my sincerest thanks to my supervisor, Dr. Robert E. Campbell, who gave me the freedom and resources to go where my mind takes me while always being there when I inevitably ventured too far. I'm also exceedingly thankful for your attention to detail – my writing and presentations have improved immensely from your feedback. Under your mentorship, I grew not just as a scientist but as a person, and I am eternally grateful you responded to my out-of-nowhere email five years ago.

To members of the Campbell lab, past and present, who offered advice and support, thank you. I would especially like to thank my undergrad, Anna Kim, whose dedication and hard work enabled speedy progress on Chapter 2 and freed me to pursue other projects as well. We took a gamble on that project and it paid off. I would also like to thank Dr. Landon Zarowny for taking me under his wing and teaching me his tricks in the lab. Similarly, thank you to Drs. Matthew Wiens and Eason Shen for being bottomless founts of knowledge, wisdom, and most of all, patience. I'm sure I asked the same questions countless times over the years.

Thank you to my supervisory committee, Drs. Christopher Cairo and Mark McDermott, for their guidance throughout the years. I would also like to thank Drs. François St-Pierre and Allen Chan for their time and valuable input.

Grad school is the hardest journey I've had by far, and I am thankful to my friends within the Department, including those in WIC, whose friendship and support lightened the journey. I

daresay that my decision to come to that Saturday morning meeting for starting WIC was one of my smartest decisions in grad school.

To the awesome staff in the Chemistry Department and the Molecular Biology Services Unit for all their assistance for the last five years, very much obliged.

I would also like to acknowledge the Natural Sciences and Engineering Research Council of Canada, the Canadian Institutes of Health Research, Alberta Innovates, the University of Alberta and Dr. Jean Cooley for their generous funding.

Lastly, I am sincerely grateful to my family, especially my parents, Lai and Rey Dalangin, whose sacrifices made all of this possible and for feeding my curiosity as a child. Because of your efforts, I've come a long way from dismantling random electronics around the house. To my sister, I am who I am because of you. Thank you for your unwavering support and understanding (even during all those times I was late for, well, everything because I got stuck at the lab) and for all the things you did for me that I'm sure I haven't realized.

Table of Contents

List of Figures

List of Tables

List of Abbreviations

AP	Action potential
Ala or A	Alanine
AMPA	α-Amino-3-hydroxy-5-methyl-4-isoxazoleproprionic acid
Arg or R	Arginine
Asn or N	Asparagine
Asp or D	Aspartate
B-PER	Bacterial protein extraction reagent
BBB	Blood-brain barrier
BCAA	Branched chain amino acid
B. pseudomallei	*Burkholderia pseudomallei*
CaM	Calmodulin
C. jejuni	*Campylobacter jejuni*
CNS	Central nervous system
Δ	Delta (or change)
cp	Circularly permutated
Cys or C	Cysteine
dCTP	Deoxycytidine triphosphate
DNA	Deoxyribonucleic acid
dNTPs	Deoxyribonucleotide phosphates
dTTP	Deoxythymidine triphosphate
DMSO	Dimethyl sulfoxide
K_d	Dissociation constant
DMEM	Dulbecco's modified Eagle's medium
EGFP	Enhanced green fluorescent protein
EP	Error-prone
E. coli	*Escherichia coli*
EGTA	Ethylene glycol -bis(β-aminoethyl ether)-*N,N,N',N'*-tetraacetic acid
EAAT	Excitatory amino acid transporter
EC or ε	Extinction coefficient

ECM	Extracellular matrix
FBS	Fetal bovine serum
FP	Fluorescent protein
FRET	Förster resonance energy transfer
GABA	γ-Aminobutyric acid
GECI	Genetically encoded Ca^{2+} indicator
GECO	Genetically encoded Ca^{2+} indicator for optical imaging
Glu or E	Glutamate
GLAST	Glutamate aspartate transporter
Gln or Q	Glutamine
QBP	Glutamine binding protein
Gly or G	Glycine
GPCR	G-protein coupled receptor
g	Gravitational force
GFP	Green fluorescent protein
HHBSS	HEPES-buffered Hanks' balanced salt solution
n_H	Hill coefficient
His or H	Histidine
HEPES	4-(2-hydroxyethyl)-1-piperazineethanesulfonic acid)
kDa	Kilodalton
LB	Lysogeny broth
Leu or L	Leucine
Lys or K	Lysine
mGluR	Metabotropic glutamate receptor
μ	Micro
m	Milli
mTFP1	Monomeric teal fluorescent protein
MOPS	3-(*N*-morpholino)propanesulfonic acid
nM	Nanomolar
NMDA	*N*-Methyl-D-aspartate
1P	One-photon

PBP	Periplasmic binding protein
Phe or F	Phenylalanine
PBS	Phosphate-buffered saline
PA	Pipecolic acid
PNS	Peripheral nervous system
PCR	Polymerase chain reaction
Pro or P	Proline
PDB	Protein Data Bank
QY or ϕ	Quantum yield
RFP	Red fluorescent protein
ROI	Region of interest
RNA	Ribonucleic acid
Ser or S	Serine
5-HT	Serotonin
SWCNT	Single-walled carbon nanotubes
Snifit	SNAP-tag based indicator proteins with a fluorescent intramolecular tether
sfGFP	Superfolder green fluorescent protein
Thr or T	Threonine
TBS	Tris-buffered saline
2P	Two-photon
Tyr or Y	Tyrosine
UV	Ultraviolet
Val or V	Valine
λ_{ex}	Wavelength (maximum excitation)
λ_{em}	Wavelength (maximum emission)

1 Chapter 1 – Introduction

1.1 Introduction

Neurons communicate to each other by the release of chemicals stored in synaptic vesicles across specialized gaps known as synapses. These chemicals diffuse across the synapse and bind to their target receptors on adjacent neurons to modulate their physiological states. While these messenger chemicals are collectively referred to as neurotransmitters, there can be confusion regarding the difference between neurotransmitters and neuromodulators. Classically, neurotransmitters are defined as molecules that meet the following criteria (adapted from Werman [1]):

- Presence of the molecule in neurons;
- Stored in synaptic vesicles and released in a Ca^{2+}-dependent manner from neurons as a result of depolarization;
- Exogenous application of the molecule must elicit the same response from post-synaptic neurons as endogenously-released molecules;
- Molecule must have a mechanism for its removal from the synapse.

Molecules that meet some, but not all, of these criteria can be referred to as neuromodulators. However, the term "neuromodulator" has also been used to refer to known neurotransmitters whose primary mode of action is to bind G-protein coupled receptors (GPCRs) to trigger a longer-lasting second messenger signalling cascade. Moreover, molecules that exert effects over greater volumes or distances than just across synapses have also been referred to as "neuromodulators". To minimize confusion, we will confine the use of the term "neurotransmitter" for molecules that have met the criteria for classical neurotransmitters and refer to other molecules that can still modulate neuronal activity as "neuromodulators" from this point onward.

As a class of compounds, amino acids are most commonly recognized as the building blocks of proteins. However, strictly speaking, amino acids are defined as compounds that contain an amine group ($-NH_3^+$) and a carboxylic acid group ($-COO^-$) (represented here in their physiologically most relevant ionization states; **Figure 1-1A**), and not all amino acids are proteinogenic (**Figure 1-1B**). In addition to serving as protein building blocks, amino acids, for example, function throughout the body as key metabolites; precursors to other metabolites and lipids; and regulators of gene expression and cell signalling [2]. Within physiological systems, amino acids may also have specialized roles. In the nervous system alone, several amino acids, most famously glutamate, are known to be small-molecule neurotransmitters and neuromodulators or precursors for other small-molecule neurotransmitters [2]. With the prominence of several canonical amino acids in the nervous system, a review summarizing the roles of all the canonical amino acids, as well as some of the most predominant non-canonical amino acids, within the nervous system may prove to be beneficial.

Within the last few decades, fluorescence imaging has revolutionized our understanding of neurotransmission. Neurotransmission events can begin and conclude within milliseconds, and unlike classical methods such as microdialysis or cyclic voltammetry [3], fluorescence imaging enables the study of both single neurons and populations of neurons while maintaining high spatial and temporal resolution. Ideally, fluorescent probes (also interchangeably referred to as sensors, biosensors, reporters, or indicators) will be bright, fast, specific to their target and show large intensity changes upon its detection. They should also be stable, non-toxic and be easily delivered to their target location with minimal off-target labelling. Additionally, for any analyte, sensors should be available in a palette of colours to enable simultaneous imaging of different analytes.

Fluorescent probes have been synthesized using a variety of materials and strategies, each of which have their own advantages and drawbacks.

This review aims to provide a brief overview of some of the most important roles the twenty canonical amino acids, along with β-alanine and γ-aminobutyric acid, have within the nervous system. We will focus on their immediate (i.e., not their derivates') roles in modulating neurotransmission and we will highlight the lesser known amino acids (**Figure 1-1**and **Table 1-1**). Unless stated otherwise, amino acids referred to in this review should be assumed to be the L isomer. We will also review various fluorescence-based probes for detecting endogenous amino acids in live cells and tissue. Due to the complexity and interconnectedness of neurotransmission and space limitations, this review is not meant to be exhaustive, and many relevant papers are not included.

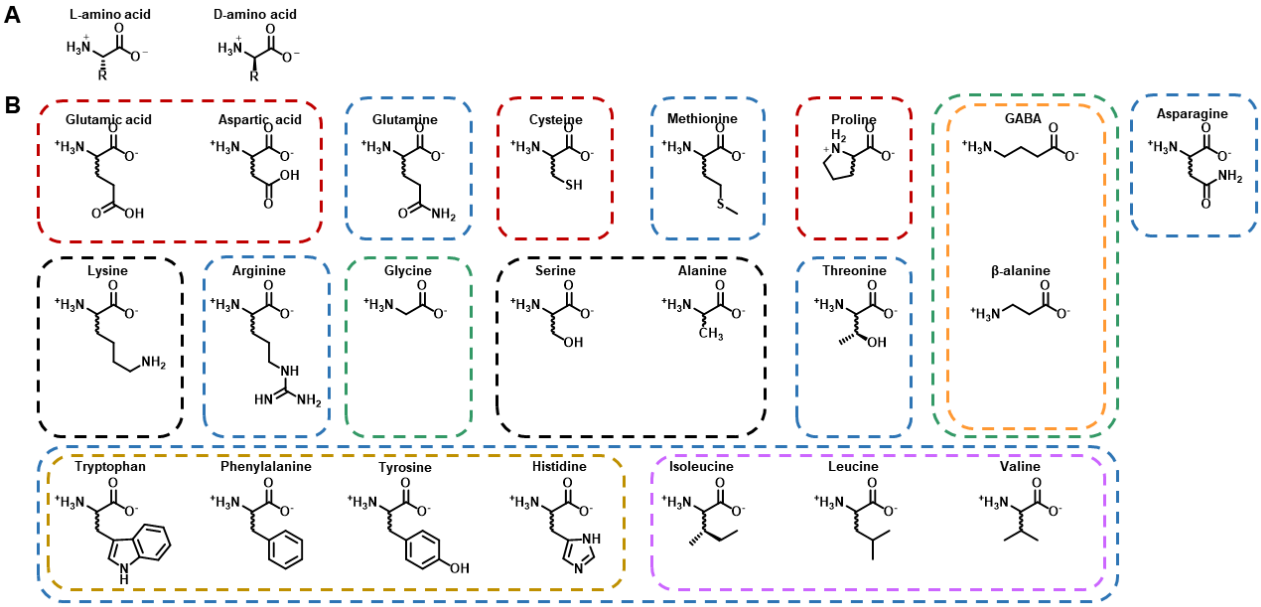

Figure 1-1 - Stereochemistry of amino acids and their side chains.

(a) Stereoisomers of amino acids are classified as D or L. The amino acids in proteins are the L stereoisomers according to the D/L system and are in the *S* configuration of the *R*/*S*

system (except for cysteine which is actually in the *R* configuration due to the presence of a sulfur atom in the side chain and naming conventions). Unless stated otherwise, amino acids referred to in this review should be assumed to be the L stereoisomer. (b) The side chains of the 22 amino acids reviewed in this paper with boxes classifying them based on their main functions within neurotransmission. Non-proteinogenic amino acids are indicated by an orange box. The red boxes denote excitatory amino acids, while the ones in green boxes are inhibitory. Amino acids in blue boxes serve primarily as precursors for neurotransmitters, and the ones in black boxes have neuromodulatory effects. The aromatic amino acids are grouped together in a yellow box, while the branched chain amino acids (BCAAs) are grouped in a purple box.

Table 1-1 – Amino acids and their roles in neurotransmission.
Unless explicitly stated, assume the L isomer. See main text for references.

Amino acid	Excitatory/ Inhibitory	Neurotransmitter/ Neuromodulator/ Precursor	Receptor	Function
Glutamic acid (Glu)	Excitatory	Neurotransmitter	Ionotropic (AMPA, NMDA, and kainate) metabotropic glutamate receptors	Main excitatory neurotransmitter in CNS. Excesses can cause excitotoxicity.
Aspartic acid (Asp)	Excitatory	Neuromodulator, neurotransmitter	NMDA, mGluR5 (D-asp)	L-Asp – neuromodulator (proposed neurotransmitter); NMDAR agonist. D-Asp – neuromodulator (proposed neurotransmitter); involved in hormone release, neurogenesis, learning and memory.
Glutamine (Gln)	N/A	Precursor	Ionotropic glutamate receptors (but requires millimolar concentrations)	Generation of glutamate, GABA, aspartate. Involved in regulating ammonia homeostasis.

				Unclear physiological relevance of glutamine-induced activation of ionotropic glutamate receptors.
Cysteine (Cys)	Excitatory	Neurotransmitter, precursor	NMDA	Physiological relevance of NMDAR activation is unclear. Excitotoxin – unknown mechanism. Precursor to glutathione, L-cysteine sulfuric acid, L-cysteic acid and hydrogen sulfide.
Methionine (Met)	N/A	Precursor	N/A	Precursor to homocysteine, which is an excitatory neuromodulator that binds to NMDA receptors.
Proline (Pro)	Excitatory	Neuromodulator	Glycine, NMDA, AMPA/Kainate	Excess leads to hyperprolinemia (seizures, hyperlocomotion, learning and other cognitive deficits). Stress response.
Asparagine (Asn)	N/A	Precursor	N/A	Precursor to aspartate. Deficiencies in synthesis leads to structural abnormalities in brain.
GABA	Inhibitory (adult); excitatory (developing)	Neurotransmitter	Ionotropic ($GABA_A$) and metabotropic ($GABA_B$)	Major inhibitory neurotransmitter in the brain. Co-released with glycine in some synapses.
Lysine (Lys)	Inhibitory	Neuromodulator, precursor	$GABA_{A,}$ $GPRC6_A$	Precursor for L-glutamate Modulator of GABAergic transmission. Indirect regulation of D-serine Stress response and pain.
Arginine (Arg)	N/A	Precursor	N/A	Precursor to NO_x species and creatine. Reduces stress-induced anxiety.
Glycine (Gly)	Inhibitory	Neurotransmitter	Glycine receptors, NMDA	Main inhibitory neurotransmitter in the spinal cord. Co-released with GABA in some synapses. Co-agonist of (extrasynaptic) NMDA receptors. Involved in cell migration and synaptogenesis.
Serine (Ser)	Both	Precursor, neurotransmitter	NMDA and glycine (D-ser)	L-Ser – precursor to glycine and D-serine; facilitate release of glutamate and aspartate. D-Ser – Co-agonist for glycine and NMDA receptors; involved in Alzheimer's disease and alcohol addiction.

Alanine (Ala)	Both	Neuromodulator	Glycine, NMDA	D-Ala - weaker agonist for glycine receptors and co-agonist for NMDA receptors.
Threonine (Thr)	N/A	Precursor	N/A	Precursor to glycine.
β-alanine (β-Ala)	Inhibitory	Neurotransmitter, precursor	MrgprD, NMDA, $GABA_{A/C}$, Glycine	Rate-limiting precursor to carnosine. Pain modulation. Histamine-independent itch mechanisms.
Aromatic amino acids (phenylalanine (Phe), tryptophan (Trp), tyrosine (Tyr) and histidine (His))	N/A	Precursors	N/A	Precursor to catecholamines, serotonin and histamine.
BCAAs (isoleucine (Ile), leucine (Leu) and valine (Val))	N/A	Precursor	N/A	Competes with aromatic acids' transport, indirectly modulating synthesis of catecholamines, serotonin and histamine. Precursor for glutamate.

1.2 Amino Acids

1.2.1 Glutamic acid

Since Curtis and colleagues first reported its excitatory effects in the late 1950s, L-glutamate, the deprotonated form of L-glutamic acid, has been established as the main excitatory neurotransmitter in the central nervous system (CNS) with glutamatergic synapses accounting for 80 to 90% percent of the brain's synapses and at least 60% of all the synapses in the CNS [1-5]. Glutamate is recycled in synapses through the glutamate-glutamine cycle [6,7]. While we aim to provide sufficient information to orient the reader for the rest of this review, due to the volume of knowledge, a thorough discussion of glutamate's importance in neurotransmission is beyond the scope of this review and we refer readers to other reviews, such as those by Meldrum [8], Featherstone [6] and Zhou and Danbolt [9].

Glutamate concentrations in the synapse can range from less than 20 nM to 5 mM while a recent study found that glutamate concentration in isolated synaptic vesicles was approximately 700 mM [10-12]. Glutamate binds to three ionotropic receptors (i.e., *N*-methyl-D-aspartate (NMDA), α-amino-3-hydroxy-5-methyl-4-isoxazolepropionic acid (AMPA), and kainate receptors) which are all channels that allow the passage of Na^+, K^+ and sometimes Ca^{2+}. Of these, NMDA receptors uniquely function as a coincidence detector as their activation requires the binding of a co-agonist, such as glycine or D-serine, and is also voltage-dependent due to a Mg^{2+} block in the pore [13,14]. Moreover, NMDA receptors conduct Ca^{2+}, which act as a secondary messenger to trigger signalling cascades. Thus, NMDA receptors are critical for synaptic plasticity and learning [15], and it has been implicated in many neurological disorders, such as addiction [16], Alzheimer's disease [17] and others that will be mentioned in this review. Glutamate also binds to three classes of metabotropic glutamate receptors, all of which are GPCRs, that trigger different signalling cascades. Excessive activation of glutamate receptors is called excitotoxicity and leads to neuronal death and degeneration [18]. Additionally, glutamate released into the synapse can diffuse out of the synapse ("spillover") and activate receptors outside of synapses and in other synapses [19-21].

1.2.2 Aspartic acid

Aspartate is a structural homologue of glutamate, with one fewer methylene ($-CH_2$) group in the sidechain. L-Aspartate was first reported to excite neurons along with L-glutamate [3,5] and is generally considered as the secondary excitatory neurotransmitter in the CNS, with some studies suggesting that aspartate and glutamate may be co-released [22-24]. However, unlike L-glutamate, whose role in the brain as the main excitatory neurotransmitter is well-characterized and undisputed, there is still some controversy regarding the status of L-aspartate as a neurotransmitter [25,26].

Stimulus-dependent release of L-aspartate has been observed in different brain regions, such as the visual cortex [27], hippocampus [22,28,29] and cerebellum [30]. It was detected in the rat brain with a concentration of approximately 2.7 μmol/g wet weight, though concentrations may vary depending on the brain region (e.g., the hippocampus has 0.6 nmol/mg tissue) [31,32]. It is mostly formed from an L-aspartate transaminase-catalyzed reaction between oxaloacetate and glutamate. Storck *et al.* [33] demonstrated that excitatory amino acid transporter 1 (EAAT1), also known as the glutamate aspartate transporter 1 (GLAST-1), transports L-aspartate out of the extracellular space, providing a mechanism for its removal. However, the mechanism for vesicular transport remains unclear as the transporters responsible for packaging L-glutamate do not transport L-aspartate [34] and reports of a possible transporter (such as sialin) are still inconclusive [35,36]. L-Aspartate is known to be a selective agonist for NMDA receptors, but a study by Herring *et al.* [25] showed that L-aspartate release is insufficient for activation of NMDA receptors in the hippocampus. However, a report by Richards *et al.* [37] found higher concentrations of aspartate than glutamate in motoneuron synapses, suggesting the possibility for physiologically relevant aspartate-evoked activation of NMDA receptors in the spinal cord. No other receptors for L-aspartate have been identified. Consequently, the significance of L-aspartate signalling remains unclear.

D-Aspartate, the enantiomer of L-aspartate, is found in the brain in significant quantities, although at concentrations ~100× lower than L-aspartate, and meets most of the criteria to be considered a classical neurotransmitter [32,38] (also reviewed by Ota *et al.* [39]). Found in different endocrine tissues and throughout the brain with higher levels occurring during development, D-aspartate's roles include being an agonist for NMDA receptors, and regulating hormone release (e.g., prolactin and luteinizing hormone) and neurogenesis in developing and

adult brains [40-44] (for a review on its neuroendocrine function, see D'Aniello *et al.* [45] and for a deeper discussion on its role in learning and memory, see Errico *et al.* [46]). Additionally, D-aspartate has been reported to activate metabotropic glutamate receptor 5 (mGluR5) [47]. The existence of specific D-aspartate receptors has also been demonstrated [38]; however, these receptors have not yet been identified. Moreover, contrary to the long-standing belief that NMDA is not endogenous in mammals, D-aspartate was also suggested to be a precursor to NMDA in rats [40]. Although serine racemase, to a degree, is able to produce D-aspartate from L-aspartate, the main synthetic pathway for D-aspartate remains an open question since reports of an aspartate racemase have been questioned [32,41,48-50]. However, to the best of our knowledge, like L-aspartate, the transporter responsible for loading D-aspartate into vesicles has not been identified.

1.2.3 Glutamine

Glutamine's main role in neurotransmission is through its participation in the glutamate/GABA-glutamine cycle [6,7,51]. For a deeper discussion of the glutamate/GABA-glutamine cycle, as well as glutamine's other roles in neurotransmission, we refer readers to the reviews by Bak et al. [7] and Albrecht et al. [51].

In glutamatergic synapses, most of the released glutamate is taken up by astrocytes, where it is converted to glutamine by glutamine synthetase. Glutamine is then exported to the extracellular space, where it is taken up by neurons and converted back into glutamate by phosphate-activated glutaminase and packaged into vesicles. Some of the synthesized glutamate may also be metabolized to aspartate. Reflecting this cycle's importance, glutamine is found with concentrations of ~2-8 nmol/mg tissue in the brain, with the highest levels in the hippocampus and higher concentrations in the extracellular fluid (up to 1 mM) [51,52]. Glutamine metabolism is also linked to arginine/nitric oxide (NO_x) metabolism as glutamine synthetase both regulates, and is

regulated by, NO_x [51,53]. Altered expression or activity of glutamine synthetase in the brain has been implicated in epilepsy [51,54], depression [55], and suicidal behavior [56], among others.

The glutamate/GABA-glutamine cycle is a key player in regulating ammonia homeostasis because one molecule of ammonia is consumed or released during the production and metabolism of glutamine, respectively. Ammonia levels must be carefully regulated as excess ammonia can trigger oxidative and nitrosative stress, which lead to increased levels of free radicals and detrimental signalling cascades [57,58]. Additionally, Albrecht and colleagues have proposed that the effects of oxidative and nitrosative stress are exacerbated by excessive glutamine synthesis, a process that consumes ammonia but is proposed to impair mitochondrial function ("the Trojan horse" hypothesis) as the excess glutamine is transported to the mitochondria as an excessive source of ammonia [57,59,60].

Evidence suggests that millimolar concentrations of glutamine can trigger currents carried by ionotropic glutamate receptors, including NMDA receptors, and induce increases in synaptic potential [61,62]. However, Luengo et al. [62] observed a decrease in field excitatory postsynaptic potential for the first 30 minutes upon glutamine application. The physiological relevance of this phenomenon remains unclear.

1.2.4 Cysteine and methionine: sulfur-containing amino acids

The presence of a nucleophilic thiol group bestows cysteine and its derivatives with unique chemical properties that enable them to serve specialized functions within cells. L-Cysteine is most broadly recognized as a precursor for glutathione, the body's main antioxidant (for more thorough discussions on the roles of glutathione in the nervous system, see the reviews by Dringen and colleagues [63-65]). However, despite lacking the carboxylic acid-containing side chain characteristic of excitatory neurotransmitters, L-cysteine possesses many of their characteristics. Specifically, cysteine can: 1) be released by neuron depolarization in a Ca^{2+}-dependent manner; 2)

activate NMDA receptors; and 3) be taken up by neurons and glia [66-68]. However, while L-cysteine is able to trigger synaptic activity and is a known excitotoxin, its exact mechanisms of action remain unclear (reviewed by Janàky *et al.* [69]). Beyond excitatory targets, Gonzáles and colleagues recently showed that L-cysteine antagonized $GABA_A\rho1$ receptors [70]. L-Cysteine also acts as scavenger for acetaldehyde, the first metabolite of ethanol, reducing acetaldehyde-induced activation of the mesolimbic dopamine pathway and dampening its motivational properties indirectly [71-74]. Additionally, in the extracellular space, cysteine can be oxidized into cystine (i.e., two cysteines connected by a disulfide bond) and taken up by astrocytes through cystine/glutamate antiporter system x_c^- (for a comprehensive review, see Lewerenz *et al.* [75]), where this extrasynaptic release of glutamate has been shown to activate extrasynaptic NMDA receptors [76]. Lastly, cysteine can be metabolized into other neuroactive compounds, such as L-cysteine sulfinic acid, L-cysteic acid and hydrogen sulfide [77-79]

Besides cysteine, methionine is the other sulfur-containing proteinogenic amino acid, albeit with a methylated thiol group. As an essential amino acid, methionine is transported into the CNS using the same systems used by the branched chain and aromatic amino acids [80,81]. Methionine serves as the precursor to homocysteine, which, like cysteine, can activate glutamatergic receptors and excite neurons, even to the point of excitotoxicity through an NMDA receptor-mediated pathway [82-84]. In addition to activating neurons by itself, evidence also suggests that homocysteine can trigger release of other excitatory amino acids [85]. Homocysteine has been implicated in anxiety [86], alcoholism [87], Alzheimer's disease [88] and schizophrenia [89].

1.2.5 Proline

L-Proline is a non-essential amino acid that can be synthesized from L-glutamate [90]. Hyperprolinemia, a genetic condition causing excessive levels of proline due to impaired proline

metabolism, is associated with seizures, hypolocomotion, learning and other cognitive deficits, and an increased risk for schizophrenia [91-93]. L-Proline is a known neuromodulator in the brain and fulfills many of the criteria of a classic neurotransmitter [90,94-96], arguably even more so than L-aspartate, which is generally considered to be a neurotransmitter. For example, unlike L-aspartate, a vesicular transporter for L-proline, NTT4, has been identified [97]. Although a proline-specific receptor has not been identified, L-proline is a weak agonist for glycine receptors, as well as the glutamate-responsive NMDA and AMPA/kainate receptors [98]. The lower limit of the extracellular concentration of L-proline was estimated to be 10 nM [99,100]. Regardless, physiological extracellular concentrations of L-proline have been shown to modulate glutamate transmission with the ability to induce excitotoxicity [101-103]. Behaviorally, activation of NMDA receptors by L-proline has also been shown to mediate stress responses in chicks under acute stress by altering the stress-induced metabolism of dopamine and serotonin [104,105].

Multiple transport systems, such as the PROT transporter, have been identified for L-proline, and the specific contribution of each transport system with respect to regulating L-proline levels and their physiological importance remains unclear [106-109]. A recent study by Schulz and colleagues [110] showed that $PROT^{-/-}$ mice lost more than 70% of L-proline uptake in brain regions where PROT is the most strongly expressed transporter such as the cortex, hippocampus, thalamus and striatum without resulting in extreme increases in extracellular L-proline concentration. However, PROT was previously shown to be more highly localized in synaptic vesicles than plasma membrane but is not considered to participate in loading L-proline into synaptic vesicles [99,100]. These vesicles were instead believed to act as a reserve pool of transporters that can then be moved to the plasma membrane to regulate L-proline uptake and neuronal activity [100]. Instead, B^0AT2, another L-proline transporter, was proposed to be the major transporter responsible for

uptake of extracellular L-proline [81]. Behaviorally, these mice showed deficits in memory extinction and locomotion, in line with the observed reductions in PROT activity and downstream effectors important in learning and memory in some regions [110-112]. At the same time, this study also reported that the reduction in PROT activity did not cause changes in the levels of the downstream effectors in the hippocampus, a region with one of the highest levels of PROT expression, suggesting possible compensatory mechanism in some regions.

Furthermore, L-proline has been demonstrated in rats to induce oxidative stress in the cerebral cortex, reducing the total radical-trapping antioxidant potential and increasing lipid peroxidation [113]. This proline-induced oxidative stress has been linked to proline's inhibitory effects on both Na^+/K^+ pump and acetylcholinesterase activity [114,115]. Despite these advances, our understanding of proline's role in neurotransmission and the CNS is incomplete, even more so when we consider the implications of glycine receptor activation by L-proline.

1.2.6 Asparagine

Evidence to date suggests that L-asparagine is present in the brain at low concentrations and, outside of protein synthesis, is limited to serving as a precursor L-aspartate production by asparaginases like the astrocyte-exclusive Gliap [32,116]. Asparagine can be synthesized from aspartate by asparagine synthetase, and deficiencies in this enzyme have been reported to cause brain structural abnormalities and cognitive impairments [117,118]. Asparagine is transported into the brain in competition with glutamine and histidine [80]; however, despite this competition, L-asparagine supplementation was not reported to significantly reduce glutamine levels in the brain and did not affect the levels of related neurotransmitters (i.e., glutamate, aspartate or GABA levels) in the cerebellum and medulla oblongata [119], unlike the case with BCAAs and aromatic amino

acids-derived neurotransmitters (discussed below). This lack of effect is likely because asparagine can be endogenously synthesized.

1.2.7 γ-Aminobutyric acid

γ-Aminobutyric acid (GABA) is known as the major inhibitory neurotransmitter in the brain. Although it is an amino acid, GABA is not used in proteogenesis, but functions as a signaling molecule, with the ability to induce changes in signal transduction in both presynaptic and postsynaptic neurons [120]. It is synthesized from the decarboxylation of glutamate by glutamate decarboxylase and is recycled through the GABAergic synapses in a process analogous to the glutamate-glutamine cycle [7]. GABA, upon binding to its receptors $GABA_A$ and $GABA_C$, causes chloride channels in neurons to open [120]. This opening can lead to depolarization in immature mammals and hyperpolarization in mature mammals [121]. Therefore, abnormal levels of GABA are commonly implicated in many psychiatric disorders, most commonly in epilepsy [122]. Other psychiatric diseases have aberrant GABA signaling. For example, late stages of Alzheimer's disease are associated with decreased GABA levels as well as aberrant $GABA_A$ receptor presence [120]. GABAergic transmission is also implicated in anxiety disorders, schizophrenia [122], Huntington's [123] and pharmacological manipulation of GABA levels is a therapeutic strategy.

1.2.8 Lysine

L-Lysine is an essential charged amino acid transported into the CNS by multiple amino acid transporters [80,106]. L-Lysine is metabolized by either the saccharopine pathway or the pipecolic acid (PA) pathway, which ultimately converge (Figure 2) [124]. While the PA pathway was long believed to be the dominant pathway in the brain [124,125], an initial report by Papes *et al.* [126] challenged this view and reopened the discussion. Almost a decade later, an enzyme was discovered that converts piperideine-6-carboxylic acid back to pipecolic acid, which was initially believed to be a metabolite exclusive to the PA pathway [127,128]. Subsequent work by Pena *et*

al. [129] and Crowther *et al.* [130] have since shown that the saccharopine pathway is the major pathway for lysine metabolism. The distribution of lysine metabolism was of particular interest because L-lysine, through the saccharopine pathway and separate from the glutamate/GABA-glutamine cycle, is a precursor for L-glutamate, with the initial report by Papes *et al.* [126] estimating that approximately a third of glutamate in the CNS is from L-lysine. On the other hand, piperideine-2-carboxylic acid is an inhibitor of D-amino acid oxidase, which regulates levels of D-serine, a co-agonist of the NMDA receptor, and thus implicating lysine metabolism in schizophrenia (see review by Hallen *et al.* [124]).

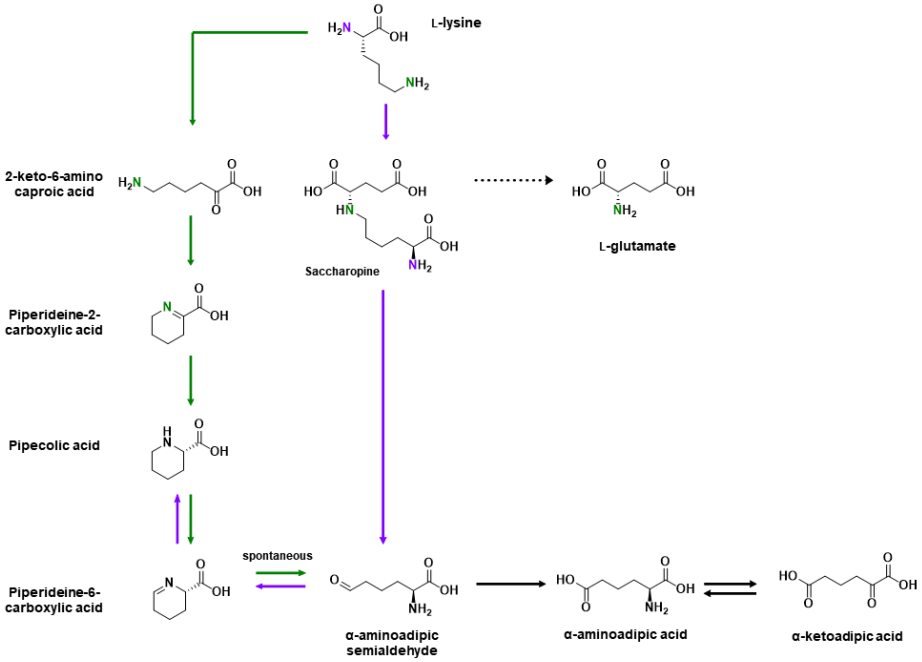

Figure 1-2 - Metabolic pathways of L-lysine.

L-Lysine is metabolized either through the saccharopine pathway (purple arrows) or the pipecolic acid pathway (green arrows), highlighting the two pathways' convergence through spontaneous cyclization and ring opening. Because a more thorough discussion of lysine's metabolic pathways is beyond the scope of this review, the enzymes involved in these pathways were omitted. The two nitrogen atoms from lysine are coloured in purple

and green to enable atom tracing, but this distinction is lost in metabolites accessible to both pathways (i.e., pipecolic acid to α-ketoadipic acid). Adapted from Crowther *et al.* [130].

One of the earliest discovered neuromodulatory effects of L-lysine is its effect on GABAergic transmission. In a series of works, Chang and colleagues showed that L-lysine, but not necessarily its metabolites, delayed the onset of seizures induced by pentylenetetrazol and increased seizure protection by acting through $GABA_A$ receptors in a barbiturate-like manner to increase the affinity of benzodiazepines to its receptor [131-133]. D-Lysine was also able to delay seizure onset and confer seizure protection but with a different time course [131]. However, chronic administration of L-lysine was found to cause tolerance, with maximum protective effects peaking at 10 days of administration and decreasing when treatment time was extended to 20 days [134]. However, a clinical study by Ebrahimi and Ebrahimi [135] reported that oral administration of lysine did not reduce seizure frequency in uncontrolled epilepsy patients, suggesting that in addition to bioavailability, the type of seizure is probably relevant.

L-Lysine has also been shown to ameliorate stress-induced anxiety, likely by inhibiting serotonin (5-HT) binding to the 5-HT_4 receptors found in the CNS and in intestines [136,137]. It was also found to be a ligand for the orphan GPRC6A receptor, which has been implicated in the endocrine system through insulin and testosterone functions [138]. L-Lysine, by itself and in conjunction with L-arginine, has also been shown to protect against ischemic insults resulting from suppression of glutamate-induced neuronal activity [139]. Recently, L-lysine was shown to affect pain-induced behavior in rats [140].

1.2.9 Arginine

L-Arginine is a semi-essential amino acid that is transported in the brain by a multitude of systems [80,106,141]. In the extracellular space of the rat brain, its resting concentration was estimated to be 17 μM [142]. Its metabolism is closely related to two other amino acids, L-citrulline and L-ornithine (reviewed thoroughly by Wiesinger [143,144]). Briefly, L-arginine can be metabolized to produce L-citrulline or L-ornithine, and it can also be recycled back from L-citrulline through the citrulline- NO_x cycle in neurons and glia. The main role of L-arginine in the nervous system is to serve as a precursor for NO_x, producing citrulline as a by-product, via the activity of nitric oxide synthases. NO_x possesses many physiological functions, and in the brain, it plays roles in development, protection against brain injury, and learning and memory [139,145-148]. Additionally, while L-arginine's effect on ameliorating stress-induced anxiety is likely due to NO_x production [136,149], evidence of L-ornithine, either directly administered or administered as L-arginine, having an ameliorating effect on stress responses suggests the possibility of a NO_x -independent pathway [150-152]. L-Arginine is also a precursor for creatine, and deficiencies in creatine synthesis have been related to different neurological conditions, such as speech impairments and movement disorders [153].

1.2.10 Glycine

Glycine is primarily synthesized from L-serine but is also metabolized to produce L-serine [154]. Glycine is the main inhibitory neurotransmitter in the spinal cord, brainstem and cerebellum, where it binds to glycine receptors (ionotropic Cl^- channels) when released [3,155-157]. A subset of synapses co-release glycine and GABA, leading to a mixture of variable cytosolic concentrations and an effective tuning of the degree of, inhibition [158-161]. Released glycine is removed from the extracellular space by glycine transporters. GlyT-2 is a transporter that is mostly involved with synaptic glycine reuptake into presynaptic terminals for recycling [156,162]. GlyT-1 is involved in

glycine clearance from the synapse but is also involved in the release of glycine from astrocytes in glutamatergic synapses [163]. Accordingly, it can regulate extrasynaptic glycine levels through both release and removal. Extrasynaptic GlyT-1 has an increased sensitivity to glycine [163]. It is involved in pain perception and movement, and its dysfunction has been implicated in neuropathic pain [164] and several startle conditions (reviewed in [165,166]). During embryonic and early postnatal development, the activation of glycine receptors is involved in cell migration and synaptogenesis with their activation causing depolarization due to the Cl^- gradient (reviewed by Avila *et al.* [167]). During development, glycine receptors tend to be expressed in the cortex though these channels may be primarily activated by taurine due to insufficient levels of glycine [167-169].

Glycine is also a co-agonist required for the activation of NMDA receptors [13]. At glutamatergic synapses, glycine released into the synapse is reported to spill over and activate extrasynaptic NMDA receptors preferentially (due to increased sensitivity relative to synaptic NMDA receptors) [170]. Ahmadi *et al.* [171] reported that, in the spinal cord, glycine released in the synapses of inhibitory interneurons can spillover out of the synapse and activate nearby NMDA receptors. This rate of glycine spill over is influenced by GlyT-1 [163,170].

1.2.11 Serine

Both enantiomers of serine are neurologically active. L-Serine acts as an important developmental and signalling molecule as well as a precursor for neuroactive molecules. L-Serine is synthesized in the brain by astrocytes using four different pathways, and deficiencies have been linked to many developmental disorders and neuropathies [172,173]. A case study has noted various developmental deficiencies such as retardation in growth, ichthyosis, polyneuropathy, and delayed puberty in one female patient [174].

A study by Buratta *et al.* [175] found that L-serine may be involved in the extracellular release of glutamate and aspartate through a signalling intermediate, ethanolamine. Further *in vitro*

studies have observed that L-serine administration increased growth of the cerebellum's Purkinje fibres and enhanced growth of dendrites in hippocampal slices [176,177]. In addition to aiding growth and the release of other amino acid neurotransmitters, L-serine also serves as a precursor to the synthesis of both glycine and D-serine, the latter of which is synthesized by serine racemase [52,154,178,179].

Although D-serine is a known neuromodulator, it does satisfy the conditions to be a neurotransmitter. Though initially reported to be a glial enzyme, serine racemase is present in significant quantities in neurons [180,181]. D-Serine competitively binds to the glycine co-agonist binding site, evoking ~90% of the glycine response [13,182]. Indeed, Papouin *et al.* [170] reported that D-serine is the co-agonist for NMDA receptors. Unlike most neurotransmitters, D-serine is also released by glia (reviewed by van Horn *et al.* [183]). Its role in NMDA modulation has implicated functions in Alzheimer's disease and alcohol addiction, where elevated levels of D-serine were positively correlated with increased symptoms for Alzheimer's disease on the Alzheimer's Disease Assessment Scale, as well as to decreased dependency on alcohol use [184,185]. Comprehensive reviews by Mustafa *et al.* [182] and Wolosker [186] can provide detailed information on D-serine function in the brain.

1.2.12 Alanine

D-Alanine is present in brain tissues, with the highest concentration in the anterior pituitary gland (~86 nmol/g wet tissue) [32,187]. It is a known ligand for glycine receptors and can act as a co-agonist for NMDA receptors, albeit only evoking 62% of the glycine response [3,13]. Its enantiomer is also a weak agonist of NMDA receptors (evoking 12% of the glycine response) as well as glycine receptors [3,13]. D-Alanine is believed to be sourced, in part, from intestinal bacteria, with antibiotic-induced psychosis hypothesized to be caused a by a reduction of D-alanine producing bacteria in the gut [188,189]. However, the systems involved in transporting D-amino

acids through the blood-brain barrier (BBB) remain unidentified [190]. Like other D-amino acids, it is metabolized by D-amino acid oxidase [191].

Amphetamines are stimulants long known to induce hyperlocomotion through aberrant dopaminergic transmission. In 1971, Iversen *et al.* [192] reported that lesions on the frontal cortex, whose projections excite neurons in the caudate nucleus that inhibit motor functions, enhanced amphetamine-induced hyperlocomotion without affecting dopamine levels. This observed connection suggests that a reduction in glutamatergic transmission may be upstream of amphetamine-induced hyperlocomotion. Atsushi *et al.* [193] then demonstrated that D-alanine, but not L-alanine, could inhibit methamphetamine-induced hyperlocomotion, suggesting that NMDA receptor hypofunction may be responsible for the observed hyperlocomotion. Further studies identified the dopamine D_3 receptor to be a major downstream target for these NMDA receptor-mediated locomotor effects [194].

In addition to understanding the effects of stimulants in the brain and on behavior, animal models with drug-induced manipulations of the nervous system (e.g., methamphetamine-induced hyperlocomotion or psychosis) are useful in understanding schizophrenia (reviewed by Jones *et al.* [195]). The initial hypothesis that schizophrenia is caused by excessive dopaminergic transmission ("dopamine hypothesis") has since expanded to be the NMDA receptor hypofunction hypothesis, where decreased NMDA receptor function may lead to aberrant signalling, such as in dopaminergic pathways (reviewed by Olney *et al.* [196] and Hashimoto [197]). In line with this hypothesis, studies have demonstrated that supplementing antipsychotic drugs or D-amino acid oxidase inhibitors with D-alanine shows promise for treatment of schizophrenia [198,199].

1.2.13 Threonine

Originally probed as a possible amino acid neurotransmitter in the 1980s, threonine is a proteogenic, essential amino acid that is transported into the brain by multiple transport systems

[80,106]. However, no neurotransmitter-like function has been reported, and the main non-proteinogenic role for threonine in the brain may be to a precursor for glycine [200,201]. Oral administration of threonine for those with spinal spasticity, a disorder related to aberrant peripheral nervous system (PNS) signalling, led to alleviation of spastic symptoms [202]. However, a systematic review of oral treatments for spasticity as a symptom of multiple sclerosis found that threonine administration generally did not relieve symptoms [203].

1.2.14 β-Alanine

β-Alanine is a non-proteinogenic amino acid neurotransmitter found in the CNS that is a structural intermediate of α-amino acids (e.g., alanine) and γ-amino acids (e.g., GABA). For a comprehensive review of the biochemistry of β-alanine and its role as a neurotransmitter, we refer readers to the review by Tiedje and colleagues [204].

Expanding on the evidence presented by Tiedje et al. [204] suggesting that β-alanine is a neurotransmitter, vesicular GABA transporter (VGAT) was reported to be capable of transporting β-alanine, providing a possible mechanism for β-alanine transport into vesicles [205]. In 2004, over forty years after the first reports of β-alanine's inhibitory effects on neurons, Shinohara and colleagues identified β-alanine, out of over 1500 compounds, as a specific ligand for the orphan GPCR, MrgprD [206-208].

MrgprD belongs to the Mas-related genes, a subfamily of GPCRs expressed mostly in sensory neurons of the dorsal root ganglia. It is co-expressed with major nociceptors in a subset of small diameter neurons that exclusively target a specific layer of the epidermis, suggesting an involvement in pain modulation [206,207,209]. Early reports regarding MrgprD function found that silencing MrgprD expression reduced the sensitivity of mice to noxious mechanical stimuli by inhibiting a specific type of K^+ current and thereby enhancing the excitability of MrgprD-

expressing neurons [210,211]. MrgprD activation also opened Ca^{2+}-activated chloride channels through the phospholipase C pathway [212]. Consistent with its proposed role in pain modulation, upregulated MrgprD expression caused enhanced mechanical hypersensitivity in mice models for neuropathic pain induced by chronic constriction injury [206,213]. MrgprD has been reported to play a role in the perception of noxious thermal stimuli [210,213].

MrgprD has also been implicated in histamine-independent itch mechanisms. Liu and colleagues showed that intradermal or oral β-alanine supplementation triggered an itch response in humans and confirmed with animal models that this response is mediated by MrgprD activation [214]. They also observed that β-alanine induced itch response only in a subset of MrgprD-expressing neurons, and that these neurons were also activated by heat. Taken together, these findings suggest a possible functional division between MrgprD-expressing neurons, with some neurons mediating itch and others mediating pain.

1.2.15 Aromatic amino acids

The aromatic amino acids consist of phenylalanine, tryptophan, tyrosine, and histidine. All but tyrosine are essential amino acids, while tyrosine is considered semi-essential because it can be synthesized by hydroxylation of phenylalanine. Therefore, tyrosine must only be consumed if insufficient phenylalanine is consumed or if the conversion of phenylalanine to tyrosine is deficient, such as in patients suffering from phenylketonuria [215]. These amino acids are transported into the CNS through the BBB, which occurs via the same transporters (and thus in competition) with other amino acids, such as the branched chain amino acids (BCAAs) [80,106,216]. Notably, unlike the other aromatic amino acids, histidine is also transported by system N (prefers amino acids with nitrogen in the side chain), which also transports asparagine and glutamine [80]. To our knowledge, the main role of these amino acids in neurotransmission is as precursors for the synthesis of key neurotransmitters.

Tryptophan is converted into 5-HT through a two-step synthesis catalyzed first by tryptophan hydroxylase as the rate-limiting step followed by 5-HTP decarboxylase [217]. Under normal conditions, tryptophan hydroxylase is not saturated by tryptophan, thus changes to tryptophan levels in the brain, such as those caused by dietary changes, can affect the rate of 5-HT synthesis and release [217]. Indeed, the (highly variable) effects of tryptophan levels on mood (which is well-known to be modulated by 5-HT) have been extensively studied (for a recent review, see Jenkins *et al.* [218]). Furthermore, patients with hypertryptophanemia have presented with neurological deficits such as mood swings, reduced IQs and impaired memory [219]. The kynurenine pathway, the other metabolic pathway for tryptophan, has been linked to the pipecolic acid pathway for lysine metabolism on account of shared enzymes, and this connection has been implicated in different neurological conditions (for a more thorough discussion, we refer readers to Hallen *et al.* [124]).

Similarly, dopamine, norepinephrine and epinephrine are sequentially synthesized from tyrosine (either taken up from diet or synthesized by phenylalanine hydroxylation) with the initial step being rate-limiting and catalyzed by tyrosine hydroxylase [217,220]. The hydroxylation of phenylalanine can also be catalyzed by tyrosine hydroxylase in the brain [221]. Acute phenylalanine and tyrosine depletion has been used to temporarily reduce dopamine synthesis with some demonstrated effects on mood and cognition [222-224]. Although these conditions can be controlled by a combination of dietary restrictions and/or drugs, patients suffering from hypertyrosinemia or phenylketonuria were found to have cognitive deficits relative to healthy controls [225,226].

Likewise, histidine decarboxylase converts histidine to histamine, a neurotransmitter most known for its role in regulating sleep and wakefulness but is also involved in other important functions like arousal, feeding, motivation and endocrine regulation (for a comprehensive review

of histamine and its roles and actions in the nervous system, we refer readers to Haas *et al.* [227]). Histidine decarboxylase is not saturated under normal conditions, and changes in plasma histidine levels can lead to changes in brain histidine and histamine levels [228]. However, unlike with the other aromatic amino acids where their acute depletion is an established paradigm for manipulating neurotransmitter levels, there has been little investigation of the effects of histidine depletion on cognition [229].

1.2.16 Branched chain amino acids

Isoleucine, leucine and valine have similar biochemical properties, and are collectively referred to as the BCAAs. BCAAs are essential and must be transported into the CNS through the BBB in competition with the aromatic and other large neutral amino acids [80,106,216]. Consequently, fluctuations in BCAA levels affect the synthesis and concentrations of these aromatic amino acid-derived neurotransmitters, indirectly modulating the synthesis and release of these neurotransmitters [215,217]. For example, rats on diets supplemented with BCAA exhibited anxiety-like behaviors that can be reversed by tryptophan supplementation [230]. This relationship between BCAAs and aromatic amino acid precursors have been explored as a possible avenue for treatment of serotonin or catecholamine imbalance-related symptoms for different neurological conditions such as phenylketonuria, bipolar disorders, and anorexia, with increased BCAA intake leading to some improvements (reviewed by Fernstrom *et al.* in [215]). In healthy humans, there is some debate regarding the use of BCAAs to combat central fatigue, where changes in levels of serotonin and catecholamines in the CNS are believed to reduce muscle function and exercise performance after prolonged exercise, with evidence both favouring and rejecting the benefits of BCAAs (see the review by Meeusen *et al.* [231] for a discussion on the central fatigue hypothesis, as well as the reviews by Fernstrom *et al.* [215] and Newsholme *et al.* [232] for examples of studies analyzing the benefits of BCAAs and their possible mechanisms).

In the brain, BCAAs can also be converted into glutamate through branched chain amino acid transaminases, replenishing the more commonly known glutamate-glutamine cycle [233]. LaNoue and colleagues [234] found that approximately 30% of de novo glutamate synthesis came from transamination of BCAAs in the retina, and the ubiquity of the branched-chain aminotransferase in the CNS suggests that BCAA transamination is a significant contributor to de novo glutamate synthesis in the rest of the CNS as well [235]. High concentrations of BCAAs, such as those found in patients with maple syrup urine disease, were found to be neurotoxic due to increased excitotoxicity and oxidative stress [236-238].

1.3 Fluorescence imaging

Fluorescent probes generally consist of two components: a sensing domain that interacts with the ligand and a fluorescent reporter domain that shows a change in fluorescence intensity upon ligand binding. In this review, fluorescent sensors will first be categorized by their component scaffolds' type (i.e., synthetic dye-based, genetically encoded single fluorescent protein (FP)-based, quantum dots (QDs)-based, nanotubes-based, or hybrids), consisting of single or non-interacting fluorophores, followed by the last section focusing on Förster Resonance Energy Transfer (FRET)-based sensors, which require transfers of energy between two fluorophores, using these different scaffolds. Additionally, although there is an array of fluorescent sensors available for visualizing amino acids, especially for synthetic dye-based sensors, we will mostly confine our review to sensors that have been demonstrated in live cells with limited toxicity.

For the sake of this review, we will be summarizing the past work in the area and stating the various sensors that have been reported. However, it is important to consider that not all of the reported sensors provide the same degree of performance and some only possess small signal changes that may render them impractical for many applications. In addition, the quality of the reported data is also highly variable, with some sensor characterization data seeming to be of

questionable quality [239-251]. More specifically, in the course of preparing this review, we found that the data (such as the spectra, affinity titrations, or specificity tests) for some reported sensors were not internally consistent within a single publication. With these sensors, the responses we calculated from either provided spectra, the affinity titrations, or specificity tests do not agree with each other. Consequently, we express some reservations concerning the performance of some of these sensors because of the lack of internal consistencies within the data. Nevertheless, we included these sensors to present a more complete portrait of the toolbox of available sensors. We caution that researchers using these sensors perform their own validation and run experiments in parallel with a non-responsive control construct.

Table 1-2 - Fluorescent indicators for amino acids.

Ligand	Type	Name	Multiple Variants?	Color	$\Delta F/F_{min}$ or $\Delta R/R_{min}$	Response *in vitro*[a]	Ref.
Glu	Synthetic	N,N-SP-BPY	No	Green	$\Delta F/F_{min}$	~8.8[b,c]	[244]
	Genetically encoded (GE)	iGluSnFR		Green	$\Delta F/F_{min}$	4.5	[252]
		$iGlu_f$ and $iGlu_u$	Yes			3.0	[253]
		sf-iGluSnFR		Blue to green		4.5	[254]
		R-iGluSnFR		Green and red		3.9	[255]
	FRET (GE)	FLIPE	Yes	Cyan/yellow	$\Delta R/R_{min}$	0.27	[256]
		SuperGluSnFR	No			0.44	[20]
		FLIP-cpGltI210				0.31	[257]
	Hybrid	EOS	No	Green	$\Delta F/F_{min}$	0.37	[258]
		EOS-K716A and EOS-L401C	Yes			0.48	[259]
		eEOS	No			24	[260]
	Hybrid FRET	Snifit-iGluR5	No	Green/far red	$\Delta R/R_{min}$	0.93	[261]
Asp	Synthetic	8MPS	No	Green	$\Delta F/F_{min}$	~30[c]	[262]
		N,N-SP-BPY				~8.8[b,c]	[244]
	FRET (GE)	FLIP-cpGltI210	No	Cyan/yellow	$\Delta R/R_{min}$	0.31	[257]
Gln	FRET (GE)	FLIP-cpGlnH183	No	Cyan/yellow	$\Delta R/R_{min}$	0.13	[257]
		FLIPQ	Yes			0.26	[263]
		$EGFP_{-10}$-GlnBP-N138CouA	No	Blue/green		0.89	[264]
Cys	Synthetic	Probe **1**		Blue	$\Delta F/F_{min}$	66	[265]
		Probe **1**		Blue		~120[c]	[266]
		NCQ		Blue/green		~4.7,3[c]	[267]
		Nap-Cys			$\Delta R/R_{min}$	22	[268]

		TCS		Cyan	$\Delta F/F_{min}$	25[b]	[245]
		Probe **1**		Green		130[b]	[246]
		GT-Cys			$\Delta F/F_{min}$	110[b]	[247]
		NPCC				13	[269]
		Gol-Cys				20	[270]
		Ly-1				8.8	[271]
		CyP				~33[c]	[272]
		Compound 1				~9[c]	[273]
		BDY-NBD		Green/NIR		~7400,9.8[c,d,e]	[274]
		hCy-A		Green/red	$\Delta R/R_{min}$	~8[c]	[275]
		PYR			$\Delta R/R_{min}$	163	[276]
		XCN		Red	$\Delta F/F_{min}$	1081	[277]
		P-Cy				3	[248]
		DCIP				~5[b,c]	[249]
		CyA		NIR		~6.5[c]	[278]
		Cy-S-diOMe				250	[279]
		NFL1				~20[c]	[280]
		DDNA				31[f]	[281]
		CP-NIR				40	[282]
		Mito-CP				12[b]	[250]
		DP-NIR				7.5[b]	[251]
	QDs	T-$CuInS_2$ QDs	No	Red	$\Delta F/F_{min}$	0.72	[283]
	FRET (GE)	Cys-FS	Yes	Cyan/yellow	$\Delta R/R_{min}$	0.42[b]	[239]
	FRET	TP-Ratio-Cys	No	Blue/yellow		36	[284]
	(Synthetic)	Probe **1**	No	Blue/green		50	[285]
Met	FRET (GE)	FLIPM	Yes	Cyan/yellow	$\Delta R/R_{min}$	0.42[b]	[243]
		YFP-MetQ-R189CouA		Blue/yellow		1.7	[286]
GABA	GE	iGABASnFR	Yes	Green	$\Delta F/F_{min}$	4.5	[287]
	Hybrid	Pf622.V278C-JF585	No	Red	$\Delta F/F_{min}$	~0.7	[287]
		GABA-Snifit	Yes	Green/far red	$\Delta R/R_{min}$	0.8	[288]
Lys	FRET (GE)	ECFP-cpLAO-BP-Citrine	Yes	Cyan/yellow	$\Delta R/R_{min}$	~0.83	[289]
		FLIPK				~0.26[b,c]	[242]
Arg	FRET (GE)	QBP/Citrine/ECFP	Yes	Cyan/yellow	$\Delta R/R_{min}$	~0.25	[290]
		FLIP-cpArgT194	No			0.54	[257]
		cpFLIPR				0.35	[142]
Gly	FRET (GE)	GlyFS	No	Cyan/yellow	$\Delta R/R_{min}$	0.28	[291]
Thr	QDs	T-$CuInS_2$ QDs	No	Red	$\Delta F/F_{min}$	0.37	[283]
Trp	FRET (GE)	FLIPW-CTYT	No	Cyan/yellow	$\Delta R/R_{min}$	0.35	[292]
His	Synthetic	CAQA	No	Blue	$\Delta F/F_{min}$	~18[c]	[293]
		NPC		Green	$\Delta F/F_{min}$	6	[294]
		NCH-Cu^{2+}		Green		10[c]	[295]
	GE	FHisJ	Yes	Yellow	$\Delta F/F_{min}$	5.2	[296]
	QDs	T-$CuInS_2$ QDs	No	Red	$\Delta F/F_{min}$	0.46	[283]
		Y-CDs		Yellow		4.5	[297]

	FRET	FLIP-cpHisJ194	No	Cyan/yellow	$\Delta R/R_{min}$	0.63	[257]
Ile	FRET	FLIP-cpLivJ261	Yes	Cyan/yellow	$\Delta R/R_{min}$	0.25	[257]
		GEII	Yes			0.44[b]	[240]
		OLIVe	No			1.05	[298]
Leu	FRET	FLIP-cpLivJ261	Yes	Cyan/yellow	$\Delta R/R_{min}$	0.25	[257]
		FLIP-Leu				~0.7[b]	[241]
		OLIVe	No			1.05	[298]
Val	FRET	FLIP-cpLivJ261	No	Cyan/yellow	$\Delta R/R_{min}$	0.25	[257]
		OLIVe				~0.9	[298]

[a] For sensors with multiple variants, the maximum response is reported.

[b] These sensors show an apparent lack of internal consistency in the characterization data.

[c] Response was not explicitly reported or easily calculatable from an equation and was consequently estimated based on the provided data.

[d] Response estimated using a non-zero minimum concentration of ligand in the linear range.

[e] Two fluorescent species with their own responses to cysteine.

[f] Response calculated with maximum concentration for linear range, which is below the maximum tested concentration.

1.3.1 Synthetic dye-based indicators (excluding FRET-based sensors)

Synthetic dye-based indicators can be employed for the detection of amino acids. Generally speaking, synthetic dye-based indicators can provide a convenient method for imaging the concentration of their respective analytes, often showing large responses due to their turn on/off nature and fast response kinetics, though many designs involve an irreversible reaction to detect their target, and are not applicable to imaging dynamic reversible changes. Unlike simpler ions, (such as metal cations, non-metal anions and small polyatomic ions), which have more readily available synthetic sensors using a range of different recognition moieties (often referred to in the literature as "synthetic receptors") [299-302], amino acids have a common backbone and different (yet typically quite flexible) side chains, which complicates efforts to design synthetic receptors for amino acids with high specificity. This difficulty is because synthetic receptors require precise spatial organization of small organic and inorganic molecule building blocks, which are not significantly larger than amino acids, to form complexes with their targets. Thus, because of the

limited availability of synthetic amino acid receptors, many of the available synthetic dye-based sensors require a reaction to detect their targets, though significant strides have been made in recent years in designing synthetic amino acid receptors [303]. In addition, synthetic dye-based indicators may show poor photostability and be toxic to cells [304,305]. For a review of synthetic dyes and a comparison with quantum dots, we refer readers to the review by Resch-Genger *et al.* [305].

Many previously reported efforts have focused on the synthesis of dyes for cysteine detection, with at least 24 synthetic dye-based reported to function in detecting cysteine in the past five years (**Table 1-2**) [245-251,265-282]. Of these, several can be targeted to the mitochondria [250,276,279,280], the Golgi apparatus [247,270], the endoplasmic reticulum [268,269] and the lysosome [271]. Five act as non-specific sensors, detecting cysteine and other molecules that contain thiol groups or cysteine metabolites, with some using different wavelengths to distinguish between the different ligands [246,265,267,274,277]. These synthetic sensors all require irreversible reactions to detect cysteine, negatively affecting kinetics and requiring at least 5 minutes to an hour for maximum fluorescence [245,247,248,250,265-280,282].

Outside of these cysteine- and thiol-sensitive dyes, three synthetic sensors, one based on coumarin and the other two based on naphthalimide were published for the detection of histidine in cells (**Table 1-2**) [293-295]. The first, CAQA, was reported to be specific but retained a significant response to cysteine and other thiols present in cells; in this study, cells were treated with a thiol scavenger to eliminate any interfering thiols [293]. The other two can reversibly detect histidine, show emission wavelengths at similar ranges (~530 nm), but have different upper limits of detection and localization patterns. NCH-Cu^{2+}, is reversible and shows good specific response between zero to 5 μM as well as possible sublocalization to lysosomes [295]. On the other hand, NPC, shows a linear response up to 16 μM and has been demonstrated to be applicable in HeLa

cells and *Caenorhabditis elegans* [294]. However, NPC does show modest responses (<1-fold) to other amino acids.

Finally, two synthetic sensors have been reported for aspartate. A green Cu^{2+}-dependent aspartate-sensing synthetic reporter, 8MPS, was shown to detect exogenously added aspartate in live MCF-7 cells and *C. elegans* but retained a significant response to other amino acids (**Table 1-2**) [262]. The second, N,N-SP-BPY, showed the largest fluorescent change towards aspartate and glutamate, but also responds to other amino acids, especially cysteine [244]. 8MPS and the histidine sensors require Cu^{2+} ions to quench the sensor's fluorescence while the presence of histidine or aspartate rescues the fluorescence. They suffer from the same limitations, as similar levels of fluorescence may be observed with the presence of both Cu^{2+} ions and the ligand of interest or with neither present. Therefore, although they can image the presence of the amino acids, measurement of real-time flux of each amino acid may be difficult. To our knowledge, these are the current extant amino acid sensors capable of being used in live cell imaging.

1.3.2 Genetically encoded single FP-based indicators

Genetically encoded indicators are a popular class of indicators for neuronal imaging due to their ease of delivery (i.e., plasmid transfection or packaged into viruses) and the specificity of their targeting (e.g., expression in different organelles or in a specific subset of cells). These indicators consist of a ligand binding protein, usually a periplasmic binding protein (PBP) or a GPCR, as the sensing domain and a FP as the reporter domain such that binding of the ligand by the sensing domain induces a change in the chromophore's environment, causing a change in fluorescent intensity. Unlike synthetic dye-based amino acid indicators, which often required the synthesis of a recognition moiety, genetically encoded indicators often capitalize on naturally occurring proteins that have evolved to have specificity and affinity for binding their target. The first single FP-based indicator for an amino acid was iGluSnFR, a glutamate indicator that used a

glutamate/aspartate binding protein from *Escherichia coli* and green FP (GFP) (**Table 1-2**) [252]. Though it showed a greater response to L-glutamate, it retained a smaller response to L-aspartate with comparable affinity. Since then, a functionally brighter variant as well as different chromatic variants, ranging from blue to red, have also been reported [254,255]. Further engineering of iGluSnFR also led to different variants with faster kinetics or greater sensitivity [253,254].

Single FP-based indicators have also been developed for GABA and histidine (**Table 1-2**). The iGABASnFR series utilized a GABA-binding protein from *Pseudomonas fluorescens* and had different variants possessing a range of affinities and dynamic ranges [287]. iGABASnFR was also shown to have low affinity for glycine, alanine and histidine. Its uses in mice models and zebra fish for detecting concentration changes in GABA were also demonstrated. Notably, however, its use for imaging GABA events longer than 1 s in duration may be limited as it undergoes a second fluorescence change after 1 s.

On the other hand, the yellow histidine indicator, FHisJ, used the HisJ binding protein from *E. coli* showed a 520% increase in the fluorescence excitation ratio at 420 and 485 nm ($R_{485/420}$) when histidine is added [296]. FHisJ has a high affinity for histidine but does show a three-fold increase in $R_{485/420}$ in response to 100 mM L-arginine. The authors also expressed FHisJ in the cytosol and the mitochondrial matrix of HeLa cells, where they used FHisJ to estimate the histidine concentration (~159 and 77 μM, respectively) and to study histidine transport into cells.

1.3.3 Nanostructures (excluding FRET-based sensors)

1.3.3.1 Quantum dots

QDs are semiconductor nanoparticles with optical and chemical properties that are influenced by their size. They are attractive for biological investigations because of their brightness, narrow (and tunable) emission profiles (which facilitates multiplex imaging), high photochemical and thermal stability, resistance to photobleaching and long fluorescence lifetimes

[305]. However, QDs are limited by possible toxicity depending on their composition (especially cadmium-based QDs [306]), challenges associated with their delivery for intracellular applications, and their tendency to blink (intermittent periods of no observable emission) [305]. We refer readers to the review by Resch-Genger [305] for a discussion of their properties as well as a thorough comparison of quantum dots against synthetic dyes.

A red sensor using copper indium sulfide ($CuInS_2$)-based QDs functionalized with tyrosine was reported as a sensor for cysteine, glutathione, histidine and threonine (**Table 1-2**) [283]. For this sensor, the addition of copper (II) ions quenches the fluorescence, which can then be restored by the addition of the ligands. However, this sensor appears to also respond to aspartate and tryptophan and its use has not been demonstrated in living cells. Another sensor, using bright yellow carbon dots functionalized with *o*-phenylenediamine and GABA, has also been reported to detect histidine specifically (**Table 1-2**) [297]; however, similar to the $CuInS_2$-based sensor [283], this sensor requires the addition of a fluoroqinolone to first quench the fluorescence before recovery with histidine [297]. Testing of these carbon dots in human hepatoma cells showed good intracellular uptake with minimal cytotoxicity, suggesting that they may be used to image intracellular histidine dynamics in living cells.

1.3.3.2 Carbon nanotubes

Carbon nanotubes are semi-conducting hollow tubes of graphene that are categorized based on their thickness as either single-walled carbon nanotubes (SWCNTs), consisting of one layer of graphite (and are thus an allotrope of carbon), or multi-walled carbon nanotubes (MWCNTs). Although their lengths may vary, carbon nanotubes have a diameter ranging from one to several nm. Carbon nanotubes are a promising scaffold for building biosensors because of their unique physical and chemical properties (for thorough discussions on carbon nanotubes, we refer readers to the reviews by Liu *et al.* [307], Kruss *et al.* [308], and Yang *et al.* [309]). From a fluorescence

imaging perspective, SWCNTs are of particular interest because they possess tunable near-infrared (NIR) emission profiles [310]. The emission profile of these carbon nanotubes is preferable to that of most other sensors using different building blocks as light in this region allows for greater penetration [311,312]. Carbon nanotubes can be functionalized by coating them with biomolecules, forming a "corona", to tweak their properties, such as in order to confer specificity towards a target analyte or increase solubility. This strategy has been employed, using DNA or RNA for the corona, to engineer SWCNTs for the detection of catecholamines, a class of key neurotransmitters [313-315]. Although carbon nanotube-based fluorescent sensors, to our knowledge, do not yet exist for amino acids, the successful development of sensors for catecholamines, which are derived from amino acids, bode well for the development of carbon nanotube-based fluorescent sensors for amino acids.

1.3.4 Hybrid strategies (excluding FRET-based sensors)

Hybrid sensors for amino acids incorporate a genetically encoded component for sensing the amino acid and a synthetic fluorophore as the reporter. This approach combines the advantages of proteins' specificity for their ligands with the brightness of some synthetic dyes but requires the delivery of a dye in the system. Additionally, hybrid sensors are, by design, modular since the synthetic dyes can be replaced; however, in reality, replacing the dye may affect the sensor's properties, such as dynamic range, kinetics and stability.

The first hybrid sensor that was demonstrated in cells was for glutamate, dubbed glutamate (E) Optical Sensor (EOS), and utilized the S1S2 glutamate binding domain of the GluR2 subunit of AMPA receptors with a cysteine mutation engineered for attaching an environmentally-sensitive fluorophore (**Table 1-2**) [258]. The first-generation EOS showed a modest response ($\Delta F/F_{min} = 0.20$) on the cell surface but was sufficient for mapping synaptically-released glutamate in hippocampal cultures. Two improved EOS variants with improved dynamic ranges were then

shown to be used in slices and *in vivo* [259]. However, tethering of all these EOS variants required the unspecific labelling of EOS and cells with biotin by chemical reagents. In 2014, a high throughput development system was used to engineer enhanced EOS (eEOS) which showed a $\Delta F/F_{min}$ of 5 (better than iGluSnFR [252]) on the surface of cultured neurons [260]. In this work, the unspecific biotinylation of the cell surface was avoided by conjugating eEOS to biotinylated BoNT/C-Hc, a domain of a neurotoxin that binds to gangliosides on neuronal surfaces. Lastly, a hybrid GABA sensor using the same binding domain as iGABASnFR showed a $\Delta F/F_{min}$ of ~0.7 (**Table 1-2**) [287].

1.3.5 FRET-based sensors

FRET-based sensors require a donor fluorophore that, upon excitation, transfers its energy to an acceptor fluorophore without emission of a photon. The efficiency of this transfer, known as the FRET efficiency, is dependent on the distance and orientation of the fluorophores as well as the spectral overlap between the emission spectrum of the donor and the absorption spectrum of the acceptor. Ligand binding induces a change in the distance and orientation of the fluorophores, causing a change in the ratios of fluorescence intensities of both donor and acceptor fluorophores. The presence of two fluorophores is both advantageous and disadvantageous. The 1:1 ratio of donor and acceptor fluorophores can be advantageous because it ideally reduces any changes caused by differences in expression and allows for quantification, although the addition of a second colour channel has been shown to increase noise if the two fluorophores are not evenly matched [316]. However, the necessity for two fluorophores also poses a disadvantage since the two fluorophores consume more spectral bandwidth, limiting the possibilities for multicolour imaging and/or use of optogenetic actuators.

Most FRET-based sensors for amino acids are genetically encoded sensors that utilize PBPs from bacteria as the ligand binding domain with cyan variants of GFP as the donor and

yellow variants as the acceptor. Genetically encoded FRET sensors for cysteine [239], glutamate [20,256], glycine [291], histidine [257], isoleucine [240], lysine [242,289], leucine [241], methionine [243], glutamine [263], arginine [142,257,290], and tryptophan [292] have been reported (**Table 1-2**). Of these, the first arginine sensor [290] is unique as it uses the glutamine binding protein from *E. coli* as its recognition motif, while the glycine indicator, GlyFS [291], utilized a binding domain that originally bound GABA, proline and alanine and was engineered to bind glycine. The latest arginine sensor utilized an arginine-binding protein identified from ancestral protein reconstruction [142]. Additionally, FRET sensors that recognize multiple ligands have also been reported, such as one for lysine and arginine [257], aspartate and glutamate [257], and BCAAs [257,298]. FRET sensors that use L-(7-hydroxycoumarin-4-yl)ethylglycine, an unnatural fluorescent amino acid, for glutamine and methionine have also been reported [264,286]. Beyond genetically encoded sensors, two irreversible FRET-based synthetic probes selective for cysteine with applications in mammalian cells are also recently available (**Table 1-2**) [284,285].

Snifits (**SN**AP-tag based **i**ndicator proteins with a **f**luorescent **i**ntramolecular **t**ether), are hybrid FRET-based sensors for glutamate and GABA (**Table 1-2**) [261,288]. Snifits consist of a receptor protein fused to both SNAP and CLIP tags, which are two orthogonal tags that can be used for the attachment of FRET-capable fluorophores, that is also tethered to a competitive antagonist. Displacement of the competitive antagonist induces a change in FRET efficiency, which can then be quantified. The glutamate sensor, called Snifit-iGluR5 for the glutamate receptor used as the binding protein, showed a decrease in FRET efficiency upon glutamate binding ($\Delta R/R_{min}$ = 0.9 for the purified sensor and 0.6 on the surface of HEK293T cells) [261]. On the other hand, GABA-Snifit is based on the metabotropic $GABA_B$ receptor with a decrease in FRET efficiency for a $\Delta R/R_{min}$ of 0.8, while a variant with a GB1/2 chimera instead of the $GABA_B$

receptor, which could bind ligands but not interact with G proteins, showed $\Delta R/R_{min}$ of 0.4 with reduced affinity [288].

1.4 Conclusions

Amino acids have specific, but interconnected, roles for proper neurotransmission (**Table 1-1**). Beyond their role in protein synthesis, many of the proteinogenic amino acids possess neuromodulatory effects while others act as essential precursors to neurotransmitters without which deficiencies in neurotransmission will result. Additionally, due to the shared nature of the amino acid transport systems, perturbations in the levels of some essential amino acids may affect others. Despite the significant strides made in understanding neurotransmission over the last several decades, there is much more that needs to be clarified, especially with respect to the roles amino acids have in neurotransmission. Indeed, several amino acids, including some D-amino acids, are known to have neurotransmitter-like effects, yet key mechanistic questions about their release – and their neurological relevance – remain unanswered.

Fluorescence imaging is a powerful technique that has the potential to answer many of these unresolved questions and advance our understanding of neurotransmission. However, its potential is handicapped by the limited availability and performance of sensors for amino acids. Out of the 22 amino acids reviewed here, sensors whose use has been demonstrated in living cells have only been reported for 14 amino acids (**Table 1-2**). Our survey of available fluorescent probes for amino acids revealed that most synthetic dye-based sensors are for cysteine and other biological thiols, taking advantage of the unique nucleophilicity of thiols. Similarly, despite the advantages they offer, there is a limited number of QD-based sensors. None are carbon nanotube-based, but given the platform's infancy, we believe that carbon nanotube-based sensors for amino acids would be forthcoming. On the other hand, sensors which utilized amino acid binding proteins have been reported for 13 amino acids (only threonine, of the 14 amino acids with published sensors,

did not have an amino acid binding protein-based sensor; **Table 1-2**), suggesting that strategies that incorporate an amino acid binding protein as the recognition motif might provide the fastest route for sensors. Although existing sensors with genetically encoded recognition motifs have generally relied on known periplasmic binding proteins, recent advancements in utilizing GPCRs as a scaffold [317] and protein engineering for engineering specificity for new ligands [318] should facilitate the engineering of new and better biosensors for amino acids.

Ultimately, however, the most effective strategy would be through the collaborative efforts of tool developers, using a combination of materials and strategies, and researchers who intend to use these tools for their investigations. Open feedback loops between developers and users will maximize the impact of tool development efforts and lead to further advancements in our understanding of neurotransmission.

1.5 Thesis scope

In this thesis, we report our work in expanding the toolbox of FP-based indicators for imaging neurotransmission using a combination of directed evolution and rational design. We hypothesize that our new indicators will prove useful for neuroscientists interested in investigating the dynamics of these analytes within the nervous system.

Beyond the commonly recognized amino acid neurotransmitters, amino acids play an underappreciated role in neurotransmission with limited tools for their study. In Chapters 2 and 3, we describe our efforts to address this limitation by engineering single FP-based indicators for aspartate and glutamine, respectively. In these efforts, we depended on analyses of protein structures, coupled with saturation mutagenesis, throughout the whole engineering process, from identification of promising scaffolds to choosing insertion points to shaping their affinities. By carefully designing and screening mutant libraries to compensate for a more laborious screening

protocol, variants with desirable properties (e.g., dynamic range, affinities, brightness) were identified, leading to functional indicators for aspartate and glutamine.

Though protein engineering has made great strides in engineering indicators for imaging Ca^{2+} dynamics in neurons, better versions of existing indicators – or new indicators fulfilling a particular need – remain in demand. Chapters 4 and 5 detail my work in engineering new variants of Ca^{2+} indicators using directed evolution and a well-established design. In Chapter 4, I discuss my work updating an existing indicator with one of the brightest red FPs (RFPs) available in an effort to engineer a brighter and better Ca^{2+} indicator. In Chapter 5, we report on our work to fill a gap in the palette of available Ca^{2+} indicators by engineering the first far-red Ca^{2+} indicators using the recently published mKelly2. Finally, the last chapter offers a summary of this thesis and discusses possible future directions.

Before proceeding further, however, a brief discussion of the terminologies, especially with respect to the *in vitro* performance metrics with which we evaluated sensors described in this thesis, is warranted. For most of the screening process, the main criteria used to evaluate variants is sensitivity, which is defined as the change in fluorescence signal over a specific change in ligand concentration (i.e., $\Delta F/F_0$). When measured from a ligand-free state to a saturating concentration, sensitivity may also be referred to as the sensor's dynamic range. Notably, this use of "dynamic range" is different from the conventional definition used by chemistry. In this thesis, dynamic ranges obtained from screening or with purified protein *in vitro* are reported in two notations, $\Delta F/F_{min}$ or F_{sat}/F_{apo}. For direct (or positive) response sensors (i.e., the fluorescence signal increases upon ligand binding), F_{min} is interchangeable with F_{apo} while F_{max} is synonymous to F_{sat}, and the two notations are related as follows:

$$\frac{\Delta F}{F_{min}} = \frac{F_{max}\ (or\ F_{sat}) - F_{min}(or\ F_{apo})}{F_{min}\ (or\ F_{apo})} = \frac{F_{max}}{F_{min}} - 1$$

Conversely, for inverse response sensors (i.e., the fluorescence signal decreases upon ligand binding), F_{min} would be equivalent to F_{sat} and F_{max} would be F_{apo}. Indicators were also evaluated for their affinities and specificities for their ligands. Affinities are reported as dissociation constants (K_d) which are measured by titrating samples with different ligand concentrations and fitting the data to the Hill equation:

$$\theta = \frac{[L]^{n_H}}{K_d + [L]^{n_H}}$$

Where L refers to the ligand and n_H is the Hill coefficient, which is a measure of ligand binding cooperativity. θ is the fractional saturation, which is the ligand-bound fraction of the indicator population that is therefore unable to contribute to ligand detection, and is defined as follows for fluorescence:

$$\theta = \frac{F - F_{min}}{F_{max} - F_{min}}$$

In addition to its use for evaluating affinity, the same equations and experiment can be used to evaluate an indicator's acid sensitivity using H^+ as the ligand. In this case, the "dissociation constant" is reported as the pK_a, which is the pH at which the indicator retains 50% of its fluorescence signal. Related to affinity, the kinetics of an indicator describes how fast ligand binding (and unbinding) events are converted to fluorescence changes, with higher affinity indicators often accompanied with slower kinetics. Specificity refers to the indicator's ability to respond only to the ligand of interest, with highly specific indicators only responding to the ligand of interest and non-specific indicators responding to multiple ligands. Specificity is affected by both sensitivity and affinity; an indicator that responds to multiple ligands may still be useful if the other ligands are present in concentrations that do not induce fluorescence changes. Finally, an indicator's brightness (i.e., how strong the fluorescence signal is) must also

be considered. Strictly speaking, brightness (or “molecular brightness”) is defined as the product of the extinction coefficient, which is a measure of how strongly the chromophore absorbs light, and quantum yield, which is a measure of how efficiently absorbed photons are converted into fluorescence. However, brightness may also be affected by the indicator’s expression level. When expression levels are considered, we refer to this property as “functional brightness” or “apparent brightness”.

2 Chapter 2 – A green aspartate indicator based on a new scaffold

2.1 Introduction

Aspartate (or aspartic acid in the protonated form) is a proteinogenic amino acid that was first discovered in 1827 [319]. Beyond its role as one of the 20 common amino acids of which proteins are composed, L-aspartate was first reported to excite neurons in the early 1960s [3-5]. It has since been generally considered as a secondary excitatory neurotransmitter in the nervous system with evidence suggesting that aspartate and glutamate, the main excitatory neurotransmitter, may be co-released in some synapses [22,23,27,30]. Indeed, there is evidence to suggest that aspartate levels in the spinal cord are significantly reduced in patients with amyotrophic lateral sclerosis (ALS) [320]. However, aspartate's status as a neurotransmitter has recently been called into question as a specific mechanism for how aspartate modulates neuronal circuitry and affects cognition, as well as the mechanism for its packaging into vesicles for release upon neuron activation (a criterion required for classical neurotransmitters) remain unclear [35,36]. Furthermore, in 2015, a study by Herring *et al.* [25] reported that the amount of L-aspartate found in excitatory synapses of the hippocampus is insufficient to activate NMDA receptors, the only known receptor for L-aspartate.

To help resolve this controversy, a specific tool for imaging aspartate dynamics would be highly useful for understanding the role of aspartate in the nervous system. Specifically, imaging studies with a specific aspartate indicator investigating the reported co-release of aspartate and glutamate or the presence of aspartate in synaptic vesicles and identification of any possible transporters would help resolve the controversy surrounding aspartate. Genetically encoded FP-based indicators have emerged as powerful tools for studying neuronal circuits due to their specificity, ease of targeting, and high spatiotemporal resolution. While indicators that can detect

neuronal activation are aplenty (for a recent review, see Shen *et al.* [317]), a specific indicator for aspartate has not yet been reported. To address this shortage, we have engineered a green aspartate indicator from the aspartate/glutamate binding domain, PEB1a, of *Campylobacter jejuni* [321].

2.2 Materials and Methods

2.2.1 General

Synthetic DNA oligonucleotides and double-stranded DNA fragments (gBlocks) were purchased from Integrated DNA Technologies. High fidelity polymerase chain reactions (PCRs) were performed using several different polymerases: CloneAmp HiFi PCR Premix from Takara Bio USA, Inc., Q5 polymerase from New England BioLabs, and Platinum SuperFi DNA Polymerase and Platinum SuperFi II DNA Polymerase from Thermo Fisher Scientific. Each polymerase was used according to the manufacturer's instructions. Recombinant Taq polymerase was purchased from Thermo Fisher Scientific. PCR products were purified by preparative agarose gel electrophoresis and extracted with the GeneJET Gel Extraction Kit from Thermo Fisher Scientific. Restriction enzymes and T4 DNA ligase were purchased from Thermo Fisher Scientific and used according to the manufacturer's recommended protocols. Digested PCR products were extracted with the GeneJET Gel Extraction Kit before ligation. In-Fusion HD was purchased from Takara Bio USA, Inc. and used for assembly reactions. Plasmid DNA extractions were performed with GeneJET Plasmid Miniprep Kits (Thermo Fisher Scientific). Ligands were obtained as solids from Fisher, Alfa Aesar or Acros Organics with at least 98.5% purity or molecular biology grade. Sanger sequencing reactions using BigDye sequencing kits (Thermo Fisher Scientific) were performed by the Molecular Biology Services Unit at the University of Alberta. Fluorescence measurements were performed on a Safire^2 plate reader (Tecan), while absorbance measurements were collected on a DU-800 UV-Visible Spectrophotometer (Beckman). Protein structure images were generated using UCSF Chimera 1.14 [322,323].

2.2.2 Plasmid construction and evolution

2.2.2.1 Plasmid and library construction

General procedure for plasmid construction. Plasmids were constructed either through traditional cloning (i.e., with restriction enzymes to generate sticky ends followed by ligation with a ligase) or seamless homology-based assembly (i.e., In-Fusion). For traditional cloning, the vector backbone and double-stranded DNA fragments (either purified PCR product or gBlocks) were digested with two restriction enzymes before ligation with T4 DNA ligase. For assembly, double-stranded DNA, sharing at least 15-bp overlap with the linearized vector backbone in both 5' and 3' ends, is incubated with vector backbone linearized by amplification or restriction enzymes and In-Fusion enzyme mix. Following completion of the ligation or assembly, the reaction was used to transform electrocompetent *E. coli* strain DH10B (Invitrogen) and cultured overnight on agar plates of lysogeny broth (LB) prepared using Lennox's formula with the appropriate antibiotics and inducer at 37 °C. Plasmids were then isolated from single colonies grown overnight in liquid LB cultures with the appropriate antibiotics and inducer at 37 °C. Sequences were confirmed by Sanger sequencing.

Construction of library for insertion points in PEB1a. Double stranded DNA encoding PEB1a (codon optimized for mammalian expression based on the structure in the Protein Data Bank (PDB ID: 2V25)) [321] was commercially synthesized with overlapping sequences with pBAD/HisB (Thermo Fisher Scientific) in the 5' and 3' directions to facilitate insertion between the *XhoI* and *HindIII* sites. This fragment was then assembled into similarly digested pBAD/HisB vector, and grown as described above on agar plates supplemented with 400 μg/mL ampicillin (Thermo Fisher Scientific) and 0.02% (w/v) L-arabinose (Alfa Aesar) and liquid cultures with 100 μg/mL ampicillin and 0.002% L-arabinose. This plasmid, called pBAD-PEB1a, served as the

template in which circularly permutated (cp) superfolder GFP (cpsfGFP) [324] will be genetically inserted.

To facilitate insertion of cpsfGFP, pBAD-PEB1a was linearized by high fidelity PCR amplification with primers incorporating an overlap region with the gene encoding cpsfGFP and whose 5' end immediately following the overlap region start at codons that encode for residues adjacent to the insertion site (e.g., for insertion between residues 65 and 66, the region of the forward primer that binds pBAD-PEB1a starts at the codon encoding for residue 66 while the region of the reverse primer that binds the template starts at the codon for residue 65). The cpsfGFP DNA fragment was amplified from mammalian codon-optimized pBAD-sfGASP. Constructs were assembled as described earlier and insertion of cpsfGFP was verified by diagnostic digestion using XhoI and HindIII. The complete list of primer sequences used for this library can be found in **Table A-1**.

Construction of mutated libraries. For random mutagenesis libraries, the template was amplified by error-prone PCR (EP-PCR) performed with Taq polymerase in the presence of 0.15 mM $MnCl_2$ and four-fold excess of dCTP and dTTP [325,326]. The purified PCR product was then cloned into digested pBAD/HisB with In-Fusion. Libraries for site-directed mutagenesis at one position (including deletions) were prepared with Platinum SuperFi II DNA Polymerase or CloneAmp HiFi PCR Premix followed by DpnI digestion. For simultaneous mutations at different positions, the QuikChange Lightning Multi Site-Directed Mutagenesis kit (Agilent Technologies) was used.

Plasmids for expression in mammalian cells. Plasmids for cytosolic expression (or secretion) in mammalian cells were prepared by digesting the pBAD/HisB plasmid carrying the gene for the protein of interest and ligating the insert into a similarly digested version of

pcDNA3.1(+) (Invitrogen) modified to allow for direct subcloning of constructs from pBAD/HisB (pcDNA3.1m). For membrane expression of constructs, the genes for the proteins of interest were amplified by PCR and assembled into pMiniDisplay (pDisplay with the hemagglutinin tag removed) [252].

Plasmids for variants with SpyTag003. pET28a-SpyTag003-mKate2 (Addgene #133452) and pENTR4-TfR-sfGFP-myc tag-SpyCatcher003 (Addgene #133451) were kind gifts from Mark Howarth [327]. The gene for mKate2 was replaced by genes encoding proteins of interest (e.g., ODIN constructs and EGFP) by PCR amplification of the desired genes to append at least 15 bp overlap with the pET28a-SpyTag003 vector as well as PCR amplification of the pET28a-SpyTag003 vector prior to assembly by In-Fusion. Replacement of sfGFP with mApple in the SpyCatcher003 construct was performed similarly. The SpyTagged constructs were then re-inserted back into pBAD/HisB or a modified pBAD/HisB with the His-tag moved to the C-terminus and the rest of the pBAD leader sequence deleted (cHis-pBAD).

2.2.2.2 Library screening in *E. coli*

Assembled libraries and the plasmid encoding the round's starting template were transformed into DH10B and cultured overnight on LB agar plates supplemented with ampicillin and L-arabinose at 37 °C. Bacteria carrying GltI-based constructs were grown on plates supplemented with 0.02% L-arabinose (called "high arabinose"), while bacteria expressing PEB1a-based constructs were grown on plates with 0.002% L-arabinose ("low arabinose") after the initial tests for insertion point optimization due to overexpression causing abnormal bacterial growth. Colonies on the plate were then screened using a custom imaging system [328] to ensure that variants subjected to the response-based screen were fluorescent. Single fluorescent colonies, including three from the starting template as controls, were then cultured overnight at 37 °C in 4 mL LB media with ampicillin and high or low arabinose for GltI-based or PEB1a-based constructs,

respectively. Protein was then extracted from bacteria using B-PER (Thermo Fisher Scientific) and batch-purified with Ni-NTA (G Biosciences). Briefly, after incubation with B-PER, the supernatant was separated from the cell pellet and incubated with 50 µL of Ni-NTA resin for at least 30 min. Following incubation, the beads were washed once with 700 µL of 1× PBS (10 mM Na_2HPO_4, 1.8 mM KH_2PO_4, 137 mM NaCl, 2.7 mM KCl, pH 7.4) with 20 mM imidazole and adjusted to pH 8.0. Protein was eluted from the resin with the addition of 1× PBS supplemented with 250 mM imidazole at pH 7.8. Beads were pelleted by centrifugation and the supernatant was aspirated in between washes. The purified protein was then diluted into wells containing blank (30 mM 3-(*N*-morpholino)propanesulfonic acid (MOPS),100 mM KCl), L-aspartate (30 mM MOPS, 100 mM KCl, 10 mM L-aspartate), or L-glutamate (30 mM MOPS, 100 mM KCl, 10 mM L-glutamate) buffers, corrected to pH 7.2. The fluorescence intensities for the proteins in each solution were measured and the intensities for each ligand condition were compared to the intensities from the blank buffer to yield the dynamic range. The ratio between the dynamic ranges for L-aspartate and L-glutamate was calculated and used as a measure of specificity. From each library, variants were designated as "winners" if they had a larger dynamic range and/or had better specificity than the controls. The winning variants were then streaked out on LB agar plates and re-tested in triplicate against the starting template. Plasmids were extracted and sequenced from variants that showed consistent improvement in the retest compared to the controls, and the extracted plasmids were used as template for the next round.

2.2.3 *In vitro* characterization

2.2.3.1 Protein expression and purification

Electrocompetent *E. coli* strain DH10B or BL21(DE3) (Thermo Fisher Scientific or New England BioLabs) were transformed with pBAD/HisB or pET28a plasmids, respectively, harbouring the gene for the required proteins, and grown on LB agar supplemented with the

required antibiotics (400 μg/mL ampicillin or 50 μg/mL kanamycin) and inducers (0.02 or 0.002% L-arabinose or 1 mM IPTG). Four millilitres of LB media with the necessary additives (e.g., 0.0002% L-arabinose for PEB1a-based constructs) were inoculated with single bacteria colonies and shaken overnight at 37 °C and 225 rpm. Each of the starter cultures was added to 500 mL of LB with antibiotics, and the cultures were shaken at 37 °C for 3-4 h before the necessary inducers were added. After induction, the temperatures were lowered to 30 °C for incubation. Bacteria cultures carrying pBAD plasmids were induced with 0.02% L-arabinose (regardless of construct identity) and shaken for at least 20 h. On the other hand, bacteria carrying pET28a plasmids were shaken for at least 40 h, and an extra dose of kanamycin was added 24 h after inoculation. Bacteria were then collected by centrifugation and resuspended in 1× PBS. After discovering that GASP undergoes significant proteolysis, protease inhibitors (cOmplete™, EDTA-free Protease Inhibitor Cocktail; Roche) were added according to the manufacturer's protocol to minimize proteolysis. Cells were lysed by sonication and then clarified by centrifugation. The cleared lysate was incubated with Ni-NTA resin for at least 1 h with gentle mixing. The lysate-bead mixture was then transferred to a propylene centrifuge column and washed with at least three packed column volumes of wash buffer (1× PBS with 20 mM imidazole, pH 8.0) before elution with elution buffer (1× PBS with 250 mM imidazole, pH 7.8). The purified protein was then concentrated and buffer exchanged into 1× PBS (pH 7.4) using 10 kDa centrifugal filter units (Millipore). All steps of the extraction and purification were carried out 4 °C or on ice.

2.2.3.2 Spectral characterization

Brightness is defined to be the product of the extinction coefficient (EC or ε) and the quantum yield (QY or φ).

Determination of EC. ECs of sf-GASP and ODIN variants were measured using the previously established base denaturation method [329]. Briefly, for each variant, an equal volume

of purified protein was diluted to 700 µL with blank, L-aspartate and L-glutamate buffers, as well as NaOH. The absorption spectrum for each sample was collected, and the concentration of protein present in each sample was derived from the denatured sample using Beer's Law and assuming an EC of 44,000 M^{-1} cm^{-1} for the peak around 450 nm, which corresponds to the denatured GFP chromophore [329,330]. The variant's EC for each condition can then be calculated. Measurements were performed in triplicate and the results were averaged.

Determination of QY. Quantum yields were measured according to previously described protocols [328,331]. EGFP was used as the standard (QY = 0.67) [329]. From the samples used for EC measurements, a dilution series for each sample were prepared with the corresponding buffers such that the peak absorbance was equal to, or less than, 0.05. For each dilution series, the emission spectra were collected from 480 to 650 nm with an excitation wavelength of 460 nm and the total fluorescence intensity for each dilution was integrated. The total fluorescence intensities were then plotted against the absorbance and the slope of each line (*m*) was calculated**.** QYs were calculated according to the following equation:

$$\varphi_{\text{protein}} = \varphi_{\text{standard}} \times \frac{m_{\text{protein}}}{m_{\text{standard}}} \quad (1)$$

2.2.3.3 Specificity and affinity measurements

Specificity measurements. The responses of aspartate indicator variants to possible ligands were characterized by comparing the fluorescence intensity of purified protein diluted in blank buffer supplemented with the ligand (4 mM or 10 mM) against the intensity recorded from purified protein diluted in blank buffer alone at pH 7.2.

***K_d* determination.** For ligands eliciting substantial responses, titrations with varying concentrations of ligand were performed to measure the K_d. Buffers for the K_d titration were

prepared by diluting the stock buffer with the blank buffer. The stock concentrations for L-aspartate, L-glutamate and D-aspartate were 10 mM, 300 mM and 100 mM buffers, respectively. Purified protein variants were diluted in these buffers and the fluorescence intensities of the protein in each solution were measured in triplicate. The readings were plotted against the ligand concentration on a logarithmic scale, and the data fitted to the following equation for the K_d [332]:

$$F = F_{min} + \frac{F_{max} - F_{min}}{1 + 10^{(log K_d - X)n_H}} \quad (2)$$

Where F is the normalized fluorescence and X is the log of the concentration of the ligand. The Hill coefficient (n_H) in equation 2 is constrained to 1 since there is only one ligand binding site and no cooperative binding is expected.

2.2.3.4 pK_a measurements

The pH buffers were prepared from a dual-buffer system of 30 mM citrate and sodium borate with pH adjusted by the addition of HCl or NaOH [331]. To determine the pK_a, 1 µL of purified protein were diluted in 98 µL of buffers with pH ranging from 3 to 11. One µL of 1× PBS (pH 7.5) was added to wells for the apo condition, while 1 µL of either 1 M of ligand (dissolved in 1× PBS and pH adjusted to 7.5) were added for the L-aspartate or L-glutamate conditions. Measurements were performed in triplicate, and the readings were plotted against pH with the data fitted to equation 2 with H^+ as the ligand as follows:

$$F = F_{min} + \frac{F_{max} - F_{min}}{1 + 10^{(pK_a - pH)n_H}} \quad (3)$$

Similar to the affinity titration, the Hill coefficient is constrained to 1 since no cooperativity is expected for the protonation of the chromophore.

2.2.3.5 Kinetics

Approximate kinetic measurements were performed by mixing purified protein immediately before repeated spectra acquisition with the shortest possible intervals (~2 s) on a

Tecan Safire^2 spectrophotometer. Measurements were repeated in triplicate, and the data were then plotted for trends.

2.2.4 Imaging in mammalian cells

HeLa cells were plated on 35 mm glass bottom dishes until they reached ~50% confluency. Transfections were performed by suspending 1 µg of plasmid DNA (for co-transfections 500 ng of each plasmid were mixed together) and Turbofect (Thermo Fisher Scientific) according to the manufacturer's instructions. The transfection solution was then either incubated with cells in complete media (Dulbecco's modified Eagle's medium (DMEM) supplemented with 10% fetal bovine serum (FBS), 2 mM GlutaMax (Invitrogen), and streptomycin-penicillin) overnight or incubated with cells in serum-free media (complete media without FBS) for 2 to 4 h at 37 °C. Cells were left to incubate for at least 20 h before imaging. Prior to imaging, cells were washed with twice with HEPES-buffered Hanks' Balanced Salt Solution (HHBSS) prior to replacement of the media with HHBSS. Imaging was performed on an inverted Zeiss 200M microscope equipped with 470/40 nm excitation and 525/50 emission filters for the green channel and 535/50 nm and 609/57 nm for the excitation and emission, respectively, for the red channel and OrcaFlash 4.0 – C13440 (Hamamatsu) at 40× or 63× magnification. Imaging analyses were performed with ImageJ.

For SpyTagged constructs, pENTR4-TfR-mApple-myc tag-SpyCatcher003 was transfected in cells as described above to express SpyCatcher003. To minimize protein degradation, SpyTagged proteins were purified as described above the day before imaging. After concentration and removal of the imidazole, the concentration of each protein stock was measured using the same protocol used for determining the EC. After incubation of the cells post-transfection and immediately prior to imaging, protein, with a final concentration of 10 µM, was incubated with the cells for 10 minutes at room temperature. Cells were then washed twice with HHBSS and

the media replaced with HHBSS for imaging. Expression of mApple-SpyCatcher003 and tethering of ODIN1 were confirmed by imaging in both green and red channels prior to testing the dynamic range in cells. For time-lapse imaging to measure their responses to ligand, images were only captured in the green channel.

2.2.5 Statistical analysis

Statistical analyses were performed as described in the results. All statistical analyses were conducted using Prism8 (GraphPad, La Jolla, CA).

2.3 Results and discussion

2.3.1 Protein engineering

2.3.1.1 Engineering an aspartate-specific variant of iGluSnFR

Our first strategy for engineering an aspartate indicator relied on a previously published indicator for glutamate, iGluSnFR [252]. This indicator utilized the glutamate/aspartate periplasmic binding protein (GltI) from *E. coli*, and though it had a larger response for glutamate (F_{sat}/F_{apo} = 5.5), it also retained good response to aspartate with a F_{sat}/F_{apo} ~ 3 with similar affinities (K_d = 107 ± 9 μM for glutamate and 145 ± 18 μM for aspartate). Thus, we reasoned that mutations introduced in the binding pocket of GltI could yield a variant with a strong response to aspartate and minimal response to glutamate. We studied the interactions between GltI and the ligand and targeted the residues interacting with the side-chain carboxylic acid: Arg24, Ser72, Ser90, and His164 (**Figure 2-1A** and **B**).

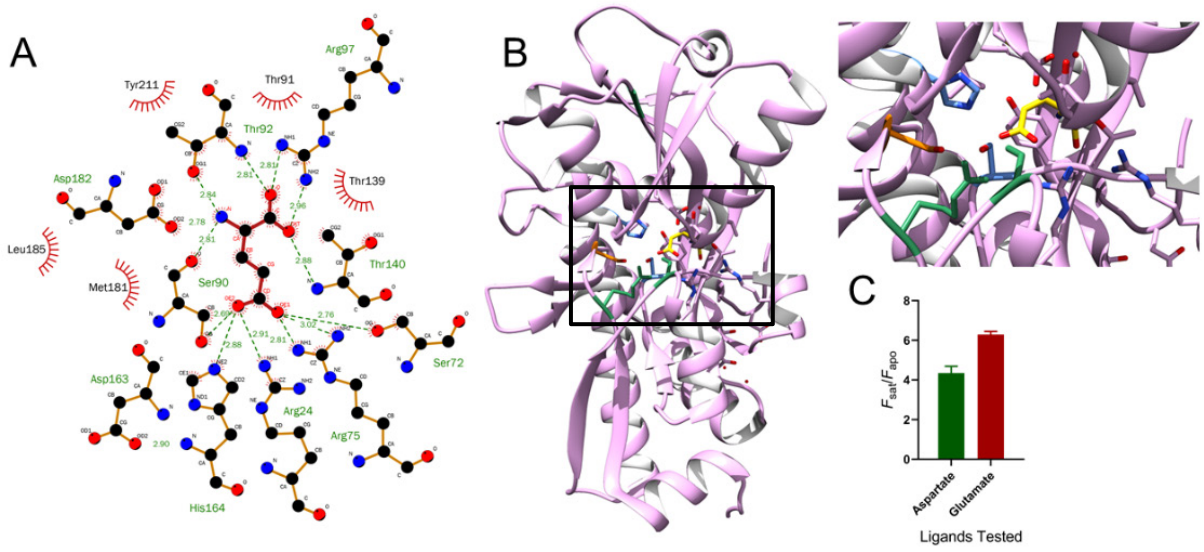

Figure 2-1 – Structure of GltI, the binding protein used for iGluSnFR, and iGluSnFR's response profile.

A) Two-dimensional representation generated by LigPlot+ for the binding pocket of GltI with the ligand (glutamate) in the center (dark brown bonds) and the interacting residues from GltI. Green dashed bonds indicate hydrogen bonding with numbers indicating distance in angstroms (Å). Hydrophobic interactions with specific residues are indicated by red half-circles with projections around the residue labels. B) Structure of GltI (purple) showing the positions of the targeted residues with the glutamate ligand in yellow. Green residues indicate a successful mutation at that position, while blue and orange residues indicate targeted residues without successful mutations. Ser72 is colored orange for identification. Left image shows the full structure of GltI, while the right image shows a close-up of the binding pocket (region bounded by black box). C) Response profile of pBAD-iGluSnFR. Data presented as mean ± SD (n = 3, independent).

For screening in *E. coli*, we first amplified iGluSnFR using primers containing *XhoI* and *HindIII* restriction sites to generate fragments that can be inserted in pBAD/HisB vector using traditional cloning methods, and used the resulting plasmid, pBAD-iGluSnFR, as the template for future libraries (**Figure 2-2A**). In our hands, iGluSnFR had a F_{sat}/F_{apo} of ~6 (6.29 ± 0.16; n = 3) and ~4 (4.35 ± 0.34; n =3) for L-glutamate and L-aspartate, respectively. Randomization libraries were generated with the NNK codon (N = any base, K = G or T; encodes for all 20 amino acids with 32 codons and reduces the number of possible STOP codons) at the targeted position, while codons used to introduce specific mutations were chosen to be the most balanced for expression in both *E. coli* and mammalian cells. In addition to individual mutagenesis at each position, we also generated libraries with two positions simultaneously mutated. Simultaneous mutations were limited to two residues at a time to keep library sizes manageable. We screened libraries by picking fluorescent colonies from a plate and culturing them overnight in liquid media before extracting and purifying the proteins with Ni-NTA. Though purification by Ni-NTA severely limited our screening throughput, we found that the combined glutamate present in the media and from the extraction due to high cytosolic concentration of glutamate was enough to interfere with our measurements [333]. To increase the probability of encountering specific mutations of interest (either individually or in combination), we ran separate site-directed mutagenesis reactions with primers carrying the desired mutations and screened the resulting libraries.

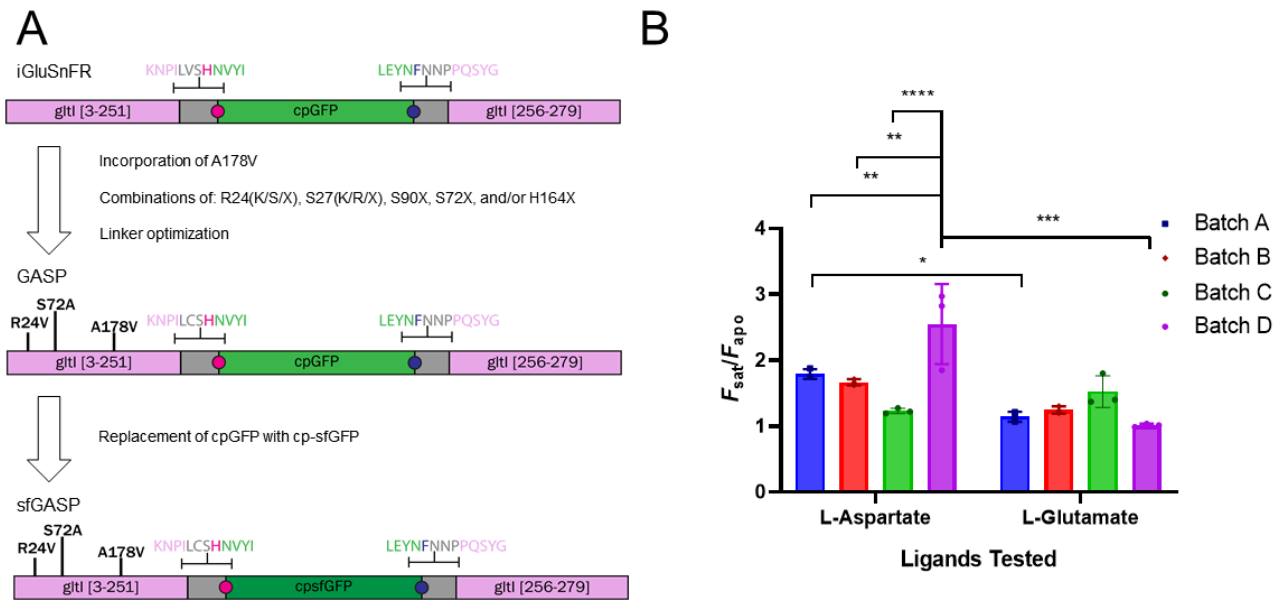

Figure 2-2 – Engineering sfGASP.

A) Schematic representation of sfGASP engineering. Residues at both linker interfaces are shown above the schematic representations, and colored according to their classification (i.e., pink residues are part of the GltI domain, grey residues are considered the linker, and green residues are considered part of the cpFP). The gatepost residues are represented by the pink and navy circles. Mutations introduced into the GltI binding domain are indicated by the black lines with the specific mutations indicated above the line. Schematic is not drawn to scale. B) Ligand-induced fluorescence response test for sfGASP purified at different time points under the same conditions. Ligands are indicated by the x-axis, and the response, F_{sat}/F_{apo}, plotted on the y-axis. Significant differences between groups are indicated above the bars (****, $p < 0.0001$; ***, $0.0001 < p < 0.001$; **, $0.001 < p < 0.01$; *, $0.01 < p < 0.05$). All values are reported as mean ± SD, with individual values superimposed (n = 3, independent).

The evolution of our aspartate indicator based on iGluSnFR is illustrated in **Figure 2-2A**. The first mutation, Ala178Val, was a serendipitous off-target mutation identified from one of the site-directed mutagenesis libraries and reduced the dynamic range upon binding to glutamate without affecting aspartate. From site-directed mutagenesis of key binding site residues and linker optimization, we identified other mutations (Arg24Val, Ser72Ala, and Val253Cys) that, in conjunction with Ala178Val, yielded a variant that has a stronger response to aspartate than glutamate, which we named GASP (**G**reen **A**spartate **S**ensing **P**rotein). However, while we were successful in engineering a variant with a shifted response profile, GASP remained quite dim. Soon after we finished engineering GASP, a report describing a variant of iGluSnFR that incorporated superfolder GFP and exhibited better expression (i.e., it was functionally brighter when expressed in cells) was published [254,324]. Thus, we replaced the GFP domain of GASP with superfolder GFP to yield a variant we called sfGASP.

Our initial efforts to characterize sfGASP revealed problems that our screening did not account for. We performed repeated measures two-way ANOVA analysis on the response profiles of sfGASP samples purified at four different points over an extended period of time (**Figure 2-2B**) using batch (for time) and ligand as the main factors. Two-way ANOVA revealed a significant main effect for ligand ($p = 0.0004$), as well as a significant interaction effect between batch and ligand ($p = 0.0012$). A main effect for batch approached, but did not reach, significance ($p = 0.069$). Post-hoc analysis for simple effects within batches by Sidak's multiple comparisons test showed significant differences between Batch D and Batch A ($p = 0.007$), Batch B ($p = 0.002$), and Batch C ($p < 0.0001$) in their response to aspartate. However, no significant differences were found in the glutamate condition. Comparing each batch's response to the ligands, Sidak's multiple comparisons test revealed significant differences in Batch A ($p = 0.04$) and Batch D ($p = 0.0002$).

While the main effects for ligand were expected and desirable, the analysis revealed that there is significant variability in indicator performance across batches with respect to their responses to the ligands, as well as significant differences within the batches' response to the ligands. Additionally, we observed that most of the expressed GASP and sfGASP proteins remained in the insoluble pellet even after incubation with BPER, as judged by comparing the intensity of pellet colour before and after incubation. On the other hand, while not all of the produced iGluSnFR was extracted by B-PER in our current protocol, we still observe an appreciable change in pellet colour. These results suggested that GASP variants are more prone to forming inclusion bodies when expressed in bacteria. Taken together, these results indicated that, relative to iGluSnFR, both GASP variants have poor protein folding efficiency and stability, which, in turn, affects their performance.

Directed evolution is a powerful technique that can be used to improve protein function, folding, and stability [255,328,331,334,335]. Therefore, we subjected sfGASP to directed evolution in an effort to address its issues and improve indicator performance. Specifically, we performed EP-PCR with Taq polymerase on sfGASP to generate libraries of sfGASP mutants that could then be screened for performance. We consider apparent brightness on a plate to be influenced by folding efficiency, so we initially screened bacteria on plates to identify the brightest colonies that we then cultured and tested. For each library, thousands of colonies were screened on plates, and secondary testing was conducted until variants showed apparent improvements in at least one property (e.g., brightness) were identified. Unfortunately, despite our efforts, we were unable to identify variants demonstrating improved overall performance. Our most advanced variant, which was the product of three iterative rounds of evolution, had comparable performance to the original sfGASP.

Because we were unable to improve the folding efficiency of sfGASP even after multiple rounds of evolution, we sought to identify the underlying cause of the problem by analyzing the changes we introduced relative to iGluSnFR (**Figure 2-2A**). Our last modification to iGluSnFR, the replacement of cpGFP with cpsfGFP, had been independently shown to not have a detrimental effect by Marvin *et al.* [254], and was therefore kept. Immediately preceding that would be the introduction of the Val253Cys mutation. However, the variant without this mutation was also observed to be trapped in inclusion bodies, suggesting that the issue was present before this mutation was incorporated, although this did not eliminate the possibility of a synergistic effect with the other mutations. Thus, we focussed our attention on the mutations introduced into GltI. While we considered our first mutation, Ala178Val, to be a conservative mutation due to similar biochemical properties, previous work [336] had shown that it can have detrimental consequences for folding. However, a new screen of a library with that position randomized returned variants favouring valine in that position.

The other two mutations, Arg24Val and Ser72Ala, introduced hydrophobic residues into a highly charged binding pocket (**Figure 2-1**). Nevertheless, in the same report, Marvin *et al.* [332] reported that a soluble variant with a decreased affinity for glutamate (K_d = 200 μM) could be engineered by mutation of Ser72 to alanine. Communications with the authors revealed that, in their hands, the Ser72Ala variant has a stronger affinity for aspartate than glutamate. When we incorporated this mutation into original iGluSnFR, we found that the dynamic ranges for aspartate and glutamate were now similar (4.3 ± 0.3 and 4.1 ± 0.6; p = 0.375, n = 4) according to the Wilcoxon matched-pairs signed rank test, and more importantly, verified that the Ser72Ala variant had comparable solubility with iGluSnFR. Thus, we turned our attention to Arg24Val. A search through the literature revealed PEB1a, an aspartate/glutamate binding protein from *C. jejuni* that

is homologous to GltI with a slightly stronger affinity for L-aspartate [321]. An alignment of their sequences (**Figure 2-3**) showed that the residues interacting with glutamate and aspartate in GltI and PEB1a, respectively, are largely conserved with three mutations: Arg24Lys, Ser90Thr, and His164Tyr (numbered as residues in GltI to PEB1a). We screened a library generated by multi-site-directed-mutagenesis reaction with primers encoding for these mutations in an effort to identify a variant with better performance. Instead, our results showed that variants that incorporate some combination of these mutations either reverted their specificity back to glutamate or lost their specificity altogether.

While we were successful in engineering an aspartate-specific variant from iGluSnFR, we were unable to address the issues we encountered and optimize the sensor. Because of this and having identified PEB1a (a homologue of GltI that already has a slight preference for aspartate) as a promising alternative, we decided to explore PEB1a's potential as a scaffold for a new indicator.

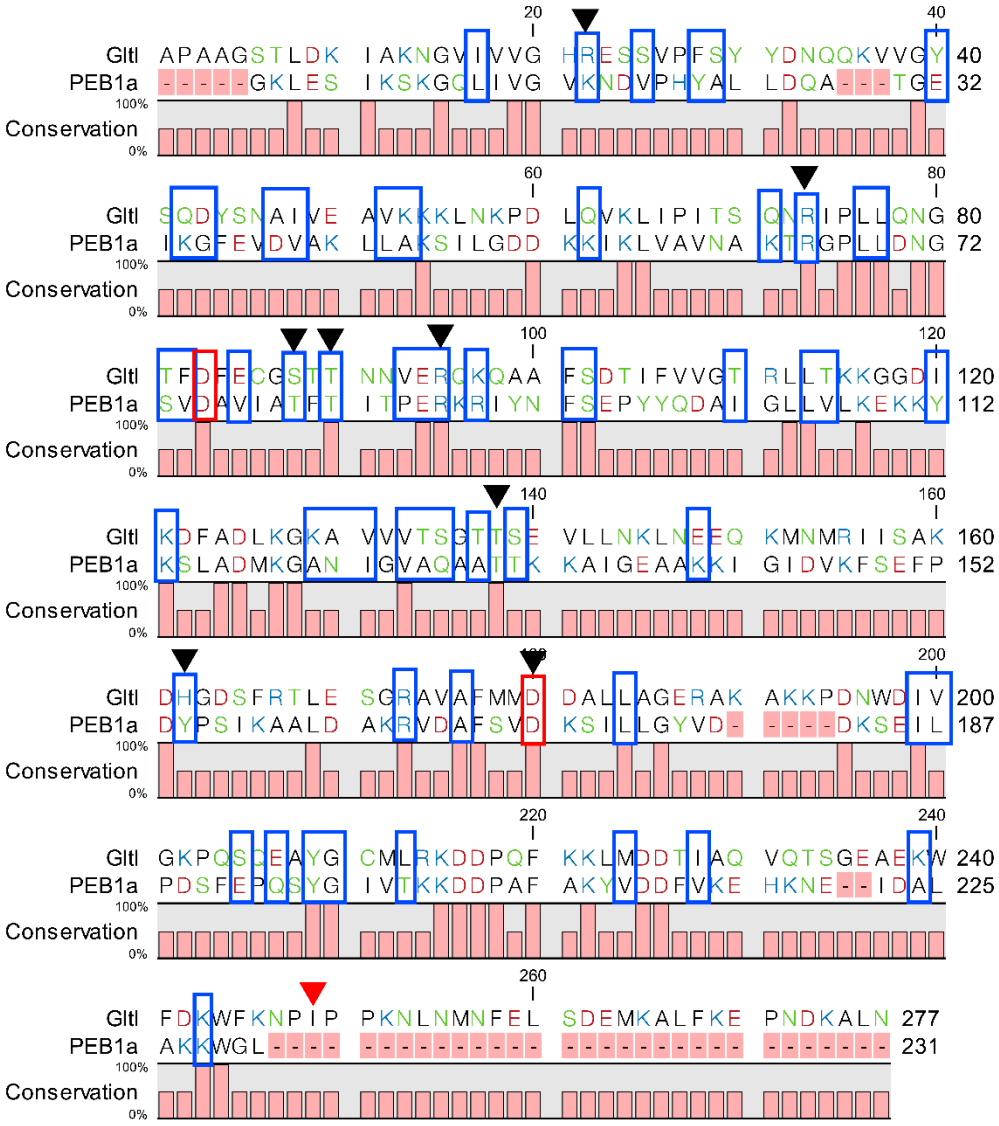

Figure 2-3 – Sequence alignment between GltI and PEB1a.

Conserved residues between GltI and PEB1a are indicated by the bar graph in the third row, with 100% indicating conserved residues and 50% indicating different residues. Residues are grouped and colored according to the polarity of their side chains. Boxes highlight residues conserved for PEB1a, GltI, PEB1 from *Streptococcus thermopilus*, PA14_46910 (a GltI homologue from Pseudomonas aeruginosa strain PA14), GltI from *Acinetobacter sp.* ADP1, GlnH from *E. coli* K12, BztA from *Rhodobacter capsulatus*, and

AapJ from *Rhizobium leguminosarum*. Blue boxes indicate partial conservation, and red boxes indicate fully conserved aspartate residues. Black arrows show residues that make contact to aspartate when bound by PEB1a. The red arrow indicates the insertion point for cpGFP in iGluSnFR. Figure was adapted from Müller *et al.* [321].

2.3.1.2 Engineering ODIN

2.3.1.2.1 Initial engineering of ODIN

When engineering a FP-based indicator, the choices made regarding the ligand binding domain and the insertion point of the FP are arguably the most critical factors that determine the indicator's success [332]. PEB1a, like GltI, is a member of the periplasmic binding protein (PBP) family [321,337,338]. PBPs have a conserved structure where two domains, with the ligand binding site at their interface and connected by a hinge region, can undergo a large reversible conformational change upon ligand binding to produce both an "open" form in the ligand-free state and "closed" form when the ligand is bound [338]. Genetically encoded indicators for specific ligands can be – and have been – successfully engineered by inserting an FP into the PBP so that ligand binding modulates the chromophore environment, producing reversible fluorescence changes [252,318,332,339,340]. At the beginning of the engineering process, an insertion point must be chosen such that the conformational change resulting from ligand binding induces as large of a change as possible in the local chromophore environment without disrupting folding of both PBP and FP [332,339].

Sequence alignment of GltI and PEB1a showed that the analogous insertion point in PEB1a does not exist (red triangle in **Figure 2-3**), necessitating a new insertion point. Because a ligand-free structure of PEB1a was unavailable, preventing us from comparing the open and closed structures, we initially analyzed the structure of PEB1a (PDB: 2V25) using B-factors, which have previously been used as a measure of flexibility for residues, to identify possible insertion points

[321,341]. However, despite its classification as a PBP, our B-factor analysis showed PEB1a to be a relatively rigid structure with a limited number of possible insertion sites (**Figure 2-4**). Though we could have tested these insertion sites and identified a variant with some response to aspartate before proceeding with further engineering, we wanted to find the optimal insertion point, and doing so required a larger library. To that effect, we performed another analysis, based on solvent accessibility, to identify positions that can accommodate a FP. This analysis revealed a much larger set of possible insertion points (**Figure 2-4**). However, we reasoned that insertions inside a secondary structure are likely to disrupt protein folding, so we narrowed our library down to 36 insertion sites that are all located in loops or at the ends of secondary structures.

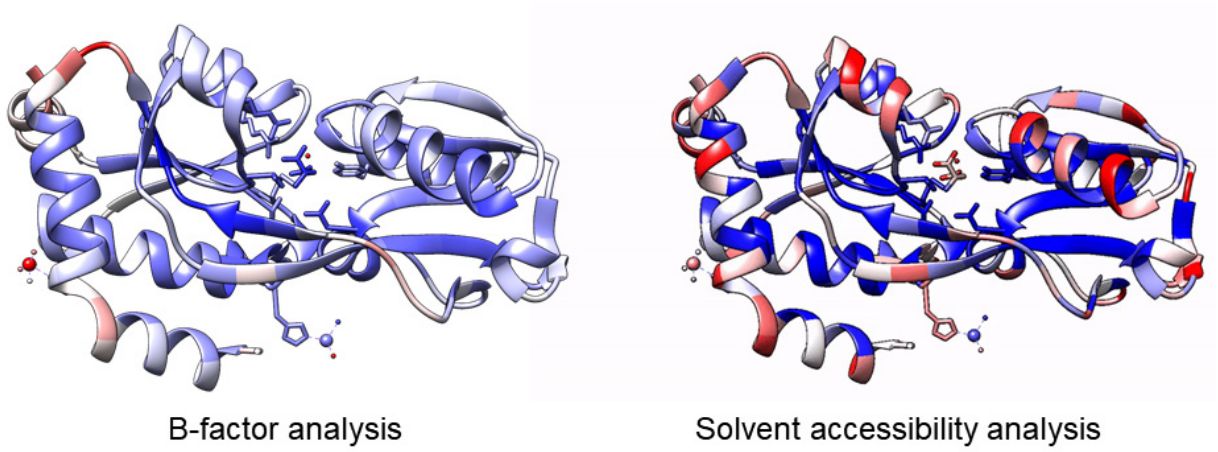

Figure 2-4 – Analysis of PEB1a crystal structure.

Crystal structures of PEB1a are coloured according to the results of either B-factor (left) or solvent accessibility (right) analyses. Relative scores are indicated by a colour gradient where low scoring residues are coloured blue, middle residues are white, and high scoring residues are red. Cut-off scores for each representation were arbitrarily chosen to best represent the relative results.

To test our library of insertion points, we designed a two-step screening system that first screens for protein folding followed by response and specificity for aspartate (**Figure 2-5A**). We used the time it takes for a construct to be fluorescent as a measure of protein folding efficiency since fluorescence would indicate proper folding of the cpsfGFP, while assuming that unsuccessful folding of the ligand binding domain should impair ligand binding, and consequently, a reduced fluorescence response in the second screen. Out of the 36 insertion sites tested, 29 were fluorescent within two days (**Figure 2-5B**) and were therefore tested for their response to aspartate and glutamate. The results showed a clear winner; insertion of cpsfGFP between residues 194 and 195 produced a construct that showed a ~60% response to both aspartate and glutamate (**Figure 2-6**). We designated this construct as ODIN V1 (**O**ptical Aspartate [**D**] **In**dicator, version 1).

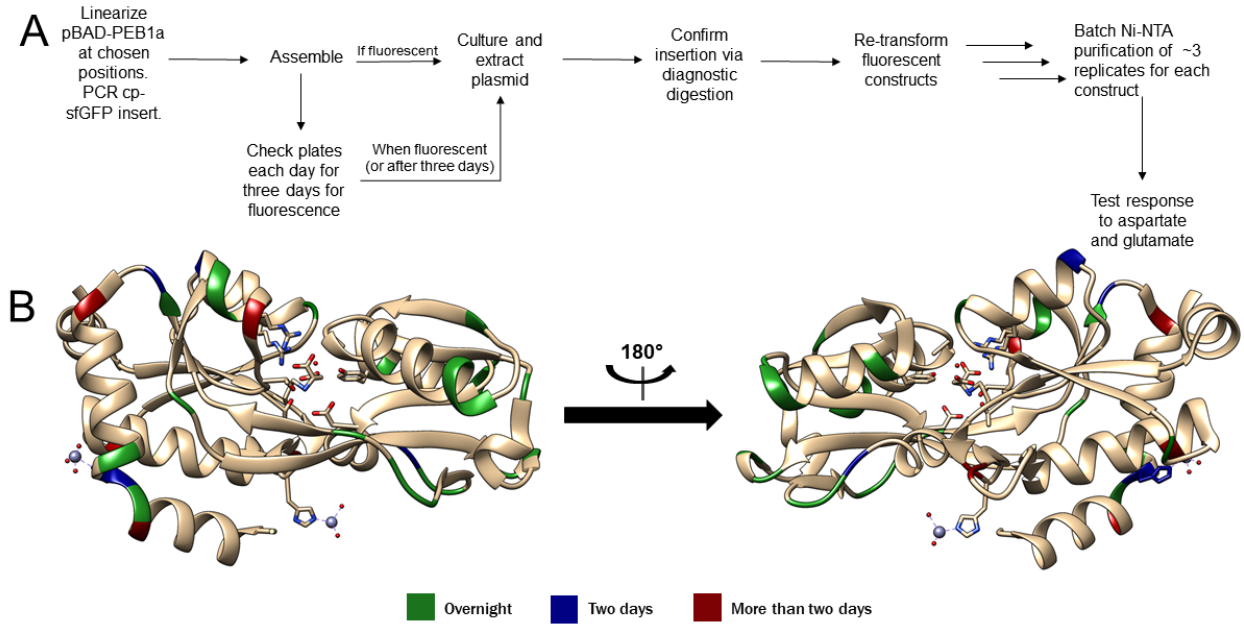

Figure 2-5 - Testing PEB1a insertion sites.

A) Workflow for determining the optimal insertion point in PEB1a. The gene encoding PEB1a was assembled into pBAD, and the resulting plasmid was then linearized at each of

the insertion points using PCR to facilitate insertion of cpsfGFP. The gene for cpsfGFP, with the original LV/NP linkers from iGluSnFR appended, was amplified from pBAD-sfGASP. After insertion of cpsfGFP into the linearized PEB1a PCR product and transformation into E. coli, colonies on a plate were inspected overnight (~16 h) following the transformation for fluorescent colonies. Six colonies were then cultured, and the plasmids were then extracted. Insertion was verified by digesting the extracted plasmids with XhoI and HindIII. Plates that were not fluorescent after ~16 h were checked again 8 h later, and ~24 h after these two time points for two more days. If there were no fluorescent colonies on the plater by the second inspection on the third day, six colonies were cultured immediately after for plasmid extraction and diagnostic digestion on the following day. Once successful assembly of all the constructs was confirmed by diagnostic digestion, plasmids for all the constructs that were fluorescent within two days were transformed into *E. coli*, and the expressed proteins were purified by Ni-NTA and assayed for their response to aspartate and glutamate (n = 3). B) Structure of PEB1a with the first residue of an insertion point coloured as indicated to indicate the time required before fluorescence was observed. Two perspectives, differing by a 180° rotation about the y-axis, are shown.

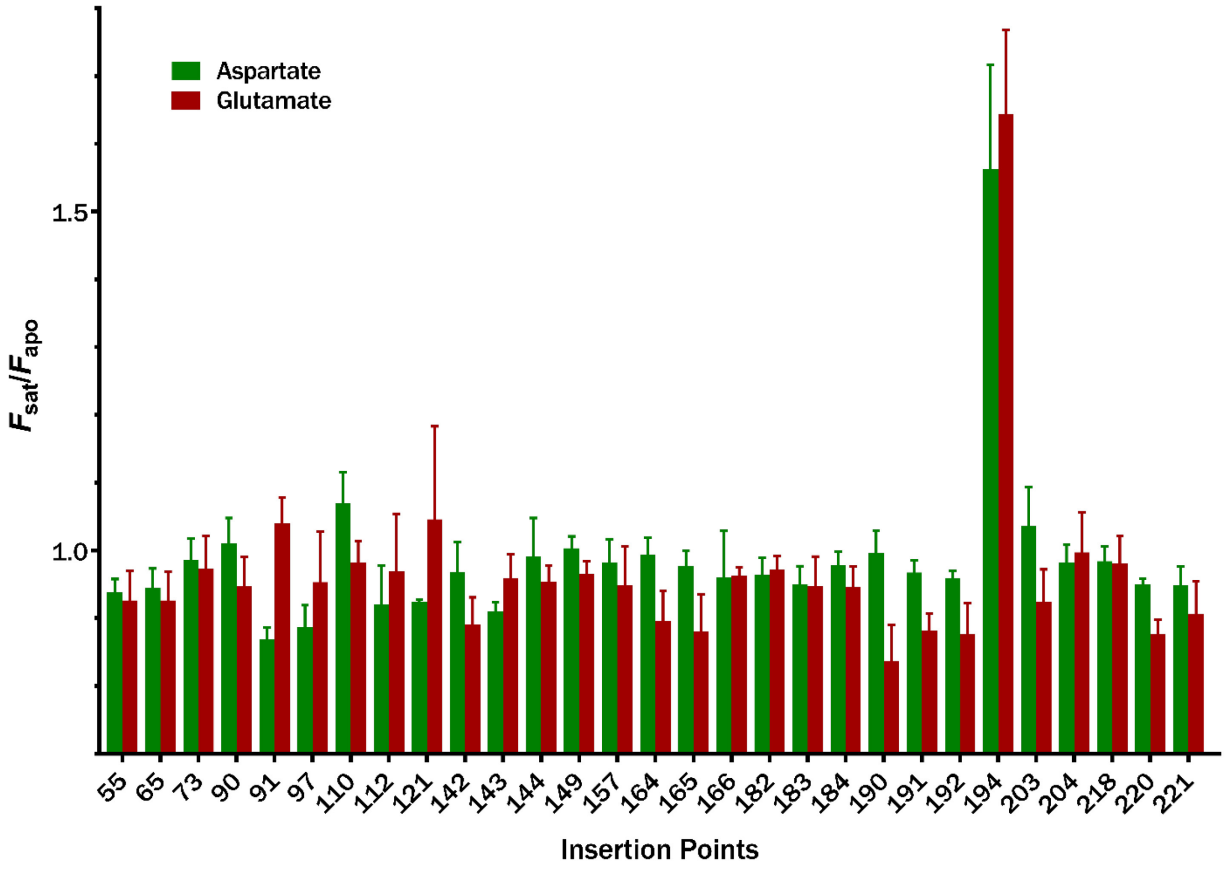

Figure 2-6 - Ligand-induced responses from different insertion points.

For clarity, only the first residue of an insertion point pair is shown on the y-axis.

During testing, we observed that the growth of *E. coli* expressing ODIN V1, as observed from culture turbidity, was impaired, and that, despite the large quantities of soluble protein extracted (as measured by the fluorescence intensity of the supernatant), binding to Ni-NTA resin was impaired. Given the strong expression of the construct, we hypothesized that the overexpression may be interfering with bacteria growth and confirmed that reducing the inducer concentration restored normal growth. Analysis of the construct sequence revealed a signal peptide

for export to the periplasm between the N-terminus 6×His tag and the construct that gets cleaved upon export. Deletion of this signal peptide (ODIN V2) not only restored binding to Ni-NTA, but also increased the F_{sat}/F_{apo} to ~3 (**Figure 2-7A** and **B**). We randomized both residues simultaneously for both linkers using NNK codons in parallel, and isolated a variant carrying Asn441Thr and Pro442Arg in the second linker that showed 11-fold increases in the presence of aspartate or glutamate. Subsequent randomization of the first linker did not produce any hits, but a round of directed evolution gave us ODIN V4, which had a 15-fold fluorescence increase to both ligands. Titrations of purified ODIN V4 showed a K_d of 260 μM and 709 μM, respectively, for aspartate and glutamate (**Figure 2-7C** and **Table 2-1**). Therefore, while we have successfully engineered an aspartate indicator with a large dynamic range, our best variant, to this point, still did not possess the required specificity to aspartate.

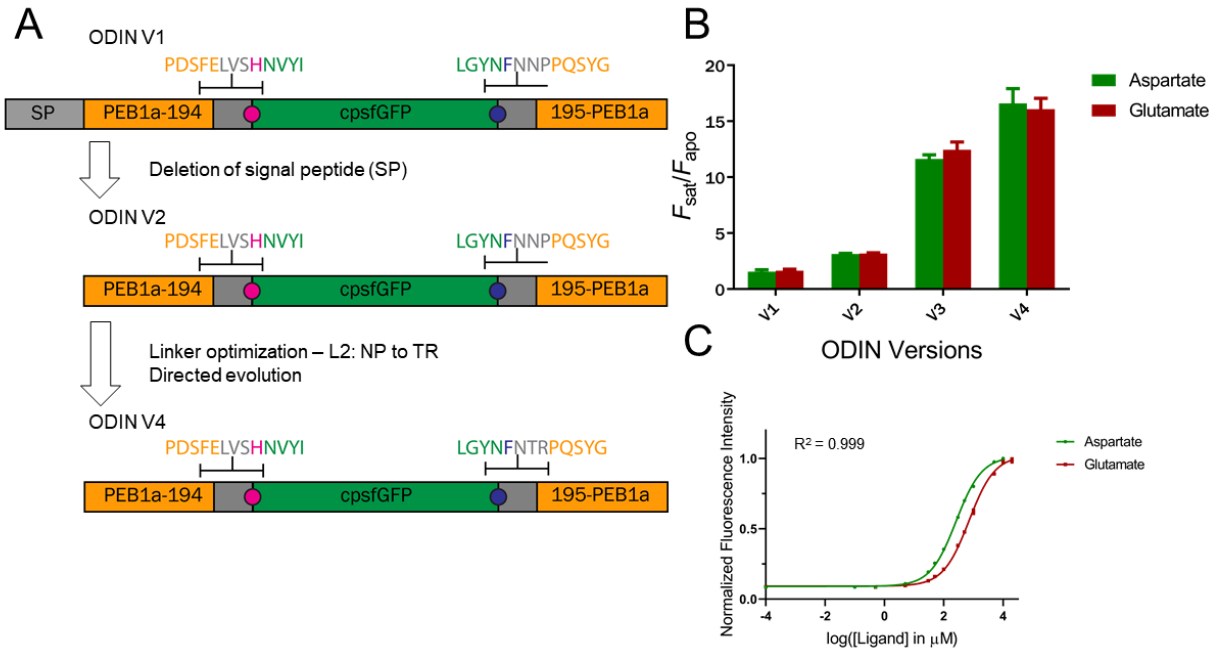

Figure 2-7 - Initial engineering of ODIN.

A) Lineage and schematic of engineering process up to ODIN V4. As with Figure 2-2, residues at both linker interfaces are shown above the schematic representations and

colored according to their domain, with the gatepost residues represented by the pink and navy circles. The numbers after and before PEB1a indicate the last and first residues, respectively, for that segment. B) Responses of batch-purified ODIN variants, up to ODIN V4, to aspartate and glutamate. C) K_d titration of purified ODIN V4 with aspartate and glutamate (n =3; technical).

2.3.1.2.2 Engineering specificity into ODIN

From our efforts with GASP, we learned that drastic changes to the polarity of the binding pocket can negatively impact protein folding. As such, we hypothesized that a rearrangement of the hydrogen bonds in the binding pocket may shift specificity in favour of aspartate without significant effects on protein folding. Our analysis of the binding pocket suggested that removal of the hydroxyl group on Tyr156 may disrupt a hydrogen bond to either ligand, but that Ala64, Ala128 and Ala131 were all close enough to aspartate's carboxylic acid side chain, but not glutamate's, such that a hydroxyl group at any of these positions may form a hydrogen bond to aspartate (**Figure 2-8**). To that effect, we screened a library combining these mutations. Unfortunately, variants either showed a stronger response to glutamate or diminished responses for both ligands and were discarded.

We returned to directed evolution, using ODIN V4 as the template and the ratio between the aspartate and glutamate responses as the screening criterion in an effort to engineer in greater specificity. We identified a variant, which we called ODIN V4.1, that had both an extremely low affinity ($K_d \approx 25$ mM) and a high response for glutamate ($F_{sat}/F_{apo} = 10.3 \pm 1.1$; n = 3, technical), but was hindered by low affinity for aspartate and, more importantly, extremely slow kinetics (on the order of minutes) (**Figure 2-9**).

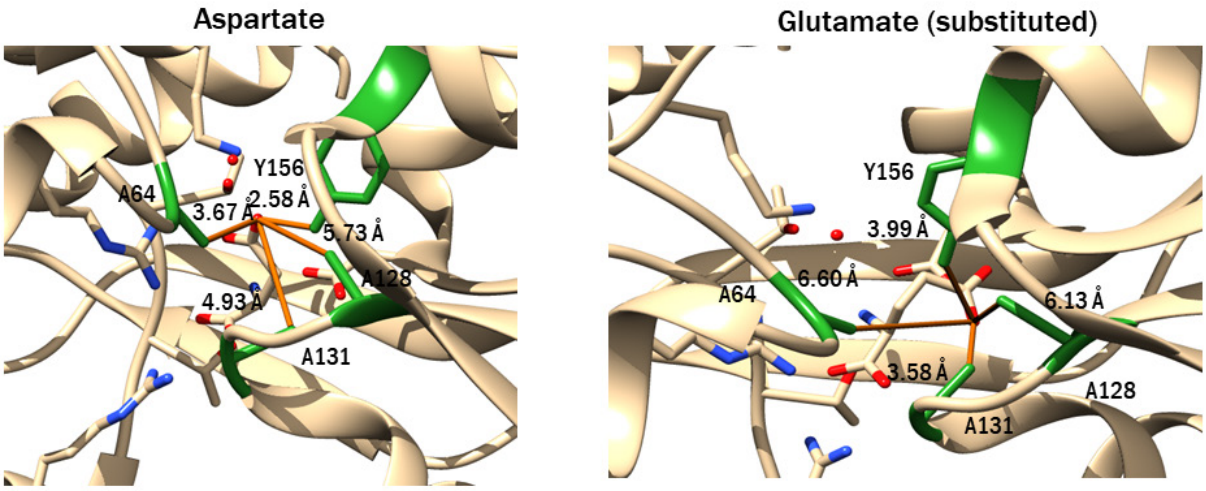

Figure 2-8 – PEB1a binding pocket residues targeted for hydrogen bond re-arrangement. Residues highlighted in green were mutated to re-arrange the positioning of hydrogen bonds in the binding pocket. Tyr156 was mutated to Phe, while the alanine residues were mutated to serine. Orange lines show represent distances from the side chain to the side-chain carboxylic acid group (aspartate on the left image and glutamate on the right) with the measurements shown. Glutamate was modelled into the binding pocket by replacement of the aspartate with a predicted rotamer. Primers containing each of these mutations were combined in a QuikChange Lightning Multi reaction and the resulting library screened.

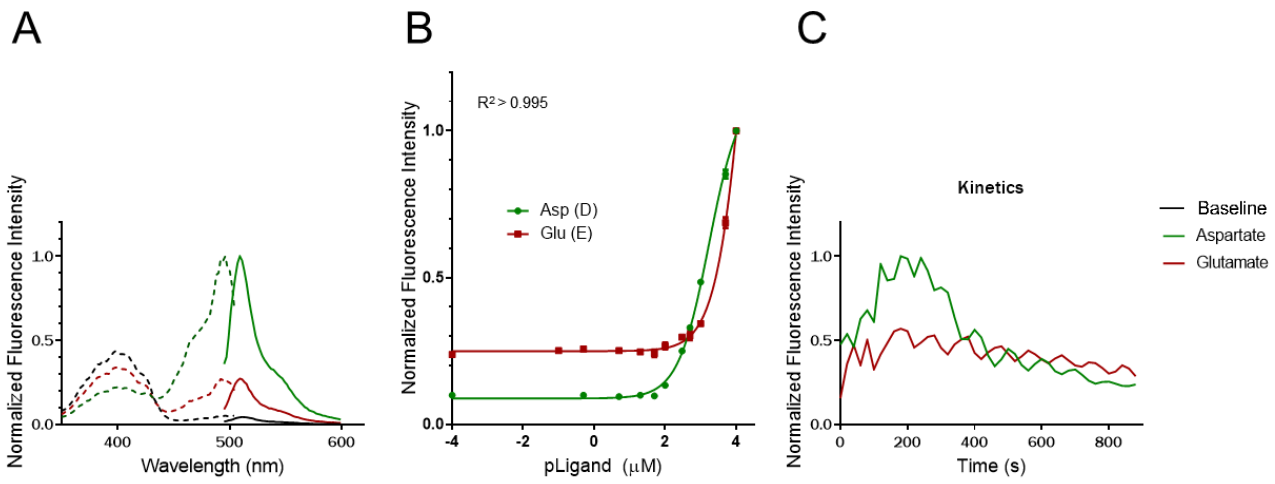

Figure 2-9 – ODIN V4.1 characterization.

A) Excitation (dashed) and emission (solid) spectra of ODIN V4.1 in different conditions. B) K_d titration with aspartate and glutamate (n = 3; technical). Error bars show SEM. C) Kinetics run.

We determined that a Val173Ala mutation was responsible for the significant shifts in affinity and response. Based on the PEB1a structure, we suspected that Val173 may have had such a strong influence on ligand binding due to a combination of its own hydrophobic interactions with the ligand, as well as by influencing its neighbor, Asp174, which has its own hydrophobic interactions with the ligand (**Figure 2-10**). Extrapolating from this finding, we randomized Phe83, Thr133, I177, Gly199, and Val173 in parallel using ODIN V4 as our template and modified our protocol to screen for K_d by measuring the response of each variant to two concentrations of aspartate (500 μM and 10 mM) and glutamate (1 mM and 10 mM). We then combined the favourable mutations (Val173Thr, Val173Gly, and Thr133Gly) to check for any synergistic effects between the mutations. At the end of this process, we had engineered our final variants (ODIN1a,b,c) (**Figure 2-11**) with different affinities and different F_{sat}/F_{apo} for aspartate and

glutamate (**Table 2-1** and **Figure 2-12**). Though the reduced dynamic range for glutamate as a result of mutation of Val173 to Gly was desirable, this variant was ultimately excluded from the final set because its affinity for aspartate relative to glutamate was not sufficiently enhanced.

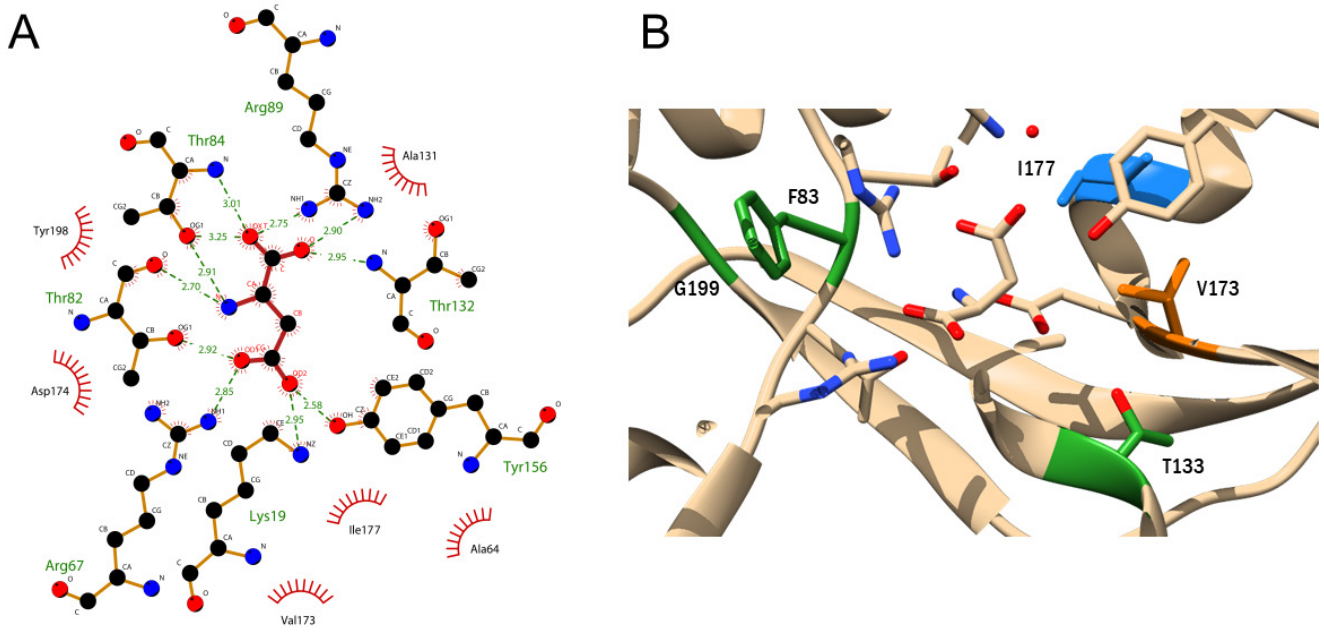

Figure 2-10 - PEB1a binding pocket.

A) Two-dimensional representation of the PEB1a binding pocket residues with aspartate using a similar scheme as Figure 1-1A. B) PEB1a binding pocket with targeted residues highlighted. Residues coloured green are those who are beside residues that interact with aspartate. Ile177, which has hydrophobic interactions with the ligand, is coloured blue, while Val173 is colored orange.

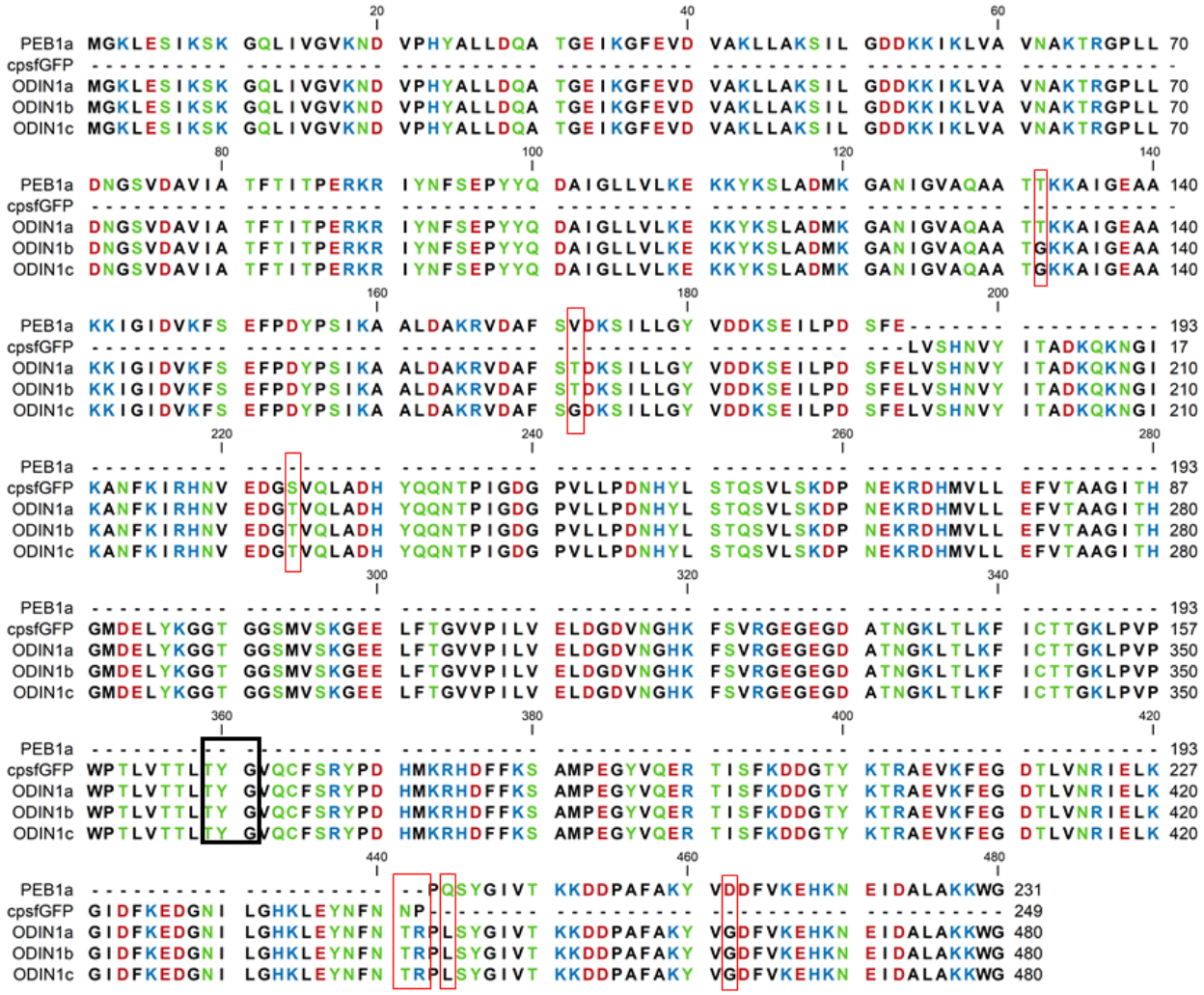

Figure 2-11 – Sequence alignment of ODIN1 variants with constituent proteins.

Sequence alignment for PEB1a (without the signal peptide; PDB: 2V25) [321], cpsfGFP, and the final ODIN1 variants. Residues are coloured according to polarity. The first and last two residues for cpsfGFP are the linkers from iGluSnFR [252]. Chromophore-forming residues are indicated by the black box, and mutations are highlighted by the red boxes.

2.3.2 *In vitro* characterization of ODIN1 variants

We then undertook a systematic characterization of our ODIN1 variants (**Table 2-1** and **Figure 2-12**). All three of the ODIN1 variants had an emission peak of 509 nm and an excitation peak of 492 nm with no significant wavelength shifts upon ligand binding (**Figure 2-12C**). Given

the different properties of our three variants (**Table 2-1**), we believe that each of these variants can be useful for different applications.

ODIN1a, incorporating a Val173Thr mutation, was slightly dimmer than ODIN V4, but is the brightest out of all our variants with almost 90% of EGFP's brightness and 30% brighter than iGluSnFR (**Table 2-1**). Additionally, although it has a similar affinity for L-glutamate as ODIN V4, it shows 6-fold lower K_d for L-aspartate, yielding a 19-fold difference in affinity without significantly affecting the dynamic range for either L-aspartate or L-glutamate (**Table 2-1** and **Figure 2-12C** and **E**). ODIN1a had a stronger affinity for its primary ligand and improved specificity relative to iGluSnFR, which showed strong affinity for both ligands. ODIN1a showed maximum specificity for L-aspartate at <100 μM concentrations (**Figure 2-12B**). Considering that glutamate concentrations in the synapse can range from less than 20 nM to at least 1 mM, if not up to 5 mM [8,11,12,342], use of ODIN1a, despite its stronger affinity towards L-aspartate, may not be ideal in systems where both L-aspartate and L-glutamate are present and specificity is desired. Conversely, however, it retained a strong enough affinity towards L-glutamate to function as a glutamate indicator, possibly providing an alternative to iGluSnFR.

ODIN1b, which carries an additional Thr133Gly mutation relative to ODIN1a, showed a similar, if not slightly stronger, affinity to L-aspartate, but has a favourable 4.5-fold weaker affinity to L-glutamate, widening the difference in affinity to over 150-fold (**Table 2-1** and **Figure 2-12E**). As a result of this increased gap in affinities, ODIN1b demonstrated good specificity for ligand concentrations as high as 10 mM with over 2.5-fold difference in fluorescence intensities, although maximum specificity was still obtained at ~100 μM (**Figure 2-12B**). Therefore, while ODIN1b retained some response to L-glutamate at the upper range of the estimated physiologically relevant concentrations [11], these responses are likely to be small and should still be differentiable from its

L-aspartate. Although it was dimmer than ODIN1a, ODIN1b was still brighter than ODIN1c and iGluSnFR (**Table 2-1** and **Figure 2-12C**). Interestingly, despite significantly reducing the affinity for L-glutamate, Thr133Gly did not significantly affect the maximum dynamic range for L-glutamate. Thus, given its properties, we believe that ODIN1b presents the best balance between specificity, having the largest difference in affinities among the ODIN1 variants up to ~600 μM, and other properties.

ODIN1c differs from ODIN1b with a Val173Gly mutation instead of Val173Thr. Unlike either of the first two mutations discussed, this mutation reduced the indicator's affinity towards both L-aspartate and L-glutamate as well as the dynamic ranges for L-aspartate and L-glutamate relative to ODIN1a and ODIN1b (9.64 ± 0.05 and 8.35 ± 0.14, respectively, compared to ~10.5 for both ligands; **Table 2-1** and **Figure 2-12C and E**). As a result, there was an over 20-fold difference in affinities for L-aspartate and L-glutamate, which was still larger than that of ODIN1a, and more importantly, its K_d for L-glutamate (8.77 mM) is beyond the 5 mM upper estimate for the synaptic concentration of glutamate [11]. However, it is worth noting that the K_d for L-glutamate may be an underestimation as the titration curve did not appear to plateau. Regardless, ODIN1c had the largest difference in fluorescence intensities at the estimated range of peak synaptic concentrations for neurotransmitters (**Figure 2-12B**) [11]. ODIN1c was the dimmest out of the three variants, though it was still brighter than iGluSnFR and retained 70% of EGFP's brightness. Thus, we propose that ODIN1c would be best suited for studies requiring maximum specificity for L-aspartate at concentrations between ~600 μM and 10 mM.

The pH titration results indicated that the affinity-shifting mutations did not significant affect the chromophore environment as all three variants have similar pK_a values (**Figure 2-12D**). In the apo state, all three ODIN1 variants have a pK_a of ~4.8, but ligand binding shifted the pK_a to

~6.4, indicating a change in the chromophore environment. The titrations also revealed that in the saturated state, the indicators were not at maximum brightness during testing (pH = 7.2) nor would it be reached under physiological conditions (pH = 7.4). The bound-state pK_a limits the application of ODIN1 in synaptic vesicles, which have a pH of ~5.5 [343].

Table 2-1 - ODIN variants' *in vitro* characterization.

Variant		EGFP[b]	iGluSnFR[c]	V4	1a	1b	1c
Mutations[a]		n/a	n/a	n/a	V173T	T133G, V173T	T133G, V173G
$\Delta F/F_{min}$[d]	L-Asp[g]	n/a	3.25 ± 0.10 (2.0)	11.3 ± 0.3	10.7 ± 0.08	10.6 ± 0.1	9.64 ± 0.05
	L-Glu	n/a	5.83 ± 0.19 (4.5)	11.2 ± 0.7 [g]	11.0 ± 0.08[h]	10.4 ± 0.3[h]	8.35 ± 0.14[h]
	D-Asp[i]	n/a	0.44 ± 0.07	4.28 ± 0.19	8.6 ± 1.1	8.05 ± 0.05	3.77 ± 0.02
K_d (μM)[e]	L-Asp	n/a	81.0 (145)	260 [247, 273]	37.6 [33.5, 42.0]	27.4 [24.8, 30.4]	388 [363, 413]
	L-Glu	n/a	48.2 (107)	709 [658, 766]	763 [678, 861]	4200 [3810, 4620]	8770 [7910, 9710]
	D-Asp	n/a	n.d.	n.d.	9080 [6970, 11800]	1500 [12800, 17700]	n.d.
Brightness[f]	Apo	40.3 (37.5)	6.1	2.66	3.53	3.43	3.29
	L-Asp[g]	38.9 (37.5)	25.4[j]	35.3	33.0	30.8	27.4
ε x 1000 ($M^{-1}cm^{-1}$)	Apo	58.2 (56.0)	9.29 ± 0.09	4.5	4.98 ± 0.06	4.97 ± 0.03	4.58 ± 0.07
	L-Asp[g]	58.7 (56.0)	38.8 ± 0.3[j]	61.6	59.3 ± 1.4	56.9 ± 0.6	50.3 ± 1.0
Φ	Apo	0.67	0.65 ± 0.02	0.59	0.71	0.69	0.72
	L-Asp[g]	0.67	0.66 ± 0.02[j]	0.57	0.56	0.54	0.55
pK_a[e]	Apo	n.d.	(7.0)	n.d.	4.66 [4.22, 5.03]	4.86 [4.34, 5.30]	4.77 [4.60, 4.94]
	L-Asp[g]	n.d.	(6.5)[j]	n.d.	6.35 [6.26, 6.44]	6.40 [6.30, 6.50]	6.43 [6.37, 6.48]

[a] Relative to ODIN V4.
[b] Literature values in parentheses are from Cranfill *et al.* [329].
[c] Literature values in parentheses are from Marvin *et al.* [252] and Helassa *et al.* [253].
[d] Calculated from the emission spectra's peaks without and with ligand at specified concentrations.
[e] Brackets represent 95% confidence intervals.
[f] Brightness is defined as the product of ε and ϕ.
[g] Measurements were performed at 10 mM ligand concentration.
[h] Measurements were performed at 300 mM ligand concentration.
[i] Measurements were performed at 100 mM ligand concentration.
[j] Measurement for glutamate.
Measurements are reported as means ± SEM (n = 3; technical).
n.d. = not determined. n/a = not applicable.

When we tested our ODIN variants against a panel of structurally related amino acids, we discovered that they, to a lesser extent than L-aspartate and L-glutamate, respond to D-aspartate

(**Table 2-1** and **Figure 2-12C**). Albeit significantly smaller than its response to L-aspartate or L-glutamate, ODIN V4 had a significant response to D-aspartate, likely due to the aspartate's near symmetry. Introducing the Val173Thr mutation in both ODIN1a and ODIN1b nearly doubled the dynamic range for D-aspartate relative to ODIN V4. Interestingly, replacing the Thr in position 173 with Gly had the opposite effect, narrowing the dynamic range for D-aspartate relative to ODIN V4, further suggesting that this position has a direct influence on the binding pocket. It should be noted that the reported $\Delta F/F_{min}$ for ODIN1c with respect to D-aspartate may be an underestimation, similar to L-glutamate, as the titration curve suggest that 100 mM may be insufficient to saturate the sensor. Consequently, we were unable to determine the D-aspartate K_d for ODIN1c. A growing body of literature suggests that D-aspartate is a neurotransmitter with roles in hormone regulation, development, learning and memory (reviewed in [38,45,46]). Given our results and assuming that the concentration of D-aspartate in the synapse does not exceed that of L-glutamate, we believe that interference from D-aspartate will be minimal. None of the ODIN1 variants showed significant responses in the presence of L-glutamine, L-asparagine, D-glutamate, D-asparagine, D-glutamine.

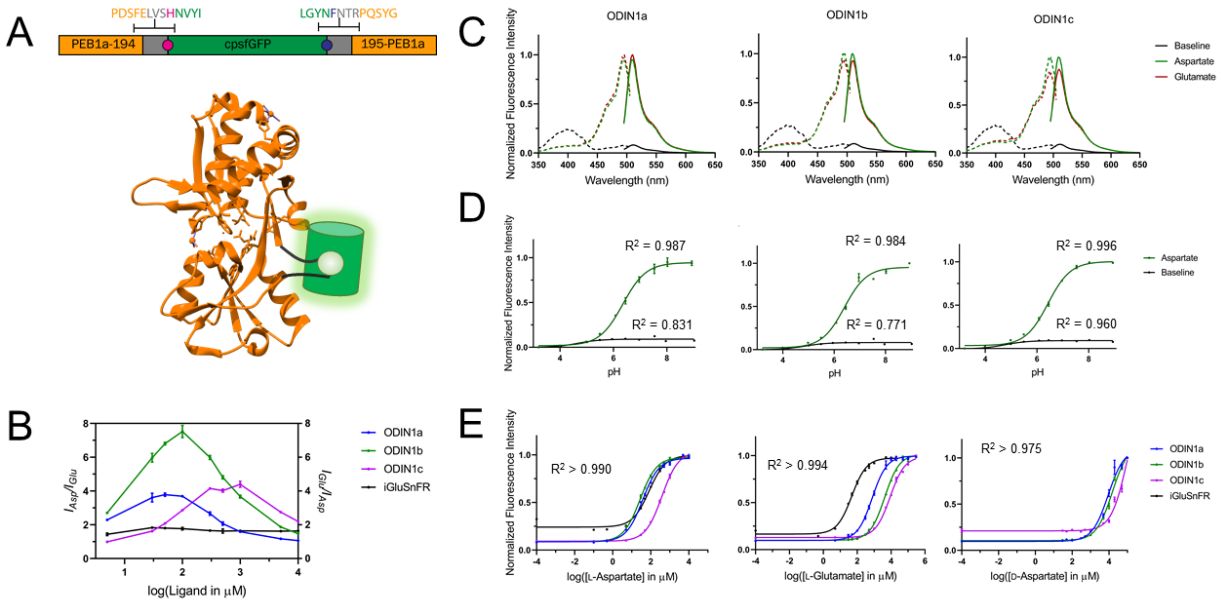

Figure 2-12 - ODIN1 structure and spectral characterization.

A) Representation of the structure of ODIN1 using the structure of PEB1a (PDB: 2V25) and cpsfGFP represented as a barrel [321]. The insertion point residues have been removed to illustrate connectivity to cpsfGFP. B) Ratio of fluorescence intensities of ODIN1 variants (left y- axis) and iGluSnFR (right y-axis) against the concentration (in micromolars) expressed in logarithmic values (n = 3; technical). C) Excitation (dashed) and emission (solid) spectra of ODIN1a (left), ODIN1b (middle), and ODIN1c (right) with 10 mM L-aspartate or 300 mM L-glutamate. Colour scheme is consistent with Figure 1-9. D) pH titration curves for ODIN1 variants (n = 3; technical). E) K_d titration of ODIN1 variants for L-aspartate (left), L-glutamate (middle), and D-aspartate (n = 3; technical). For the L-aspartate and L-glutamate titrations, iGluSnFR (black) is shown for comparison. The D-aspartate titration was not performed with iGluSnFR. Fitted values are shown in Table 2-1. Error bars represent SEM.

2.3.3 Imaging in mammalian cells

Near the beginning of engineering ODIN1, we cloned ODIN V3 into pMiniDisplay and transfected the plasmid into HeLa cells to confirm proper localization to the cell membrane (**Figure 2-13A**). However, when we later expressed ODIN1b on the surface of HeLa cells and measured the change in fluorescence intensity upon addition of 10 mM L-aspartate, we only observed a ~20% increase at best, which is much smaller than the values observed in the purified protein *in vitro* (**Figure 2-13B** and **Table 2-1**).

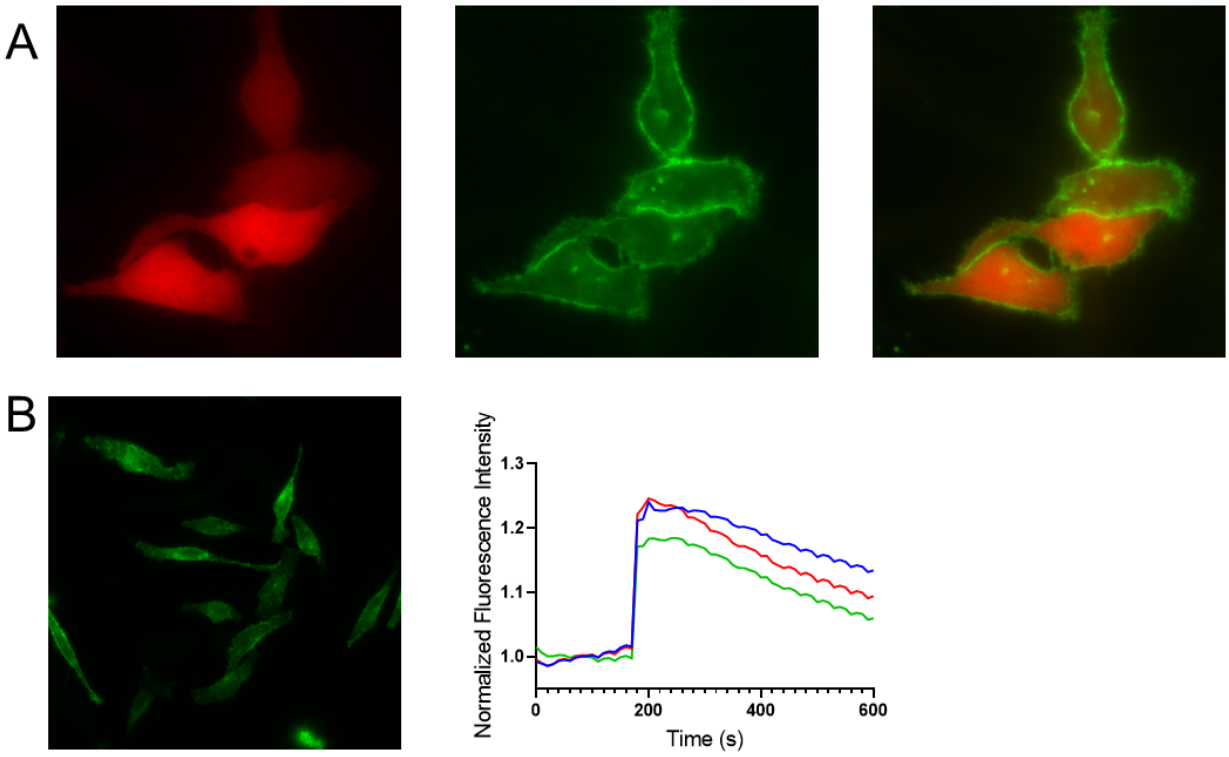

Figure 2-13 - Imaging ODIN constructs in HeLa cells

A) Co-transfection of membrane-localized ODIN V3 with cytosolic mApple. The left image shows mApple expressed in the cytosol (modified pcDNA3.1(+)-mApple), and the center image shows ODIN V3 localized to the membrane (pMiniDisplay-ODIN V3). The right image

shows the merged image, confirming membrane localization. Images are coloured using lookup tables. B) Functional test of ODIN1b in HeLa cells. The left panel shows HeLa cells expressing ODIN1b on their membrane surface at 40x magnification. Right image shows corresponding individual cell traces of the change in fluorescence intensity upon addition of 10 mM L-aspartate.

In an effort to recover the performance we observed *in vitro* with purified protein, we attempted to tether bacteria-expressed ODIN variants to the plasma membrane surface using the SpyTag and SpyCatcher system [327,344]. SpyTag is a 1.7 kDa peptide that forms a covalent isopeptide bond with its partner, SpyCatcher (15 kDa). We first labelled TfR-SpyCatcher003 (Addgene #133451), which utilized the transferrin receptor to tether SpyCatcher003 to the membrane, with mApple and tagged our ODIN constructs with SpyTag003 at the N-terminus. To ensure that the addition of the relatively long SpyTag (18 residues plus a 6 residue linker) did not interfere with the His-tag, we moved the His-tag to the C-terminus and removed the rest of the pBAD leader sequence. Our results demonstrated that ODIN1 can be localized to the membrane using the SpyTag and SpyCatcher system with a brief incubation and that the tethered indicators are responsive to their ligands, with $\Delta F/F_{min}$ ranging from ~3 to 4 for L-aspartate and ~2 to 3 for L-glutamate compared to ~20% increase seen in pMiniDisplay (**Figure 2-14**). This response towards aspartate is comparable to the responses observed from iGluSnFR upon addition of glutamate on HEK293 cells [252]. Though the ODIN1 variants showed a significant response to L-glutamate, these were still smaller than their response to L-aspartate, albeit the differences were markedly narrower than what was observed *in vitro* (**Figure 2-12B**). To confirm that these changes in fluorescence intensities are due to ODIN1 responding to L-aspartate or L-glutamate specifically,

we also measured the tethered sensors' response to L-glutamine, which none of the ODIN1 variants respond to *in vitro*, but did not observe a significant change in fluorescence, as expected (data not shown). Therefore, we present the SpyTag/SpyCatcher system as a viable solution for expressing ODIN1 onto the cell surface and imaging aspartate dynamics.

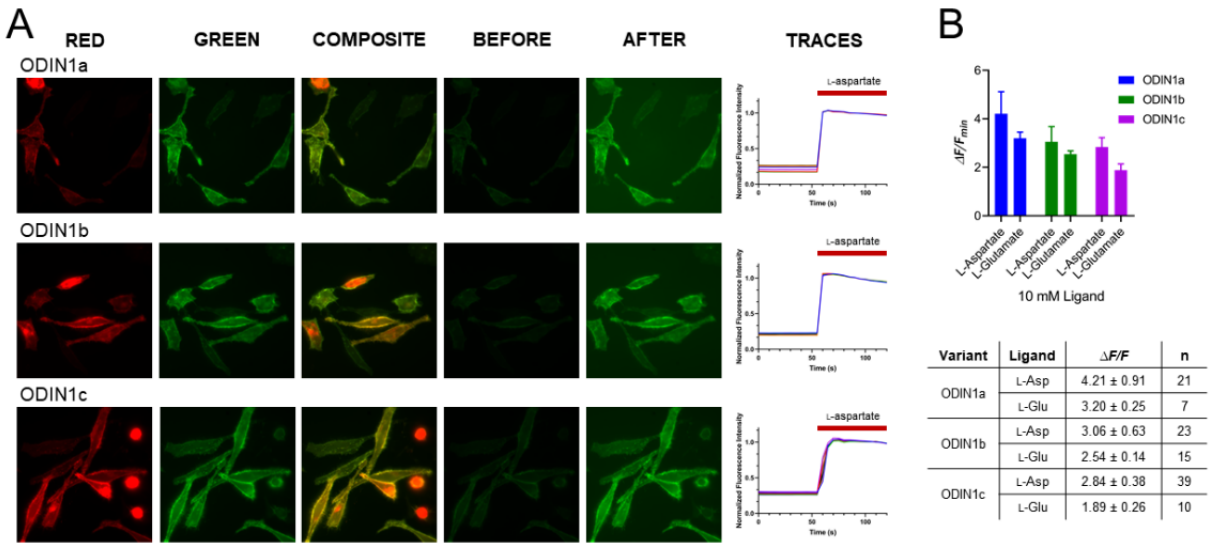

Variant	Ligand	ΔF/F	n
ODIN1a	L-Asp	4.21 ± 0.91	21
	L-Glu	3.20 ± 0.25	7
ODIN1b	L-Asp	3.06 ± 0.63	23
	L-Glu	2.54 ± 0.14	15
ODIN1c	L-Asp	2.84 ± 0.38	39
	L-Glu	1.89 ± 0.26	10

Figure 2-14 - SpyTagged ODIN1 in HeLa cells.

A) Representative images of cells expressing mApple-SpyCatcher003 on the membrane and tagged with ODIN1 variants. From the left, the first column of images was taken in the red channel, showing expression of mApple-SpyCatcher003 on the membrane, and the second column of images was taken in the green channel, showing the localization of the SpyTagged ODIN1 constructs. These images were merged to generate the composite images in the third column. The fourth column shows images of cells before the addition of 10 mM L-aspartate, and the rightmost column shows the same cells after the addition of 10 mM L-aspartate at the peak of the response. Images were coloured in ImageJ using lookup tables. The traces are representative, showing the change in fluorescence intensity of cells upon the addition of L-aspartate. Each trace represents one cell, where each cell

was manually labelled as a region of interest in ImageJ. B) Responses of tethered ODIN1 constructs on the cell surface. Error bars and values represent SD (n = number of cells; technical because measurements were taken using one stock of purified protein for each ODIN1 variant).

2.3.4 Alternatives to membrane localization and progress towards ODIN2

To date, genetically encoded neurotransmitter indicators have been expressed on the cell membrane [252,254,287,291,345]. However, one limitation of using a cell-surface sensor is that the sensor is constrained to a 2D surface, limiting the number of copies that can be displayed and consequently, the fluorescence signal. On the other hand, the extracellular matrix (ECM), which provide structural and biochemical support to cells and is rich in hyaluronic acid, makes up 20% of the brain's volume [346,347]. Therefore, a possible advantage of targeting genetically encoded indicators to the ECM, instead of the membrane, is a stronger fluorescence signal since more copies of the indicator can be targeted to the ECM, which encloses the synapse, than can be packed into the part of the membrane close to the synapse. Additionally, given that previous work has shown that the ECM plays a role in modulating neural circuitry, and has, indeed, been implicated in addiction and memory [348-350], indicators targeted to the ECM can open a new avenue of questions that can be investigated regarding synaptic spillover.

Inspired by a report from Zhang *et al.* that described the detection of hyaluronan in mice brains by fusing GFP to a hyaluronan binding domain [351], we inserted FPs and iGluSnFR between a secretion signal with linker containing a His-tag and a LINK domain, a 97-amino acid protein that binds hyaluronan (**Figure 2-15A**). As a proof-of-principle experiment, we transfected the secretion constructs carrying EGFP, iGluSnFR, and sfGFP into HeLa cells and collected the media ~24 h after transfection, which we then incubated with Ni-NTA resin. We measured the

fluorescence spectra of each, and in the case of the iGluSnFR construct, measured its response to aspartate and glutamate (**Figure 2-15B**). Our results indicate that although the secretion appeared to be inefficient, and in the case of iGluSnFR, affected its performance, some protein did successfully get secreted. Additionally, we observed that we collected more sfGFP than we did EGFP or iGluSnFR, though it is unclear whether this is due to increased expression of sfGFP [254,324] or better secretion.

Previous work by the Snapp group suggest that the presence of cysteine residues, which have the potential to erroneously form disulfide bonds in the oxidizing environment of the endoplasmic reticulum, may affect secretion [352]. To address this potential problem, Snapp and coworkers have engineered a palette cysteine-free FPs named oxFPs [352,353]. Accordingly, we engineered the oxGFP mutations, Cys48Ser and Cys70Ser (numbered relative to sfGFP), into ODIN1b. Our preliminary results suggested that, regardless of their yet-to-be-determined effect on the indicator's ability to be secreted, these mutations widened the construct's dynamic ranges for L-aspartate and L-glutamate while reducing that of D-aspartate (**Table 2-2**).

Table 2-2 – ODIN1b *versus* ODIN1b + oxGFP mutations.

Ligand	ODIN1b	ODIN1b + C48S + C70S
L-aspartate	10.6 ± 0.1	24.3 ± 0.2
L-glutamate	10.4 ± 0.3	13.9 ± 0.1
D-aspartate	8.05 ± 0.05	6.35 ± 0.06

Performed with 10 mM ligand. All values reported as mean ± SEM (n = 3).

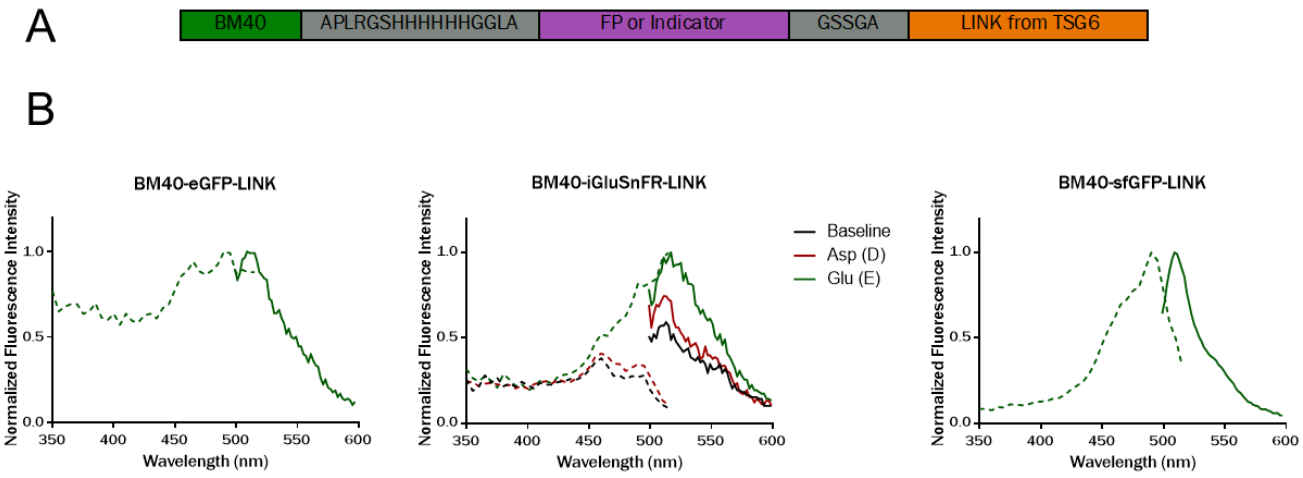

Figure 2-15 Proof-of-principle for secretion strategy.

A) Schematic representation of secretion construct. BM40 is a signal peptide for secretion, which, along with the linker, was first utilized by Zhang and colleagues [351]. LINK from TSG6 is the hyaluronan binding domain used by Ghosh and coworkers [354]. B) Excitation (dashed) and emission (solid) spectra from proteins secreted in the media of cells transfected with each construct and collected with Ni-NTA.

2.4 Conclusion

We have successfully engineered a series of aspartate indicators from PEB1a, an aspartate/glutamate binding protein from *C. jejuni*. Insertion of cpsfGFP in the hinge region close to the binding pocket produced a functional aspartate/glutamate indicator whose dynamic range we were able to increase by a factor 5 following linker optimization and directed evolution. While there was a 2-fold separation in the early prototype's affinities for aspartate and glutamate, we were able to enhance this separation to an over 150-fold difference by building on a mutation identified through directed evolution and using the crystal structure of PEB1a and to identify other residues that are important for specificity. We found that mutation of just two residues, Val173 and Thr133, acted as handles to manipulate the sensor's affinities for its ligands and were sufficient

to produce variants with a range of affinities for both ligands though at the cost of sensor brightness. Thus, our ODIN1 series consist of three different variants with different strengths that may be leveraged for different applications.

However, as a first-generation sensor, there is much room for improvement. Currently, the biggest limitation to ODIN1 is its poor performance when expressed on the membrane of cells, and our efforts are focused on addressing this limitation. Though we have successfully demonstrated that the SpyTag and SpyCatcher system enabled the expression of ODIN1 while retaining its function, the need to purify and introduce it into the system of interest is an additional complication that can limit its use. While we hope that optimizing the signal peptide and membrane-tethering domain will rescue its performance, our preliminary results suggest that secreting ODIN1 may also be a promising avenue. Additionally, though diminished, their affinity for L-glutamate may still be physiologically relevant [11]. While the specificity of these ODIN1 variants may be sufficient for distinguishing between aspartate and glutamate in co-release studies when used with red iGluSnFR (R-iGluSnFR) [255], ODIN variants with weaker affinities for L-glutamate would still be preferable. Red fluorescent ODIN variants would also be extremely useful as it allows for multiplex imaging and, depending on the choice of FP, enable the engineering of a less pH-sensitive variant. Given that a key question regarding classifying L-aspartate as a neurotransmitter is the identity of its vesicular transporter, variants that remain unquenched upon ligand binding in synaptic vesicles (i.e., variants with a pK_a below 5.5 in the bound state) would be highly useful in probing this issue.

Through a combination of directed evolution and semi-rational design guided by the crystal structure of PEB1a, we have successfully engineered the first generation of the ODIN series, a family of bright green aspartate indicators with large dynamic ranges. Mutations at two key

positions yielded three variants, each with a different balance of affinities and dynamic ranges for aspartate and glutamate. Though there is room for improvement, we believe that the ODIN1 series will open new avenues for probing the specific role of aspartate in the nervous system.

3 Chapter 3 – Green single-FP based glutamine indicator

3.1 Introduction

L-Glutamine (one letter code: Q), has a plasma concentration that exceeds the concentrations of all the other amino acids by at least ten-fold, a fact that underscores its importance in human physiology [355]. In addition to its role as a proteinogenic amino acid, some of glutamine's roles include acting as a nitrogen or carbon donor for the syntheses of key metabolites; and regulating protein turnover and ammonia levels (for detailed discussions, see the reviews by Wu [356], Cruzat *et al.* [355] and Mazat and Ransac [357]). In the nervous system, glutamine is most recognized for its role in the glutamate/GABA-glutamine cycle, where glutamate in excitatory synapses (or GABA in inhibitory synapses) is taken up by astrocytes after release and converted to glutamine by glutamine synthetase (reviewed by Bak *et al.* [7] and Albrecht *et al.* [51]). Glutamine is then transported back into neurons for conversion back to glutamate or GABA and packaged into vesicles for release upon excitation. Additionally, this cycle is important in regulating ammonia homeostasis as the production of glutamine consumes one molecule of ammonia while its metabolism produces one molecule. Aberrations in this cycle, such as those caused by altered activity of glutamine synthetase, have been implicated in neurological conditions, such as epilepsy [54,358]. Furthermore, the Trojan Horse hypothesis proposes that excessive glutamine synthesis, despite consuming ammonia, actually increases oxidative and nitrosative stress by impairing mitochondrial function [57,59,60].

Improved methods for imaging glutamine concentration dynamics in living cells, especially methods that utilize genetically encoded FP-based indicators (because of their ease of use and the high spatiotemporal resolution of fluorescence imaging), would be of interest to both neuroscientists and cell biologists. Currently, the only fully genetically encoded glutamine sensor

is the FLIPQ series, with six variants possessing a range of affinities and dynamic ranges [263]. FLIPQ sensors are FRET-based ratiometric indicators that utilize the glutamine binding domain from *Escherichia coli* with monomeric teal FP (mTFP1) and Venus as the donor and acceptor, respectively. Although they allow for ligand quantification, FRET-based indicators are generally less desirable than single FP-based indicators because of the need to image in two channels and their generally smaller responses. Indeed, the best FLIPQ variant shows a maximum $\Delta R/R_0$ of 0.26, where R is the ratio of the emission peaks for Venus/mTFP1 [263]. Another FRET sensor using the same glutamine binding domain with a $\Delta R/R$ of 0.9 has been reported; however, this FRET sensor utilized CouA, an unnatural amino acid, as the donor and EGFP as the acceptor [264]. Here, as an alternative to these sensors, we report the engineering of the first single FP-based glutamine indicator using the glutamine binding protein from *Burkholderia pseudomallei.*

3.2 Materials and Methods

3.2.1 General

Double-stranded DNA and DNA oligonucleotides were synthesized by Integrated DNA Technologies. Several polymerases were used for high-fidelity PCR according to the manufacturer's instructions: CloneAmp HiFi PCR Premix from Takara Bio USA, Inc., Q5 polymerase from New England BioLabs, and Platinum SuperFi DNA Polymerase and Platinum SuperFi II DNA Polymerase from Thermo Fisher Scientific. Recombinant Taq polymerase was used for EP-PCRs and purchased from Thermo Fisher Scientific. PCR products were purified by agarose gel electrophoresis and extracted with the GeneJET Gel Extraction Kit (Thermo Fisher Scientific). Restriction enzymes and T4 DNA ligase were purchased from Thermo Fisher Scientific and used according to the manufacturer's recommendations. Digested PCR products were directly extracted with the GeneJET Gel Extraction Kit before ligation. In-Fusion HD was used for assembly reactions and was purchased from Takara Bio USA, Inc. Plasmids were

extracted from small (~4 mL) cultures with GeneJET Plasmid Miniprep Kits (Thermo Fisher Scientific). Ligands were obtained as solids from Fisher, Alfa Aesar or Acros Organics with at least 98.5% purity or molecular biology grade. Sanger sequencing reactions using BigDye were performed by the Molecular Biology Services Unit at the University of Alberta. Fluorescence measurements were performed on a Safire^2 plate reader (Tecan), and absorbance measurements were collected on a DU-800 UV-Visible Spectrophotometer (Beckman). Most protein structure images were generated using UCSF Chimera 1.14 [322,323] except when specified otherwise.

3.2.2 Plasmid construction and directed evolution

3.2.2.1 Plasmid and library construction

Generic procedure for plasmid construction. Unless described otherwise, plasmids were constructed through seamless homology-based assembly using In-Fusion. Double-stranded DNA, sharing at least 15-bp overlap with the linearized vector backbone in both 5' and 3' ends, is incubated at 50 °C for 15 min with vector backbone linearized by amplification or restriction enzymes and In-Fusion enzyme mix. Following completion of the assembly, the reaction is used to transform electrocompetent *E. coli* strain DH10B (Invitrogen) and cultured overnight at 37 °C on LB agar plates with 400 µg/mL ampicillin (Thermo Fisher Scientific) and 0.02% L-arabinose (Alfa Aesar). Plasmids were then isolated from single colonies cultured overnight in liquid LB cultures with 100 µg/mL ampicillin and 0.02% % L-arabinose at 37 °C. Sequences were then confirmed by Sanger sequencing.

Construction of plasmids for testing insertion points in glutamine binding proteins. Double-stranded DNA encoding either GlnH from *E. coli* (codon optimized for mammalian expression based on the amino acid sequence in the PDB structures (ID: 1GGG (open) and 1WDN (closed)) or glutamine binding protein from *Burkholderia pseudomallei* (BpQBP; also codon optimized for mammalian expression based on the protein sequence in the PDB (ID: 4F3P)) were

assembled into pBAD/HisB vector prepared by digestion with XhoI and HindIII [359-361]. The assembly was used to transform DH10B and the transformed bacteria were grown on LB agar plates supplemented with 400 μg/mL ampicillin and 0.02% L-arabinose as described above. Single colonies were then used to inoculate 4 mL of LB with 100 μg/mL ampicillin and 0.002% L-arabinose for overnight incubation at 37 °C for plasmid extraction. These plasmids, called pBAD-GlnH or pBAD-BpQBP, were then linearized at each insertion site by high-fidelity PCR and assembled with the gene for cpsfGFP [324] with the optimized linkers from ODIN V3 (amplified from mammalian codon-optimized pBAD-ODIN V3; Chapter 2), as described previously.

Construction of mutated libraries. For site-directed mutagenesis libraries of *B. pseudomallei* binding protein-based indicators, the template was amplified with Platinum SuperFi DNA Polymerase or Platinum SuperFi II DNA Polymerase and primers designed using the 22-codon trick to reduce the library size [362]. Briefly, for each targeted position, three sets of primers carrying NDT (N = any base; D = A, G or T) , VHG (V = A, C or G; H = A, C or T), or TGG codons (and their complements) at the targeted position were mixed in a 12:9:1 ratio to prepare forward and reverse primer mixes with a total primer concentration of 10 μM in each mix that were then used for the PCR reactions. For libraries targeting two residues close by (i.e., two residues within a single primer), such as for linker optimization libraries, a modified protocol using just the NDT and VHG codons was used for cost-effectiveness. For this protocol, four sets of primers carrying NDTNDT, NDTVHG (i.e., NDT for the first position to be randomized and VHG for the second position), VHGNDT, and VHGVHG (or their complements) were designed and mixed in a 33:24.5:24.5:18 ratio to prepare 10 μM forward and reverse primer stocks. Following the completion of the PCR, reactions were incubated with DpnI for at least 1 h at 37 °C. For

simultaneous mutations at different positions, the QuikChange Lightning Multi Site-Directed Mutagenesis kit (Agilent Technologies) was used in conjunction with the 22-codon trick [362].

For the GlnH-based design, site-directed mutagenesis libraries were prepared using the QuikChange Lightning Site-Directed Mutagenesis kit (Agilent Technologies). Linker optimization was performed by randomizing two adjacent linker residues using NNK codons. Random mutagenesis libraries were prepared by amplifying the template by EP-PCR using Taq polymerase in the presence of 0.15 mM $MnCl_2$ and four-fold excess of dCTP and dTTP [325,326]. The purified PCR product was then cloned into pBAD/HisB digested with XhoI and HindIII using In-Fusion.

Plasmids for SpyTag and SpyCatcher system. As described in Chapter 2, the plasmid encoding SpyCatcher003 tagged with mApple was assembled by linearizing pENTR4-TfR-sfGFP-myc tag-SpyCatcher003 (Addgene #133451) [327] without sfGFP and assembling with mApple amplified by PCR and extended with at least 15 bp overlap to the linearized vector. The gene encoding for ODIN1 in cHis-pBAD-SpyTag003-ODIN1 was replaced with Qigon1 using a similar approach.

3.2.2.2 Library screening in *E. coli*

General screening protocol. Libraries and the plasmid encoding the starting template (which served as controls) were transformed into DH10B and cultured overnight at 37 °C on LB agar plates supplemented with ampicillin and L-arabinose. Plated colonies were then screened using a custom-built imaging system [328] to ensure that variants chosen for the response-based screen were fluorescent. Single fluorescent colonies, including three expressing the starting template, were then cultured overnight in 4 mL LB media with ampicillin and L-arabinose at 37 °C. Protein was extracted from bacteria using B-PER (Thermo Fisher Scientific) and the supernatant was then incubated with 50 µL of Ni-NTA (G Biosciences) for at least 30 min. After incubation, the beads were washed once with 700 µL of 1× PBS (10 mM Na_2HPO_4, 1.8 mM

KH_2PO_4, 137 mM NaCl, 2.7 mM KCl) with 20 mM imidazole and adjusted to pH 8.0. Protein was eluted from the resin using 1× PBS augmented with 250 mM imidazole at pH 7.8. Beads were pelleted by centrifugation and the supernatant was manually aspirated. Each purified protein was then diluted into wells containing blank (30 mM MOPS, 100 mM KCl) or L-glutamine (blank + 10 mM L-glutamine) buffers, corrected to pH 7.2. The fluorescence intensities for the proteins in solution were measured and the intensities between the L-glutamine and blank conditions were ratioed to yield the dynamic range. From each library, variants were considered "winners" if they had a larger dynamic range than the controls. Winning variants were then streaked out on LB agar plates and re-tested in triplicate against the starting template. Plasmids were extracted from winning variants and sequenced. The new variants identified were then used as template for the next round. Modifications to this protocol are described below or in the results as required.

Screening protocol for best insertion site in GlnH and linker optimization of first design. Plasmids harboring *GlnH* with the gene for cpsfGFP inserted at different positions or reactions for libraries were transformed into DH10B and cultured overnight on LB agar plates with the required additives at 37 °C. Single colonies from the library were cultured in ~1.3 mL of LB media with 100 μg/mL ampicillin and 0.02% % L-arabinose in 96-well blocks (Thermo Fisher Scientific) at 37 °C overnight. Blocks were centrifuged to pellet the bacteria and the media was discarded. To remove amino acids present in the media, pellets were subjected to at least three cycles of resuspension with 1× PBS and centrifugation for discarding the supernatant. After washing, pellets were incubated with B-PER to extract the protein followed by centrifugation. Supernatant from each well were then loaded into individual wells containing either blank or L-glutamine buffers, and the fluorescence spectrum for each sample was collected. Variants showing the largest dynamic range were then chosen for further engineering.

3.2.3 *In vitro* characterization

3.2.3.1 Protein expression and purification

Electrocompetent *E. coli* strain DH10B (Thermo Fisher Scientific) were transformed with pBAD/HisB plasmid carrying the gene for the protein of interest and cultured on LB agar supplemented with ampicillin and L-arabinose. Starter cultures of 4 mL LB with the required additives were inoculated with single colonies and shaken overnight at 37 °C and 225 rpm. The starter culture was added to 500 mL of LB with ampicillin, and the cultures were shaken for 3-4 h at 37 °C before induction with L-arabinose. After addition of L-arabinose, cultures were shaken for at least 20 h at 30 °C before bacteria were harvested by centrifugation and resuspended in 1× PBS augmented with protease inhibitors (cOmplete™, EDTA-free Protease Inhibitor Cocktail; Roche) according to the manufacturer's specifications. Cells were lysed by sonication and then clarified by centrifugation. The clarified lysate was then gently mixed with Ni-NTA for at least 1 h. The lysate-bead mixture was then transferred to a propylene centrifuge column and washed with at least three packed column volumes of wash buffer (1× PBS with 20 mM imidazole, pH 8.0) and eluted with elution buffer (1× PBS with 250 mM imidazole, pH 7.8). The purified protein was then concentrated and buffer-exchanged into 1× PBS (pH 7.4) using 10 kDa centrifugal filter units (Millipore). All steps of the extraction and purification were carried out at 4 °C or on ice.

3.2.3.1.1 Spectral characterization

Brightness is calculated as the product of the EC and the QY.

EC measurements. ECs for indicator variants were measured using alkaline denaturation method [329]. An equal volume of purified protein for each variant was diluted to 700 µL with blank or L-glutamine buffers or NaOH. The absorption spectrum for each sample was collected, and the concentration of protein in each sample was derived from the denatured sample (sample added to NaOH) using an assumed EC of 44,000 M^{-1} cm^{-1} for the denatured chromophore peak

(~450 nm) [329,330] and Beer's Law. The EC for each variant under each condition can then be calculated by further applications of Beer's Law. Measurements were performed in triplicate and the results were averaged.

Quantum yield measurements. Quantum yields were measured as previously described [329,331] with EGFP used as the standard (QY = 0.67) [329]. From the samples used for EC measurements, a dilution series for each sample was prepared with the corresponding buffers so that the peak absorbance was ≤ 0.05. For each dilution series, the emission spectra were collected from 480 to 650 nm with an excitation wavelength of 460 nm and the total fluorescence intensities for each dilution were integrated. The total fluorescence intensities were then plotted against the absorbance. The slope of each line (m) was calculated and used in the following equation to determine the QY:

$$\varphi_{\text{protein}} = \varphi_{\text{standard}} \times \frac{\text{m}_{\text{protein}}}{\text{m}_{\text{standard}}} \quad (1)$$

3.2.3.2 Affinity measurements

Determination of specificity. Protein was added to blank buffer and buffers supplemented with 10 mM ligand (pH = 7.2). The fluorescence intensities of each sample were recorded and compared against the intensity recorded from purified protein diluted in blank buffer alone.

Determination of K_d. For ligands that evoked substantial changes in fluorescence, titrations with varying concentrations of ligand, mostly ranging from zero to 10 mM, were performed to determine the K_d. Buffers for the titration were prepared by mixing the necessary volumes of blank and 10 mM ligand buffers. Purified protein variants were diluted in these buffers and the fluorescence intensities of each sample were measured in triplicate. The readings were

plotted against the ligand concentration on the logarithmic scale, and the data were fitted for the K_d [332]:

$$F = F_{min} + \frac{F_{max} - F_{min}}{1 + 10^{(log_{K_d} - X)n_H}} \quad (2)$$

The Hill coefficient in equation 2 is constrained to 1 since there is only one ligand binding site and no cooperative binding is expected.

3.2.3.3 pKa measurements

Buffers spanning a range of pH values (3 to 11) were prepared by addition of HCl or NaOH to a dual-buffer system of 30 mM trisodium citrate and borax (sodium borate) [331]. To perform the titration, 1 µL of purified protein was diluted in the buffer series that was either supplemented with 1 mM L-glutamine for the saturated condition or not for the apo condition. The titrations were performed in triplicate for each condition, and the measurements were plotted against pH before fitting the data to the following equation (which is identical to equation 2 but for H^+) for the pK_a:

$$F = F_{min} + \frac{F_{max} - F_{min}}{1 + 10^{(pK_a - pH)n_H}} \quad (3)$$

3.2.4 Imaging in mammalian cells

HeLa cells were plated on 35 mm glass bottom dishes until they reached 50% confluency before transfection in DMEM supplemented with 10% FBS, 2mM GlutaMax (Invitrogen) and 1% streptomycin-penicillin. Transfections were performed with Turbofect (Thermo Fisher Scientific) and 1 µg of pENTR4-TfR-mApple-myc tag-SpyCatcher003, per the manufacturer's instructions. The transfection complexes were then incubated with the cells in serum-free DMEM for 2 to 4 h at 37 °C before being replaced with the growth media for incubation overnight. To tether Qigon1 onto the cell surface, 10 µM of purified SpyTagged Qigon1 was incubated with the cells for 10 minutes at room temperature. Protein concentration was measured by alkaline denaturation [329].

Cells were then washed twice with HHBSS before adding HHBSS for imaging. Expression of mApple-SpyCatcher003 and tethering were confirmed by imaging in both green and red channels prior to testing the dynamic range. Time-lapse imaging was performed in the green channel. Imaging was performed on an inverted Zeiss 200M microscope equipped with OrcaFlash 4.0 – C13440 (Hamamatsu). Imaging analyses were performed with ImageJ.

3.2.5 Statistics

Statistical tests were performed as described in the text. All statistical analyses were conducted using the software Prism8 (GraphPad, La Jolla, CA).

3.3 Results and discussion

3.3.1 Protein engineering

3.3.1.1 Engineering of GlnH-based indicator

The earliest prototypes for a glutamine indicator were engineered by Abhi Aggarwal, a former undergraduate in the Campbell lab, using the glutamine binding protein, GlnH, from *E. coli*, which is the same binding domain used in FLIPQ and the CouA-based FRET sensor [263,264]. GlnH undergoes a large conformational change upon binding glutamine at the interface of its two domains; both open ligand unbound and closed ligand-bound structures had been previously reported [359,360]. Therefore, it was hypothesized that a genetically encoded glutamine indicator could be engineered from GlnH.

In total, 21 insertion sites were chosen on the basis of the open or closed structures' B-factors (9 sites), the difference in B-factors between the open and closed states (3), or visual inspection (9) (**Figure 3-1**). The results indicate that the best insertion point was between residues 20 and 21 (**Figure 3-2A** and **B**). Optimization of both linkers performed in parallel produced a variant with ~25% decrease in the presence of L-glutamine (**Figure 3-2C**).

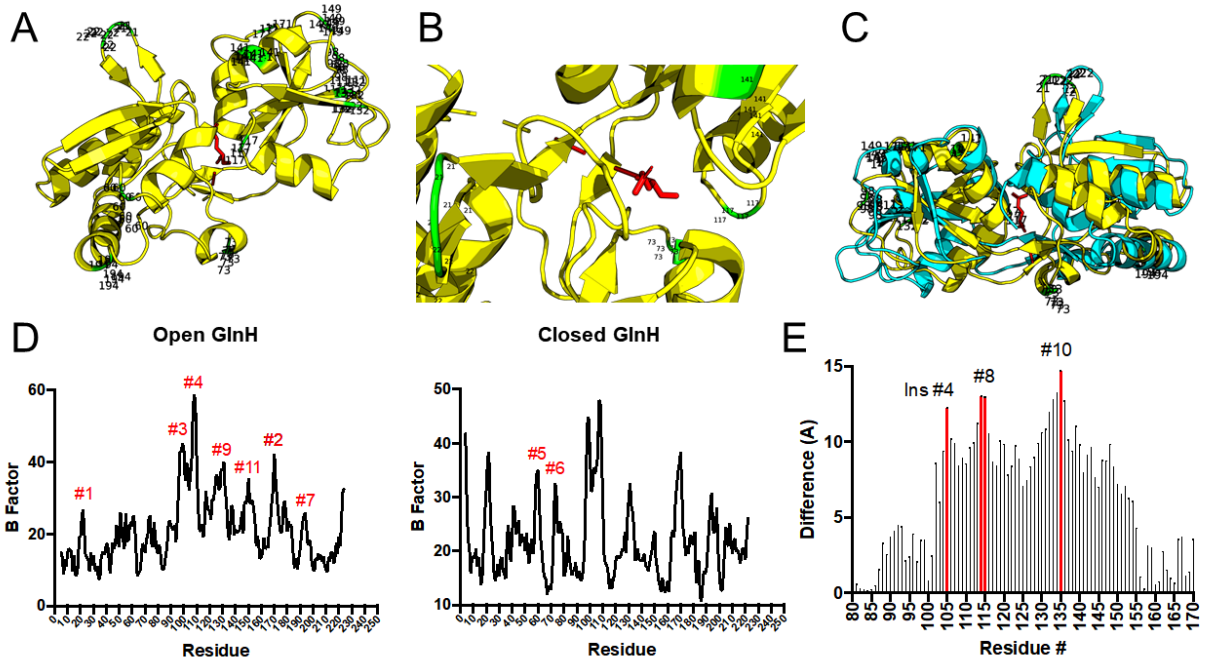

Figure 3-1 - GlnH insertion sites.

A) Full closed structure of GlnH with residues chosen as insertion sites coloured green. B) Close-up of closed structure of GlnH. C) Structural alignment of open (blue) and closed (yellow) structures. D) Plots of absolute B-factor values against residues for the open (left) and closed (right) structures with chosen insertion sites numbered in red. E) Plot of the difference in B-factors against residues with chosen insertion sites indicated by square rectangles and numbered above. Structure images were generated using PyMol [363] and the figure was courtesy of Abhi Aggarwal.

My efforts to improve this variant by optimization of the first linker and one round of directed evolution did not yield improved variants. In the course of this effort, I realized that, despite the low sequence homology, GlnH was structurally homologous with PEB1a (**Figure 3-3A**), the aspartate-glutamate binding protein that we had successfully engineered into an

aspartate indicator in Chapter 2 [321]. This realization led me to insert cpsfGFP into the analogous site with respect to the primary sequence (**Figure 3-3B**); however, even after linker optimization, my best variant still only showed ~15-20% glutamine-dependent increase in fluorescence intensity. Consequently, further optimization of this design was not pursued.

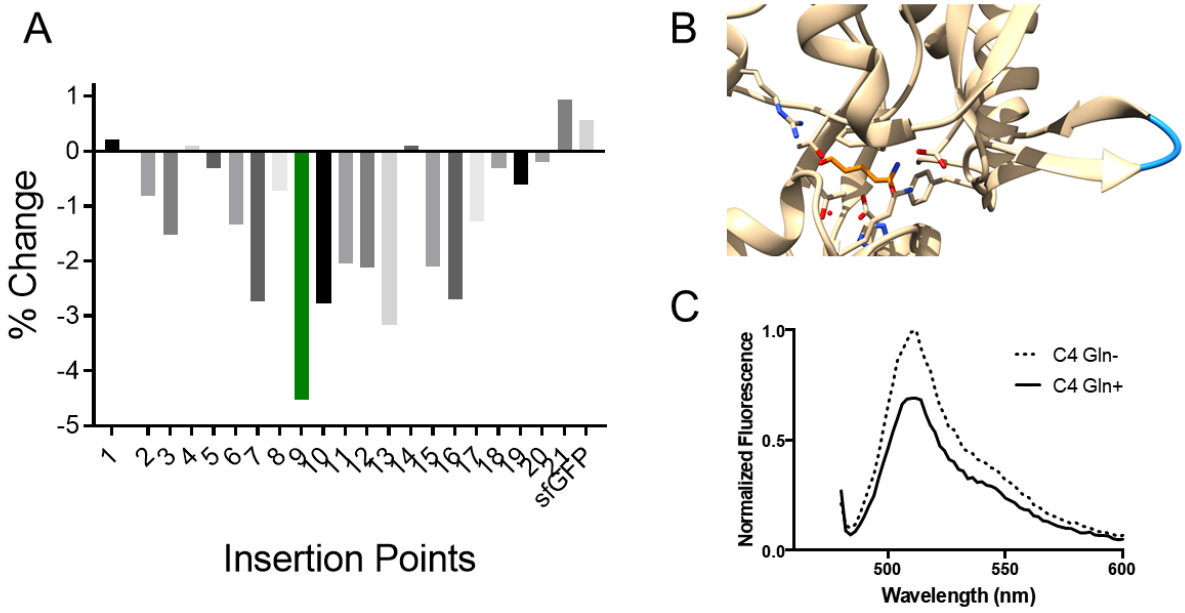

Figure 3-2 - Engineering of first prototypes based on GlnH.

A) Results of tests for GlnH-cpsfGFP constructs with different insertion points with sfGFP used as a control. The chosen insertion point, insertion point #9, is highlighted in green. B) Chosen insertion point (blue) relative to the binding pocket with the ligand bound (orange) in the closed structure. C) Emission spectra of the best variant after one round of linker optimization in the presence (solid line) and absence (dotted line) of L-glutamine. Data were provided by Abhi Aggarwal.

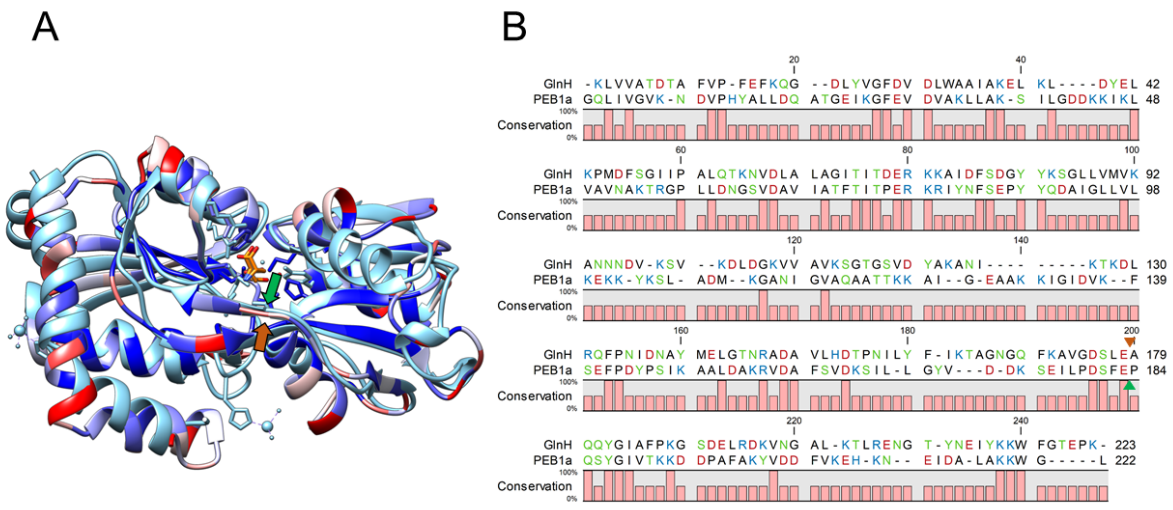

Figure 3-3 - Alignment of PEB1a and GlnH.

A) Alignment of GlnH (closed (ID: 1WDN); coloured blue to red in a gradient to indicate relative solvent accessibility) and PEB1a (ID: 2V25; blue). B) Sequence alignment of GlnH and PEB1a. Residues are colored according to the polarity of their side chains. Green arrows indicate insertion site in PEB1a (A – structure; B – sequence) and orange arrows indicate insertion site in GlnH (A – structure; B – sequence). Conservation at each position is indicated by the bar graphs at the bottom.

3.3.1.2 Engineering a BpQBP-based indicator

Given our struggles with optimizing the GlnH-based indicator, I searched through the PDB for other glutamine binding domains and found an unpublished structure for a binding protein (PDB ID: 4F3P) from *Burkholderia pseudomallei* that was predicted by UniProt (ID: Q3JIF9) to bind glutamine [361,364]. A structural alignment between PEB1a and this binding domain, which we refer to as BpQBP (***B. pseudomallei*** glutamine [**Q**] **b**inding **p**rotein), showed that BpQBP shares a similar structure with PEB1a, and a sequence alignment with PEB1a and GlnH revealed that BpQBP had a greater percentage of sequence identity with GlnH at 57% than with PEB1a at

24% although there are similarities across all three proteins (**Figure 3-4**). I made four variants from the analogous insertion site in BpQBP, between Ser204 and Gly205 (numbered according to the 4F3P structure), varying whether Ser204 and/or Gly205 were kept. Out of the four variants, only the variant with Ser204 but without Gly205 (Gly443 with cpsfGFP inserted) showed a direct increase in fluorescence intensity in the presence of glutamine (**Figure 3-5**).

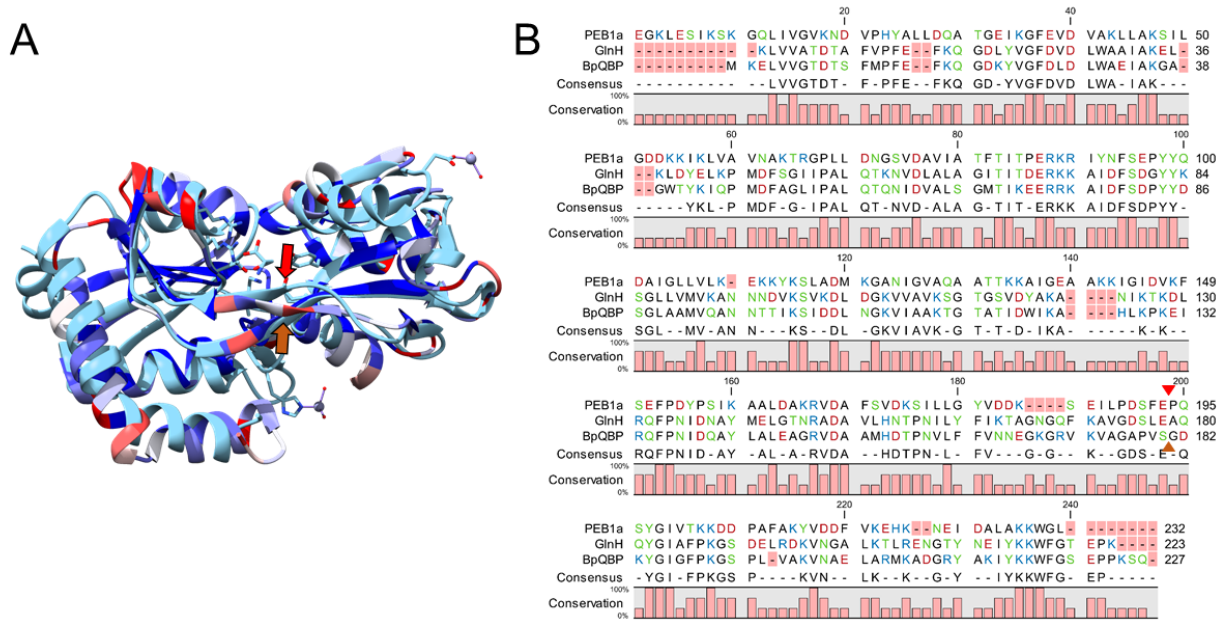

Figure 3-4 - Alignment between BpQBP and PEB1a.

A) Alignment of the protein structures of PEB1a (blue; ID: 2V25) and BpQBP (blue, white and red structure; ID: 4F3P). B) Alignment of the primary sequences for PEB1a, GlnH, and BpQBP. The unstructured signal peptide sequence for PEB1a and the corresponding residues for the other domains deleted for brevity, and as a result, the residue numbering for the alignment does not correspond with the numbering in the protein structures. The consensus sequence, defined as the majority residue at any given position, is shown.

Insertion points are indicated by matching arrows in both panels; the color scheme for the sequence is similar to the scheme used in Figure 3-3.

Given that the β-strand in which cpsfGFP was inserted is farther from the binding pocket than in PEB1a (**Figure 3-4A**), I reasoned that further deletions in the second linker may prove beneficial by bringing cpsfGFP closer to the binding pocket. Indeed, deletion of Asp444 (Asp206 in BpQBP) further improved the glutamine-evoked response to a more promising ~30% increase (**Figure 3-5**). Further optimization of the linkers by parallel screening of two libraries in which either Leu205 and Val206 or Thr440 and Arg441 were randomized led to multiple variants with improved F_{sat}/F_{apo} for glutamine and negligible (or no) response to glutamate (**Table 3-1**). Interestingly, all of the improved variants had mutations at the Val206 position. Further screening of libraries in which Leu205 or Thr440 and Arg441 were randomized using the Asp206 and Gly206 variants together as template did not lead to improved variants. I then attempted to optimize the two linker residues closest to cpsfGFP (i.e., Ser207 and Asn439) simultaneously, using just the Asp206 variant as template in order to reduce library size. From this library, I isolated an improved variant carrying a Ser207Ala mutation. I then attempted to re-optimize the 206th position in the hopes of a synergistic effect with Ser207Ala, but this library did not lead to any improved variants. Indeed, a variant with glycine as the 206th residue showed a reduced response to glutamine when combined with the Ser207Ala mutation compared to an aspartate residue in that position (**Table 3-2**). This diminished response as a result of the Ser207Ala mutation contrasted with an earlier variant without the Ser207Ala mutation that showed comparable F_{sat}/F_{apo} to glutamine and a more favorable lack of response to glutamate when compared to a variant that had

aspartate in the 206th position (**Table 3-1** and **Table 3-2**). Thus, the variant with Asp206 and Ser207 were designated as Qigon1 (Q for glutamine and G for green; **Figure 3-5**).

Table 3-1 - Dynamic ranges for glutamine and glutamate of different Val206X variants.

Val206X	F_{sat}/F_{apo} **for glutamine**	F_{sat}/F_{apo} **for glutamate**
Asp	2.91 ± 0.92	0.92 ± 0.03
Gly	2.71 ± 0.09	0.99 ± 0.02
Ala	2.55 ± 0.17	0.99 ± 0.05
Met	1.86 ± 0.08	1.13 ± 0.02

All data reported as mean ± SD (n = 3).

Table 3-2 - Dynamic ranges for Asp206X variants with Ser207Ala.

Asp206X	F_{sat}/F_{apo} for glutamine	n
Asp	3.71 ± 0.32	6
Glu	3.53 ± 0.11	3
Gly	3.17 ± 0.06	3

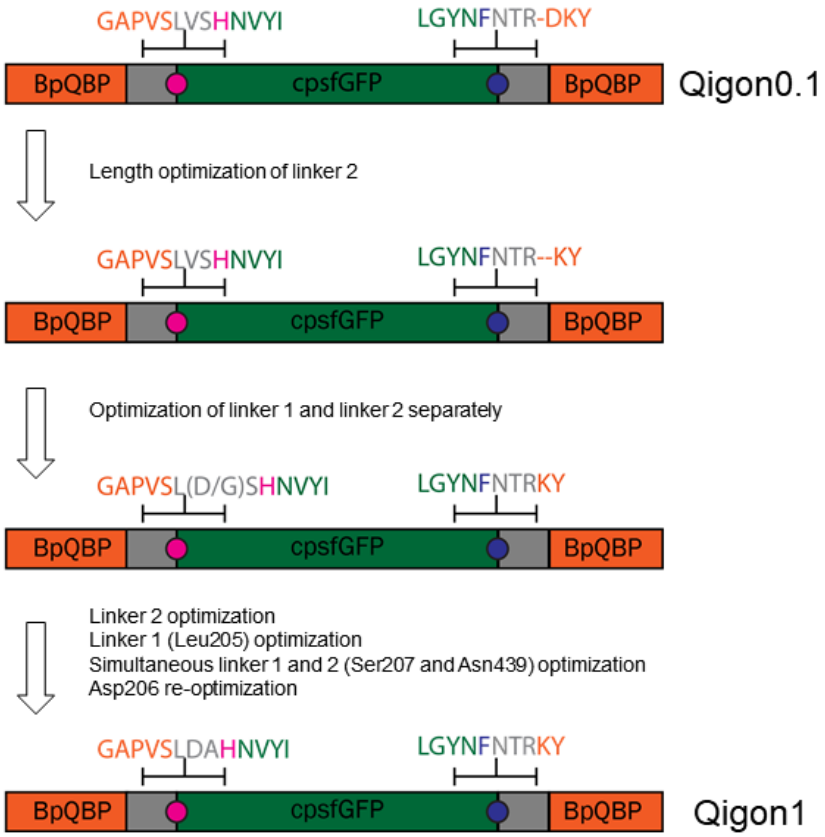

Figure 3-5 – Schematic and engineering of Qigon1.

Residues at both linkers are shown above the schematic representations and coloured according to their domains with grey residues for linkers. Grey residues in brackets indicate two variants of interest at that stage. Gatepost residues, which are residues at the interface of the cpFP and binding protein that appear to be crucial for the indicator's stability and function, are indicated by the pink and navy circles and the corresponding are highlighted in the same colours. Schematic is not drawn to scale.

3.3.2 *In vitro* characterization

I then performed a systematic characterization of purified Qigon1 *in vitro*. Relative to its original constituent protein domains, BpQBP and cpsfGFP, Qigon1 had four mutations, two of which are deletions from BpQBP and two point mutations in the linker and cpsfGFP (**Figure 3-6**).

Qigon1 had an excitation peak 496 nm, which is more red-shifted than EGFP's excitation peak, and an emission peak of 511 nm, which are consistent between the apo and saturated states (**Figure 3-7A** and **Table 3-3**). Qigon1 had a smaller EC and QY than EGFP, and was therefore significantly dimmer with 33% of its brightness (**Table 3-3**). This result was surprising given how vibrantly green the purified protein was, which looked comparable to the ODIN1 variants (which were ~1.5-2-fold brighter) at similar concentrations, possibly indicating better folding efficiency. With a similar QY in the apo and bound states, the change in fluorescence intensity upon ligand binding was primarily mediated by deprotonation of the chromophore upon binding, as evidenced by the changes in the ratios of the absorbance spectra at 400 *vs.* 490 nm and consequently, the ECs.

For the characterization, Qigon1 exhibited a modest dynamic range ($\Delta F/F_{min}$ = 1.62 ± 0.05; n = 3, technical) that was smaller than the results observed during the screening process (**Table 3-**2 and **Table 3-3**). This dynamic range is also smaller than the dynamic range of the first generation of iGluSnFR ($\Delta F/F_{min}$ = 4.5) [252]. Qigon1 showed good affinity for L-glutamine (K_d = 30.1 μM) (**Figure 3-7B** and **Table 3-3**), which was much stronger than the affinity we observed for ODIN without mutations to the binding pocket (K_d = 260 μM for ODIN V4) (Chapter 2). However, this K_d is much smaller than the reported concentration of glutamine in the extracellular fluid (~0.5 to 1 mM) [51], suggesting that Qigon1 is likely to be insensitive to physiologically relevant changes in glutamine concentration. Therefore, further engineering will be necessary to adjust the K_d to detect changes in glutamine concentration in the extracellular space. Moreover, though conversions to molarity are difficult due to differences in methodologies, Qigon1's K_d may also be too high for imaging glutamine dynamics in the cytosol with reported concentrations of ~2-8 nmol/mg tissue [51,52]. Qigon1 was unresponsive to D-glutamine as well as both L and D

enantiomers of structurally similar amino acids (i.e., glutamate, aspartate, and asparagine) (**Figure 3-7D).**

The pH titration revealed that Qigon1 underwent a shift in the pK_a upon ligand binding, with a pK_a of 5.0 in the apo state and 6.5 in the saturated state (**Figure 3-7C** and **Table 3-3**). Similar to ODIN1, Qigon1 did not appear to reach maximum brightness in the saturated state under testing and physiological conditions. However, its high pK_a may make it suitable for imaging in the mitochondrial matrix (pH = 7.8) [365]. Aberrations in glutamine dynamics in the mitochondria have been implicated in cancer cell growth [366]. Regardless, Qigon1 showed relatively large glutamine-dependent changes in fluorescence (i.e., $\Delta F/F_{min} > 1$) over a pH range from 6.5 to 9.

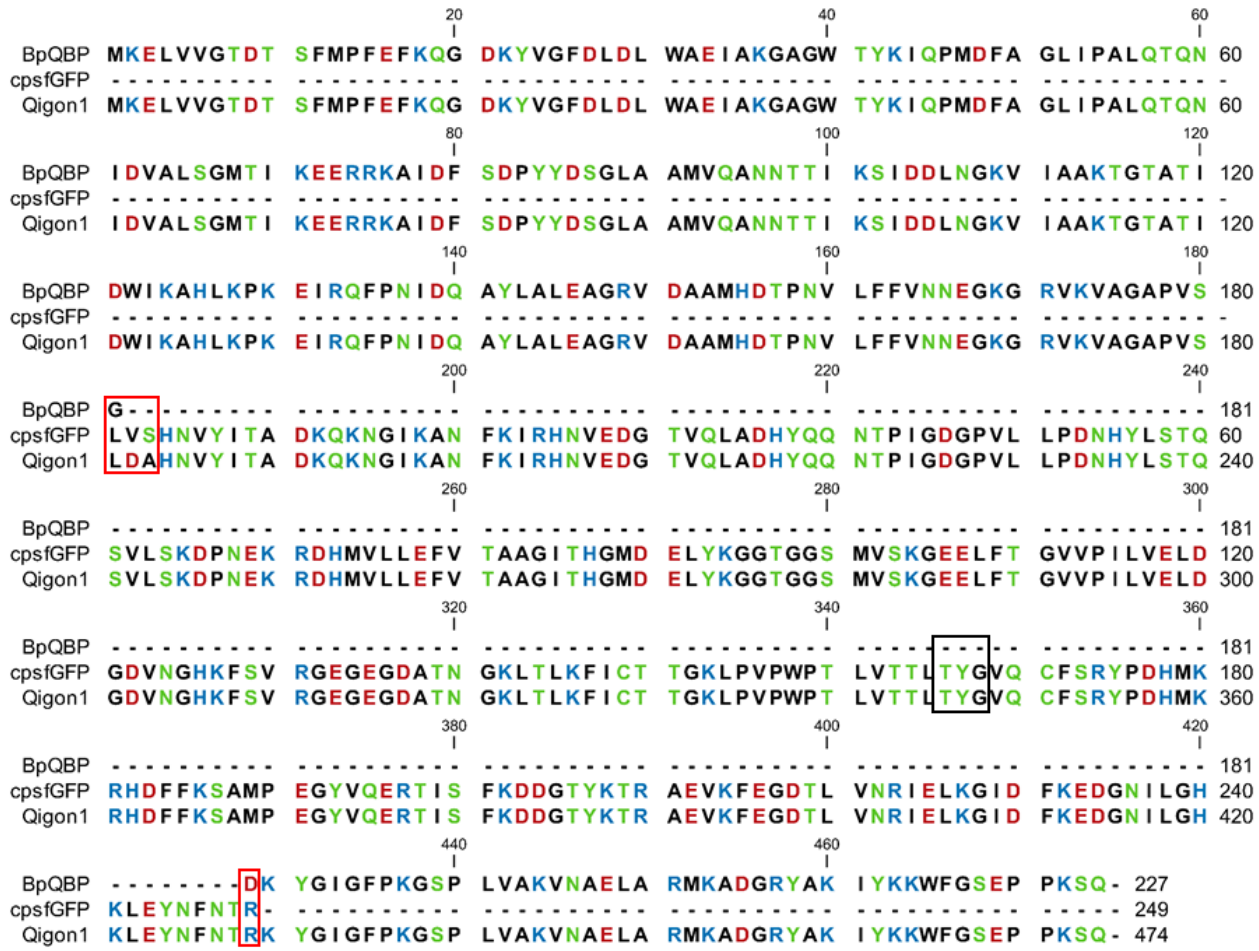

Figure 3-6 - Sequence alignment of Qigon1.

Sequence alignment for BpQBP (PDB: 4F3P), cpsfGFP from ODIN V3, and Qigon1. Residues are coloured according to polarity. Chromophore forming residues are indicated by a black box while mutations are indicated by red boxes.

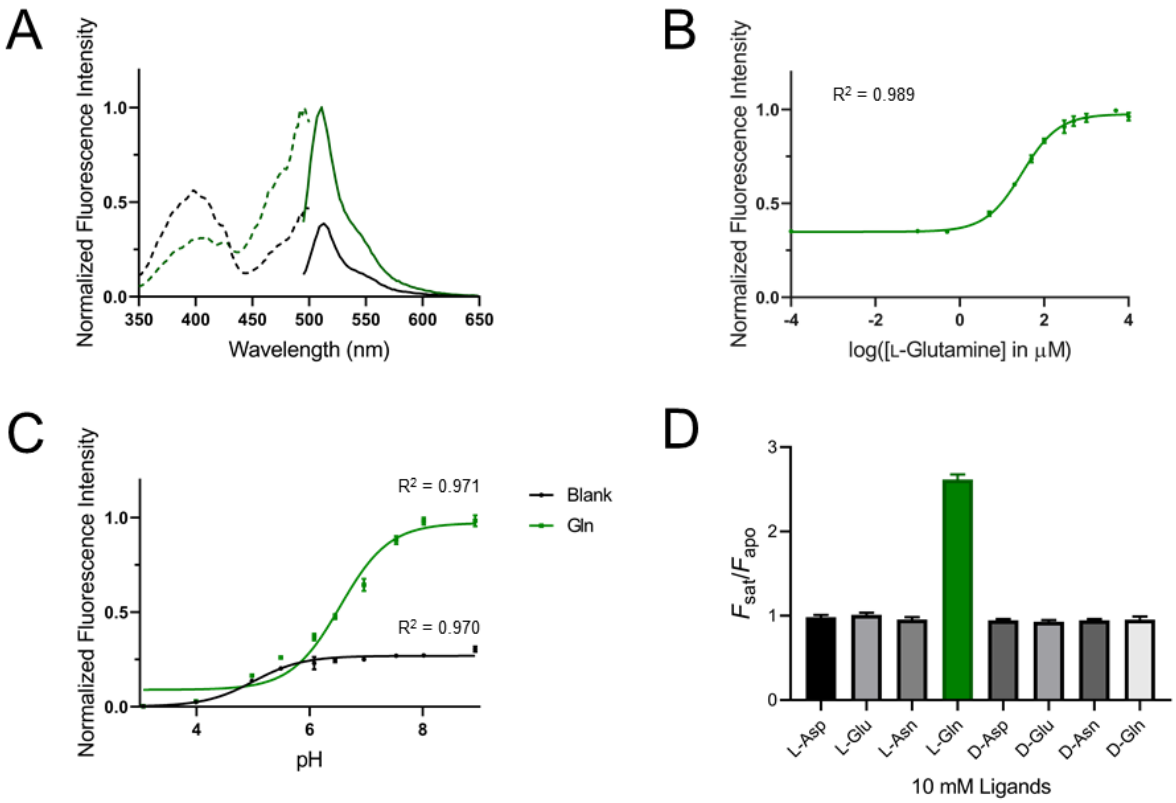

Figure 3-7 - Qigon1 *in vitro* characterization.

A) excitation (dashed) and emission (solid) spectra of Qigon1. For the glutamine condition, the measurement was performed in 10 mM L-glutamine. B) K_d titration of Qigon1. C) pH titration curves for Qigon1 in the apo and bound states. D) Specificity assay for Qigon1 to structurally similar amino acids. Fitted values are reported in Table 3-3. Error bars represent SEM (n = 3; technical).

Table 3-3 – Summary of *in vitro* characterization for Qigon1.

Variant	Ex (nm)	Em (nm)	$\Delta F/F_{min}$[b]	K_d (μM)	pK_a	Brightness[c]	ε ($M^{-1}cm^{-1}$)	ϕ
Qigon1a	496	511	1.62 ± 0.05	30.1 [25.2, 35.8]	5.01 [4.86, 5.16]	5.1	10,100 ± 200	0.50
					6.54 [6.38, 6.70]	12.7	26,500 ± 400	0.48
EGFP[a]	488	508	n/a	n/a	6.1	37.5	56,000	0.67

[a] Literature values from Cranfill *et al.* [329].
[b] Calculated from the emission spectra's peaks without and with 10 mM L-glutamine.
[c] Brightness is defined as the product of ε and ϕ.
Top values are for apo state and bottom values were measured with 10 mM L-glutamine.
Measurements are reported as means ± SEM (n = 3; technical).
n/a = not applicable.

3.3.3 Imaging in mammalian cells

We have previously demonstrated in Chapter 2 that the SpyTag and SpyCatcher system [327] enabled the membrane-localized expression of ODIN1 while retaining its function. In contrast, it was not possible to obtain functional membrane-localized ODIN1 when expressed with pMiniDisplay, the conventional vector used for membrane localization (Chapter 2). Therefore, given the structural homology between the ligand binding domains of ODIN1 and Qigon1, I expressed Qigon1 in *E. coli* with SpyTag003 at the N-terminus and tethered it to HeLa cells expressing mApple-SpyCatcher003 for a first test of its function. The results show that Qigon1, like ODIN1, can be successfully localized to the membrane (**Figure 1-7A**). Furthermore, Qigon1 was shown to be significantly more responsive to 10 mM L-glutamine ($\Delta F/F_{min}$ = 25 ± 7%; n = 23 cells) while showing no response to my negative control, 10 mM L-glutamate (n = 31 cells; Mann-Whitney U test, $p < 0.0001$) (**Figure 1-7B** and **C**). These results were expected as they mirrored

the *in vitro* results showing Qigon1 to be responsive to L-glutamine (albeit much less so in cells than *in vitro*), but not L-glutamate.

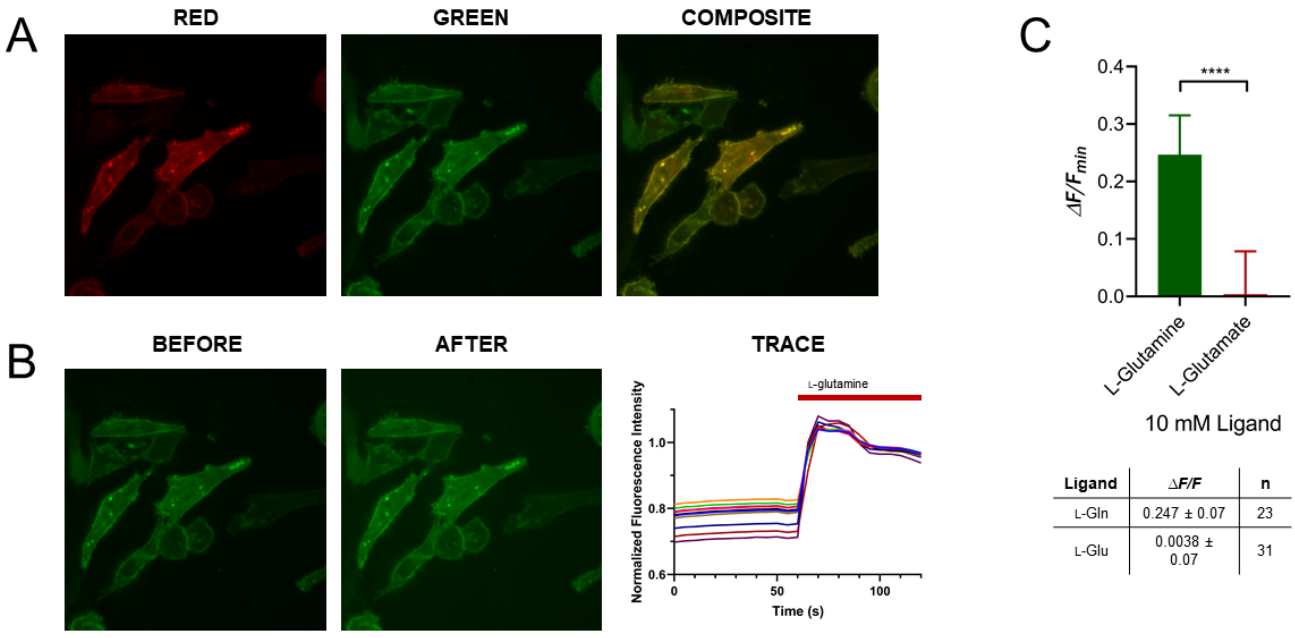

Figure 3-8 - SpyTagged Qigon1 in HeLa cells.

A) Representative images of cells expressing mApple-SpyCatcher003 on the membrane and tagged with Qigon1, showing successful tethering and localization to the membrane. The left and center images were taken in the red and green channels, respectively, and were merged to generate the composite image. B) Images of cells before (left) and after (middle) addition of 10 mM L-glutamine. The right figure shows traces of individual cells, manually labelled as regions of interest in ImageJ, and their changes in fluorescence intensity over time and upon the addition of L-glutamine. C) Response of tethered Qigon1 on the cell surface to 10 mM L-glutamine or L-glutamate (negative control). Qigon1 tethered on the surface showed a significant response to L-glutamine ($p < 0.0001$, Mann-Whitney U test). Error bars and values represent SD (n = number of cells; technical because measurements were taken from cells labelled with one stock of purified Qigon1).

3.4 Conclusion

Inspired by the results of our aspartate indicator, ODIN1, which used a structural homologue of the glutamine binding domain used in the work described in this chapter, I have successfully engineered the first single FP-based glutamine indicator, Qigon1. By optimizing the linker region between the glutamine binding domain and cpsfGFP using saturation mutagenesis, I engineered a specific glutamine indicator that exhibited a 1.6-fold increase in fluorescence intensity upon glutamine binding with high affinity. Although smaller than the responses seen *in vitro*, Qigon1 still showed a modest response (~25%) to glutamine when expressed on the surface of cells through the SpyTag and SpyCatcher system. While it still requires further engineering to increase its dynamic range, brightness, and affinity for use in cells, Qigon1 is a step in the right direction towards engineering a high-performance single FP-based glutamine indicator for use in in neuroscience and more broadly, cell biology.

4 Chapter 4 – Red Ca^{2+} indicator based on mRuby3

4.1 Introduction

Calcium ion (Ca^{2+}) is one of the most pervasive signalling molecules in cells, where it is involved in processes ranging from cell differentiation and proliferation to apoptosis [367]. In the nervous system, its importance is further enhanced as it is an integral component of neurotransmission and plasticity with a role at different stages [367,368]. Briefly, the arrival of an action potential at the axon terminals trigger Ca^{2+} influx, which, in turn, is necessary for the release of neurotransmitters into the synapse. Ca^{2+} acts as a second messenger after its entry using Ca^{2+}-permeable ionotropic receptors, most notably the NMDA receptor, and after activation of GPCRs. In some cases, Ca^{2+} is even necessary for the activation of effectors further downstream, such as protein kinase A.

Since the introduction of G-CaMP (a genetically encoded Ca^{2+} indicator that utilized cpGFP) in 2001 [369], genetically encoded Ca^{2+} indicators (GECIs) have become the preferred tools for imaging changes in Ca^{2+} dynamics, such as to detect neuronal activation and neurotransmitter release, for a number of reasons [370]. In addition to their minimal toxicity, GECIs can be easily and specifically targeted to desired cell types or organelles with stable expression for minimally invasive imaging with high spatiotemporal resolution [371,372]. Although the green GCaMPs (renamed from G-CaMP) represent the archetype of Ca^{2+} indicator engineering, red GECIs are inherently more desirable as they exhibit less autofluorescence and their longer excitation and emission wavelengths induce less phototoxicity while enabling deeper imaging into brain tissue [331,373]. Moreover, red GECIs can be used concurrently with other green indicators for simultaneous multicolour imaging of multiple analytes [331,373]. Two main families of red GECIs have been reported, with the R-GECO (**R**ed **G**enetically **E**ncoded **C**a^{2+} for **O**ptical

Imaging) series [331,374,375] using mApple, a RFP engineered from corals, and the RCaMP series [373,374] using mRuby, a red FP derived from sea anemones [376]. Here we report our efforts to engineer an improved RCaMP variant by replacing mRuby with an updated variant, mRuby3, that is 47% brighter than mRuby [377].

4.2 Materials and Methods

4.2.1 General

Single-stranded oligonucleotides and double-stranded fragments (gBlocks) were purchased from Integrated DNA Technologies. Q5 polymerase and Taq polymerase were purchased from New England BioLabs, while recombinant Taq polymerase was purchased from Thermo Fisher Scientific. PCR products were confirmed from and purified by agarose gel electrophoresis followed by extraction with GeneJET Gel Extraction Kits (Thermo Fisher Scientific). Restriction enzymes and T4 DNA ligase were sourced from Thermo Fisher Scientific and used according to the manufacturer's recommendations. Digested PCR products were directly extracted with GeneJET Extraction kits prior to ligation. In-Fusion HD was used for assembly reactions and purchased from Takara Bio USA, Inc. Plasmid DNA extractions were performed with GeneJET Plasmid Miniprep Kits (Thermo Fisher Scientific). Sequencing was performed by the Sanger method with BigDye (Thermo Fisher Scientific) were carried out by the University of Alberta's Molecular Biology Services Unit. Fluorescence measurements were collected on a Tecan Safire^2 plate reader, while absorbance readings were collected on a DU-800 UV-Visible Spectrophotometer (Beckman).

4.2.2 Plasmid construction and directed evolution

4.2.2.1 Plasmid and library construction

Starting template construction. Double-stranded fragments with *XhoI* and *HindIII* restriction sites on the 5' and 3' ends, respectively, were amplified using PCR from a gBlock

encoding jRCaMP1b with the cpmRuby sequence replaced with the sequence for cpmRuby3 [377]. This fragment was then digested with XhoI and HindIII and ligated into a similarly prepared pBAD/HisB (Thermo Fisher Scientific) vector. The ligation reaction was then used to transform electrocompetent *E. coli* DH10B (Invitrogen) and bacteria were cultured overnight on Lennox Broth (LB) agar plates with 400 µg/mL ampicillin (Thermo Fisher Scientific) and 0.02% (w/v) L-arabinose (Alfa Aesar) at 37 °C. Plasmids were isolated from single colonies grown in 4 mL LB cultures supplemented with 100 µg/mL ampicillin and 0.02% L-arabinose and sequenced.

Plasmids for standards and controls. A gBlock encoding mRuby3 was amplified to append *XhoI* and *HindIII* restriction sites to the 5' and 3' ends, and the purified PCR product was digested by XhoI and HindIII and ligated into digested pBAD/HisB. Similarly, pBAD-jRCaMP1b was prepared by cloning a gBlock encoding jRCaMP1b codon-optimized for mammalian expression to add the restriction sites prior to digestion and ligation into pBAD/HisB [374].

Domain substitutions. Complete replacements of calmodulin (CaM) or its binding peptide (RS20) were performed by first amplifying the new domain from a template plasmid as well as the entire target pBAD plasmid without the sequence to be replaced to generate the insert and linearized vector, respectively, followed by assembly with In-Fusion. The ckkap domain was amplified from pBAD-K-GECO1 (Addgene #105864) [378]. pGP-CMV-jGCaMP7s and pGP-CMV-jGCaMP7f were a gift from Douglas Kim and GENIE Project (Addgene #104463 and #104483, respectively), and were used the templates for the domain substitutions [379].

Plasmids for mammalian expression. Plasmids for cytosolic expression in mammalian cells were inserted into a version of pcDNA3.1(+) (Invitrogen) that has been previously modified in house to allow for expression of genes in the second reading frame inserted using XhoI and HindIII (pcDNA3.1m). Briefly, the pBAD/HisB plasmid harbouring the gene of interest was

digested and following purification by gel electrophoresis, the insert was ligated into digested pcDNA3.1m. To prepare mammalian expression plasmids of indicators with the N-terminal polyhistidine sequence, which had been shown to be crucial for fluorescence and sensor function at 37 °C in the GCaMP series [380], double-stranded fragments with the N-terminal polyhistidine tag were amplified by PCR from pBAD carrying the gene of interest to append a minimum of 15 bp of sequence overlap with pcDNA3.1m prior to assembly into digested vector.

Library construction. For random mutagenesis libraries, mutations were introduced into the template by PCR with Taq under EP conditions (i.e., in the presence of up to 0.15 mM $MnCl_2$ and 4-fold excess of dCTP and dTTP). The purified PCR product was then either digested with XhoI and HindIII and ligated into similarly digested pBAD/HisB vector or assembled directly into the digested vector. For site-directed mutagenesis, QuikChange Lightning Site-Directed Mutagenesis or QuikChange Lightning Multi Site-Directed Mutagenesis kits (Agilent Technologies) were used for single or 2-4 mutations, respectively. In these libraries, the NNK (N = A, G, C or T, K = G or T) codon was used for complete randomization.

4.2.2.2 Library screening in E. coli

E. coli DH10B were transformed with the library and the template plasmid (which served as controls) and grown overnight at 37 °C on LB agar plates with ampicillin and L-arabinose. The library was then screened for fluorescence intensity on the plate using a custom imaging system [328]. During the early stages of engineering, plated libraries were incubated for an additional day at room temperature and checked at the beginning and end of each day for fluorescence. Colonies displaying the brightest fluorescence intensity were cultured in 4 mL liquid LB with ampicillin and L-arabinose overnight at 37 °C followed by another day at either 30 °C or room temperature before the secondary screen. Once colonies were mostly fluorescent overnight, the second day of incubation was omitted at both steps. Later stages of engineering involved testing variants with a

range of fluorescence intensities instead of just the brightness variants in the hopes of improving the sensor's other properties. For the secondary screen, proteins were extracted from cells using B-PER (Thermo Fisher Scientific) and their fluorescence intensities in Ca^{2+}-free (30 mM MOPS, 100 mM KCl, 10 mM ethylene glycol -bis(β-aminoethyl ether)-*N,N,N',N'*-tetraacetic acid (EGTA), pH 7.2) and Ca^{2+} buffers (30 mM MOPS, 100 mM KCl, 10 mM Ca-EGTA, pH 7.2) were recorded to determine their dynamic range. Variants showing desired properties (e.g., largest dynamic range or stronger affinity) were streaked out on plates, re-cultured and re-tested to determine the final winners of that round. Plasmids were extracted from winning variants, sequenced and used as the template(s) for the next round of evolution.

After a few rounds, to ensure that the chosen variants were not overly affected by the detergents present in B-PER, the variants were batch purified by affinity chromatography on a small scale and tested in triplicate. Briefly, plasmids encoding variants of interest were transformed into DH10B and three single colonies were used to inoculate three 4 mL cultures of LB with ampicillin and L-arabinose. Proteins were extracted from bacteria using B-PER, and the supernatant was separated from the pellet and incubated with 50 µL of Ni-NTA resin for at least 30 min. The beads were then washed once with 1× TBS wash buffer (50 mM Tris-Cl, 150 mM NaCl, 20 mM imidazole, pH 8.0) and eluted with 1× TBS elution buffer (50 mM Tris-Cl, 150 mM NaCl, 250 mM imidazole, pH 7.8). Beads were collected by centrifugation and the supernatant was aspirated in between each step. The purified protein was then diluted into Ca^{2+}-free and Ca^{2+} buffers and the fluorescence measurements for each state were used to determine the dynamic range.

4.2.3 *In vitro* characterization

4.2.3.1 Protein expression and purification

Plasmids harbouring the gene for the protein of interest were transformed into DH10B *E. coli* and grown on LB agar supplemented with ampicillin and L-arabinose overnight at 37 °C. Single colonies were then used to inoculate 500 mL of LB with 100 µg/mL ampicillin and 0.02% L-arabinose, and the culture was shaken for at least 24 h at 37 °C and 225 rpm. If necessary, cultures were given another dose of ampicillin and shaken for an additional day at 30 °C or room temperature. Bacteria were harvested by centrifugation, resuspended in 1× TBS, and lysed by sonication. The mixture was then clarified by centrifugation, and the cleared lysate was incubated with Ni-NTA resin for at least 1 h with gentle shaking. The lysate-resin mixture was transferred to a column and washed with at least three packed column volumes of 1× TBS wash buffer prior to elution with 1× TBS elution buffer. The purified protein was then concentrated and then buffer exchanged to 30 mM MOPS, 100 mM KCl buffer (pH 7.2) using 10 kDa centrifugal filter units (Millipore). All steps of the extraction and purification were carried out at 4 °C or on ice.

4.2.3.1.1 Spectral characterization

Brightness is defined as the product between EC and QY.

Determination of ECs. ECs for RCaMP variants were determined by collecting the absorbance spectra from 200 to 800 nm for each variant in both apo and saturated states in triplicate. Because the numbers and positions of tryptophans between jRCaMP1b and RCaMP3 are identical, each absorbance spectrum was normalized to A280. The ECs for RCaMP3 in both states were calculated from the ratios of each state's average peak for the deprotonated chromophore to that of the saturated jRCaMP1b peak and the reported EC (EC = 53,400 $M^{-1}cm^{-1}$) [374].

Determination of QYs. Previously described protocols, with mRuby3 as the standard, were used to determine the QYs [329,331]. Two dilution series using Ca^{2+}-free and Ca^{2+} buffers and the corresponding samples from the EC measurements for each protein were prepared such that the peak absorbance of the most concentrated sample was equal to, or less than, 0.05. The emission spectrum was collected from 540 nm to 775 nm with an excitation wavelength of 525 nm, and the total fluorescence intensity for each dilution was integrated. For each series, the total intensity was plotted as a function of the absorbance the slope of each line (*m*) was calculated. Using QY of 0.45 for mRuby3 [377], QYs were calculated with the following equation:

$$\varphi_{\mathrm{protein}} = \varphi_{\mathrm{standard}} \times \frac{\mathrm{m}_{\mathrm{protein}}}{\mathrm{m}_{\mathrm{standard}}} \quad (1)$$

4.2.3.1.2 Affinity measurements

Buffers were prepared by mixing the appropriate volumes of Ca^{2+}-free and Ca^{2+} buffers [381]. Protein was diluted into a series of buffers with free [Ca^{2+}] ranging from zero to 39 μM, and the fluorescence intensities of the protein in each solution were measured. The readings were plotted against the free [Ca^{2+}] on a logarithmic scale, and the data were fitted to equation 2 for the K_d and apparent Hill coefficient (n_H):

$$F = F_{min} + \frac{F_{max} - F_{min}}{1 + 10^{(log_{K_d} - X)n_H}} \quad (2)$$

4.2.3.1.3 pKa measurements

Thirty millimolar trisodium citrate and borax buffers were adjusted with HCl and NaOH to prepare a series of buffers with pH ranging from 3 to 11. Concentrated protein was then diluted into 96-well plates containing these buffers, which were also supplemented with either EGTA or $CaCl_2$ to a final concentration of 2 mM for the Ca^{2+}-free and Ca^{2+} conditions, respectively. The

total volume in each well was 100 µL. The fluorescence intensities were measured in triplicate, and the readings were plotted against pH. Due to possible protein degradation at pH 10 or 11, measurements showing significant decreases under these conditions were excluded before the data were fitted to equation 2 for H^+ with the Hill coefficient constrained to 1 to get the pK_a:

$$F = F_{min} + \frac{F_{max} - F_{min}}{1 + 10^{(pK_a - pH)n_H}} \quad (3)$$

4.2.4 Imaging in mammalian cells

HeLa cells were seeded onto 35 mm glass bottom dishes and cultured in growth media (DMEM supplemented with 10% FBS, 2 mM GlutaMax (Invitrogen) and 1% streptomycin-penicillin). Cells were transfected when they reached 50% confluency using Turbofect (Thermo Fisher Scientific) and 1 µg of DNA, according to the manufacturer's instructions. The transfection complexes were incubated with the cells in serum-free DMEM for 2 to 3 h at 37 °C before being replaced with growth media for incubation. Cells were incubated for at least 20 h prior to imaging.

Imaging was performed following previously established protocols [370]. Immediately prior to imaging, cells were washed twice with pre-warmed HHBSS with Ca^{2+} and Mg^{2+} before adding HHBSS for imaging. After collecting a baseline for ~90 s, Ca^{2+} oscillations were induced by the addition of histamine to 50 µM final concentration and imaged for at least 20 minutes. Ionomycin calcium salt dissolved in 1:1 DMSO:HHBSS was added for a final ionomycin concentration of 5 µM around the 25 min mark. After ~2 min, EGTA was added for a final EGTA concentration of 2 mM. Imaging was performed on an inverted Zeiss 200M microscope equipped with OrcaFlash 4.0 – C13440 sCMOS camera (Hamamatsu). Image processing and analyses were performed with ImageJ. During processing, all images from a given channel for a dish were uniformly enhanced for brightness and contrast as necessary for visibility.

4.3 Results and discussion

4.3.1 Protein engineering

The first prototype for this mRuby3-based Ca^{2+} indicator, denoted as RCaMP3-v1 (3 for mRuby3), was constructed by replacing the cpFP of jRCaMP1b, which utilized cpmRuby, with cpmRuby3 (cp at Asn143 and the original N- and C-termini fused with a flexible Gly-Gly-Gly-Thr-Gly-Gly-Ser linker; numbered according to the crystal structure of mRuby (PDB: 3U0M) [373]) (**Figure 4-1A**) [374]. This circular permutation position was the equivalent position in cpmRuby, and the Met-Asn-Ser residues from the parent eqFP611 and mRuby [376] that were replaced by the universal Met-Val-Ser-Lys-Gly-Glu-Glu linker residues added in mRuby2 (and most other engineered FPs) were restored [382]. *E. coli* transformed with this construct required almost 48 h (overnight at 37 °C followed by another day of incubation at room temperature) before fluorescence, albeit dim, could be reliably observed. In addition, the extracted protein only showed a modest 20% decrease in fluorescence intensity when Ca^{2+} was added (**Figure 1-1C**). We attribute this poor expression and loss of function to the combined effect of the 26 mutations that distinguish jRCaMP-derived cpmRuby from cpmRuby3 (**Figure 4-1A**)

With a focus on improving apparent brightness to facilitate screening, I performed eight rounds of iterative directed evolution, combining beneficial mutations when possible and pooling the best variants to be used as the next round's template if no single variant was the clear winner, to produce RCaMP3-v10, an inverse-response indicator with F_{max}/F_{min} of ~7 (**Figure 4-1B** and **C**). During linker optimization, I identified a variant, where the second linker had Thr to Ile and Asp to Val mutations, that reversed the response, albeit at the cost of half the dynamic range and brightness. A modeled structure with these mutations suggested that the hydroxyl group of the threonine residue from jRCaMP1b was sufficiently close to the chromophore to possibly form a hydrogen bond while the isoleucine residue could not and is, therefore, more likely to stabilize the

neutral form (**Figure 4-2**). We suspect that in the Ca^{2+}-bound state of the direct response variant, the isoleucine residue, which likely stabilized the neutral form, moved away from the chromophore, favouring the formation of the anionic form and increasing the fluorescence intensity. Iterative optimization of each residue of the first linker followed by seven rounds of directed evolution produced RCaMP3-v16, a direct indicator with F_{sat}/F_{apo} of ~15 (**Figure 4-1C**). Over the course of these late rounds of engineering, a common scenario I encountered is that variants with improved dynamic ranges had weak affinities for Ca^{2+}, often in excess of 1 µM. Efforts to increase affinity by reverting mutations were accompanied by large losses in dynamic range; thus, these variants were abandoned.

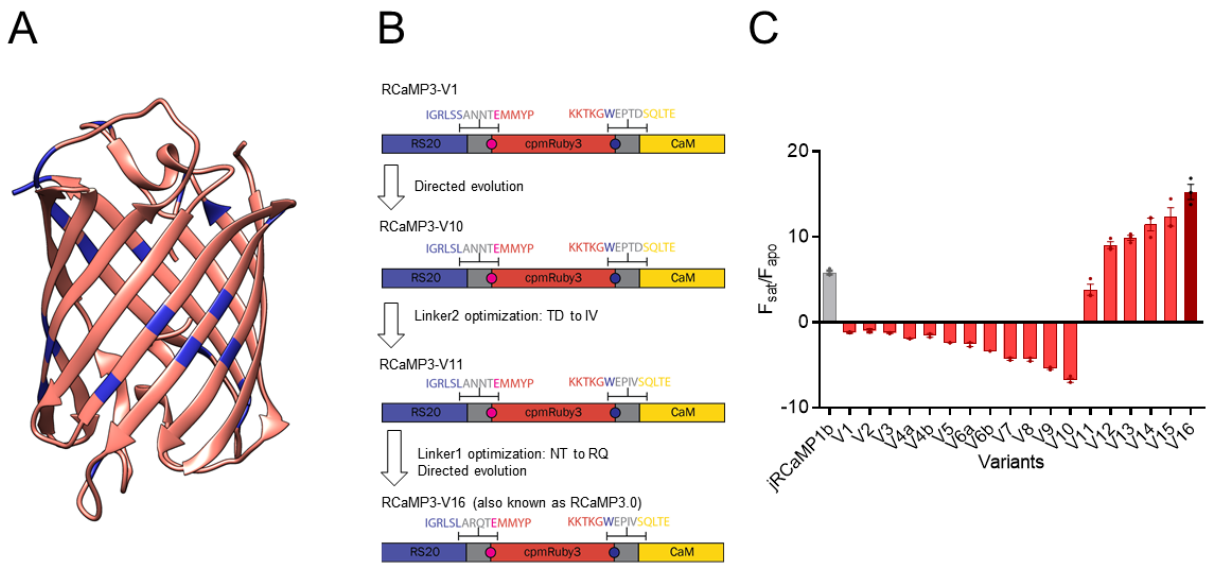

Figure 4-1 – mRuby3 mutations and directed evolution of RCaMP3.0.

A) Crystal structure of mRuby (PDB: 3U0M) highlighting the mutations (blue) between the FP domain in jRCaMP1b and mRuby3 [373]. One residue, Gly223, was unstructured and not shown. B) Schematic representation of RCaMP3 engineering. Residues at both linker interfaces are shown above the schematic representations (i.e., purple residues belong to RS20, grey residues are linker residues, red residues are part of cpmRuby3, and yellow

residues are part of CaM. Gatepost residues are indicated by pink and navy circles. Schematic is not to scale. C) Graph showing the dynamic ranges of key variants over the course of engineering. Bars indicate mean values, and individual data points are shown. jRCaMP1b is shown for comparison in grey, and the final variant, RCaMP3-v16 (now called RCaMP3.0), is coloured differently. All variants were batch purified with Ni-NTA. Error bars represent SEM.

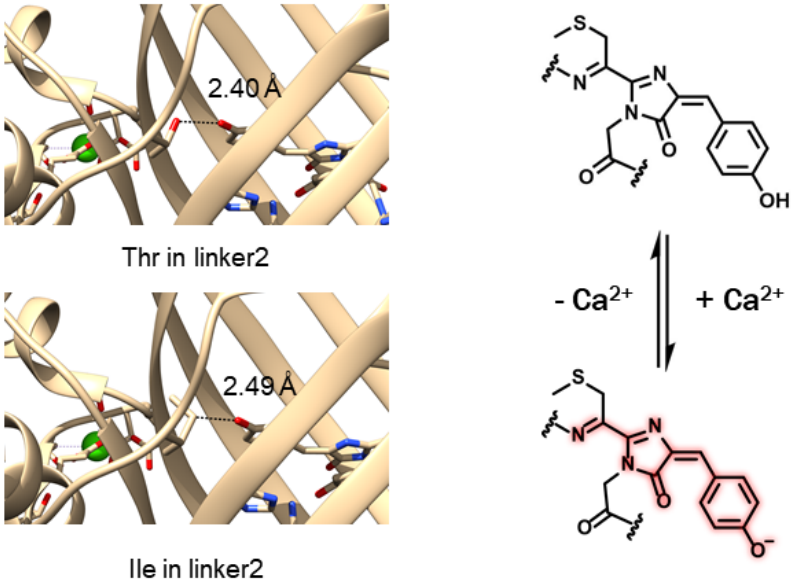

Figure 4-2 – Effect of Thr and Ile on the chromophore

Modelling of the second linker residues suggested that in the Ca^{2+}-bound state, the Thr residue (which was carried over from jRCaMP1b) is closer to the chromophore than the Ile residue. In FPs, the fluorescent form of the chromophore (shown on the right side) is the deprotonated form, where the resulting negative charge is delocalized over the conjugated system (red glow). We propose that the greater distance between the chromophore and Ile promotes the deprotonation of the chromophore.

Initial characterization of RCaMP3-v16 showed that it had a K_d of 1.1 μM, which is somewhat comparable to the published value for jRCaMP1b but much higher than other Ca^{2+} indicators [331,374,378,379]. In an effort to strengthen its affinity, we adopted the strategy employed by Inoue *et al.* and replaced the RS20 peptide in RCaMP3-v16 with the rat CaM-dependent kinase kinase peptide (ckkap) from K-GECO1 [378,383]. Like RCaMP3-v1, this ckkap-based construct required two days for fluorescence to be observed but also had no observable response to Ca^{2+}. Screening one library for optimizing the linker between the ckkap peptide and cpmRuby3 as well as another library with the GCaMP6 CaM mutations introduced by Inoue *et al*. [383] produced a dim variant with a 40% decrease in baseline fluorescence. I suspect that over the course of engineering RCaMP3, I had introduced mutations that were detrimental for a ckkap-based design and did not pursue this design further. Next, I attempted replacing either just the CaM domain or both RS20 and CaM of RCaMP3 with the corresponding domains from jGCaMP7f (fast) and jGCaMP7s (sensitive and slow), two of the latest variants from the GCaMP series [379]. jGCaMP7f and jGCaMP7s share the Ala317Leu mutation but differ on Ala52 (Val in jGCaMP7s) in RS20, as well as Arg381, Thr383, and Gly392 (Thr, Ser, and Arg, respectively, in jGCaMP7f) in the CaM. With respect to performance, relative to jGCaMP7s, jGCaMP7f had faster on and off kinetics at the cost of dynamic range (F_{sat}/F_{apo} = 30.2 for jGCaMP7f *vs.* 40.4 for jGCaMP7s), and affinity (K_d = 174 nM for jGCaMP7f *vs.* 68 nM jGCaMP7s). After overnight incubation, all the constructs were, again, dimmer than RCaMP3-v16, and the best construct was the one with RS20 from jGCaMP7s and CaM from jGCaMP7f , with the B-PER-extracted protein showing a ~60% increase in fluorescence intensity upon Ca^{2+} addition and brighter fluorescence than jGCaMP7s-cpmRuby3, which had a similar response. To recover the lost performance, I performed one round of directed evolution followed by linker optimization to produce a variant that showed almost a 3-

fold increase in fluorescence intensity after Ca^{2+} was added, which is still significantly smaller than the dynamic range of RCaMP3-v16. Thus, RCaMP3-v16 was chosen for further characterization and designated as RCaMP3.0.

4.3.2 *In vitro* characterization

There were 25 mutations introduced into RCaMP3-v1 to produce RCaMP3.0 (previously referred to as RCaMP3-v16 during engineering; **Figure 4-3A** and **Figure 4-4**), with two positions, 89 and 269, mutated twice – once when cpmRuby in jRCaMP1b was replaced by cpmRuby3 and again during engineering. The excitation and emission peaks for RCaMP3.0 were slightly red-shifted in the apo state (565 and 598 nm, respectively) relative to the saturated state (555 and 590 nm) (**Figure 4-3B** and **Table 4-1**). With brightness defined as the product between the EC and QY, RCaMP3.0 was significantly dimmer than both jRCaMP1b and mRuby3 as a result of both smaller ECs and QYs. Due to the formation of a peak at approximately 380 nm upon alkaline denaturation and taking advantage of the conserved number and positions of tryptophan residues between RCaMP3.0 and jRCaMP1b, the EC for RCaMP3.0 was measured by comparing the ratios of the deprotonated chromophore peaks against that of the saturated jRCaMP1b peak. RCaMP3.0 had a larger EC in the apo state (39,300 M^{-1} cm^{-1}) than in the saturated state (32,200 M^{-1} cm^{-1}), which is 60% of jRCaMP1b's in the saturated state. Despite the larger EC in the apo state, RCaMP3.0 is extremely dim in the apo state (brightness = 0.51) due to the extremely small QY in the apo state (Φ = 0.013). My measured QY for jRCaMP1b in the saturated state was slightly different than the reported value, but this is likely due to the different methodologies used. Regardless, the quantum yield for RCaMP3.0 in the saturated state was approximately half of both mRuby3 and jRCaMP1b.

RCaMP3.0 had a larger dynamic range (F_{sat}/F_{apo} = 16.3 ± 0.6) compared to jRCaMP1b but had a weaker affinity for Ca^{2+} than jRCaMP1b (K_d = 1.1 μM for RCaMP3.0 *vs.* 742 nM for jRCaMP1b). Relative to other red GECIs, RCaMP3.0 showed a similar dynamic range to R-GECO1 and R-CaMP1.07 but larger than all the original RCaMP1 variants, jRGECO1a and jRGECO1b, RCaMP2, XCaMP-R, and K-GECO1 [331,373,374,378,383,384]. However, except for most RCaMP1 variants, which also had a K_d greater than 1 μM, RCaMP3.0 had a weaker affinity for Ca^{2+} than the other red GECIs. For GECIs, the Hill coefficient is a measure of cooperativity for CaM binding Ca^{2+}, with a value greater than 1 indicating cooperative binding (i.e., Ca^{2+} binding facilitates binding of other Ca^{2+} ions). RCaMP3.0 had a larger Hill coefficient (n_H = 1.81) than jRCaMP1b, indicating that RCaMP3.0 bound Ca^{2+} with more cooperativity than jRCaMP1b. With the notable exception of jRCaMP1a, which had a Hill coefficient smaller than 1, this Hill coefficient for RCaMP3.0 is comparable to other RS20-based GECIs, which can range from ~1.2 (for R-CaMP2, which was specifically engineered to have a Hill coefficient close to 1) to ~3 (for some RCaMP1 variants) [331,373,374,379,383]. GECIs utilizing ckkap as the CaM binding peptide instead of RS20, such as K-GECO1 and XCaMPs, have Hill coefficients closer to 1, indicating more independent binding [378,384]. My results indicated that RCaMP3.0 has an optimal pH range of approximately 6.5 to 9 (**Figure 1-3D**). RCaMP3.0 was more pH sensitive than jRCaMP1b with a pK_a of 5.8 in the saturated state, but the pK_a was not determined for the apo state due to the quenching observed at pH greater than 7. Our measured pK_a for the apo state of jRCaMP1b (pK_a = 4.5) likely differed from the reported value (pK_a = 6.4) as a result of the lack of quenching at pH 7 and greater that was observed with RCaMP3.0.

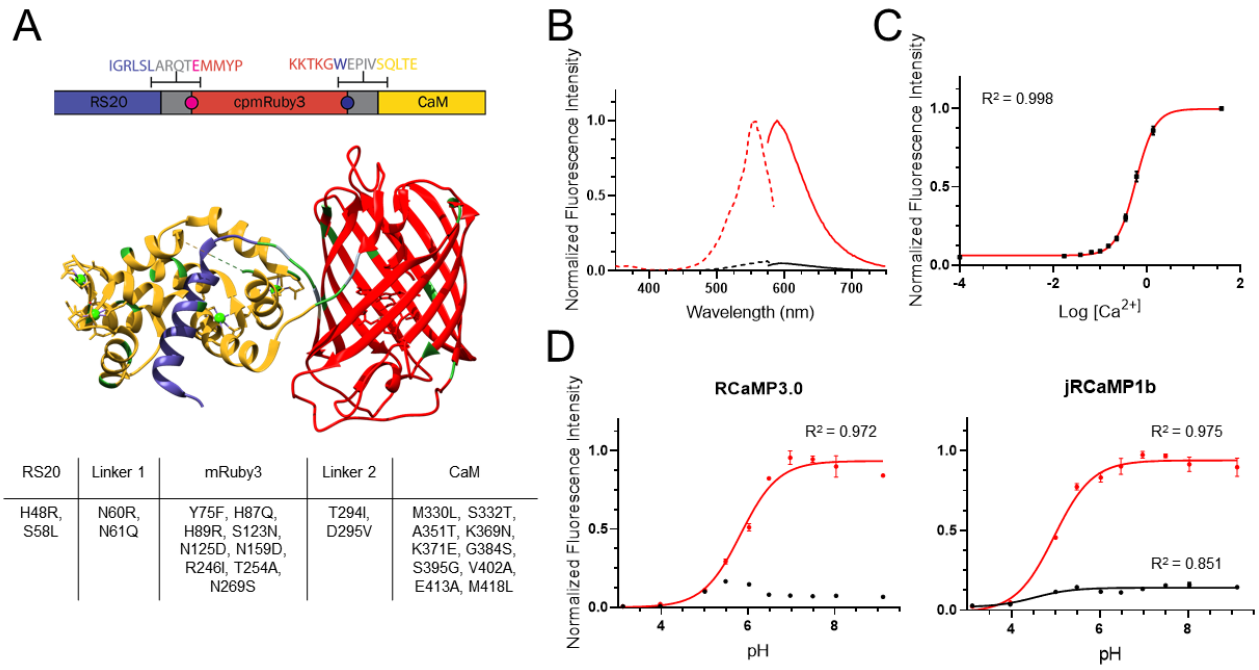

RS20	Linker 1	mRuby3	Linker 2	CaM
H48R, S58L	N60R, N61Q	Y75F, H87Q, H89R, S123N, N125D, N159D, R246I, T254A, N269S	T294I, D295V	M330L, S332T, A351T, K369N, K371E, G384S, S395G, V402A, E413A, M418L

Figure 4-3 - RCaMP3.0 *in vitro* characterization.

A) Schematic representation and modeled structure of RCaMP3 using the previously published structure of RCaMP (PDB: 3U0K) [373]. Domains in structure are coloured as in schematics, with mutations relative toRCaMP3-v0 coloured in green. Specific mutations in each domain are indicated in the table, where one mutation, Lys371Glu, is part of the unstructured region in CaM. Green spheres indicate bound Ca^{2+}. B) Excitation (dashed) and emission (solid) spectra of RCaMP3. Black lines show the spectra in the apo state, and red lines are for the saturated state. C) K_d titration of RCaMP3.0. Error bars represent SEM (n = 3; technical). D) pH titration of RCaMP3.0 (left) and jRCaMP1b (right). The red lines show the fit for the bound states while the black line shows the fit for the apo state for jRCaMP1b. Fitted values are shown in Table 4-1. Error bars represent SEM (n = 3; technical).

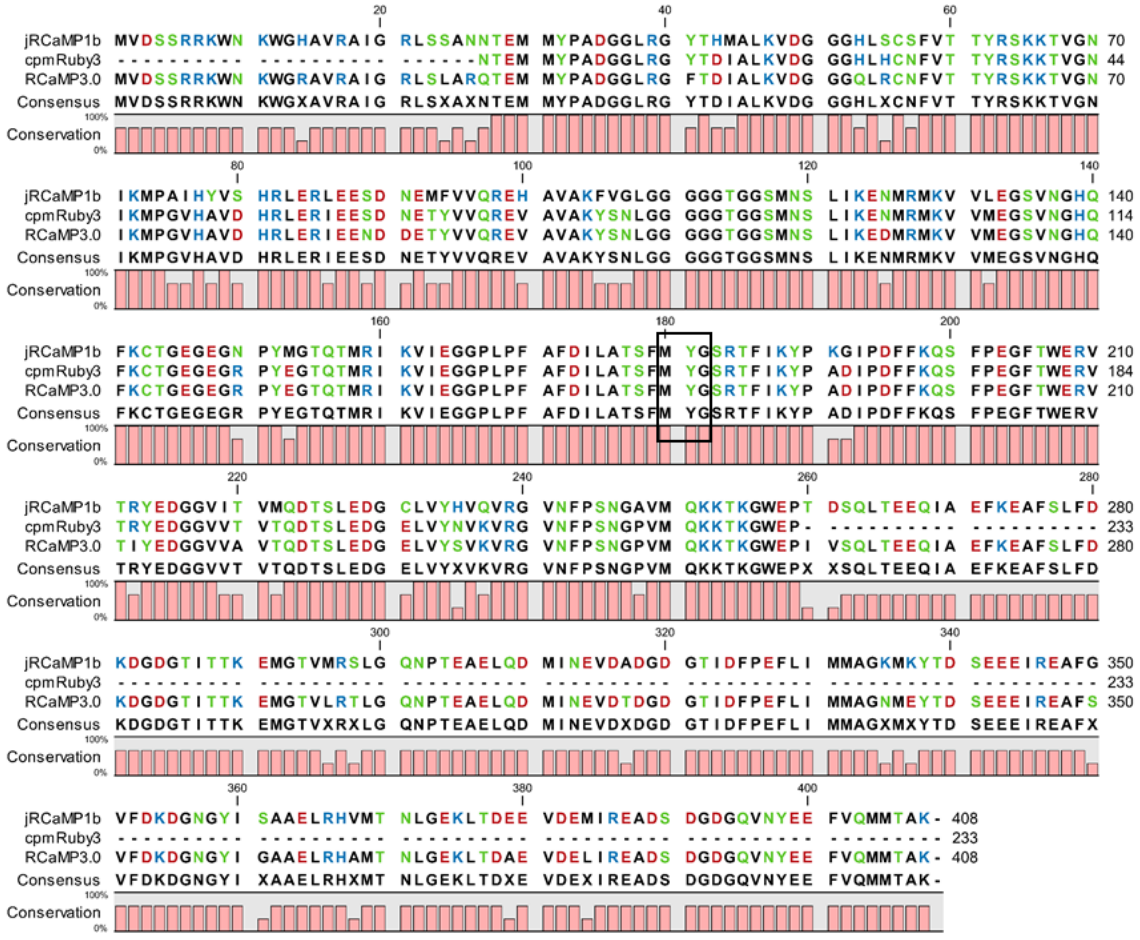

Figure 4-4 - Sequence alignment of jRCaMP1b, cpmRuby3, and RCaMP3.0.

Sequence alignment for jRCaMP1b [374], cpmRuby3, and RCaMP3.0. Residues are coloured according to polarity. Chromophore-forming residues are indicated by a black box. A bar chart for each position indicates residue conservation at that position.

Table 4-1 - *In vitro* characterization of RCaMP3.

Variant	Excitation (nm)	Emission (nm)	$\Delta F/F_{min}$[2]	K_d (nM)	Hill coefficient (n_H)	Brightness[3] (×1000)	ε ($M^{-1}cm^{-1}$)	Φ	pK_a
mRuby3[1]	562	589	n/a	n/a	n/a	51.1 (57.6)	114,000 (128,000)	0.45	5.0 (4.8)
						51.1 (57.6)	113,700 (128,000)	0.45	5.1 (4.8)
jRCaMP1b[4]	574	607	7.9 ± 0.3 (6.2 ± 0.1)	742 (712 ± 9)	1.34 (1.60 ± 0.01)	3.8 (3.8)	(25,300)	0.15 (0.15)	4.5 (6.4)
	578	597				22.4 (27.8)	(53,400)	0.42 (0.52)	5.0 (5.5)
RCaMP3.0[5]	574	598	16.3 ± 0.6	1120 [1100, 1150]	1.81	0.51	39,300	0.013	n.d.
	552	590				7.1	32,200	0.22	5.8 [5.7,6.0]

[1] Values in parentheses are from Bajar *et al.* [377].

[2] Calculated from the peaks of the emission spectra.

[3] Brightness = ε × Φ.

[4] Values in parentheses are from Dana *et al.* [374].

[5] Square brackets indicate 95% confidence intervals.

Top values are in Ca^{2+}-free state and bottom values in Ca^{2+} state.

n/a = not applicable. n.d. = not determined.

All measurements were made in triplicate. Errors represent SEM.

4.3.3 Imaging in mammalian cells

Following characterization of its performance *in vitro*, RCaMP3.0's performance in HeLa cells was tested. Cells transfected with pcDNA3.1m-jRCaMP1b or RCaMP3.0 showed expression in the cytosol; however, these cells were unresponsive to both histamine and ionomycin. Over the course of engineering GCaMP2, it was discovered that the polyHis RSET sequence at the N-terminus, similar to the leader sequence found in pBAD and normally just used for purifying protein from bacteria, was critical for maintaining fluorescence at 37 °C and has since been kept

in every GCaMP variant [379,380]. Since the RCaMP series was initially engineered from the GCaMP scaffold [373], it is possible that re-insertion of this sequence may restore function. Indeed, HeLa cells transfected with pcDNA3.1m-6His-jRCaMP1b were responsive to both histamine, triggering Ca^{2+} oscillations (with max $\Delta F/F_{min}$ of ~70%) , and ionomycin ($\Delta F/F_{min}$ ~100%) (**Figure 4-5A**). Over the course of the imaging session, however, substantial photobleaching of jRCaMP1b was observed.

For testing RCaMP3.0, one part (~250 ng) of pGP-CMV-jGCaMP7s (Addgene #104463; [379]), which served as an internal control, was co-transfected with 3 parts (~750 ng) of pcDNA3.1m-6His-RCaMP3.0. Both indicators were expressed throughout the cytosol, indicating good expression (**Figure 4-5B**). However, RCaMP3.0, like jRCaMP1b, showed substantial photobleaching while jGCaMP7 had minimal photobleaching after 30 min. Moreover, while jGCaMP7s had a max $\Delta F/F_{min}$ of ~50% during histamine treatment and ~200% after the addition of ionomycin, RCaMP3 had much smaller responses with $\Delta F/F_{min}$ of just ~65% even after ionomycin treatment. While these responses were unexpected given the *in vitro* results, it is likely that the smaller responses observed with RCaMP3 relative to jRCaMP1b during histamine treatment were due to the RCaMP3's weaker affinity for Ca^{2+} (K_d = 1.1 μM for RCaMP3 *vs.* 740 nM for jRCaMP1b). The Ca^{2+} concentration in cells was reported to peak at ~1 μM, thus preventing the saturation of RCaMP3 [385]. Given these results and evidence suggesting that the cytosolic concentration of Ca^{2+} in neurons are 50 to 100 nM at rest before rising anywhere from 10 to 100 times upon stimulation [367,386], RCaMP3, in its current form, would be unsuitable for imaging Ca^{2+} dynamics in neurons. Instead, it may have future applications in imaging Ca^{2+} dynamics in mitochondria, which, at peak levels, can have Ca^{2+} concentrations up to 100 μM [385].

However, in its current form, the modest response observed with RCaMP3 even after ionomycin treatment ($\Delta F/F_{min}$ ~65%) may hinder its use.

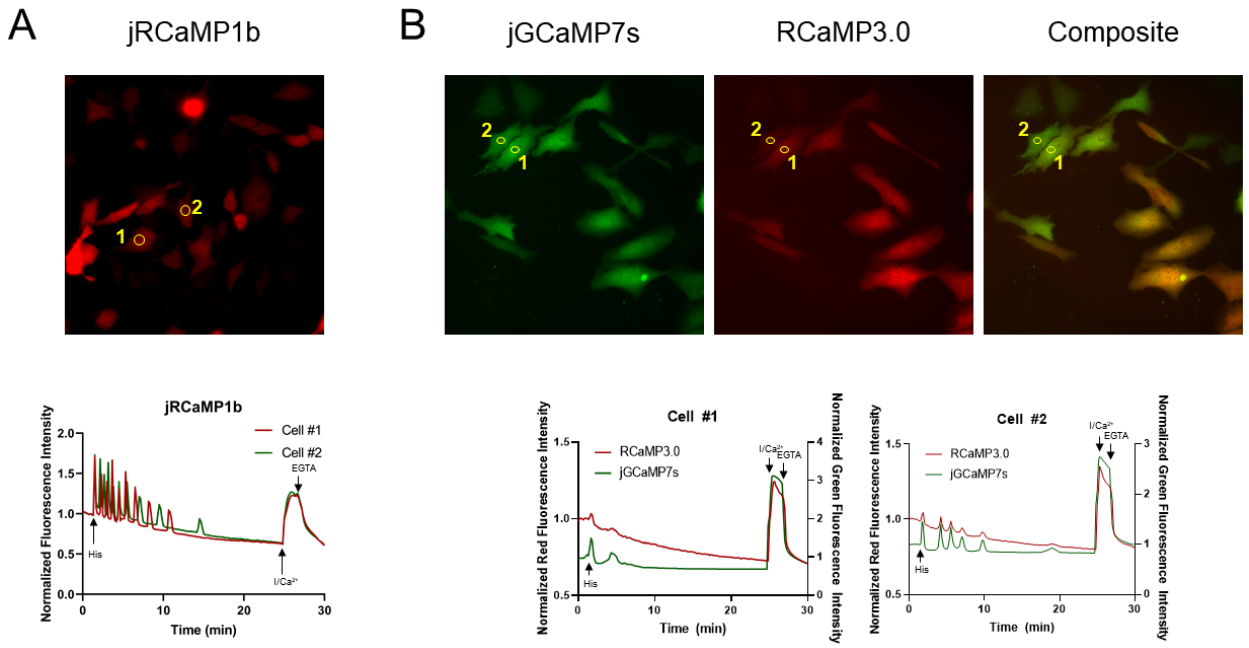

Figure 4-5 - Performance of His-tagged RCaMP3 in HeLa cells.

A) Representative image (top) of HeLa cells transfected with pcDNA3.1m-6His-jRCaMP1b. Representative traces of cells (bottom) for manually defined regions of interest indicated by yellow circles. Each trace indicates one cell. Additives are indicated by arrows (His = histamine; I/Ca^{2+} = ionomycin/Ca^{2+}). B) (Top) Representative images of HeLa cells co-transfected with pGP-CMV-jGCaMP7s (left) and pcDNA3.1m-6His-RCaMP3.0 (middle) with merged images generating the composite image (right) with individual traces of cells (bottom). Regions of interest are defined by yellow circles. Red traces (left y-axis) are for RCaMP3.0 and green traces (right y-axis) are for jGCaMP7s; added reagents are depicted by arrows as in A.

4.4 Conclusion

In an effort to capitalize on the significantly improved brightness of new RFPs, I engineered a new red GECI by replacing the cpmRuby of jRCaMP1b with its updated version, cpmRuby3. Though the initial construct was extremely dim and slow to fold, I was able to rescue its performance and engineer RCaMP3. a variant showing a 15-fold increase in fluorescence intensity upon binding Ca^{2+} *in vitro*, doubling the fluorescent response of jRCaMP1b. Unfortunately, despite extensive engineering, RCaMP3 remained significantly dimmer than jRCaMP1b with a weaker affinity, which negatively impacted its performance in HeLa cells. Although its dynamic range is an improvement, further engineering of RCaMP3, focusing on increasing both its brightness and affinity, is necessary to produce a new indicator that would be useful for imaging Ca^{2+} dynamics in neurons. Given its properties, however, RCaMP3 might instead be suitable for imaging Ca^{2+} dynamics in the mitochondria, and further experiments are needed to test its performance in the mitochondria.

5 Chapter 5 – Far-red Ca^{2+} indicators based on mKelly2

5.1 Introduction

Mammalian tissues have an "optical window" between 600 nm and 1300 nm in which light has maximum penetration depth [387,388]. This wavelength range falls between the absorbance profile of hemoglobin which predominates at wavelengths below 600 nm and the absorbance profile of water which predominates at wavelengths greater than 1300 nm. Because of the greater tissue penetration of photons in this wavelength range, fluorescent probes that absorb and excite efficiently within the optical window are highly desirable for in vivo imaging, especially when used in combination with multiphoton microscopy [389]. In addition to this advantage, fluorescent probes with longer wavelengths also provide less phototoxicity and autofluorescence, reduced crosstalk with green fluorescent indicators, as well as better potential compatibility with blue-cyan light activated optogenetics tools.

Practical realization of the potential advantages of fluorophores that excite and emit within the optical window has been a driving force for molecular tool engineers to shift the excitation and emission wavelengths of genetically-encodable fluorophores, such as RFPs, into the far-red region of the spectrum. This longstanding effort has yielded a plethora of far-red FPs (**Figure 5-1A**) with emission maxima (λ_{em}) over 620 nm [390]. Efforts in creating red-shifted RFPs from mushroom coral (Discosoma species) RFP family yielded mRaspberry (maximum excitation wavelength (λ_{ex}) ~ 598 nm, maximum emission wavelength (λ_{em}) ~ 625 nm), mPlum (λ_{ex} ~ 590 nm, λ_{em} ~ 649 nm), mGrape (λ_{ex} ~ 608 nm, λ_{em} ~ 646 nm), E2-Crimson (λ_{ex} ~ 611 nm, λ_{em} ~ 646 nm, tetrameric), and RDSmCherry (λ_{ex} ~ 600 nm, λ_{em} ~ 630 nm) [391-394]. The bubble-tip anemone (Entacmaea quadricolor) RFP family has become more prolific with the engineering of eqFP578-derived mKate (λ_{ex} ~ 588 nm, λ_{em} ~ 635 nm), mKate2 (λ_{ex} ~ 588 nm, λ_{em} ~ 633 nm), mNeptune (λ_{ex} ~ 600

nm, λ_{em} ~ 650 nm), TagRFP657 (λ_{ex} ~ 611 nm, λ_{em} ~ 657 nm), mCardinal (λ_{ex} ~ 604 nm, λ_{em} ~ 659 nm), and mMaroon1 (λ_{ex} ~ 609 nm, λ_{em} ~ 657 nm) [392,395-398] along with the eqFP611-derived mGarnet (λex ~ 598 nm, λem ~ 670 nm) and mGarnet2 (λex ~ 598 nm, λem ~ 671 nm) [399,400]. More recently, further monomerization of mCardinal resulted in two truly monomeric far-red FPs, mKelly1 (λex ~ 596 nm, λem ~ 656 nm) and mKelly2 (λex ~ 598 nm, λem ~ 649 nm) [401].

Genetically-encodable fluorophores can be engineered into genetically encoded indicators. One of the most important examples are the GECIs which can be used for detection and imaging of neuronal activity. Currently, the GFP-based GECI GCaMP series are the most commonly used GECIs for neuronal imaging [379,402]. However, red-shifted GECIs would enable imaging deeper into the brains of model organisms such as mice and adult zebrafish. Yet another advantage is that red shifted GECIs are spectrally orthogonal to most optogenetic actuators, which generally require blue to green light for activation. The combination of spectrally orthogonal indicators and optogenetic actuators enables researchers to control and monitor the neuronal activity simultaneously [403-405].

The latest generation of red GECIs for neuronal activity detection include jRCaMP1a/b, jRGECO1a, K-GECO1, and XCaMP-R, all with single-photon excitation and emission peaks outside of the optical window [331,374,378]. Among currently available RFP-based GECIs, the most red-shifted variant that uses a FP with an autocatalytic chromophore is CAR-GECO1 (λ_{ex} ~ 560 nm, λ_{em} ~ 609 nm) [403]. Further down to the red end of the spectrum, biliverdin-binding protein-based near-infrared GECI indicator NIR-GECO1 has been recently reported; however, NIR-GECO1 uses a cofactor-dependent FP that requires bound biliverdin to act as the chromophore [405]. To the best of our knowledge, there have been no published reports to date of far-red

fluorescent GECI that is analogous to the autofluorescent FP-based GCaMP series of Ca^{2+} indicators, leaving a gap in the spectral palette of available GECIs.

To expand the spectral palette of RFP-based GECIs into the far-red optical window we have developed intensiometric far-red fluorescent GECIs, FR-GECO1a (λ_{ex} ~ 596 nm, λ_{em} ~ 642 nm) and FR-GECO1c (λ_{ex} ~ 596 nm, λ_{em} ~ 646 nm). These genetically encoded far-red calcium indicators will open new avenues for multicolour Ca^{2+} imaging in combination with other optogenetic indicators and actuators, as well as functional Ca^{2+} imaging in deep tissue in vivo.

5.2 Materials and Methods

5.2.1 General

Synthetic DNA oligonucleotides and double-stranded fragments (gBlocks) were sourced from Integrated DNA Technologies. CloneAmp HiFi PCR Premix and Q5 polymerase were used for high fidelity PCRs, and were purchased from Takara Bio USA, Inc. and New England BioLabs, respectively. Taq polymerase was purchased from Thermo Fisher Scientific. PCR products were purified by preparative agarose gel electrophoresis and extracted with GeneJET Gel Extraction Kit purchased from Thermo Fisher Scientific. Restriction enzymes and T4 DNA ligase were purchased from Thermo Fisher Scientific and used according to the manufacturer's recommended protocols. Digested PCR products were extracted with the GeneJET Gel Extraction Kit before ligation. In-Fusion HD was purchased from Takara Bio USA, Inc. and used for assembly reactions. Plasmid DNA extractions were performed with GeneJET Plasmid Miniprep Kits (Thermo Fisher Scientific). Sanger sequencing reactions were performed by the Molecular Biology Services Unit at the University of Alberta. Fluorescence measurements were performed on a Safire^2 plate reader (Tecan), while absorbance measurements were collected on a DU-800 UV-Visible Spectrophotometer (Beckman).

5.3 Plasmid construction and directed evolution

5.3.1 Plasmid and library construction

Staring template construction. Double-stranded DNA encoding for K-GECO1 [378], with its cpFP replaced with cpmKelly2 [401], was commercially synthesized with overlapping sequences with pBAD/HisB (Thermo Fisher Scientific) in the 5' and 3' directions to facilitate insertion between the *XhoI* and *HindIII* sites of the vector. This fragment was then assembled into pBAD/HisB vector digested with XhoI and HindIII, transformed into electrocompetent *E. coli* strain DH10B (Invitrogen), and incubated overnight on LB agar plates supplemented with 400 μg/mL ampicillin (Thermo Fisher Scientific) and 0.02% (w/v) L-arabinose (Alfa Aesar) at 37 °C. Plasmids were isolated from single colonies grown in 4 mL liquid LB cultures with 100 μg/mL ampicillin and 0.02% L-arabinose, and sequenced by Sanger sequencing.

Library construction. To generate random mutagenesis libraries, mutations were introduced into the construct by EP-PCR amplification with Taq polymerase in the presence of MnCl2 (varies; up to 0.15 mM) and a 1:5 ratio of dATP and dGTP to dCTP and dTTP [325,326]. The purified PCR product was then assembled into digested pBAD/HisB vector, as before. On the other hand, site-directed mutagenesis libraries were generated by PCR amplification with high fidelity polymerases and primers carrying the codons for the desired mutations followed by DpnI digestion. The NNK (N = A, C, G or T, K = G or T) codon was used for complete randomization. For mutations at just one position, amplification was performed with the CloneAmp HiFi PCR Premix, while libraries with mutations at multiple locations were generated by QuikChange Lightning Multi Site-Directed Mutagenesis Kit (Agilent Technologies).

Plasmids for mammalian expression. Genes encoding FR-GECO1 and FR-GECO1c were amplified by high-fidelity PCR using primers that add vector homologous sequences to the 5' and 3' end and assembled into linearized pcDNA3.1/Puro-CAG-ASAP1 to replace the gene

encoding for ASAP1 (Addgene #52519; [406]). pcDNA3.1/Puro-CAG-ASAP1 was amplified by PCR such that the gene for ASAP1 was excluded.

5.3.1.1 Library screening in *E. coli*

Libraries were transformed into DH10B *E. coli* and cultured on LB agar plates supplemented with ampicillin and L-arabinose, as described earlier. The *E. coli* colonies expressing the library were then screened on the plate on the basis of fluorescence intensity using a custom imaging system described previously [328]. Colonies displaying the highest fluorescence intensity were then cultured in 4 mL liquid LB with ampicillin and arabinose overnight at 37 °C. Proteins were then extracted from cells using B-PER (Thermo Fisher Scientific) and subjected to a secondary screen by measuring their fluorescence intensities in Ca^{2+}-free (30 mM 3-(*N*-morpholino)propanesulfonic acid (MOPS), 100 mM KCl, 10 mM EGTA, pH 7.2) and Ca^{2+} buffers (30 mM MOPS, 100 mM KCl, 10 mM Ca-EGTA, pH 7.2) to determine their dynamic range. Plasmids for variants showing the largest dynamic range and highest fluorescence intensities were extracted, sequenced, and used as the template(s) for the next round of evolution.

5.3.2 *In vitro* characterization

5.3.2.1 Protein expression and purification

The pBAD/HisB plasmid carrying the gene encoding for the protein of interest was transformed into electrocompetent DH10B *E. coli* and grown on solid media. Single colonies from the transformed bacteria were then used to inoculate 4 mL of a starter culture supplemented with ampicillin and L-arabinose that was then shaken at 225 rpm in 37 °C overnight. The starter culture was added to 500 mL of LB with 100 μg/mL ampicillin and the culture was shaken at 37 °C. After 4 h, 0.02% L-arabinose is added to induce expression, and the culture is shaken for another 4 h at 37 °C before harvesting the bacteria by centrifugation. Bacteria were then resuspended in 1× TBS (50 mM Tris-HCl, 150 mM NaCl, pH 7.5), and lysed by sonication. The lysate was clarified by

centrifugation and the cleared lysate was incubated with Ni-NTA resin for at least 1h. Resin bound to protein was washed with TBS wash buffer (1× TBS with 20 mM imidazole, pH 8.0) followed by elution with TBS elution buffer (1× TBS with 250 mM imidazole, pH 7.8). The purified protein was then left at room temperature overnight to facilitate protein folding and chromophore maturation before concentrating and buffer exchanging into 1× TBS using 10 kDa centrifugal filter units (Millipore). All steps were carried out at 4 °C or on ice.

5.3.2.2 Spectral characterization

Brightness is the product of the EC and the QY.

EC determination. ECs of FR-GECO variants were measured using the alkali denaturation method [329]. Briefly, purified protein for each FR-GECO variant was diluted in NaOH, Ca^{2+}-free (30 mM MOPS, 100 mM KCl, 10 mM EGTA, pH 7.2), and Ca^{2+} buffer (30 mM MOPS, 100 mM KCl, 10 mM Ca-EGTA, pH 7.2), and the absorption spectrum for each sample was collected. Because the same amount of protein was used for each set of measurements for each protein, the concentration of protein present in each sample can be calculated according to Beer's Law and the previously reported EC of 44,000 for the absorbance peak around ~ 450 nm, which corresponds to the denatured tyrosine-based chromophore [329,407]. Further application of Beer's Law with the calculated concentration for each variant yields the EC in the saturated and Ca^{2+}-free states. Measurements were performed in triplicate and the results were averaged.

QY determination. Determination of QY was performed according to previously established protocols using mKelly2 as the standard [328,331,401]. For each protein, a series of diluted samples were prepared in Ca^{2+}-free and Ca^{2+} buffer from the samples used for EC measurements such that the peak absorbance was equal to, or less than, 0.05. For each dilution series, the emission spectra were collected from 590 to 750 nm with an excitation wavelength of

570 nm. The total fluorescence intensities for each dilution were integrated, plotted against the absorbance, and the slope of each line (m) was calculated. QYs were then calculated using the published QY for mKelly2 (QY = 0.18; [401]) and according to the equation:

$$\varphi_{\text{protein}} = \varphi_{\text{standard}} \times \frac{\text{m}_{\text{protein}}}{\text{m}_{\text{standard}}} \quad (1)$$

5.3.2.3 Affinity and pKa measurements

***K_d* determination.** Buffers for the K_d determination, with free [Ca^{2+}] ranging from zero to 39 μM, were prepared by mixing the appropriate volumes of Ca^{2+}-free and Ca^{2+} buffers, as described previously [381]. Purified FR-GECO variants were diluted in these buffers and the fluorescence intensities of the protein in each solution were measured in triplicate. The readings were plotted against the free Ca^{2+} concentration on a logarithmic scale, and the data fitted to equation 2 for the K_d and apparent Hill coefficient:

$$F = F_{min} + \frac{F_{max} - F_{min}}{1 + 10^{(log_{K_d} - X)n_H}} \quad (2)$$

p*K*$_a$ determination. As described previously, aliquots of a buffer containing 30 mM trisodium citrate and 30 mM borax (sodium borate) were adjusted using HCl or NaOH so that their pH ranged from 3 to 11 [331]. Concentrated protein, as well as 1 μL of either 200 mM EGTA or $CaCl_2$ for the Ca^{2+}-free and Ca^{2+} conditions, respectively, were then diluted in these buffers for a total volume of 100 μL. The fluorescence intensities were measured in triplicate, and the readings were plotted against pH before fitting to equation 2 but for H^+ and the Hill coefficient constrained to 1:

$$F = F_{min} + \frac{F_{max} - F_{min}}{1 + 10^{(pK_a - pH)n_H}} \quad (3)$$

Due to the ionization events at pH ~ 5 to 6, only the data for pH 6.5 to 11 were fitted to the Hill equation for the pK_a.

5.3.3 Two-photon (2P) characterization

Experimental setup for 2P spectral measurements includes a tunable femtosecond laser InSight DeepSee Dual (Spectra Physics) coupled with a photon counting spectrofluorometer PC1 (ISS) [408,409]. The two-photon fluorescence excitation (2PE) spectra were measured by automatically stepping laser wavelength and recording total fluorescence intensity at each step. A combination of filters, including FF01-770/SP, FF01-680/SP (both Semrock), and FGL630 long-pass (Thorlabs) was used in the left emission channel of PC1 spectrofluorometer to eliminate scattered laser light. To scale the 2P excitation spectra, we use a parameter called 2P molecular brightness $F_2(\lambda)$. This parameter depends on fractional contributions to 2P brightness of the anionic and neutral forms at excitation wavelength λ and can be presented as follows:

$$F_2(\lambda) = r_A j_A \sigma_{2,A}(\lambda) + r_N j_N \sigma_{2,N}(\lambda)$$

Where j is the fluorescence quantum yield of form A or N, and σ_2 is the 2P absorption cross section. Since we collect fluorescence spectrum through a FGL630 long-pass filter, technically j_N only comprises a part of fluorescence originating from anionic deprotonated chromophore that appears after the excited-state proton transfer from initially excited neutral form. To obtain the 2P excitation spectrum in units of molecular brightness, we independently measured r_A, j_A, and $\sigma_{2,A}(\lambda)$ of the anionic form for both FRGECO1a/c in Ca^{2+}-free and Ca^{2+}-saturated states and normalized the unscaled 2PE spectrum to the product $r_A j_A \sigma_{2,A}(\lambda)$. The cross section $\sigma_{2,A}(\lambda)$ was measured at the wavelength where the contribution of the neutral form is negligible (λ = 1064 nm). This measurement was performed using Rhodamine B in alkaline ethanol as a reference standard. Its cross section was measured relatively to Rhodamine 6G in ethanol (with the average

$<s_{2,RhB}/s_{2,Rh6G}>$ = 1.072 ± 0.017). Using this number together with the Rhodamine 6G cross section in ethanol ($s_{2,Rh6G}$) obtained after averaging of seven independent measurements: $<s_{2,Rh6G}->$ = 12.4 ± 2.6 GM, Rhodamine B in ethanol at 1064 nm was calculated $s_{2,RhB}$ = 13.3 ± 2.8 GM and used as a reference. In a modified version of previously reported methods [409], a total (without monochromator) 2P excited (at 1064 nm) fluorescence signal I as a function of laser power P were collected for both the sample and reference solutions (samples were held in 3x3 mm cuvettes (Starna) with maximum optical density less than 0.1). The fluorescence was collected at 90° to excitation laser beam through FF01-770/SP, FGL630 Longpass, and Edge BasicTM long wave pass 561 (Semrock) filters, using the left emission channel of a PC1 spectrofluorimeter working in photon counting mode. The power dependences of fluorescence were fit to a quadratic function $I = aP^2$, from which the coefficients a_S and a_R were obtained for the sample (index S) and reference (index R) solutions, respectively. Second, the one-photon (1P) excited fluorescence signals were measured for the same samples and in the same registration conditions. In this case, a strongly attenuated radiation of a 561-nm line of a Sapphire 561-50 CW CDRH (Coherent) laser was used for excitation. The fluorescence power dependences for the sample and reference were measured and fit to a linear function: $I = bP$, from which the coefficients b_S and b_R were obtained. The 2P absorption cross section was then calculated as follows:

$$\sigma_{2,S}(\lambda_2) = \frac{a_s}{a_R}\frac{b_R}{b_S}\frac{\varepsilon_s(\lambda_1)}{\varepsilon_R(\lambda_1)}\sigma_{2,R}(\lambda_2)$$

Here, λ_1 is the wavelength used for one-photon excitation (561 nm), λ_2 is the wavelength used for two-photon excitation (1064 nm), $\varepsilon_{R,S}(\lambda_1)$ are the corresponding ECs, measured at λ_1. This approach allows us to automatically correct for the laser beam properties (pulse duration and spatial intensity distribution), fluorescence collection efficiencies for 1P and 2P modes, photomultiplier tube spectral sensitivity, differences in QYs and concentrations between S and R

solutions. Molecular brightness of the anionic form was then calculated as a product $F_2 = r_A j_A s_{2,A}(l_m)$ with the 2P cross section taken at spectral maximum, l_m , for both states of the sensor. The QYs, ECs, and fractional concentrations were all measured independently (see previous sections). Finally, the 2P excitation spectra were scaled to the calculated F_2(1064 nm) values.

5.3.4 Imaging in neurons

Primary rat hippocampal neurons were prepared as described previously [410]. Cultured neurons were transfected with pCAG-FR-GECO1a and pCAG-FR-GECO1c plasmids using electroporation (Lonza Nucleofector) according to manufacturer's instructions. Prior to imaging session, transfected neurons were first washed twice with imaging buffer (145 mM NaCl, 2.5 mM KCl, 10 mM glucose, 10 mM HEPES, pH 7.4, 2 mM $CaCl_2$ and 1 mM $MgCl_2$), and treated with synaptic blockers (10 μM CNQX, 10 μM CPP, 10 μM GABAZINE, and 1 mM MCPG). Neurons were imaged using an inverted Nikon Eclipse Ti2 microscope equipped with a SPECTRA X light engine (Lumencor), a 20× objective (NA = 0.75, Nikon), and a sCMOS camera (Hamamatsu ORCA-Flash 4.0). Neurons were stimulated by field stimulation with a custom-built platinum wire electrode with a stimulus isolator (A385, World Precision Instruments). Trains of action potentials (APS) numbering 1, 2, 3, 5, 10, 20, 40, 80, 120 and 160 were stimulated and fluorescence images were acquired throughout the stimulation session. Acquired images were processed with ImageJ.

5.4 Results and discussion

5.4.1 Engineering FR-GECO1a and FR-GECO1c

Initial efforts to engineer a far-red Ca2+ indicator followed two parallel strategies. The first strategy was to graft key mutations for far-red fluorescence onto existing red GECIs. We used R-GECO1 [331], CH-GECO1 [411] and K-GECO1 [378] as templates and introduced key mutations from E2-Crimson [393], RDSmCherry [394], and mNeptune [392], respectively (Figure 5-1A). Unfortunately, loss of fluorescence or no substantial spectral shift were observed in these designed

prototypes (**Table 5-1**). The second strategy was *de novo* engineering of a GECI starting from far-red FP scaffolds. However, our attempts to engineer GECIs based on mNeptune [397] and mCardinal [397] did not yield fluorescent prototypes. As both mNeptune and mCardinal retain weak dimerization tendencies [329,392,397,401], we suspected that the failure of these prototypes to fluoresce could be due to the circular permutation site and/or insertion site of CaM and its binding peptide overlapping with the oligomerization interface, possibly disrupting the dimerization.

Table 5-1 - Key mutations of far-red FPs grafted onto existing red GECIs.

Red GECI	Far-red FP	Key mutations grafted*	Result
R-GECO1	E2-Crimson	66Phe, 197Tyr	Non-fluorescent
CH-GECO1	RDSmCherry	161Gly, 163Gly	No spectral shift
K-GECO1	mCardinal	41Gly	Non-fluorescent

* Residue numbered according to FP.

mKelly1 and mKelly2 are variants of mCardinal that were engineered to be true monomeric far-red FPs by deletion of the C-terminal "tail", directed evolution, and consensus design (**Figure 5-1A**) [401]. We rationalized that the enhanced monomericity of mKelly1 and mKelly2 might facilitate circular permutation and further engineering to create GECIs. We thus designed cpmKelly2, the brighter of the two mKelly variants, with circular permutation at Thr143 (numbering according to the crystal structure for mCardinal [397]; PDB: 4OQW). This designed cpmKelly2 was then used to replace the cpFusionRed RFP in K-GECO1 [378]. This initial construct resulted in a dimly fluorescent variant we named FR-GECO0.1 (FR for **f**ar **r**ed; **Figure 5-1B**). Optimization of linker1 (the amino acids linking the ckkap peptide to cpmKelly2) led to the identification of an improved, but still dim, variant, FR-GECO0.2, with λ_{ex} = 586 nm, λ_{em} = 632 nm and ~7-fold increase of fluorescence upon Ca^{2+} addition. We then subjected FR-GECO0.2 to eight rounds of iterative directed evolution to improve its brightness and Ca^{2+} response while

ensuring that all the variants chosen to be used as gene templates for the next round maintained a far-red emission peak. Ultimately, our efforts led to a bright and sensitive far-red GECI, FR-GECO1a, which incorporated 19 mutations relative to the initial FR-GECO0.1 gene. FR-GECO1a has λ_{ex} = 596 nm, λ_{em} = 642 nm, and exhibits a 6-fold increase in fluorescence intensity in the presence of Ca^{2+} (**Figure 5-1B**).

With the mKelly2-derived FR-GECO1a in hand, we attempted to incorporate mKelly1-specific mutations in an effort to achieve a slightly more red-shifted emission peak and a higher photostability [401]. mKelly1 was engineered from mCardinal in parallel with mKelly2 and differs from mKelly2 by six mutations. To test whether these mutations could further improve FR-GECO1a, we screened a combinatorial library of FR-GECO1a containing all possible combinations of the six mKelly1-specific mutations. From this library we isolated a variant with λ_{ex} = 596 nm and λ_{em} = 646 nm. It exhibited an 18-fold increase in fluorescence intensity in the Ca^{2+}-bound state, which was an over 2-fold improvement relative to that of FR-GECO1a. This variant, which we termed FR-GECO1c (**c** for **c**ontrast) incorporated a single mutation, Tyr35Thr (numbering according to FR-GECO1a sequence, **Figure 5-1B** and **Figure 5-2**) which is positioned right beside the first gatepost residue (**Figure 5-1B**).

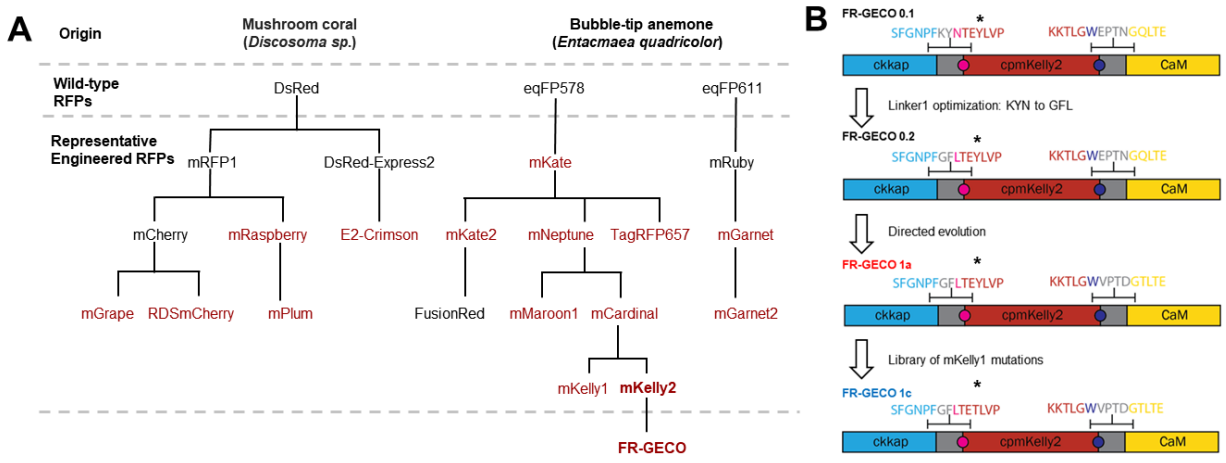

Figure 5-1 - Far-red FP genealogy and engineering of FR-GECO1.

A) Selected far-red FPs and FR-GECO1 genealogy. Far-red FPs (λem > 620 nm) are highlighted in red. B) Schematic illustration of FR-GECO1 design and engineering. Asterisk indicates position 35. Mutations outside of the linkers are visible in Figure 5-2.

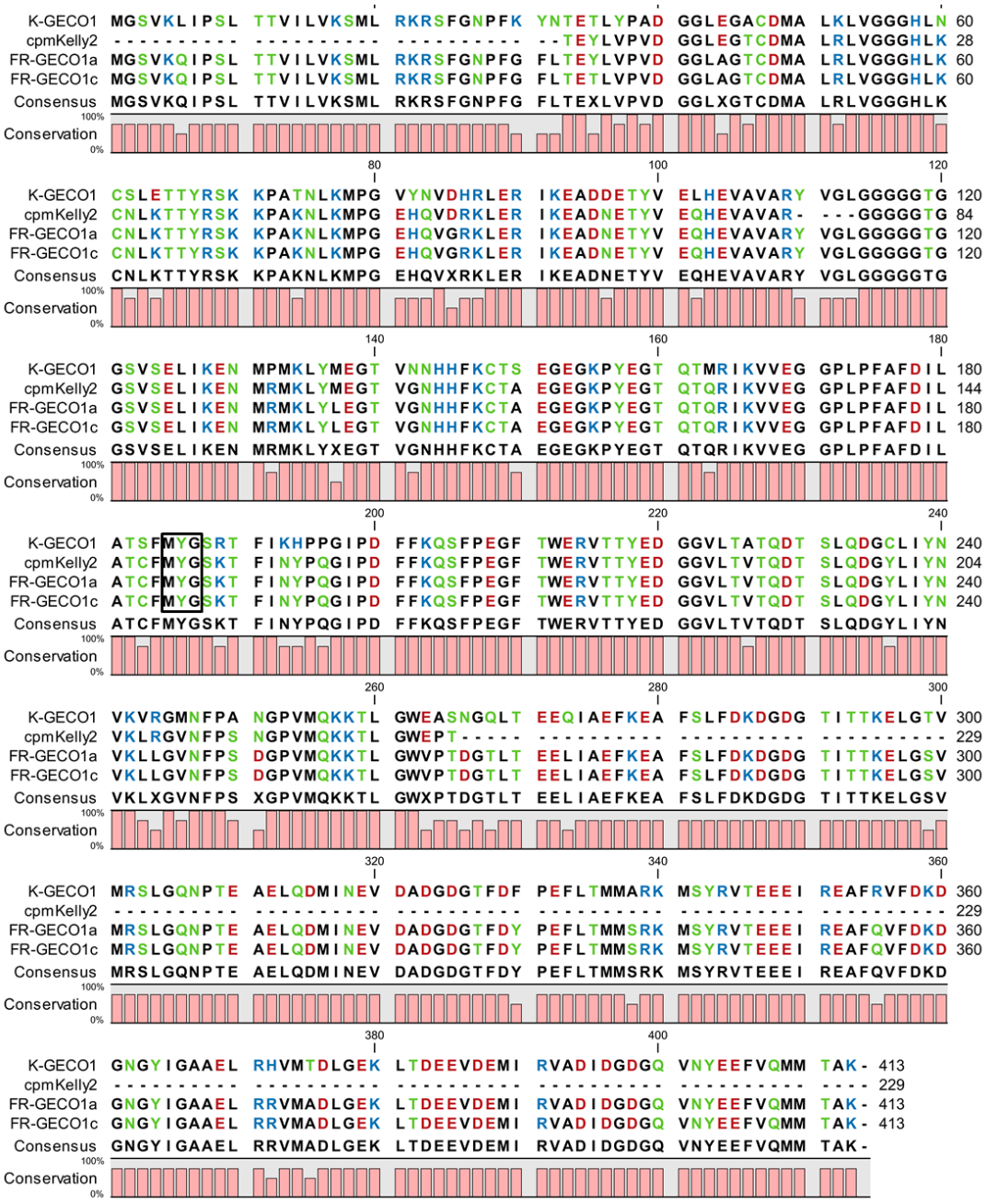

Figure 5-2 - Sequence alignment of K-GECO1, cpmKelly2, and FR-GECO1.

Sequence alignment for K-GECO1 [378], cpmKelly2, FR-GECO1a, FR-GECO1c. Residues are coloured according to polarity. Chromophore-forming residues are shown by a black box. Conservation in each position is indicated by the bar chart.

5.4.2 *In vitro* characterization of FR-GECO1

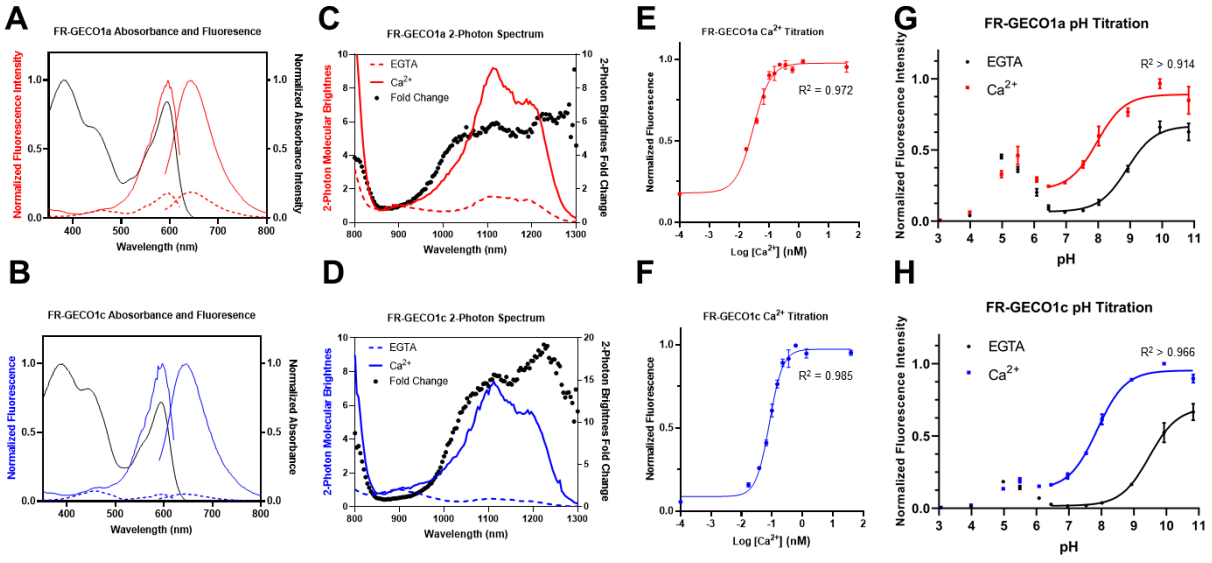

Figure 5-3 - FR-GECO1 characterization *in vitro*.

Representative absorption (black), excitation (dashed) and emission (solid) spectra of FR-GECO1a (A) and FR-GECO1c (B). Representative 2P spectra with fold change of FR-GECO1a (C) and FR-GECO1c (D). Kd titration of FR-GECO1a (E) and FR-GECO1c (F) (n = 3, technical). pH titration for FR-GECO1a (G) and FR-GECO1c (H). pK_a values were determined by fitting the points between pH 6.5 to 11. Fitted values are reported in Table 5-2 and Table 5-3. Error bars represent S.E.M.

To characterize the photophysical properties of FR-GECO1a and FR-GECO1c, we first purified the bacterially-expressed protein. Spectral analysis of the purified proteins revealed that the excitation peaks of FR-GECO1a (596 nm) and FR-GECO1c (596 nm) are slightly blue-shifted by 2 nm relative to mKelly2 (598 nm), while the emission peaks of the FR-GECO1a (642 nm) and FR-GECO1c (644 nm) are also slightly blue-shifted relative to mKelly2 (649 nm) (**Figure 5-3** and

Table 5-1). The 1P molecular brightness of both FR-GECO1a (brightness = 9.18) and FR-GECO1c (brightness = 9.28) in the Ca^{2+}-bound state are comparable and are ~20% brighter than their template FP, mKelly2 (brightness = 7.7) (**Table 5-1**). These results were attributed to a near doubling of the QY which offset the effect of the indicators' smaller ECs compared to mKelly2. In both the Ca^{2+}-free and Ca^{2+}-bound states, FR-GECO1a had ECs at 5,710 and 27,000 M^{-1} cm^{-1}, respectively, and FR-GECO1c had 4,850 and 26,500 M^{-1} cm^{-1}, respectively. The two-fold increase in the dynamic range of FR-GECO1c ($\Delta F/F_{min}$ = 18.1 ± 0.4) relative to FR-GECO1a ($\Delta F/F_{min}$ = 5.8 ± 0.2; attributable to the Tyr35Thr mutation), was found to result primarily from the two-fold smaller QY in the Ca^{2+}-free state of FR-GECO1c. As a result, FR-GECO1c exhibited a larger dynamic range *in vitro* than most other red GECIs, such as R-GECO1 [331], K-GECO1 [378], XCaMP-R [384], and the inverse-response NIR-GECO1 ($\Delta F/F_{min}$ = 9.6 with 5 mM Ca^{2+}) [405].

Consistent with other ckkap-based GECIs (i.e., K-GECO1, R-CaMP2, XCaMP-R) [378,383,384], Ca^{2+} titrations revealed that both FR-GECO1a and FR-GECO1c have relatively high affinities for Ca^{2+} and Hill coefficients greater than unity (**Figure 5-3E** and **F**). FR-GECO1a (K_d = 32 nM; n_H = 1.49) has a substantially lower K_d and n_H than FR-GECO1c (K_d = 87 nM; n_H = 1.98). These relatively high Ca^{2+} binding affinities suggested FR-GECO1a and FR-GECO1c are well-suited for neuronal activity detection. The pK_a measurements (**Figure 5-3G** and **H**) indicated that both FR-GECO1 variants undergo a shift in pK_a upon binding Ca^{2+} with a pK_a of ~ 9 in the Ca^{2+}-free state and ~ 8 in the bound state. Both variants exhibit a small peak at pH = 5 in the Ca^{2+}-free state and 5.5 in the Ca^{2+}-bound state, suggesting multiple ionizable groups, which resembles the pH characterization of CH-GECO series of red GECIs [412].

Table 5-2 - Photophysical characterization of FR-GECO1a, FR-GECO1c, and mKelly2.

Variant	FR-GECO1a[1]		FR-GECO1c[1]		mKelly2[2]
	Ca^{2+}-free	Ca^{2+}-bound	Ca^{2+}-free	Ca^{2+}-bound	
Excitation (nm)	598		596		598
Emission (nm)	642		646		649
$\Delta F/F_{min}$[3]	5.8 ± 0.2		18.1 ± 0.4		n/a
K_d **(nM)**	29 [25, 35]		83 [74, 92]		n/a
Hill coefficient (n_H)	1.49		1.98		n/a
Brightness[4] (×1000)	1.08	9.18	0.51	9.28	7.7
ε ($M^{-1}cm^{-1}$)	5,710	27,000	4,850	26,500	43,000
Φ	0.19	0.34	0.077	0.35	0.18
pK_a	8.91 [8.69, 9.12]	7.97 [7.66, 8.31]	9.48 [9.26, 9.69]	7.88 [7.75, 8.00]	5.6
2P Brightness F_2 (GM)	1.56	9.2	0.48	7.4	n.d.
$\Delta F/F_{min}$ **(2P)**	5.9		15.4		n.d.

[1] Square brackets indicate 95% confidence intervals.

[2] Values are from Wannier *et al.* [401].

[3] Calculated from the peaks of the emission spectra.

[4] Brightness = ε × Φ.

Top values are in Ca^{2+}-free state and bottom values in Ca^{2+} state.

n/a = not applicable. n.d. = not determined.

All measurements were made in triplicate. Errors represent SEM.

Under 2P conditions, both FR-GECO1a and FR-GECO1c had peak 2P excitation at 1112 nm (**Figure 5-3C** and **D**), with FR-GECO1a (9.2 GM) having a ~ 25% brighter 2P molecular brightness than FR-GECO1c (7.4 GM) in the Ca^{2+}-bound state (**Table 5-1**). Both FR-GECO1a and FR-GEOC1c, in Ca^{2+}-saturated states in vitro, are among the most 2P bright red GECIs (**Table 5-2**) [408]. The optimal wavelengths range for 2P excitation, with close to maximum fluorescence change, was between 1050 and 1200 nm (**Figure 5-3C** and **D**). This optimal wavelength range

overlaps with the range of common tunable 2P lasers, such as titanium-sapphire lasers ranging from 650 to 1100 nm. When optimally excited at 1200 nm in their Ca^{2+}-saturated states, FR-GECO1a and FR-GECO1c have very high 2P brightness ($\sigma_2 \times \phi$). At this wavelength, FR-GECO1a and FR-GECO1c are similar to only a few other far-red FPs, such as mKates, Katushkhas, and Neptunes. Both of these sensors are much brighter, at least by 5-fold, upon 2P excitation at 1200 nm than any of the red GECIs characterized so far [408]. The overall $\Delta F/F_0$ of FR-GECO1a and FR-GECO1c under 1P and 2P conditions are comparable. Taken together, FR-GECO1a and FR-GECO1c exhibited bright far-red fluorescence under both 1P and 2P illumination.

Table 5-3 - 2P *in vitro* comparison between FR-GECO1 and other red GECIs.

Red GECI	2P brightness of saturated form (φ x σ_2) GM (at $l_{2P,max}$)	2P brightness of saturated form (φ x σ_2) GM (1200 nm)	F_2 ($l_{2P,max}$) (φ x σ_2 x ρ) GM	F_2 (1200 nm) (φ x σ_2 x ρ) GM
FR-GECO1a	20 (1112 nm)	15	9.2	6.9
FR-GECO1c	15 (1112 nm)	11	7.4	5.5
R-GECO1.2	9.6 (1044 nm)	0.13	8	0.1
CAR-GECO1	9.4 (1060 nm)	0.6	8	0.54
K-GECO1	11 (1068 nm)	1.1	8	0.83
jRCaMP1a	12.4 (1076 nm)	2.7	10	2.2

5.4.3 Imaging in mammalian cells

The *in vitro* characterization of FR-GECO1a and FR-GECO1c had revealed that, fluorescent colour aside, these two new GECIs had properties, such as large fluorescence changes and high Ca^{2+} affinities, comparable to state-of-the-art GECIs. Of the two indicators, we expected that FR-GECO1a might be more suitable for labelling fine subcellular neuronal processes, such axon and dendrites, due to its brighter Ca^{2+}-free state as shown by the characterization in vitro. On the other hand, we expected that FR-GECO1c might provide better performance for the detection

of single spikes in neurons in terms of fluorescence change because of its wider dynamic range in vitro relative to FR-GECO1a. To evaluate the performance of FR-GECO1a and FR-GECO1c for imaging of neuronal activity, we expressed each GECI in dissociated rat hippocampal neurons. We observed that the fluorescence in neurons expressing either FR-GECO1 variant was evenly distributed throughout the cytosol (**Figure 5-4A** and **B**). Of the two indicators, FR-GECO1a did, indeed, have a brighter basal fluorescence, providing easier identification of transfected cells as well as facilitating visualization of the fine morphology of neural cells.

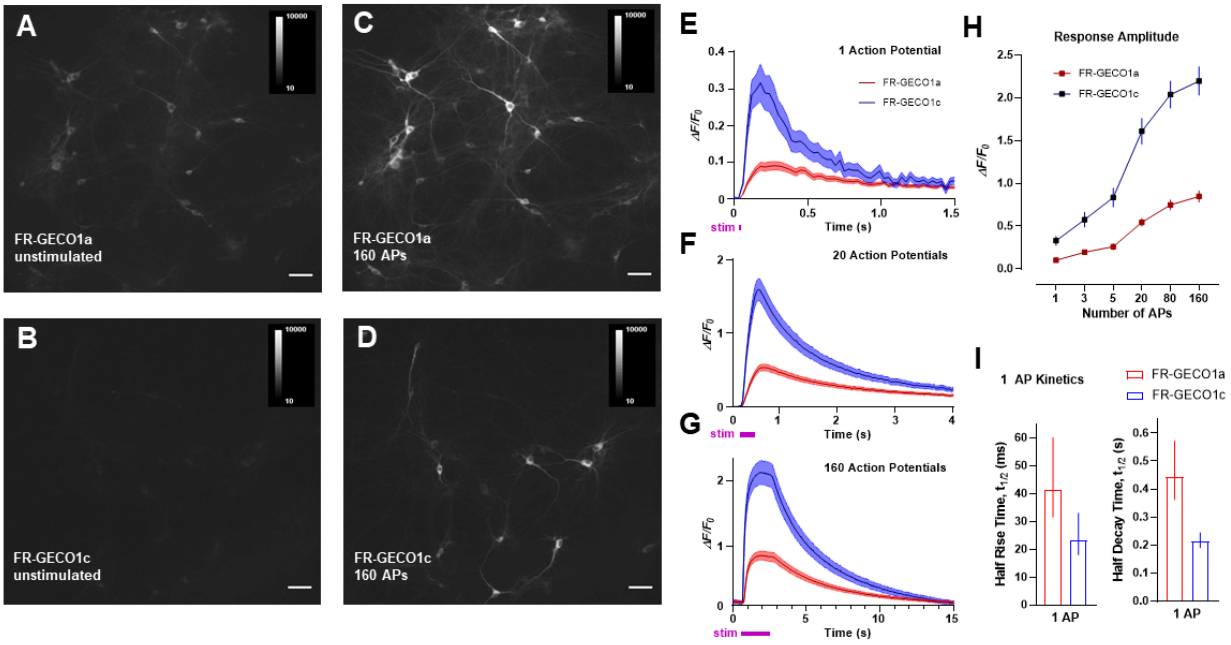

Figure 5-4 - Performance of FR-GECO1 in cultured hippocampus neurons. Representative images of neurons with FR-GECO1a at resting state (A), FR-GECO1c at resting state (B), FR-GECO1a at stimulated state (C), and FR-GECO1c at stimulated state (D). Averaged traces of FR-GECO1a (blue) and FR-GECO1c (red) recorded from neurons for 1 AP (E), 20 AP (F) and 160 AP (G). Traces were normalized to baseline. Shaded areas represent S.E.M. H) Averaged responses of FR-GECO1a (blue) and FR-GECO1c (red) as a function of the number of action potentials. Error bars represent S.E.M. (For both B and C,

n = 68 neurons for FR-GECO1a and n = 81 neurons for FR-GECO1c). l) Rise and decay time of FR-GECO1a and FR-GECO1c fluorescence changes induced by a single AP.

To evaluate indicator function, we acquired fluorescence images while delivering electric field stimuli to evoke trains of APs (in trains of 1, 2, 3, 5, 10, 20, 40, 80, 120 and 160) (**Figure 5-4C** and **D**). We observed that a single stimulus elicited a 10% $\Delta F/F_0$ response for FR-GECO1a (n = 81 neurons) and a 33% $\Delta F/F_0$ for FR-GECO1c (n = 68 neurons) (**Figure 5-4E** and **H**). These responses are ~50% higher than reported responses for jR-GECO1a, K-GECO1, and XCaMP-R, suggesting that FR-GECO1c is the most sensitive RFP-based GECI for single AP detection [374,378,384]. Additionally, both FR-GECO1 variants offer better sensitivity for single AP detection than NIR-GECO1 ($-\Delta F/F_0$ = 2.3% for 1 AP) [405]. FR-GECO1a and FR-GECO1c showed $\Delta F/F_0$ of 48% and 158% fluorescence increase, respectively, upon 20 stimuli by the field electrode (**Figure 5-4F** and **H**). When evoked with 160 stimuli, FR-GECO1c expressing neurons exhibited a peak $\Delta F/F_0$ of 220% while FR-GECO1a had a $\Delta F/F_0$ of 85% (**Figure 5-4G** and **H**). In terms of single AP response kinetics, both indicators exhibited relatively fast rise (half rise time, FR-GECO1a: 41 ms; FR-GECO1c: 23 ms) and decay (half decay time, FR-GECO1a: 0.44 s; FR-GECO1c: 0.21 s) times, with FR-GECO1c having ~2-fold faster rise and decay kinetics than FR-GECO1a (**Figure 5-4I**). Both variants are also faster than NIR-GECO1 (0.94 s rise time and 2.8 s decay time for 1AP) [405]. Overall, these results suggest that both FR-GECO1a and FR-GECO1c enable sensitive detection of neuronal activities. FR-GECO1c, in particular, offers exceptional single AP detection sensitivity, fast response times, and large fluorescence changes, compared to other state-of-art red GECIs.

5.5 Conclusion

GFP- and RFP-based GECIs have been extensively engineered and are widely used in imaging in mammalian tissue in vivo. However, there is still a demand for GECIs with more red-shifted wavelengths, such as indicators with wavelengths in the far-red or NIR range. Red-shifted indicators are generally preferable as they provide better spectral separation from green indicators as well as blue light-activated optogenetic actuators and show less phototoxicity and autofluorescence. Additionally, indicators with longer wavelengths enable deeper imaging, which may be useful for imaging subcortical structures, for example. Currently, the latest jRGECO1 and jRCaMP1 variants have an exponential decay coefficient of 130 μm, with jRGECO1a used to image layer 6 neurons 850 μm under the pia [374]. Consequently, there is a need for indicators with wavelengths in the far-red and NIR range. Here, we report the engineering of FR-GECO1, the first far-red genetically encoded Ca^{2+} indicator. Previous efforts to engineer a far-red Ca^{2+} using other FP scaffolds were unsuccessful, likely due to these scaffolds' oligomerization tendencies. On the other hand, mKelly2 is a true monomeric far-red FP, likely enabling the engineering of the first far-red fluorescence fully genetically encoded indicator. Relative to other red GECIs, which usually have λ_{ex} ~ 550-570 nm and λ_{em} ~ 580-600 nm and show significant crosstalk with *Chlamydomonas* and *Volvox* channelrhodopsins [413], both FR-GECO1 variants have significantly smaller spectral overlap with these channelrhodopsins, suggesting better compatibility with these actuators. Although their wavelengths are more blue-shifted than NIR-GECO1 [405], FR-GECO1 variants utilize a FP with the conventional barrel and an autocatalytic chromophore while NIR-GECO variants utilize mIFP, which requires the cofactor biliverdin to act as the chromophore. Additionally, we expect that the cpmKelly scaffolds of FR-GECO1 can serve as a template for engineering new FP-based far-red indicators for other ligands.

Although its performance as a first-generation sensor is already comparable to, and even better than, the most advanced GECIs in some respects, there is still room for further improvements. A general trend among FPs is that hypsochromic shifts in peak wavelengths are accompanied by reductions in quantum yield, thus limiting the brightness of available far-red and NIR FPs. Future versions of FR-GECO should be optimized for faster kinetics and improved 1P and 2P brightness (to facilitate imaging in vivo). Moreover, two-photon microscopy 1200 nm excitation will presumably provide deeper focusing ability compared to 1100 nm excitation because of less scattering, but water absorbs stronger at 1200 nm. Since the depths of imaging are not too deep (typically up 200 – 300 μm), this absorption by water would not cause any attenuation of the laser beam; however, heating due to the laser energy absorption could be stronger. Improving the two-photon brightness of the sensors should help reduce the required laser power for excitation, and consequently, tissue heating [414,415]. Alternatively, given that our pH titrations revealed that both FR-GECO1 variants have a significantly more basic pK_a relative to mKelly2 and do not exhibit their maximum brightness under physiological conditions, engineering variants with lower pKa values may also lead to improved brightness for imaging in tissue. Additionally, we believe that FR-GECO1 variants with shifted excitation peaks, especially further red-shifted for better compatibility with helium-neon lasers in 1P experiments, will be of particular interest to researchers.

In summary, we have developed a far-red GECI, the FR-GECO series, expanding the spectral palette of available GECIs that utilize non-biliverdin-binding FPs. As the first iteration, FR-GECO1 showed strong affinity for Ca^{2+} and good sensitivity for neuronal activity, and we have demonstrated their use in cultured hippocampal neurons. In the future, we aim to improve its brightness and demonstrate its application in vivo. Specifically, we are particularly interested in

testing the how deep into the brain FR-GECO1 enables imaging and if it shows better performance than jRGECO1a in layer 6 neurons [374]. Furthermore, we expect that the cpmKelly2 scaffold can be used to further expand the color palette of single FP-based genetically-encodable indicators for a wide range of analytes (i.e., other than Ca^{2+}) [416,417]. Thus, we believe that development of FR-GECO1 is a valuable addition to the toolkit of both protein engineers and the biology research community.

6 Conclusions and future directions

6.1 Summary of thesis

Neurotransmission – the flow of information within the nervous system – relies on the carefully regulated movement of ions and molecules within and without neurons. Within neurotransmission, Ca^{2+} is ubiquitous. Ca^{2+} influx is necessary to trigger the release of neurotransmitters into the synapse, and downstream, Ca^{2+} acts as a secondary messenger, triggering downstream cascades for neuroplasticity [368]. Although some of the most recognized neurotransmitters are amino acids, a review of the literature revealed that the canonical amino acids are directly or indirectly involved in neurotransmission, and yet, there is a limited selection of fluorescent sensors available for imaging amino acid dynamics (Chapter 1). Thus, the objective of my thesis was to engineer FP-based Ca^{2+} and amino acid indicators and expand the available repertoire of practically useful tools for imaging their dynamics.

L-Aspartate has long been recognized as the secondary excitatory neurotransmitter in the nervous system [22,23,27,30]. Despite the early excitement, however, its mechanism and physiological relevance remains unclear, and its status has since been called into question [25]. In Chapter 2, we detail the engineering of ODIN1, a series of green aspartate indicators using an aspartate/glutamate binding protein from *C. jejuni* [321] to help address this controversy. The three ODIN1 variants are bright, show large changes in fluorescence intensity upon aspartate binding and span a range of affinities for aspartate. However, given aspartate's structural similarity to glutamate, ODIN1 variants still bound and responded to glutamate, though with much weaker affinity. While we were not successful in expressing functional copies of ODIN1 on the surface of mammalian cells with a membrane-targeting vector, we were able to tether ODIN1 to the cell surface of HeLa cells using the latest iterations of the SpyTag/SpyCatcher system [327]. With this setup, we demonstrated that the three ODIN1 variants showed significant aspartate or glutamate-

induced increases in fluorescence intensities. We also discussed preliminary data that suggested that a secretion strategy for these sensors may be a viable alternative to membrane expression with mutations meant to improve secretion efficiency also enhancing performance.

L-Glutamine's most important contribution to neurotransmission is through its role in the glutamate/GABA-glutamine cycle [7,51]. In Chapter 3, we discuss our efforts to engineer a specific green glutamine indicator, Qigon1, with relatively high affinity and good dynamic range by capitalizing on the structural homology between the binding protein used for ODIN1 and a glutamine binding protein from *B. pseudomallei* [361] and several rounds of linker optimization. Using the SpyTag/SpyCatcher system [327], we tethered Qigon1 to the surface of HeLa cells and showed that it retained a modest response to glutamine.

Chapters 4 and 5 describe my work on engineering new GECIs. Chapter 4 is focussed on describing my efforts to engineer an mRuby3-based Ca^{2+} indicator by replacing cpmRuby in jRCaMP1b [374] with cpmRuby3. The latest variant, RCaMP3.0, possessed a significantly larger dynamic range than jRCaMP1b, but falls short with respect to its affinity and brightness. Testing in HeLa cells revealed that RCaMP3.0 only showed small changes in response to histamine treatment, and more disappointingly, a smaller dynamic range than jRCaMP1b. In Chapter 5, we describe our efforts to engineer far-red Ca^{2+} indicators based on mKelly2 [401], which we called the FR-GECO series, filling in a gap between available red and NIR GECIs. Furthermore, we demonstrate that the FR-GECO variants offer fast and sensitive detection of single action potentials in neurons.

6.2 Perspective and future directions

6.2.1 Optimization and further work on the described sensors

There is always room for improvement with every sensor, especially for the three first generation sensors described in this thesis. Although ODIN1 is functional when tethered by SpyTag and SpyCatcher [327], this tethering system would limit its use for two reasons. First, the need to purify ODIN1 would be a roadblock for researchers who do not have the resources or expertise for bacterial protein expression and purification. Secondly, challenges associated with the delivery of the purified indicators would limit the systems it can be applied in, especially *in vivo* with the possibility of triggering an immune response. Thus, identifying a construct that enables functional expression either on the membrane surface or by secretion, which the preliminary data suggested may be an option, remains a high priority. Additionally, since ODIN1 was shown to still respond to L-glutamate, variants with smaller responses to, or even weaker affinities for, L-glutamate would also be desirable. Lastly, while we demonstrated that all the ODIN1 variants respond to L-aspartate in HeLa cells, the sensors still need to be tested and characterized in neurons. Following validation in neurons, we would like to use ODIN1, likely in conjunction with R-iGluSnFR [255], for studies investigating aspartate and glutamate co-release.

Though Qigon1 is functional in our tests, it requires further engineering for robust performance in cells and neurons. First, its affinity is likely to be too high for detecting changes in glutamine concentration in both the cytosol and extracellular space. Mutations around the binding pocket, either in positions that directly interact with the ligand such as those in the affinity variants of iGluSnFR [254] or in positions near residues with interactions such as those positions targeted during the engineering of ODIN1, should reduce the affinity sufficiently. Further engineering is also necessary to improve Qigon1's brightness and dynamic range.

RCaMP3.0 requires further engineering to increase both affinity and brightness. Variants with increased affinity may be identified by revisiting mutated positions to identify variants with

higher affinity followed by directed evolution to recover the dynamic range and increase the brightness. Alternatively, if characterization of the latest jGCaMP7s-cpmRuby3 variant shows a significantly higher affinity, that variant may serve as the new template for further evolution.

An important, but unexplored, advantage of far-red indicators is the deeper penetration of these longer wavelengths into tissue, facilitating imaging of structures located deeper into the brain. Thus, demonstrations with FR-GECO1 showing deeper penetration would be ideal, such as the experiments performed with jRGECO1a and jRCaMP1a/b [374]. Additionally, a study comparing the performance of state-of-the-art red GECIs and FR-GECO1 with optogenetic actuators, especially the Volvox channelrhodopsin would be desirable [413]. As a first generation sensor, future optimization efforts for FR-GECO1 should focus on improving brightness, either by engineering for better expression, EC or QY or by engineering less pH sensitive variants as our results showed that both FR-GECO1 variants have such high pK_a values that their maximum brightness is not achieved under physiological conditions.

6.3 Engineering single FP-based indicators for other amino acids

Albeit to varying degrees, the canonical amino acids modulate neurotransmission; however, there is a limited selection of probes available for these amino acids. Many of these available probes are FRET sensors that utilize PBPs. Our approach for engineering ODIN1 and Qigon1 relied on identifying structurally homologous PBPs and utilizing a common insertion site. It is likely that other structurally homologous amino acid binding proteins, such as those that have been engineered into FRET sensors (**Table 1-2**), would be amenable to engineering to single FP-based sensors, and we propose that for structurally homologous proteins, the insertion site we used for ODIN1 and Qigon1 would be a good starting point. For example, the cysteine indicator engineered by Singh *et al.* [239] utilized a PBP from *C. jejuni*, the same organism PEB1a was identified from. Moreover, the review by Scheepers *et al.* [418] provides a collection of ligand

binding proteins up to 2016 that ought to be useful in identifying other ligand binding proteins that may make ideal candidates for sensor engineering.

An important consideration for current and future engineering efforts would be the challenges associated with screening. A key challenge in our efforts to engineer an aspartate indicator was the saturating levels of endogenous glutamate in *E. coli*, leading to diminished responses of sensors extracted from bacteria in our hands [333]. iGluSnFR was engineered by screening proteins extracted from bacteria after repeated washes of the bacteria pellet [252]; however, in our hands, this technique only yielded marginal, if any, improvements. The uncertainty of this technique would be problematic for the early stages of engineering, where responses are generally modest to begin with. We were able to circumvent this problem by batch purifying our libraries prior to testing, but this protocol was far more resource- and labour-intensive, reducing the number of variants that can be tested in a given run while requiring more hands-on time. Thus, there is a need for better screening protocols. However, while an optimized screening protocol that is applicable for any ligand would be ideal, it is more likely that prior to every new sensor, there would be a need to tailor screening protocols for maximum efficiency, balancing the usually competing interests of speed, resources and accuracy.

6.3.1 Engineering more red-shifted indicators

An important goal in sensor engineering is the expansion of the spectral palette available for any given class of sensor. The availability of sensors in different colours facilitates multicolour imaging and enables the simultaneous study of multiple analytes. Our work on FR-GECO1 showed that, unlike previously published far-red FPs, the recently reported mKelly2 [401] can be successfully used as a scaffold for engineering sensors. Further down the spectrum, NIR-GECO1 [405], which utilized the biliverdin-binding FP, mIFP, achieved a significant milestone and provided a possible scaffold for engineering NIR sensors. We expect that the successful

engineering of red-shifted variants of existing amino acid sensors (such as FHisJ [296], ODIN1 and Qigon1), likely starting with the cpmApple domain from R-iGluSnFR [255] or cpmKelly2 from FR-GECO1, would provide highly useful tools for cell biologists and neuroscientists alike. Though NIR-GECO utilized a non-cp topology (i.e., fused Ca^{2+}-binding domain and non-cpmIFP), previous work from our lab [255] has shown that altering the topology may not necessarily have deleterious effects, enabling the possibility of using the mIFP domain from NIR-GECO to engineer NIR variants of these sensors.

References

1. Nadler, J.V. Plasticity of glutamate synaptic mechanisms. In *Jasper's Basic Mechanisms of the Epilepsies [Internet]. 4th edition*, National Center for Biotechnology Information (US): Bethesda, MD, 2012.
2. Hassel, B.; Dingledine, R. Glutamate. In *Basic Neurochemistry: Molecular, Cellular, and Medical Aspects*, 7th ed.; Elsevier Academic Press: San Diego, CA, 2005; pp. 267-290.
3. Curtis, D.; Watkins, J. The excitation and depression of spinal neurones by structurally related amino acids. *J. Neurochem.* **1960**, *6*, 117-141, doi:10.1111/j.1471-4159.1960.tb13458.x.
4. Curtis, D.; Phillis, J.; Watkins, J. The chemical excitation of spinal neurones by certain acidic amino acids. *J. Physiol. (Lond.)* **1960**, *150*, 656-682, doi:10.1113/jphysiol.1960.sp006410.
5. Curtis, D.; Watkins, J. Acidic amino acids with strong excitatory actions on mammalian neurones. *J. Physiol. (Lond.)* **1963**, *166*, 1-14, doi:10.1113/jphysiol.1963.sp007087.
6. Featherstone, D.E. Intercellular glutamate signaling in the nervous system and beyond. *ACS Chem. Neurosci.* **2010**, *1*, 4-12, doi:10.1021/cn900006n.
7. Bak, L.K.; Schousboe, A.; Waagepetersen, H.S. The glutamate/GABA-glutamine cycle: aspects of transport, neurotransmitter homeostasis and ammonia transfer. *J. Neurochem.* **2006**, *98*, 641-653, doi:10.1111/j.1471-4159.2006.03913.x.
8. Meldrum, B.S. Glutamate as a neurotransmitter in the brain: Review of physiology and pathology. *J. Nutr.* **2000**, *130*, 1007S-1015S, doi:10.1093/jn/130.4.1007S.
9. Zhou, Y.; Danbolt, N.C. Glutamate as a neurotransmitter in the healthy brain. *J. Neural Transm.* **2014**, *121*, 799-817, doi:10.1007/s00702-014-1180-8.

10. Wang, Y.; Fathali, H.; Mishra, D.; Olsson, T.; Keighron, J.D.; Skibicka, K.P.; Cans, A.-S. Counting the Number of Glutamate Molecules in Single Synaptic Vesicles. *J. Am. Chem. Soc.* **2019**, *141*, 17507-17511, doi:10.1021/jacs.9b09414.

11. Clements, J.D. Transmitter timecourse in the synaptic cleft: its role in central synaptic function. *Trends Neurosci.* **1996**, *19*, 163-171, doi:10.1016/S0166-2236(96)10024-2.

12. Clements, J.D.; Lester, R.; Tong, G.; Jahr, C.E.; Westbrook, G.L. The time course of glutamate in the synaptic cleft. *Science* **1992**, *258*, 1498-1501, doi:10.1126/science.1359647.

13. Kleckner, N.W.; Dingledine, R. Requirement for glycine in activation of NMDA-receptors expressed in Xenopus oocytes. *Science* **1988**, *241*, 835-837, doi:10.1126/science.2841759.

14. Mayer, M.L.; Westbrook, G.L.; Guthrie, P.B. Voltage-dependent block by Mg2+ of NMDA responses in spinal cord neurones. *Nature* **1984**, *309*, 261-263, doi:10.1038/309261a0.

15. Morris, R.G.M. NMDA receptors and memory encoding. *Neuropharmacology* **2013**, *74*, 32-40, doi:10.1016/j.neuropharm.2013.04.014.

16. Dong, Y.; Nestler, E.J. The neural rejuvenation hypothesis of cocaine addiction. *Trends Pharmacol. Sci.* **2014**, *35*, 374-383, doi:10.1016/j.tips.2014.05.005.

17. Liu, J.; Chang, L.; Song, Y.; Li, H.; Wu, Y. The role of NMDA receptors in Alzheimer's disease. *Frontiers in Neuroscience* **2019**, *13*, doi:10.3389/fnins.2019.00043.

18. Lau, A.; Tymianski, M. Glutamate receptors, neurotoxicity and neurodegeneration. *Pflügers Archiv - European Journal of Physiology* **2010**, *460*, 525-542, doi:10.1007/s00424-010-0809-1.

19. Kullmann, D.M.; Asztely, F. Extrasynaptic glutamate spillover in the hippocampus: evidence and implications. *Trends Neurosci.* **1998**, *21*, 8-14, doi:10.1016/S0166-2236(97)01150-8.

20. Hires, S.A.; Zhu, Y.; Tsien, R.Y. Optical measurement of synaptic glutamate spillover and reuptake by linker optimized glutamate-sensitive fluorescent reporters. *Proc. Natl. Acad. Sci. USA* **2008**, *105*, 4411-4416, doi:10.1073/pnas.0712008105.

21. Parsons, Matthew P.; Raymond, Lynn A. Extrasynaptic NMDA receptor involvement in central nervous system disorders. *Neuron* **2014**, *82*, 279-293, doi:10.1016/j.neuron.2014.03.030.

22. Fleck, M.; Henze, D.; Barrionuevo, G.; Palmer, A. Aspartate and glutamate mediate excitatory synaptic transmission in area CA1 of the hippocampus. *J. Neurosci.* **1993**, *13*, 3944-3955, doi:10.1523/jneurosci.13-09-03944.1993.

23. Docherty, M.; Bradford, H.; Wu, J.-Y. Co-release of glutamate and aspartate from cholinergic and GABAergic synaptosomes. *Nature* **1987**, *330*, 64-66, doi:10.1038/330064a0.

24. Gundersen, V.; Holten, A.T.; Storm-Mathisen, J. GABAergic synapses in hippocampus exocytose aspartate on to NMDA receptors: quantitative immunogold evidence for co-transmission. *Mol. Cell. Neurosci.* **2004**, *26*, 156-165, doi:10.1016/j.mcn.2004.01.017.

25. Herring, B.E.; Silm, K.; Edwards, R.H.; Nicoll, R.A. Is aspartate an excitatory neurotransmitter? *J. Neurosci.* **2015**, *35*, 10168-10171, doi:10.1523/jneurosci.0524-15.2015.

26. Nadler, J.V. Aspartate release and signalling in the hippocampus. *Neurochem. Res.* **2011**, *36*, 668-676, doi:10.1007/s11064-010-0291-3.

27. Baughman, R.W.; Gilbert, C.D. Aspartate and glutamate as possible neurotransmitters in the visual cortex. *J. Neurosci.* **1981**, *1*, 427-439, doi:10.1523/jneurosci.01-04-00427.1981.

28. Bradford, S.; Nadler, J. Aspartate release from rat hippocampal synaptosomes. *Neuroscience* **2004**, *128*, 751-765, doi:10.1016/j.neuroscience.2004.06.065.

29. Nadler, J.V.; Vaca, K.W.; White, W.F.; Lynch, G.S.; Cotman, C.W. Aspartate and glutamate as possible transmitters of excitatory hippocampal afferents. *Nature* **1976**, *260*, 538-540, doi:10.1038/260538a0.

30. Wiklund, L.; Toggenburger, G.; Cuénod, M. Aspartate: Possible neurotransmitter in cerebellar climbing fibers. *Science* **1982**, *216*, 78-80, doi:10.1126/science.6121375.

31. Hashimoto, A.; Nishikawa, T.; Oka, T.; Takahashi, K.; Hayashi, T. Determination of free amino acid enantiomers in rat brain and serum by high-performance liquid chromatography after derivatization with N-tert.-butyloxycarbonyl-L-cysteine and o-phthaldialdehyde. *J. Chromatogr. B Biomed. Sci. Appl.* **1992**, *582*, 41-48, doi:10.1016/0378-4347(92)80300-F.

32. Horio, M.; Ishima, T.; Fujita, Y.; Inoue, R.; Mori, H.; Hashimoto, K. Decreased levels of free d-aspartic acid in the forebrain of serine racemase (Srr) knock-out mice. *Neurochem. Int.* **2013**, *62*, 843-847, doi:10.1016/j.neuint.2013.02.015.

33. Storck, T.; Schulte, S.; Hofmann, K.; Stoffel, W. Structure, expression, and functional analysis of a Na (+)-dependent glutamate/aspartate transporter from rat brain. *Proc. Natl. Acad. Sci. USA* **1992**, *89*, 10955-10959, doi:10.1073/pnas.89.22.10955.

34. Reimer, R.J.; Edwards, R.H. Organic anion transport is the primary function of the SLC17/type I phosphate transporter family. *Pflügers Archiv - European Journal of Physiology* **2004**, *447*, 629-635, doi:10.1007/s00424-003-1087-y.

35. Miyaji, T.; Echigo, N.; Hiasa, M.; Senoh, S.; Omote, H.; Moriyama, Y. Identification of a vesicular aspartate transporter. *Proc. Natl. Acad. Sci. USA* **2008**, *105*, 11720-11724, doi:10.1073/pnas.0804015105.

36. Morland, C.; Nordengen, K.; Larsson, M.; Prolo, L.M.; Farzampour, Z.; Reimer, R.J.; Gundersen, V. Vesicular uptake and exocytosis of L-aspartate is independent of sialin. *FASEB J.* **2013**, *27*, 1264-1274, doi:10.1096/fj.12-206300.

37. Richards, D.S.; Griffith, R.W.; Romer, S.H.; Alvarez, F.J. Motor axon synapses on renshaw cells contain higher levels of aspartate than glutamate. *PLoS ONE* **2014**, *9*, e97240-e97240, doi:10.1371/journal.pone.0097240.

38. D'Aniello, S.; Somorjai, I.; Garcia-Fernàndez, J.; Topo, E.; D'Aniello, A. D-Aspartic acid is a novel endogenous neurotransmitter. *FASEB J.* **2011**, *25*, 1014-1027, doi:10.1096/fj.10-168492.

39. Ota, N.; Shi, T.; Sweedler, J.V. D-Aspartate acts as a signaling molecule in nervous and neuroendocrine systems. *Amino Acids* **2012**, *43*, 1873-1886, doi:10.1007/s00726-012-1364-1.

40. D'Aniello, A.; Di Fiore, M.M.; Fisher, G.H.; Milone, A.; Seleni, A.; D'Aniello, S.; Perna, A.F.; Ingrosso, D. Occurrence of D-aspartic acid and N-methyl-D-aspartic acid in rat neuroendocrine tissues and their role in the modulation of luteinizing hormone and growth hormone release. *FASEB J.* **2000**, *14*, 699-714, doi:10.1096/fasebj.14.5.699.

41. Kim, P.M.; Duan, X.; Huang, A.S.; Liu, C.Y.; Ming, G.-l.; Song, H.; Snyder, S.H. Aspartate racemase, generating neuronal D-aspartate, regulates adult neurogenesis. *Proc. Natl. Acad. Sci. USA* **2010**, *107*, 3175-3179, doi:10.1073/pnas.0914706107.

42. Wolosker, H.; D'Aniello, A.; Snyder, S.H. D-aspartate disposition in neuronal and endocrine tissues: ontogeny, biosynthesis and release. *Neuroscience* **2000**, *100*, 183-189, doi:10.1016/S0306-4522(00)00321-3.

43. Sakai, K.; Homma, H.; Lee, J.-A.; Fukushima, T.; Santa, T.; Tashiro, K.; Iwatsubo, T.; Imai, K. Emergence of D-aspartic acid in the differentiating neurons of the rat central nervous system. *Brain Res.* **1998**, *808*, 65-71, doi:10.1016/S0006-8993(98)00599-X.

44. D'Aniello, G.; Tolino, A.; D'aniello, A.; Errico, F.; Fisher, G.H.; Di Fiore, M.M. The role of D-aspartic acid and N-methyl-D-aspartic acid in the regulation of prolactin release. *Endocrinology* **2000**, *141*, 3862-3870, doi:10.1210/endo.141.10.7706.

45. D'Aniello, A. D-Aspartic acid: an endogenous amino acid with an important neuroendocrine role. *Brain Res. Rev.* **2007**, *53*, 215-234, doi:10.1016/j.brainresrev.2006.08.005.

46. Errico, F.; Napolitano, F.; Nisticò, R.; Usiello, A. New insights on the role of free d-aspartate in the mammalian brain. *Amino Acids* **2012**, *43*, 1861-1871, doi:10.1007/s00726-012-1356-1.

47. Molinaro, G.; Pietracupa, S.; Di Menna, L.; Pescatori, L.; Usiello, A.; Battaglia, G.; Nicoletti, F.; Bruno, V. d-Aspartate activates mGlu receptors coupled to polyphosphoinositide hydrolysis in neonate rat brain slices. *Neurosci. Lett.* **2010**, *478*, 128-130, doi:10.1016/j.neulet.2010.04.077.

48. Ito, T.; Hayashida, M.; Kobayashi, S.; Muto, N.; Hayashi, A.; Yoshimura, T.; Mori, H. Serine racemase is involved in d-aspartate biosynthesis. *The Journal of Biochemistry* **2016**, *160*, 345-353, doi:10.1093/jb/mvw043.

49. Matsuda, S.; Katane, M.; Maeda, K.; Kaneko, Y.; Saitoh, Y.; Miyamoto, T.; Sekine, M.; Homma, H. Biosynthesis of d-aspartate in mammals: the rat and human homologs of mouse aspartate racemase are not responsible for the biosynthesis of d-aspartate. *Amino Acids* **2015**, *47*, 975-985, doi:10.1007/s00726-015-1926-0.

50. Tanaka-Hayashi, A.; Hayashi, S.; Inoue, R.; Ito, T.; Konno, K.; Yoshida, T.; Watanabe, M.; Yoshimura, T.; Mori, H. Is d-aspartate produced by glutamic-oxaloacetic transaminase-1 like 1 (Got1l1): a putative aspartate racemase? *Amino Acids* **2015**, *47*, 79-86, doi:10.1007/s00726-014-1847-3.

51. Albrecht, J.; Sidoryk-Wegrzynowicz, M.; Zielinska, M.; Aschner, M. Roles of glutamine in neurotransmission. *Neuron Glia Biol.* **2010**, *6*, 263-276, doi:10.1017/s1740925x11000093.

52. Horio, M.; Kohno, M.; Fujita, Y.; Ishima, T.; Inoue, R.; Mori, H.; Hashimoto, K. Levels of d-serine in the brain and peripheral organs of serine racemase (Srr) knock-out mice. *Neurochem. Int.* **2011**, *59*, 853-859, doi:10.1016/j.neuint.2011.08.017.

53. Kosenko, E.; Llansola, M.; Montoliu, C.; Monfort, P.; Rodrigo, R.; Hernandez-Viadel, M.; Erceg, S.; Sánchez-Perez, A.M.; Felipo, V. Glutamine synthetase activity and glutamine content in brain: modulation by NMDA receptors and nitric oxide. *Neurochem. Int.* **2003**, *43*, 493-499, doi:10.1016/S0197-0186(03)00039-1.

54. Eid, T.; Tu, N.; Lee, T.-S.W.; Lai, J.C.K. Regulation of astrocyte glutamine synthetase in epilepsy. *Neurochem. Int.* **2013**, *63*, 670-681, doi:10.1016/j.neuint.2013.06.008.

55. Rajkowska, G.; A. Stockmeier, C. Astrocyte pathology in major depressive disorder: Insights from human postmortem brain tissue. *Curr. Drug Targets* **2013**, *14*, 1225-1236, doi:10.2174/13894501113149990156.

56. Bernstein, H.-G.; Tausch, A.; Wagner, R.; Steiner, J.; Seeleke, P.; Walter, M.; Dobrowolny, H.; Bogerts, B. Disruption of glutamate-glutamine-GABA cycle significantly impacts on suicidal behaviour: survey of the literature and own findings on glutamine synthetase. *CNS Neurol. Disord. Drug Targets* **2013**, *12*, 900-913, doi:10.2174/18715273113129990091.

57. Skowrońska, M.; Albrecht, J. Oxidative and nitrosative stress in ammonia neurotoxicity. *Neurochem. Int.* **2013**, *62*, 731-737, doi:10.1016/j.neuint.2012.10.013.

58. Norenberg, M.D.; Rama Rao, K.V.; Jayakumar, A.R. Signaling factors in the mechanism of ammonia neurotoxicity. *Metab. Brain Dis.* **2009**, *24*, 103-117, doi:10.1007/s11011-008-9113-6.

59. Albrecht, J.; Norenberg, M.D. Glutamine: A Trojan horse in ammonia neurotoxicity. *Hepatology* **2006**, *44*, 788-794, doi:10.1002/hep.21357.

60. Albrecht, J.; Zielińska, M.; Norenberg, M.D. Glutamine as a mediator of ammonia neurotoxicity: A critical appraisal. *Biochem. Pharmacol.* **2010**, *80*, 1303-1308, doi:10.1016/j.bcp.2010.07.024.

61. Kolbaev, S.; Draguhn, A. Glutamine-induced membrane currents in cultured rat hippocampal neurons. *Eur. J. Neurosci.* **2008**, *28*, 535-545, doi:10.1111/j.1460-9568.2008.06365.x.

62. Luengo, J.G.; Muñoz, M.-D.; Álvarez-Merz, I.; Herranz, A.S.; González, J.C.; Martín del Río, R.; Hernández-Guijo, J.M.; Solís, J.M. Intracellular accumulation of amino acids

increases synaptic potentials in rat hippocampal slices. *Amino Acids* **2019**, *51*, 1337-1351, doi:10.1007/s00726-019-02771-w.

63. Dringen, R. Metabolism and functions of glutathione in brain. *Prog. Neurobiol.* **2000**, *62*, 649-671, doi:10.1016/S0301-0082(99)00060-X.

64. Dringen, R.; Gutterer, J.M.; Hirrlinger, J. Glutathione metabolism in brain: Metabolic interaction between astrocytes and neurons in the defense against reactive oxygen species. *Eur. J. Biochem.* **2000**, *267*, 4912-4916, doi:10.1046/j.1432-1327.2000.01597.x.

65. Dringen, R.; Hirrlinger, J. Glutathione pathways in the brain. *Biol. Chem.* **2003**, *384*, 505-516, doi:10.1515/bc.2003.059

66. Keller, H.J.; Do, K.Q.; Zollinger, M.; Winterhalter, K.H.; Cuenod, M. Cysteine - depolarization-induced release from rat brain in vitro. *J. Neurochem.* **1989**, *52*, 1801-1806, doi:10.1111/j.1471-4159.1989.tb07260.x.

67. Olney, J.W.; Zorumski, C.; Price, M.T.; Labruyere, J. L-Cysteine, a bicarbonate-sensitive endogenous excitotoxin. *Science* **1990**, *248*, 596-599, doi:10.1126/science.2185543.

68. Sagara, J.i.; Miura, K.; Bannai, S. Maintenance of neuronal glutathione by glial cells. *J. Neurochem.* **1993**, *61*, 1672-1676, doi:10.1111/j.1471-4159.1993.tb09802.x.

69. Janáky, R.; Varga, V.; Hermann, A.; Saransaari, P.; Oja, S.S. Mechanisms of L-cysteine neurotoxicity. *Neurochem. Res.* **2000**, *25*, 1397-1405, doi:10.1023/a:1007616817499.

70. Gonzalez, A.N.B.; Vicentini, F.; Calvo, D.J. Negative modulation of the GABA(A)rho 1 receptor function by L-cysteine. *J. Neurochem.* **2018**, *144*, 50-57, doi:10.1111/jnc.14237.

71. Peana, A.T.; Assaretti, A.R.; Muggironi, G.; Enrico, P.; Diana, M. Reduction of ethanol-derived acetaldehyde-induced motivational properties by L-cysteine. *Alcoholism-Clinical and Experimental Research* **2009**, *33*, 43-48, doi:10.1111/j.1530-0277.2008.00809.x.

72. Peana, A.T.; Muggironi, G.; Calvisi, G.; Enrico, P.; Mereu, M.; Nieddu, M.; Boatto, G.; Diana, M. L-Cysteine reduces oral ethanol self-administration and reinstatement of ethanol-drinking behavior in rats. *Pharmacol. Biochem. Behav.* **2010**, *94*, 431-437, doi:10.1016/j.pbb.2009.10.005.

73. Peana, A.T.; Muggironi, G.; Fois, G.R.; Zinellu, M.; Sirca, D.; Diana, M. Effect of L-cysteine on acetaldehyde self-administration. *Alcohol* **2012**, *46*, 489-497, doi:10.1016/j.alcohol.2011.10.004.

74. Sirca, D.; Enrico, P.; Mereu, M.; Peana, A.T.; Diana, M. L-cysteine prevents ethanol-induced stimulation of mesolimbic dopamine transmission. *Alcoholism - Clinical and Experimental Research* **2011**, *35*, 862-869, doi:10.1111/j.1530-0277.2010.01416.x.

75. Lewerenz, J.; Hewett, S.J.; Huang, Y.; Lambros, M.; Gout, P.W.; Kalivas, P.W.; Massie, A.; Smolders, I.; Methner, A.; Pergande, M., et al. The cystine/glutamate antiporter system x(c)(-) in health and disease: from molecular mechanisms to novel therapeutic opportunities. *Antioxidants & Redox Signaling* **2013**, *18*, 522-555, doi:10.1089/ars.2011.4391.

76. Soria, F.N.; Pérez-Samartín, A.; Martin, A.; Gona, K.B.; Llop, J.; Szczupak, B.; Chara, J.C.; Matute, C.; Domercq, M. Extrasynaptic glutamate release through cystine/glutamate antiporter contributes to ischemic damage. *The Journal of Clinical Investigation* **2014**, *124*, 3645-3655, doi:10.1172/JCI71886.

77. McBean, G. Sulfur-containing amino acids. In *Handbook of Neurochemistry and Molecular Neurobiology: Amino Acids and Peptides in the Nervous System*, Springer, Berlin, Heidelberg: 2007; 10.1007/978-0-387-30411-3pp. 133-154.

78. Qu, K.; Lee, S.; Bian, J.; Low, C.-M.; Wong, P.-H. Hydrogen sulfide: neurochemistry and neurobiology. *Neurochem. Int.* **2008**, *52*, 155-165, doi:10.1016/j.neuint.2007.05.016.

79. Zhang, X.; Bian, J.-S. Hydrogen sulfide: A neuromodulator and neuroprotectant in the central nervous system. *ACS Chem. Neurosci.* **2014**, *5*, 876-883, doi:10.1021/cn500185g.

80. Hawkins, R.A.; O'Kane, R.L.; Simpson, I.A.; Vina, J.R. Structure of the blood–brain barrier and its role in the transport of amino acids. *J. Nutr.* **2006**, *136*, 218S-226S, doi:10.1093/jn/136.1.218S.

81. Bröer, A.; Tietze, N.; Kowalczuk, S.; Chubb, S.; Munzinger, M.; Bak, L.K.; Bröer, S. The orphan transporter v7-3 (slc6a15) is a Na+-dependent neutral amino acid transporter (B(0)AT2). *Biochem. J.* **2006**, *393*, 421-430, doi:10.1042/bj20051273.

82. Lipton, S.A.; Kim, W.-K.; Choi, Y.-B.; Kumar, S.; D'Emilia, D.M.; Rayudu, P.V.; Arnelle, D.R.; Stamler, J.S. Neurotoxicity associated with dual actions of homocysteine at the N-methyl-D-aspartate receptor. *Proc. Natl. Acad. Sci. USA* **1997**, *94*, 5923-5928, doi:10.1073/pnas.94.11.5923.

83. Poddar, R.; Paul, S. Homocysteine-NMDA receptor-mediated activation of extracellular signal-regulated kinase leads to neuronal cell death. *J. Neurochem.* **2009**, *110*, 1095-1106, doi:10.1111/j.1471-4159.2009.06207.x.

84. Brosnan, J.T.; Brosnan, M.E. The sulfur-containing amino acids: an overview. *J. Nutr.* **2006**, *136*, 1636S-1640S, doi:10.1093/jn/136.6.1636S.

85. Ganguly, P.K.; Maddaford, T.G.; Edel, A.L.; Karmin, O.; Smeda, J.S.; Pierce, G.N. Increased homocysteine-induced release of excitatory amino acids in the striatum of spontaneously hypertensive stroke-prone rats. *Brain Res.* **2008**, *1226*, 192-198, doi:10.1016/j.brainres.2008.05.090.

86. Hrncic, D.; Mikić, J.; Rasic-Markovic, A.; Velimirović, M.; Stojković, T.; Obrenović, R.; Rankov-Petrović, B.; Šušić, V.; Djuric, D.; Petronijević, N., et al. Anxiety-related behavior in hyperhomocysteinemia induced by methionine nutritional overload in rats: role of the brain oxidative stress. *Can. J. Physiol. Pharmacol.* **2016**, *94*, 1074-1082, doi:10.1139/cjpp-2015-0581.

87. Bleich, S.; Spilker, K.; Kurth, C.; Degner, D.; Quintela-Schneider, M.; Javaheripour, K.; Rüther, E.; Kornhuber, J.; Wiltfang, J. Oxidative stress and an altered methionine metabolism in alcoholism. *Neurosci. Lett.* **2000**, *293*, 171-174, doi:10.1016/S0304-3940(00)01505-6.

88. Ho, P.I.; Collins, S.C.; Dhitavat, S.; Ortiz, D.; Ashline, D.; Rogers, E.; Shea, T.B. Homocysteine potentiates β-amyloid neurotoxicity: role of oxidative stress. *J. Neurochem.* **2001**, *78*, 249-253, doi:10.1046/j.1471-4159.2001.00384.x.

89. Susser, E.; Brown, A.S.; Klonowski, E.; Allen, R.H.; Lindenbaum, J. Schizophrenia and impaired homocysteine metabolism: a possible association. *Biol. Psychiatry* **1998**, *44*, 141-143, doi:10.1016/S0006-3223(97)00427-7.

90. Johnson, J.L.; Roberts, E. Proline, glutamate and glutamine metabolism in mouse brain synaptosomes. *Brain Res.* **1984**, *323*, 247-256, doi:10.1016/0006-8993(84)90295-6.

91. Clelland, C.L.; Read, L.L.; Baraldi, A.N.; Bart, C.P.; Pappas, C.A.; Panek, L.J.; Nadrich, R.H.; Clelland, J.D. Evidence for association of hyperprolinemia with schizophrenia and a measure of clinical outcome. *Schizophr. Res.* **2011**, *131*, 139-145, doi:10.1016/j.schres.2011.05.006.

92. Roussos, P.; Giakoumaki, S.G.; Bitsios, P. A risk PRODH haplotype affects sensorimotor gating, memory, schizotypy, and anxiety in healthy male subjects. *Biol. Psychiatry* **2009**, *65*, 1063-1070, doi:10.1016/j.biopsych.2009.01.003.

93. Paterlini, M.; Zakharenko, S.S.; Lai, W.-S.; Qin, J.; Zhang, H.; Mukai, J.; Westphal, K.G.; Olivier, B.; Sulzer, D.; Pavlidis, P. Transcriptional and behavioral interaction between 22q11. 2 orthologs modulates schizophrenia-related phenotypes in mice. *Nat. Neurosci.* **2005**, *8*, 1586-1594, doi:10.1038/nn1562.

94. Takemoto, Y.; Semba, R. Immunohistochemical evidence for the localization of neurons containing the putative transmitter L-proline in rat brain. *Brain Res.* **2006**, *1073*, 311-315, doi:10.1016/j.brainres.2005.12.064.

95. Mulder, A.H.; Snyder, S.H. Potassium-induced release of amino acids from cerebral cortex and spinal cord slices of the rat. *Brain Res.* **1974**, *76*, 297-308, doi:10.1016/0006-8993(74)90461-2.

96. Nickolson, V.J. "On" and "Off" Responses of K+-Induced Synaptosomal Proline Release: Involvement of the Sodium Pump. *J. Neurochem.* **1982**, *38*, 289-292, doi:10.1111/j.1471-4159.1982.tb10885.x.

97. Parra, L.A.; Baust, T.; El Mestikawy, S.; Quiroz, M.; Hoffman, B.; Haflett, J.M.; Yao, J.K.; Torres, G.E. The orphan transporter Rxt1/NTT4 (SLC6A17) functions as a synaptic vesicle amino acid transporter selective for proline, glycine, leucine, and alanine. *Mol. Pharmacol.* **2008**, *74*, 1521-1532, doi:10.1124/mol.108.050005.

98. Henzi, V.; Reichling, D.B.; Helm, S.W.; Macdermott, A.B. L-Proline activates glutamate and glycine receptors in cultured rat dorsal horn neurons. *Mol. Pharmacol.* **1992**, *41*, 793-801.

99. Crump, F.T.; Fremeau, R.T.; Craig, A.M. Localization of the brain-specific high-affinity L-proline transporter in cultured hippocampal neurons: Molecular heterogeneity of synaptic terminals. *Mol. Cell. Neurosci.* **1999**, *13*, 25-39, doi:10.1006/mcne.1998.0727.

100. Renick, S.E.; Kleven, D.T.; Chan, J.; Stenius, K.; Milner, T.A.; Pickel, V.M.; Fremeau, R.T. The mammalian brain high-affinity L-proline transporter is enriched preferentially in synaptic vesicles in a subpopulation of excitatory nerve terminals in rat forebrain. *J. Neurosci.* **1999**, *19*, 21-33, doi:10.1523/jneurosci.19-01-00021.1999.

101. Cohen, S.M.; Nadler, J.V. Proline-induced inhibition of glutamate release in hippocampal area CA1. *Brain Res.* **1997**, *769*, 333-339, doi:10.1016/S0006-8993(97)00721-X.

102. Cohen, S.M.; Nadler, J.V. Proline-induced potentiation of glutamate transmission. *Brain Res.* **1997**, *761*, 271-282, doi:10.1016/S0006-8993(97)00352-1.

103. Nadler, J.V.; Wang, A.; Hakim, A. Toxicity of L-proline toward rat hippocampal neurons. *Brain Res.* **1988**, *456*, 168-172, doi:10.1016/0006-8993(88)90358-7.

104. Hamasu, K.; Shigemi, K.; Tsuneyoshi, Y.; Yamane, H.; Sato, H.; Denbow, D.M.; Furuse, M. Intracerebroventricular injection of L-proline and D-proline induces sedative and hypnotic effects by different mechanisms under an acute stressful condition in chicks. *Amino Acids* **2010**, *38*, 57-64, doi:10.1007/s00726-008-0204-9.

105. Hamasu, K.; Shigemi, K.; Kabuki, Y.; Tomonaga, S.; Denbow, D.M.; Furuse, M. Central L-proline attenuates stress-induced dopamine and serotonin metabolism in the chick forebrain. *Neurosci. Lett.* **2009**, *460*, 78-81, doi:10.1016/j.neulet.2009.05.036.

106. Kandasamy, P.; Gyimesi, G.; Kanai, Y.; Hediger, M.A. Amino acid transporters revisited: New views in health and disease. *Trends Biochem. Sci.* **2018**, *43*, 752-789, doi:10.1016/j.tibs.2018.05.003.

107. Fremeau, R.T.; Caron, M.G.; Blakely, R.D. Molecular cloning and expression of a high-affinity L-proline transporter expressed in putative glutamatergic pathways of rat brain. *Neuron* **1992**, *8*, 915-926, doi:10.1016/0896-6273(92)90206-s.

108. Fremeau, R.T.; Velaz-Faircloth, M.; Miller, J.W.; Henzi, V.A.; Cohen, S.M.; Nadler, J.V.; Shafqat, S.; Blakely, R.D.; Domin, B. A novel nonopioid action of enkephalins: competitive inhibition of the mammalian brain high affinity L-proline transporter. *Mol. Pharmacol.* **1996**, *49*, 1033-1041.

109. Velaz-Faircloth, M.; Guadanoferraz, A.; Henzi, V.A.; Fremeau, R.T. Mammalian brain-specific L-proline transporter. *J. Biol. Chem.* **1995**, *270*, 15755-15761, doi:10.1074/jbc.270.26.15755.

110. Schulz, D.; Morschel, J.; Schuster, S.; Eulenburg, V.; Gomeza, J. Inactivation of the mouse L-proline transporter PROT alters glutamatergic synapse biochemistry and perturbs behaviors required to respond to environmental changes. *Front. Mol. Neurosci.* **2018**, *11*, 279, doi:10.3389/fnmol.2018.00279.

111. O'Brien, R.J.; Kamboj, S.; Ehlers, M.D.; Rosen, K.R.; Fischbach, G.D.; Huganir, R.L. Activity-dependent modulation of synaptic AMPA receptor accumulation. *Neuron* **1998**, *21*, 1067-1078, doi:10.1016/S0896-6273(00)80624-8.

112. Zalcman, G.; Federman, N.; Romano, A. CaMKII isoforms in learning and memory: Localization and function. *Front. Mol. Neurosci.* **2018**, *11*, doi:10.3389/fnmol.2018.00445.

113. Delwing, D.; Bavaresco, C.S.; Wannmacher, C.M.; Wajner, M.; Dutra-Filho, C.S.; Wyse, A.T. Proline induces oxidative stress in cerebral cortex of rats. *Int. J. Dev. Neurosci.* **2003**, *21*, 105-110, doi:10.1016/S0736-5748(02)00109-0.

114. Delwing, D.; Chiarani, F.; Delwing, D.; Bavaresco, C.S.; Wannmacher, C.M.; Wajner, M.; Wyse, A.T. Proline reduces acetylcholinesterase activity in cerebral cortex of rats. *Metab. Brain Dis.* **2003**, *18*, 79-86, doi:10.1023/A:1021934803724.

115. Franzon, R.; Lamers, M.L.; Stefanello, F.M.; Wannmacher, C.M.; Wajner, M.; Wyse, A.T. Evidence that oxidative stress is involved in the inhibitory effect of proline on Na+, K+-ATPase activity in synaptic plasma membrane of rat hippocampus. *Int. J. Dev. Neurosci.* **2003**, *21*, 303-307, doi:10.1016/S0736-5748(03)00076-5.

116. Dieterich, D.C.; Landwehr, M.; Reissner, C.; Smalla, K.-H.; Richter, K.; Wolf, G.; Böckers, T.M.; Gundelfinger, E.D.; Kreutz, M.R. Gliap − a novel untypical l-asparaginase localized to rat brain astrocytes. *J. Neurochem.* **2003**, *85*, 1117-1125, doi:10.1046/j.1471-4159.2003.01766.x.

117. Ruzzo, E.K.; Capo-Chichi, J.-M.; Ben-Zeev, B.; Chitayat, D.; Mao, H.; Pappas, A.L.; Hitomi, Y.; Lu, Y.-F.; Yao, X.; Hamdan, F.F., et al. Deficiency of asparagine synthetase causes congenital microcephaly and a progressive form of encephalopathy. *Neuron* **2013**, *80*, 429-441, doi:10.1016/j.neuron.2013.08.013.

118. Palmer, E.E.; Hayner, J.; Sachdev, R.; Cardamone, M.; Kandula, T.; Morris, P.; Dias, K.-R.; Tao, J.; Miller, D.; Zhu, Y. Asparagine synthetase deficiency causes reduced proliferation of cells under conditions of limited asparagine. *Mol. Genet. Metab.* **2015**, *116*, 178-186, doi:10.1016/j.ymgme.2015.08.007.

119. Butterworth, R.F.; Landreville, F.; Hamel, E.; Merkel, A.; Giguere, F.; Barbeau, A. Effect of asparagine, glutamine and insulin on cerebral amino acid neurotransmitters. *Can. J. Neurol. Sci.* **1980**, *7*, 447-450, doi:10.1017/S0317167100023040.

120. Li, Y.; Sun, H.; Chen, Z.; Xu, H.; Bu, G.; Zheng, H. Implications of GABAergic neurotransmission in Alzheimer's disease. *Frontiers in Aging Neuroscience* **2016**, *8*, 31, doi:10.3389/fnagi.2016.00031.

121. Li, K.; Xu, E. The role and the mechanism of gamma-aminobutyric acid during central nervous system development. *Neurosci. Bull.* **2008**, *24*, 195-200, doi:10.1007/s12264-008-0109-3.

122. Ting Wong, C.G.; Bottiglieri, T.; Snead III, O.C. GABA, γ-hydroxybutyric acid, and neurological disease. *Ann. Neurol.* **2003**, *54*, S3-S12, doi:10.1002/ana.10696.

123. Garret, M.; Du, Z.; Chazalon, M.; Cho, Y.H.; Baufreton, J. Alteration of GABAergic neurotransmission in Huntington's disease. *CNS Neurosci. Ther.* **2018**, *24*, 292-300, doi:10.1111/cns.12826.

124. Hallen, A.; Jamie, J.F.; Cooper, A.J.L. Lysine metabolism in mammalian brain: an update on the importance of recent discoveries. *Amino Acids* **2013**, *45*, 1249-1272, doi:10.1007/s00726-013-1590-1.

125. Posset, R.; Opp, S.; Struys, E.A.; Völkl, A.; Mohr, H.; Hoffmann, G.F.; Kölker, S.; Sauer, S.W.; Okun, J.G. Understanding cerebral L-lysine metabolism: the role of L-pipecolate metabolism in Gcdh-deficient mice as a model for glutaric aciduria type I. *J. Inherited Metab. Dis.* **2015**, *38*, 265-272, doi:10.1007/s10545-014-9762-z.

126. Papes, F.; Surpili, M.J.; Langone, F.; Trigo, J.R.; Arruda, P. The essential amino acid lysine acts as precursor of glutamate in the mammalian central nervous system. *The FEBS Letters* **2001**, *488*, 34-38, doi:10.1016/S0014-5793(00)02401-7.

127. Struys, E.A.; Jansen, E.E.W.; Salomons, G.S. Human pyrroline-5-carboxylate reductase (PYCR1) acts on Δ1-piperideine-6-carboxylate generating L-pipecolic acid. *J. Inherited Metab. Dis.* **2014**, *37*, 327-332, doi:10.1007/s10545-013-9673-4.

128. Struys, E.A.; Jakobs, C. Metabolism of lysine in α-aminoadipic semialdehyde dehydrogenase-deficient fibroblasts: Evidence for an alternative pathway of pipecolic acid formation. *FEBS Lett.* **2010**, *584*, 181-186, doi:10.1016/j.febslet.2009.11.055.

129. Pena, I.A.; Marques, L.A.; Laranjeira, Â.B.; Yunes, J.A.; Eberlin, M.N.; MacKenzie, A.; Arruda, P. Mouse lysine catabolism to aminoadipate occurs primarily through the saccharopine pathway; implications for pyridoxine dependent epilepsy (PDE). *Biochim. Biophys. Acta* **2017**, *1863*, 121-128, doi:10.1016/j.bbadis.2016.09.006.

130. Crowther, L.M.; Mathis, D.; Poms, M.; Plecko, B. New insights into human lysine degradation pathways with relevance to pyridoxine-dependent epilepsy due to antiquitin deficiency. *J. Inherited Metab. Dis.* **2019**, *42*, 620-628, doi:10.1002/jimd.12076.

131. Chang, Y.-F.; Myslinski, N.R. Effects of L-lysine and its metabolites on pentylenetetrazol-induced seizures. *Neurosci. Lett.* **1985**, *59*, 79-84, doi:10.1016/0304-3940(85)90218-6.

132. Gao, X.-M.; Chang, Y.-F. Enhancement of benzodiazepine receptor binding by L-lysine is chloride-dependent and due to increase in binding affinity. *Eur. J. Pharmacol.* **1989**, *173*, 197-200, doi:10.1016/0014-2999(89)90520-7.

133. Chang, Y.-F.; Gao, X.-M. L-lysine is a barbiturate-like anticonvulsant and modulator of the benzodiazepine receptor. *Neurochem. Res.* **1995**, *20*, 931-937, doi:10.1007/BF00970739.

134. Chang, Y.F.; Wang, Y.; Cauley, R.K.; Gao, X.M. Chronic L-lysine develops anti-pentylenetetrazol tolerance and reduces synaptic GABAergic sensitivity. *Eur. J. Biochem.* **1993**, *233*, 209-217, doi:10.1016/0014-2999(93)90052-j.

135. Ebrahimi, H.A.; Ebrahimi, S. Evaluation of the effects of charged amino acids on uncontrolled seizures. *Neurol. Res. Int.* **2015**, *2015*, doi:10.1155/2015/124507.

136. Smriga, M.; Torii, K. Prolonged treatment with l-lysine and l-arginine reduces stress-induced anxiety in an elevated plus maze. *Nutr. Neurosci.* **2003**, *6*, 125-128, doi:10.1080/1028415031000079685.

137. Smriga, M.; Torii, K. L-Lysine acts like a partial serotonin receptor 4 antagonist and inhibits serotonin-mediated intestinal pathologies and anxiety in rats. *Proc. Natl. Acad. Sci. USA* **2003**, *100*, 15370-15375, doi:10.1073/pnas.2436556100.

138. Clemmensen, C.; Smajilovic, S.; Wellendorph, P.; Bräuner-Osborne, H. The GPCR, class C, group 6, subtype A (GPRC6A) receptor: From cloning to physiological function. *Br. J. Pharmacol.* **2014**, *171*, 1129-1141, doi:10.1111/bph.12365.

139. Kondoh, T.; Kameishi, M.; Mallick, H.; Ono, T.; Torii, K. Lysine and arginine reduce the effects of cerebral ischemic insults and inhibit glutamate-induced neuronal activity in rats. *Frontiers in Integrative Neuroscience* **2010**, *4*, doi:10.3389/fnint.2010.00018.

140. Severyanova, L.A.; Lazarenko, V.A.; Plotnikov, D.V.; Dolgintsev, M.E.; Kriukov, A.A. L-Lysine as the molecule influencing selective brain activity in pain-induced behavior of rats. *Int. J. Mol. Sci.* **2019**, *20*, 1899, doi:10.3390/ijms20081899.

141. Bae, S.; Xu, Q.; Hutchinson, D.; Colton, C. Y+ and y+ L arginine transporters in neuronal cells expressing tyrosine hydroxylase. *Biochim. Biophys. Acta* **2005**, *1745*, 65-73, doi:10.1016/j.bbamcr.2004.12.006.

142. Whitfield, J.H.; Zhang, W.H.; Herde, M.K.; Clifton, B.E.; Radziejewski, J.; Janovjak, H.; Henneberger, C.; Jackson, C.J. Construction of a robust and sensitive arginine biosensor through ancestral protein reconstruction. *Protein Sci.* **2015**, *24*, 1412-1422, doi:10.1002/pro.2721.

143. Wiesinger, H. Arginine, citrulline, and ornithine. In *Handbook of Neurochemistry and Molecular Neurobiology: Amino Acids and Peptides in the Nervous System*, Lajtha, A., Oja, S.S., Schousboe, A., Saransaari, P., Eds. Springer US: Boston, MA, 2007; 10.1007/978-0-387-30373-4_5pp. 99-115.

144. Wiesinger, H. Arginine metabolism and the synthesis of nitric oxide in the nervous system. *Prog. Neurobiol.* **2001**, *64*, 365-391, doi:10.1016/S0301-0082(00)00056-3.

145. Contestabile, A. Roles of NMDA receptor activity and nitric oxide production in brain development. *Brain Res. Rev.* **2000**, *32*, 476-509, doi:10.1016/S0165-0173(00)00018-7.

146. Cherian, L.; Hlatky, R.; Robertson, C.S. Nitric oxide in traumatic brain injury. *Brain Pathol.* **2004**, *14*, 195-201, doi:10.1177/1073858403261226.

147. Myslivecˇek, J.; Hassmannová, J.; Barcal, J.; Sˇafanda, J.; Zˇalud, V. Inhibitory learning and memory in newborn rats influenced by nitric oxide. *Neuroscience* **1996**, *71*, 299-312, doi:10.1016/0306-4522(95)00503-X.

148. Susswein, A.J.; Katzoff, A.; Miller, N.; Hurwitz, I. Nitric oxide and memory. *Neuroscientist* **2004**, *10*, 153-162, doi:10.1177/1073858403261226.

149. Kumar, A.; Chanana, P. Role of nitric oxide in stress-induced anxiety: From pathophysiology to therapeutic target. *Vitam. Horm.* **2017**, *103*, 147-167, doi:10.1016/bs.vh.2016.09.004.

150. Suenaga, R.; Yamane, H.; Tomonaga, S.; Asechi, M.; Adachi, N.; Tsuneyoshi, Y.; Kurauchi, I.; Sato, H.; Denbow, D.M.; Furuse, M. Central L-arginine reduced stress responses are mediated by L-ornithine in neonatal chicks. *Amino Acids* **2008**, *35*, 107-113, doi:10.1007/s00726-007-0617-x.

151. Kurata, K.; Nagasawa, M.; Tomonaga, S.; Aoki, M.; Morishita, K.; Denbow, D.M.; Furuse, M. Orally administered L-ornithine elevates brain L-ornithine levels and has an anxiolytic-like effect in mice. *Nutr. Neurosci.* **2011**, *14*, 243-248, doi:10.1179/1476830511Y.0000000018.

152. Miyake, M.; Kirisako, T.; Kokubo, T.; Miura, Y.; Morishita, K.; Okamura, H.; Tsuda, A. Randomised controlled trial of the effects of L-ornithine on stress markers and sleep quality in healthy workers. *Nutr. J.* **2014**, *13*, 53, doi:10.1186/1475-2891-13-53.

153. Schulze, A. Creatine deficiency syndromes. In *Guanidino Compounds in Biology and Medicine*, Springer: 2003; 10.1007/978-1-4615-0247-0pp. 143-150.

154. de Koning, T.J.; Fuchs, S.A.; Klomp, L.W.J. Serine, glycine, and threonine. In *Handbook of Neurochemistry and Molecular Neurobiology: Amino Acids and Peptides in the Nervous System*, Lajtha, A., Oja, S.S., Schousboe, A., Saransaari, P., Eds. Springer US: Boston, MA, 2007; 10.1007/978-0-387-30373-4_2pp. 23-45.

155. Curtis, D.; Hösli, L.; Johnston, G. Inhibition of spinal neurones by glycine. *Nature* **1967**, *215*, 1502-1503, doi:10.1038/2151502a0.

156. Zafra, F.; Aragon, C.; Olivares, L.; Danbolt, N.C.; Gimenez, C.; Storm-Mathisen, J. Glycine transporters are differentially expressed among CNS cells. *J. Neurosci.* **1995**, *15*, 3952-3969, doi:10.1523/jneurosci.15-05-03952.1995.

157. Dutertre, S.; Becker, C.-M.; Betz, H. Inhibitory glycine receptors: an update. *J. Biol. Chem.* **2012**, *287*, 40216-40223, doi:10.1074/jbc.R112.408229.

158. Jonas, P.; Bischofberger, J.; Sandkühler, J. Corelease of two fast neurotransmitters at a central synapse. *Science* **1998**, *281*, 419-424, doi:10.1126/science.281.5375.419.

159. Aubrey, K.R.; Supplisson, S. Heterogeneous signaling at GABA and glycine co-releasing terminals. *Front. Synaptic Neurosci.* **2018**, *10*, 40-40, doi:10.3389/fnsyn.2018.00040.

160. Russier, M.; Kopysova, I.L.; Ankri, N.; Ferrand, N.; Debanne, D. GABA and glycine co-release optimizes functional inhibition in rat brainstem motoneurons in vitro. *The Journal of Physiology* **2002**, *541*, 123-137, doi:10.1113/jphysiol.2001.016063.

161. Apostolides, P.F.; Trussell, L.O. Rapid, activity-independent turnover of vesicular transmitter content at a mixed glycine/GABA synapse. *J. Neurosci.* **2013**, *33*, 4768-4781, doi:10.1523/jneurosci.5555-12.2013.

162. López-Corcuera, B.; Geerlings, A.; Aragón, C. Glycine neurotransmitter transporters: an update. *Mol. Membr. Biol.* **2001**, *18*, 13-20, doi:10.1080/09687680010028762.

163. Harsing Jr, L.G.; Matyus, P. Mechanisms of glycine release, which build up synaptic and extrasynaptic glycine levels: The role of synaptic and non-synaptic glycine transporters. *Brain Res. Bull.* **2013**, *93*, 110-119, doi:10.1016/j.brainresbull.2012.12.002.

164. Miraucourt, L.S.; Dallel, R.; Voisin, D.L. Glycine inhibitory dysfunction turns touch into pain through PKCgamma interneurons. *PLoS ONE* **2007**, *2*, doi:10.1371/journal.pone.0001116.

165. Rajendra, S.; Lynch, J.W.; Schofield, P.R. The glycine receptor. *Pharmacol. Ther.* **1997**, *73*, 121-146, doi:10.1016/S0163-7258(96)00163-5.

166. Lynch, J.W. Native glycine receptor subtypes and their physiological roles. *Neuropharmacology* **2009**, *56*, 303-309, doi:10.1016/j.neuropharm.2008.07.034.

167. Avila, A.; Nguyen, L.; Rigo, J.-M. Glycine receptors and brain development. *Front. Cell Neurosci.* **2013**, *7*, 184, doi:10.3389/fncel.2013.00184.

168. Flint, A.C.; Liu, X.; Kriegstein, A.R. Nonsynaptic glycine receptor activation during early neocortical development. *Neuron* **1998**, *20*, 43-53, doi:10.1016/S0896-6273(00)80433-X.

169. Avila, A.; Vidal, P.M.; Dear, T.N.; Harvey, R.J.; Rigo, J.-M.; Nguyen, L. Glycine receptor α2 subunit activation promotes cortical interneuron migration. *Cell Rep.* **2013**, *4*, 738-750, doi:10.1016/j.celrep.2013.07.016.

170. Papouin, T.; Ladépêche, L.; Ruel, J.; Sacchi, S.; Labasque, M.; Hanini, M.; Groc, L.; Pollegioni, L.; Mothet, J.-P.; Oliet, Stéphane H.R. Synaptic and extrasynaptic NMDA receptors are gated by different endogenous coagonists. *Cell* **2012**, *150*, 633-646, doi:10.1016/j.cell.2012.06.029.

171. Ahmadi, S.; Muth-Selbach, U.; Lauterbach, A.; Lipfert, P.; Neuhuber, W.L.; Zeilhofer, H.U. Facilitation of spinal NMDA receptor currents by spillover of synaptically released glycine. *Science* **2003**, *300*, 2094-2097, doi:10.1126/science.1083970.

172. Jaeken, J.; Detheux, M.; Fryns, J.P.; Collet, J.F.; Alliet, P.; Van Schaftingen, E. Phosphoserine phosphatase deficiency in a patient with Williams syndrome. *J. Med. Genet.* **1997**, *34*, 594-596, doi:10.1136/jmg.34.7.594.

173. Tabatabaie, L.; Klomp, L.; Berger, R.; De Koning, T. L-serine synthesis in the central nervous system: a review on serine deficiency disorders. *Mol. Genet. Metab.* **2010**, *99*, 256-262, doi:10.1016/j.ymgme.2009.10.012.

174. Quackenbush, E.J.; Kraemer, K.H.; Gahl, W.A.; Schirch, V.; Whiteman, D.A.; Levine, K.; Levy, H.L. Hypoglycinaemia and psychomotor delay in a child with xeroderma pigmentosum. *J. Inherited Metab. Dis.* **1999**, *22*, 915-924, doi:10.1023/a:1005691424004.

175. Buratta, S.; Hamberger, A.; Ryberg, H.; Nyström, B.; Sandberg, M.; Mozzi, R. Effect of serine and ethanolamine administration on phospholipid-related compounds and neurotransmitter amino acids in the rabbit hippocampus. *J. Neurochem.* **1998**, *71*, 2145-2150, doi:10.1046/j.1471-4159.1998.71052145.x.

176. Furuya, S.; Tabata, T.; Mitoma, J.; Yamada, K.; Yamasaki, M.; Makino, A.; Yamamoto, T.; Watanabe, M.; Kano, M.; Hirabayashi, Y. L-Serine and glycine serve as major astroglia-derived trophic factors for cerebellar Purkinje neurons. *Proc. Natl. Acad. Sci. USA* **2000**, *97*, 11528-11533, doi:10.1073/pnas.200364497.

177. Mitoma, J.; Furuya, S.; Hirabayashi, Y. A novel metabolic communication between neurons and astrocytes: non-essential amino acid l-serine released from astrocytes is essential for developing hippocampal neurons. *Neurosci. Res.* **1998**, *30*, 195-199, doi:10.1016/S0168-0102(97)00113-2.

178. De Miranda, J.; Santoro, A.; Engelender, S.; Wolosker, H. Human serine racemase: moleular cloning, genomic organization and functional analysis. *Gene* **2000**, *256*, 183-188, doi:10.1016/S0378-1119(00)00356-5.

179. Wolosker, H.; Blackshaw, S.; Snyder, S.H. Serine racemase: a glial enzyme synthesizing D-serine to regulate glutamate-N-methyl-D-aspartate neurotransmission. *Proc. Natl. Acad. Sci. USA* **1999**, *96*, 13409-13414, doi:10.1073/pnas.96.23.13409.

180. Miya, K.; Inoue, R.; Takata, Y.; Abe, M.; Natsume, R.; Sakimura, K.; Hongou, K.; Miyawaki, T.; Mori, H. Serine racemase is predominantly localized in neurons in mouse brain. *J. Comp. Neurol.* **2008**, *510*, 641-654, doi:10.1002/cne.21822.

181. Kartvelishvily, E.; Shleper, M.; Balan, L.; Dumin, E.; Wolosker, H. Neuron-derived D-serine release provides a novel means to activate N-methyl-D-aspartate receptors. *J. Biol. Chem.* **2006**, *281*, 14151-14162, doi:10.1074/jbc.M512927200.

182. Mustafa, A.K.; Kim, P.M.; Snyder, S.H. D-Serine as a putative glial neurotransmitter. *Neuron Glia Biol.* **2004**, *1*, 275-281, doi:10.1017/S1740925X05000141.

183. Van Horn, M.R.; Sild, M.; Ruthazer, E.S. D-serine as a gliotransmitter and its roles in brain development and disease. *Front. Cell Neurosci.* **2013**, *7*, 39, doi:10.3389/fncel.2013.00039.

184. Lin, C.H.; Yang, H.T.; Lane, H.Y. D-Glutamate, D-serine, and D-alanine differ in their roles in cognitive decline in patients with Alzheimer's disease or mild cognitive impairment. *Pharmacol. Biochem. Behav.* **2019**, *185*, doi:10.1016/j.pbb.2019.172760.

185. Wegner, S.A.; Hu, B.; De Oliveira Sergio, T.; Darevsky, D.; Kwok, C.C.-Y.; Lei, K.; Hopf, F.W. A novel NMDA receptor-based intervention to suppress compulsion-like alcohol drinking. *Neuropharmacology* **2019**, *157*, 107681, doi:10.1016/j.neuropharm.2019.107681.

186. Wolosker, H. D-serine regulation of NMDA receptor activity. *Sci. STKE* **2006**, *2006*, pe41-pe41, doi:10.1126/stke.3562006pe41.

187. Morikawa, A.; Hamase, K.; Zaitsu, K. Determination of D-alanine in the rat central nervous system and periphery using column-switching high-performance liquid chromatography. *Anal. Biochem.* **2003**, *312*, 66-72, doi:10.1016/S0003-2697(02)00432-3.

188. Konno, R.; Niwa, A.; Yasumura, Y. Intestinal bacterial origin of D-alanine in urine of mutant mice lacking D-amino-acid oxidase. *Biochem. J.* **1990**, *268*, 263, doi:10.1042/bj2680263.

189. Mehdi, S. Antibiotic-induced psychosis: A link to D-alanine? *Med. Hypotheses* **2010**, *75*, 676-677, doi:10.1016/j.mehy.2010.07.021.

190. Oldendorf, W.H. Stereospecificity of blood-brain barrier permeability to amino acids. *American Journal of Physiology - Legacy Content* **1973**, *224*, 967-969, doi:10.1152/ajplegacy.1973.224.4.967.

191. Hashimoto, A.; Nishikawa, T.; Konno, R.; Niwa, A.; Yasumura, Y.; Oka, T.; Takahashi, K. Free D-serine, D-aspartate and D-alanine in central nervous system and serum in mutant mice lacking D-amino acid oxidase. *Neurosci. Lett.* **1993**, *152*, 33-36, doi:10.1016/0304-3940(93)90476-2.

192. Iversen, S.D.; Wilkinson, S.; Simpson, B. Enhanced amphetamine responses after frontal cortex lesions in the rat. *Eur. J. Pharmacol.* **1971**, *13*, 387-390, doi:10.1016/0014-2999(71)90231-7.

193. Atsushi, H.; Toru, N.; Takae, O.; Kiyohisa, T. D-Alanine inhibits methamphetamine-induced hyperactivity in rats. *Eur. J. Pharmacol.* **1991**, *202*, 105-107, doi:10.1016/0014-2999(91)90261-N.

194. Leriche, L.; Schwartz, J.-C.; Sokoloff, P. The dopamine D3 receptor mediates locomotor hyperactivity induced by NMDA receptor blockade. *Neuropharmacology* **2003**, *45*, 174-181, doi:10.1016/S0028-3908(03)00145-X.

195. Jones, C.A.; Watson, D.J.G.; Fone, K.C.F. Animal models of schizophrenia. *Br. J. Pharmacol.* **2011**, *164*, 1162-1194, doi:10.1111/j.1476-5381.2011.01386.x.

196. Olney, J.W.; Newcomer, J.W.; Farber, N.B. NMDA receptor hypofunction model of schizophrenia. *J. Psychiatr. Res.* **1999**, *33*, 523-533, doi:10.1016/S0022-3956(99)00029-1.

197. Hashimoto, K. The NMDA receptor hypofunction hypothesis for schizophrenia and glycine modulatory sites on the NMDA receptors as potential therapeutic drugs. *Clin. Psychopharmacol. Neurosci.* **2006**, *4*, 3-10.

198. Tsai, G.E.; Yang, P.; Chang, Y.-C.; Chong, M.-Y. D-alanine added to antipsychotics for the treatment of schizophrenia. *Biol. Psychiatry* **2006**, *59*, 230-234, doi:10.1016/j.biopsych.2005.06.032.

199. Horio, M.; Fujita, Y.; Ishima, T.; Iyo, M.; Ferraris, D.; Tsukamoto, T.; Hashimoto, K. Effects of D-amino acid oxidase inhibitor on the extracellular D-alanine levels and the efficacy of D-alanine on dizocilpine-induced prepulse inhibition deficits in mice. *The Open Clinical Chemistry Journal* **2009**, *2*, doi:10.2174/1874241600902010016.

200. Bird, M.I.; Nunn, P.B.; Lord, L.A.J. Formation of glycine and aminoacetone from l-threonine by rat liver mitochondria. *Biochim. Biophys. Acta* **1984**, *802*, 229-236, doi:10.1016/0304-4165(84)90166-1.

201. Maher, T.J.; Wurtman, R.J. L-Threonine administration increases glycine concentrations in the rat central nervous system. *Life Sci.* **1980**, *26*, 1283-1286, doi:10.1016/0024-3205(80)90086-7.

202. Lee, A.; Patterson, V. A double-blind study of L-threonine in patients with spinal spasticity. *Acta Neurol. Scand.* **1993**, *88*, 334-338, doi:10.1111/j.1600-0404.1993.tb05353.x.

203. Paisley, S.; Beard, S.; Hunn, A.; Wight, J. Clinical effectiveness of oral treatments for spasticity in multiple sclerosis: a systematic review. *Mult. Scler.* **2002**, *8*, 319-329, doi:10.1191/1352458502ms795rr.

204. Tiedje, K.E.; Stevens, K.; Barnes, S.; Weaver, D.F. β-Alanine as a small molecule neurotransmitter. *Neurochem. Int.* **2010**, *57*, 177-188, doi:10.1016/j.neuint.2010.06.001.

205. Juge, N.; Omote, H.; Moriyama, Y. Vesicular GABA transporter (VGAT) transports β-alanine. *J. Neurochem.* **2013**, *127*, 482-486, doi:10.1111/jnc.12393.

206. Shinohara, T.; Harada, M.; Ogi, K.; Maruyama, M.; Fujii, R.; Tanaka, H.; Fukusumi, S.; Komatsu, H.; Hosoya, M.; Noguchi, Y. Identification of a G protein-coupled receptor specifically responsive to β-alanine. *J. Biol. Chem.* **2004**, *279*, 23559-23564, doi:10.1074/jbc.M314240200.

207. Dong, X.; Han, S.-k.; Zylka, M.J.; Simon, M.I.; Anderson, D.J. A diverse family of GPCRs expressed in specific subsets of nociceptive sensory neurons. *Cell* **2001**, *106*, 619-632, doi:10.1016/S0092-8674(01)00483-4.

208. Curtis, D.; Phillis, J.; Watkins, J. The depression of spinal neurones by γ-amino-n-butyric acid and β-alanine. *J. Physiol. (Lond.)* **1959**, *146*, 185-203, doi:10.1113/jphysiol.1959.sp006188.

209. Zylka, M.J.; Dong, X.; Southwell, A.L.; Anderson, D.J. Atypical expansion in mice of the sensory neuron-specific Mrg G protein-coupled receptor family. *Proc. Natl. Acad. Sci. USA* **2003**, *100*, 10043-10048, doi:10.1073/pnas.1732949100.

210. Cavanaugh, D.J.; Lee, H.; Lo, L.; Shields, S.D.; Zylka, M.J.; Basbaum, A.I.; Anderson, D.J. Distinct subsets of unmyelinated primary sensory fibers mediate behavioral

responses to noxious thermal and mechanical stimuli. *Proc. Natl. Acad. Sci. USA* **2009**, *106*, 9075-9080, doi:10.1073/pnas.0901507106.

211. Crozier, R.A.; Ajit, S.K.; Kaftan, E.J.; Pausch, M.H. MrgD activation inhibits KCNQ/M-currents and contributes to enhanced neuronal excitability. *J. Neurosci.* **2007**, *27*, 4492-4496, doi:10.1523/jneurosci.4932-06.2007.

212. Zhuo, R.G.; Ma, X.Y.; Zhou, P.L.; Liu, X.Y.; Zhang, K.; Wei, X.L.; Yan, H.T.; Xu, J.P.; Zheng, J.Q. Mas-related G protein-coupled receptor D is coupled to endogenous calcium-activated chloride channel in Xenopus oocytes. *J. Physiol. Biochem.* **2014**, *70*, 185-191, doi:10.1007/s13105-013-0292-1.

213. Wang, C.; Gu, L.; Ruan, Y.; Geng, X.; Xu, M.; Yang, N.; Yu, L.; Jiang, Y.; Zhu, C.; Yang, Y., et al. Facilitation of MrgprD by TRP-A1 promotes neuropathic pain. *The FASEB Journal* **2019**, *33*, 1360-1373, doi:10.1096/fj.201800615RR.

214. Liu, Q.; Sikand, P.; Ma, C.; Tang, Z.; Han, L.; Li, Z.; Sun, S.; LaMotte, R.H.; Dong, X. Mechanisms of itch evoked by β-alanine. *J. Neurosci.* **2012**, *32*, 14532-14537, doi:10.1523/jneurosci.3509-12.2012.

215. Fernstrom, J.D. Branched-chain amino acids and brain function. *J. Nutr.* **2005**, *135*, 1539S-1546S, doi:10.1093/jn/135.6.1539S.

216. Pardridge, W.M. Brain metabolism: a perspective from the blood-brain barrier. *Physiol. Rev.* **1983**, *63*, 1481-1535, doi:10.1152/physrev.1983.63.4.1481.

217. Fernstrom, J.D. Aromatic amino acids and monoamine synthesis in the central nervous system: influence of the diet. *J. Nutr. Biochem.* **1990**, *1*, 508-517, doi:10.1016/0955-2863(90)90033-H.

218. Jenkins, T.A.; Nguyen, J.C.D.; Polglaze, K.E.; Bertrand, P.P. Influence of tryptophan and serotonin on mood and cognition with a possible role of the gut-brain axis. *Nutrients* **2016**, *8*, 56, doi:10.3390/nu8010056.

219. Snedden, W.; Mellor, C.S.; Martin, J.R. Familial hypertryptophanemia, tryptophanuria and indoleketonuria. *Clin. Chim. Acta* **1983**, *131*, 247-256, doi:10.1016/0009-8981(83)90094-3.

220. Fernstrom, J.D.; Fernstrom, M.H. Tyrosine, phenylalanine, and catecholamine synthesis and function in the brain. *J. Nutr.* **2007**, *137*, 1539S-1547S, doi:10.1093/jn/137.6.1539S.

221. Katz, I.; Lloyd, T.; Kaufman, S. Studies on phenylalanine and tyrosine hydroxylation by rat brain tyrosine hydroxylase. *Biochim. Biophys. Acta* **1976**, *445*, 567-578, doi:10.1016/0005-2744(76)90111-X.

222. Roiser, J.P.; McLean, A.; Ogilvie, A.D.; Blackwell, A.D.; Bamber, D.J.; Goodyer, I.; Jones, P.B.; Sahakian, B.J. The subjective and cognitive effects of acute phenylalanine and tyrosine depletion in patients recovered from depression. *Neuropsychopharmacology* **2005**, *30*, 775-785, doi:10.1038/sj.npp.1300659.

223. McLean, A.; Rubinsztein, J.S.; Robbins, T.W.; Sahakian, B.J. The effects of tyrosine depletion in normal healthy volunteers: implications for unipolar depression. *Psychopharmacology* **2004**, *171*, 286-297, doi:10.1007/s00213-003-1586-8.

224. Grevet, E.H.; Tietzmann, M.R.; Shansis, F.M.; Hastenpflug, C.; Santana, L.C.; Forster, L.; Kapczinski, F.; Izquierdo, I. Behavioural effects of acute phenylalanine and tyrosine depletion in healthy male volunteers. *J. Psychopharm.* **2002**, *16*, 51-55, doi:10.1177/026988110201600103.

225. van Ginkel, W.G.; Jahja, R.; Huijbregts, S.C.J.; Daly, A.; MacDonald, A.; De Laet, C.; Cassiman, D.; Eyskens, F.; Körver-Keularts, I.M.L.W.; Goyens, P.J., et al. Neurocognitive outcome in tyrosinemia type 1 patients compared to healthy controls. *Orphanet J. Rare Dis.* **2016**, *11*, 87, doi:10.1186/s13023-016-0472-5.

226. Gassió, R.; Artuch, R.; Vilaseca, M.A.; Fusté, E.; Boix, C.; Sans, A.; Campistol, J. Cognitive functions in classic phenylketonuria and mild hyperphenyl-alaninaemia: experience in a paediatric population. *Dev. Med. Child Neurol.* **2005**, *47*, 443-448, doi:10.1017/S0012162205000861.

227. Haas, H.L.; Sergeeva, O.A.; Selbach, O. Histamine in the nervous system. *Physiol. Rev.* **2008**, *88*, 1183-1241, doi:10.1152/physrev.00043.2007.

228. Yoshikawa, T.; Nakamura, T.; Shibakusa, T.; Sugita, M.; Naganuma, F.; Iida, T.; Miura, Y.; Mohsen, A.; Harada, R.; Yanai, K. Insufficient intake of L-histidine reduces brain histamine and causes anxiety-like behaviors in male mice. *J. Nutr.* **2014**, *144*, 1637-1641, doi:10.3945/jn.114.196105.

229. Van Ruitenbeek, P.; Sambeth, A.; Vermeeren, A.; Young, S.; Riedel, W. Effects of L-histidine depletion and L-tyrosine/L-phenylalanine depletion on sensory and motor processes in healthy volunteers. *Br. J. Pharmacol.* **2009**, *157*, 92-103, doi:10.1111/j.1476-5381.2009.00203.x.

230. Coppola, A.; Wenner, B.R.; Ilkayeva, O.; Stevens, R.D.; Maggioni, M.; Slotkin, T.A.; Levin, E.D.; Newgard, C.B. Branched-chain amino acids alter neurobehavioral function in rats. *Am. J. Physiol. Endocrinol. Metabol.* **2013**, *304*, E405-E413, doi:10.1152/ajpendo.00373.2012.

231. Meeusen, R.; Watson, P.; Hasegawa, H.; Roelands, B.; Piacentini, M.F. Central fatigue: the serotonin hypothesis and beyond. *Sports Med.* **2006**, *36*, 881-909, doi:10.2165/00007256-200636100-00006.

232. Newsholme, E.A.; Blomstrand, E. Branched-chain amino acids and central fatigue. *The Journal of Nutrition* **2006**, *136*, 274S-276S, doi:10.1093/jn/136.1.274S.

233. Yudkoff, M. Interactions in the metabolism of glutamate and the branched-chain amino acids and ketoacids in the CNS. *Neurochem. Res.* **2017**, *42*, 10-18, doi:10.1007/s11064-016-2057-z.

234. LaNoue, K.F.; Berkich, D.A.; Conway, M.; Barber, A.J.; Hu, L.-Y.; Taylor, C.; Hutson, S. Role of specific aminotransferases in de novo glutamate synthesis and redox shuttling in the retina. *J. Neurosci. Res.* **2001**, *66*, 914-922, doi:10.1002/jnr.10064.

235. García-Espinosa, M.A.; Wallin, R.; Hutson, S.M.; Sweatt, A.J. Widespread neuronal expression of branched-chain aminotransferase in the CNS: implications for leucine/glutamate metabolism and for signaling by amino acids. *J. Neurochem.* **2007**, *100*, 1458-1468, doi:10.1111/j.1471-4159.2006.04332.x.

236. Contrusciere, V.; Paradisi, S.; Matteucci, A.; Malchiodi-Albedi, F. Branched-chain amino acids induce neurotoxicity in rat cortical cultures. *Neurotox. Res.* **2010**, *17*, 392-398, doi:10.1007/s12640-009-9115-0.

237. Caioli, S.; Candelotti, E.; Pedersen, J.Z.; Saba, L.; Antonini, A.; Incerpi, S.; Zona, C. Baicalein reverts L-valine-induced persistent sodium current up-modulation in primary cortical neurons. *Biochim. Biophys. Acta* **2016**, *1862*, 566-575, doi:10.1016/j.bbadis.2015.12.021.

238. Bridi, R.; Araldi, J.n.; Sgarbi, M.B.; Testa, C.G.; Durigon, K.; Wajner, M.; Dutra-Filho, C.S. Induction of oxidative stress in rat brain by the metabolites accumulating in maple syrup urine disease. *Int. J. Dev. Neurosci.* **2003**, *21*, 327-332, doi:10.1016/S0736-5748(03)00074-1.

239. Singh, S.; Sharma, M.P.; Ahmad, A. Construction and characterization of protein-based cysteine nanosensor for the real time measurement of cysteine level in living cells. *Int. J. Biol. Macromol.* **2020**, *143*, 273-284, doi:10.1016/j.ijbiomac.2019.12.025.

240. Singh, S.; Sharma, M.P.; Alqarawi, A.A.; Hashem, A.; Abd_Allah, E.F.; Ahmad, A. Real-time optical detection of isoleucine in living cells through a genetically-encoded nanosensor. *Sensors* **2020**, *20*, 146, doi:10.3390/s20010146.

241. Mohsin, M.; Abdin, M.; Nischal, L.; Kardam, H.; Ahmad, A. Genetically encoded FRET-based nanosensor for in vivo measurement of leucine. *Biosensors Bioelectron.* **2013**, *50*, 72-77, doi:10.1016/j.bios.2013.06.028.

242. Ameen, S.; Ahmad, M.; Mohsin, M.; Qureshi, M.I.; Ibrahim, M.M.; Abdin, M.Z.; Ahmad, A. Designing, construction and characterization of genetically encoded FRET-based nanosensor for real time monitoring of lysine flux in living cells. *J. Nanobiotechnology* **2016**, *14*, 49, doi:10.1186/s12951-016-0204-y.

243. Mohsin, M.; Ahmad, A. Genetically-encoded nanosensor for quantitative monitoring of methionine in bacterial and yeast cells. *Biosensors Bioelectron.* **2014**, *59*, 358-364, doi:10.1016/j.bios.2014.03.066.

244. Guria, S.; Ghosh, A.; Manna, K.; Pal, A.; Adhikary, A.; Adhikari, S. Rapid detection of aspartic acid and glutamic acid in water by BODIPY-Based fluorescent probe: Live-cell

imaging and DFT studies. *Dyes Pigm.* **2019**, *168*, 111-122, doi:10.1016/j.dyepig.2019.04.052.

245. Zhang, Y.; Wang, X.; Bai, X.; Li, P.; Su, D.; Zhang, W.; Zhang, W.; Tang, B. Highly Specific Cys Fluorescence Probe for Living Mouse Brain Imaging via Evading Reaction with Other Biothiols. *Anal. Chem.* **2019**, *91*, 8591-8594, doi:10.1021/acs.analchem.9b01878.

246. Yue, Y.; Huo, F.; Ning, P.; Zhang, Y.; Chao, J.; Meng, X.; Yin, C. Dual-Site Fluorescent Probe for Visualizing the Metabolism of Cys in Living Cells. *J. Am. Chem. Soc.* **2017**, *139*, 3181-3185, doi:10.1021/jacs.6b12845.

247. Zhang, X.; Liu, C.; Cai, X.; Tian, B.; Zhu, H.; Chen, Y.; Sheng, W.; Jia, P.; Li, Z.; Yu, Y., et al. A highly specific Golgi-targetable fluorescent probe for tracking cysteine generation during the Golgi stress response. *Sensors Actuators B: Chem.* **2020**, *310*, 127820, doi:10.1016/j.snb.2020.127820.

248. Duan, Z.; Zhu, Y.; Yang, Y.; He, Z.; Liu, J.; Li, P.; Wang, H.; Tang, B. Fluorescent imaging for cysteine detection in vivo with high selectivity. *ChemistryOpen* **2019**, *8*, 316-320, doi:10.1002/open.201900045.

249. Hou, J.Q.; Cai, P.F.; Wang, C.Y.; Shen, Y.J. A novel fluorescent probe with a large stokes shift for cysteine based on dicyanoisophorone. *Tetrahedron Lett.* **2018**, *59*, 2581-2585, doi:10.1016/j.tetlet.2018.05.057.

250. Li, S.J.; Song, D.; Huang, W.J.; Li, Z.; Liu, Z.H. In situ imaging of cysteine in the brains of mice with epilepsy by a near-infrared emissive fluorescent probe. *Anal. Chem.* **2020**, *92*, 2802-2808, doi:10.1021/acs.analchem.9b05211.

251. Yu, Y.W.; Xu, H.P.; Zhang, W.; Han, Q.R.; Wang, B.X.; Jiang, Y.L. A novel near-infrared fluorescent probe for cysteine in living cells based on a push-pull dicyanoisophorone system. *J. Photochem. Photobiol. A: Chem.* **2017**, *346*, 215-220, doi:10.1016/j.jphotochem.2017.06.001.

252. Marvin, J.S.; Borghuis, B.G.; Tian, L.; Cichon, J.; Harnett, M.T.; Akerboom, J.; Gordus, A.; Renninger, S.L.; Chen, T.-W.; Bargmann, C.I., et al. An optimized fluorescent probe for visualizing glutamate neurotransmission. *Nat. Methods* **2013**, *10*, 162-170, doi:10.1038/nmeth.2333.

253. Helassa, N.; Dürst, C.D.; Coates, C.; Kerruth, S.; Arif, U.; Schulze, C.; Wiegert, J.S.; Geeves, M.; Oertner, T.G.; Török, K. Ultrafast glutamate sensors resolve high-frequency release at Schaffer collateral synapses. *Proc. Natl. Acad. Sci. USA* **2018**, *115*, 5594-5599, doi:10.1073/pnas.1720648115.

254. Marvin, J.S.; Scholl, B.; Wilson, D.E.; Podgorski, K.; Kazemipour, A.; Mueller, J.A.; Schoch, S.; Quiroz, F.J.U.; Rebola, N.; Bao, H. Stability, affinity, and chromatic variants of the glutamate sensor iGluSnFR. *Nat. Methods* **2018**, *15*, 936-939, doi:10.1038/s41592-018-0171-3.

255. Wu, J.; Abdelfattah, A.S.; Zhou, H.; Ruangkittisakul, A.; Qian, Y.; Ballanyi, K.; Campbell, R.E. Genetically-encoded glutamate indicators with altered color and topology. *ACS Chem. Biol.* **2018**, 10.1021/acschembio.7b01085, doi:10.1021/acschembio.7b01085.

256. Okumoto, S.; Looger, L.L.; Micheva, K.D.; Reimer, R.J.; Smith, S.J.; Frommer, W.B. Detection of glutamate release from neurons by genetically encoded surface-displayed

FRET nanosensors. *Proc. Natl. Acad. Sci. USA* **2005**, *102*, 8740-8745, doi:10.1073/pnas.0503274102.

257. Okada, S.; Ota, K.; Ito, T. Circular permutation of ligand-binding module improves dynamic range of genetically encoded FRET-based nanosensor. *Protein Sci.* **2009**, *18*, 2518-2527, doi:10.1002/pro.266.

258. Namiki, S.; Sakamoto, H.; Iinuma, S.; Iino, M.; Hirose, K. Optical glutamate sensor for spatiotemporal analysis of synaptic transmission. *Eur. J. Neurosci.* **2007**, *25*, 2249-2259, doi:10.1111/j.1460-9568.2007.05511.x.

259. Okubo, Y.; Sekiya, H.; Namiki, S.; Sakamoto, H.; Iinuma, S.; Yamasaki, M.; Watanabe, M.; Hirose, K.; Iino, M. Imaging extrasynaptic glutamate dynamics in the brain. *Proc. Natl. Acad. Sci. USA* **2010**, *107*, 6526-6531, doi:10.1073/pnas.0913154107.

260. Takikawa, K.; Asanuma, D.; Namiki, S.; Sakamoto, H.; Ariyoshi, T.; Kimpara, N.; Hirose, K. High-throughput development of a hybrid-type fluorescent glutamate sensor for analysis of synaptic transmission. *Angew. Chem. Int. Ed.* **2014**, *53*, 13439-13443, doi:10.1002/anie.201407181.

261. Brun, M.A.; Tan, K.-T.; Griss, R.; Kielkowska, A.; Reymond, L.; Johnsson, K. A semisynthetic fluorescent sensor protein for glutamate. *J. Am. Chem. Soc.* **2012**, *134*, 7676-7678, doi:10.1021/ja3002277.

262. Elamathi, C.; Butcher, R.J.; Mohankumar, A.; Sundararaj, P.; Madankumar, A.; Kalaivani, P.; Prabhakaran, R. A quinoline-based probe for effective and selective sensing of aspartic acid in aqueous medium: in vitro and in vivo live cell imaging. *Inorg. Chem. Front.* **2019**, *6*, 3237-3244, doi:10.1039/C9QI00992B.

263. Gruenwald, K.; Holland, J.T.; Stromberg, V.; Ahmad, A.; Watcharakichkorn, D.; Okumoto, S. Visualization of glutamine transporter activities in living cells using genetically encoded glutamine sensors. *PLoS ONE* **2012**, *7*, doi:10.1371/journal.pone.0140088

264. Ko, W.; Kim, S.; Lee, S.; Jo, K.; Lee, H.S. Genetically encoded FRET sensors using a fluorescent unnatural amino acid as a FRET donor. *RSC Adv.* **2016**, *6*, 78661-78668, doi:10.1039/C6RA17375F

265. Feng, S.X.; Li, X.; Ma, Q.J.; Liang, B.B.; Ma, Z.Y. A highly selective and sensitive fluorescent probe for thiols based on a benzothiazole derivative. *Anal. Methods* **2016**, *8*, 6832-6839, doi:10.1039/c6ay02140a.

266. Chen, S.; Hou, P.; Wang, J.; Fu, S.; Liu, L. A simple but effective fluorescent probe with large stokes shift for specific detection of cysteine in living cells. *J. Photochem. Photobiol. A: Chem.* **2018**, *363*, 7-12, doi:10.1016/j.jphotochem.2018.05.025.

267. Yang, L.; Su, Y.; Geng, Y.; Zhang, Y.; Ren, X.; He, L.; Song, X. A Triple-Emission Fluorescent Probe for Discriminatory Detection of Cysteine/Homocysteine, Glutathione/Hydrogen Sulfide, and Thiophenol in Living Cells. *ACS Sensors* **2018**, *3*, 1863-1869, doi:10.1021/acssensors.8b00685.

268. Dong, B.; Lu, Y.; Zhang, N.; Song, W.; Lin, W. Ratiometric Imaging of Cysteine Level Changes in Endoplasmic Reticulum during H2O2-Induced Redox Imbalance. *Anal. Chem.* **2019**, *91*, 5513-5516, doi:10.1021/acs.analchem.9b01457.

269. Niu, H.; Zhang, Y.; Zhao, F.; Mo, S.; Cao, W.; Ye, Y.; Zhao, Y. Reductive stress imaging in the endoplasmic reticulum by using living cells and zebrafish. *Chem. Commun.* **2019**, *55*, 9629-9632, doi:10.1039/C9CC04711E.

270. Zhang, X.; Liu, C.; Chen, Y.; Cai, X.; Sheng, W.; Zhu, H.; Jia, P.; Li, Z.; Huang, S.; Zhu, B. Visualization of the cysteine level during Golgi stress using a novel Golgi-targeting highly specific fluorescent probe. *Chem. Commun.* **2020**, *56*, 1807-1810, doi:10.1039/C9CC08796F.

271. Yue, Y.; Huo, F.; Yue, P.; Meng, X.; Salamanca, J.C.; Escobedo, J.O.; Strongin, R.M.; Yin, C. In Situ Lysosomal Cysteine-Specific Targeting and Imaging during Dexamethasone-Induced Apoptosis. *Anal. Chem.* **2018**, *90*, 7018-7024, doi:10.1021/acs.analchem.8b01406.

272. Chen, K.; Zhang, M.; Qi, Y.; Fan, J.; Ma, X.; Zhu, H.; Qian, Y. Imaging dynamic changes of an intracellular cysteine pool that responds to the stimulation of external oxidative stress. *Analyst* **2019**, *144*, 2320-2326, doi:10.1039/C8AN02232A.

273. Shen, Y.; Zhang, X.; Zhang, Y.; Zhang, C.; Jin, J.; Li, H. A new simple phthalimide-based fluorescent probe for highly selective cysteine and bioimaging for living cells. *Spectrochim. Acta, Pt. A: Mol. Biomol. Spectrosc.* **2017**, *185*, 371-375, doi:10.1016/j.saa.2017.05.041.

274. Ye, Z.; Duan, C.; Hu, Q.; Zhang, Y.; Qin, C.Q.; Zeng, L.T. A dual-channel responsive near-infrared fluorescent probe for multicolour imaging of cysteine in living cells. *Journal of Materials Chemistry B* **2017**, *5*, 3600-3606, doi:10.1039/c7tb00489c.

275. Liu, G.T.; Liu, D.; Han, X.; Sheng, X.L.; Xu, Z.G.; Liu, S.H.; Zeng, L.T.; Yin, J. A hemicyanine-based colorimetric and ratiometric fluorescent probe for selective detection of cysteine and bioimaging in living cell. *Talanta* **2017**, *170*, 406-412, doi:10.1016/j.talanta.2017.04.038.

276. Yang, M.; Fan, J.; Sun, W.; Du, J.; Peng, X. Mitochondria-Anchored Colorimetric and Ratiometric Fluorescent Chemosensor for Visualizing Cysteine/Homocysteine in Living Cells and Daphnia magna Model. *Anal. Chem.* **2019**, *91*, 12531-12537, doi:10.1021/acs.analchem.9b03386.

277. Wang, Q.; Wei, X.D.; Li, C.J.; Xie, Y.S. A novel p-aminophenylthio- and cyano-substituted BODIPY as a fluorescence turn-on probe for distinguishing cysteine and homocysteine from glutathione. *Dyes Pigm.* **2018**, *148*, 212-218, doi:10.1016/j.dyepig.2017.09.020.

278. Zhang, J.; Wang, J.; Liu, J.; Ning, L.; Zhu, X.; Yu, B.; Liu, X.; Yao, X.; Zhang, H. Near-infrared and naked-eye fluorescence probe for direct and highly selective detection of cysteine and its application in living cells. *Anal. Chem.* **2015**, *87*, 4856-4863.

279. Zhang, H.; Yan, C.; Li, H.; Shi, L.; Wang, R.; Guo, Z.; Zhu, W.-H. Rational Design of Near-Infrared Cyanine-Based Fluorescent Probes for Rapid In Vivo Sensing Cysteine. *ACS Applied Bio Materials* **2020**, 10.1021/acsabm.0c00260, doi:10.1021/acsabm.0c00260.

280. Han, C.; Yang, H.; Chen, M.; Su, Q.; Feng, W.; Li, F. Mitochondria-targeted near-infrared fluorescent off–on probe for selective detection of cysteine in living cells and in vivo. *ACS Appl. Mater. Interfaces* **2015**, *7*, 27968-27975, doi:10.1021/acsami.5b10607.

281. Zhang, W.; Liu, J.; Yu, Y.W.; Han, Q.R.; Cheng, T.; Shen, J.; Wang, B.X.; Jiang, Y.L. A novel near-infrared fluorescent probe for highly selective detection of cysteine and its application in living cells. *Talanta* **2018**, *185*, 477-482, doi:10.1016/j.talanta.2018.04.001.

282. Qi, Y.; Huang, Y.; Li, B.W.; Zeng, F.; Wu, S.Z. Real-time monitoring of endogenous cysteine levels in vivo by near-infrared turn-on fluorescent probe with large Stokes shift. *Anal. Chem.* **2018**, *90*, 1014-1020, doi:10.1021/acs.analchem.7b04407.

283. Liu, S.; Shi, F.; Chen, L.; Su, X. Tyrosine-functionalized CuInS 2 quantum dots as a fluorescence probe for the determination of biothiols, histidine and threonine. *Analyst* **2013**, *138*, 5819-5825, doi:10.1039/C3AN00758H

284. Yang, S.; Guo, C.; Li, Y.; Guo, J.; Xiao, J.; Qing, Z.; Li, J.; Yang, R. A ratiometric two-photon fluorescent cysteine probe with well-resolved dual emissions based on intramolecular charge transfer-mediated two-photon-FRET integration mechanism. *ACS Sensors* **2018**, *3*, 2415-2422, doi:10.1021/acssensors.8b00919.

285. Bai, Y.; Wu, M.X.; Ma, Q.J.; Wang, C.Y.; Sun, J.G.; Tian, M.J.; Li, J.S. A FRET-based ratiometric fluorescent probe for highly selective detection of cysteine based on a coumarin-rhodol derivative. *New J. Chem.* **2019**, *43*, 14763-14771, doi:10.1039/c9nj03375k.

286. Ko, W.; Lee, H.S. Development of specific l-methionine sensors by FRET-based protein engineering. *RSC Adv.* **2019**, *9*, 15648-15656, doi:10.1039/C9RA01317B.

287. Marvin, J.S.; Shimoda, Y.; Magloire, V.; Leite, M.; Kawashima, T.; Jensen, T.P.; Kolb, I.; Knott, E.L.; Novak, O.; Podgorski, K., et al. A genetically encoded fluorescent sensor for in vivo imaging of GABA. *Nat. Methods* **2019**, 10.1038/s41592-019-0471-2, doi:10.1038/s41592-019-0471-2.

288. Masharina, A.; Reymond, L.; Maurel, D.; Umezawa, K.; Johnsson, K. A fluorescent sensor for GABA and synthetic GABAB receptor ligands. *J. Am. Chem. Soc.* **2012**, *134*, 19026-19034, doi:10.1021/ja306320s.

289. Steffen, V.; Otten, J.; Engelmann, S.; Radek, A.; Limberg, M.; Koenig, B.W.; Noack, S.; Wiechert, W.; Pohl, M. A toolbox of genetically encoded FRET-based biosensors for rapid l-lysine analysis. *Sensors* **2016**, *16*, 1604, doi:10.3390/s16101604.

290. Bogner, M.; Ludewig, U. Visualization of arginine influx into plant cells using a specific FRET sensor. *J. Fluoresc.* **2007**, *17*, 350-360, doi:10.1007/s10895-007-0192-2.

291. Zhang, W.H.; Herde, M.K.; Mitchell, J.A.; Whitfield, J.H.; Wulff, A.B.; Vongsouthi, V.; Sanchez-Romero, I.; Gulakova, P.E.; Minge, D.; Breithausen, B., et al. Monitoring hippocampal glycine with the computationally designed optical sensor GlyFS. *Nat. Chem. Biol.* **2018**, 10.1038/s41589-018-0108-2, doi:10.1038/s41589-018-0108-2.

292. Kaper, T.; Looger, L.L.; Takanaga, H.; Platten, M.; Steinman, L.; Frommer, W.B. Nanosensor detection of an immunoregulatory tryptophan influx/kynurenine efflux cycle. *PLoS Biol.* **2007**, *5*, doi:10.1371/journal.pbio.0050257.

293. You, Q.-H.; Lee, A.W.-M.; Chan, W.-H.; Zhu, X.-M.; Leung, K.C.-F. A coumarin-based fluorescent probe for recognition of Cu 2+ and fast detection of histidine in hard-to-transfect cells by a sensing ensemble approach. *Chem. Commun.* **2014**, *50*, 6207-6210.

294. Un, H.-I.; Wu, S.; Huang, C.-B.; Xu, Z.; Xu, L. A naphthalimide-based fluorescent probe for highly selective detection of histidine in aqueous solution and its application in in vivo imaging. *Chem. Commun.* **2015**, *51*, 3143-3146.

295. Meng, Q.; Jia, H.; Gao, X.; Wang, Y.; Zhang, R.; Wang, R.; Zhang, Z. Reversible and selective fluorescence detection of histidine using a naphthalimide-based chemosensing ensemble. *Chem. Asian J.* **2015**, *10*, 2411-2418, doi:10.1002/asia.201500690.

296. Hu, H.; Gu, Y.; Xu, L.; Zou, Y.; Wang, A.; Tao, R.; Chen, X.; Zhao, Y.; Yang, Y. A genetically encoded toolkit for tracking live-cell histidine dynamics in space and time. *Sci. Rep.* **2017**, *7*, 43479, doi:10.1038/srep43479.

297. Lu, W.; Jiao, Y.; Gao, Y.; Qiao, J.; Mozneb, M.; Shuang, S.; Dong, C.; Li, C.-z. Bright yellow fluorescent carbon dots as a multifunctional sensing platform for the label-free detection of fluoroquinolones and histidine. *ACS Appl. Mater. Interfaces* **2018**, *10*, 42915-42924, doi:10.1021/acsami.8b16710.

298. Yoshida, T.; Nakajima, H.; Takahashi, S.; Kakizuka, A.; Imamura, H. OLIVe: a genetically-encoded fluorescent biosensor for quantitative imaging of branched-chain amino acid levels inside single living cells. *ACS Sensors* **2019**, *4*, 3333-3342, doi:10.1021/acssensors.9b02067.

299. Carter, K.P.; Young, A.M.; Palmer, A.E. Fluorescent sensors for measuring metal ions in living systems. *Chem. Rev.* **2014**, *114*, 4564-4601.

300. Domaille, D.W.; Que, E.L.; Chang, C.J. Synthetic fluorescent sensors for studying the cell biology of metals. *Nat. Chem. Biol.* **2008**, *4*, 168-175, doi:10.1038/nchembio.69.

301. Snowden, T.S.; Anslyn, E.V. Anion recognition: synthetic receptors for anions and their application in sensors. *Curr. Opin. Chem. Biol.* **1999**, *3*, 740-746, doi:10.1016/S1367-5931(99)00034-4.

302. Martínez-Máñez, R.; Sancenón, F. Fluorogenic and Chromogenic Chemosensors and Reagents for Anions. *Chem. Rev.* **2003**, *103*, 4419-4476, doi:10.1021/cr010421e.

303. Maity, D.; Schmuck, C. Synthetic Receptors for Amino Acids and Peptides. In *Synthetic Receptors for Biomolecules: Design Principles and Applications*, The Royal Society of Chemistry: 2015; 10.1039/9781782622062-00326pp. 326-368.

304. Wu, W.; Tian, Z.; Li, A.D.Q. Fluorescent Nanoparticles for Biological Imaging. In *Comprehensive Biomaterials II*, Ducheyne, P., Ed. Elsevier: Oxford, 2017; 10.1016/B978-0-08-100691-7.00120-8pp. 535-548.

305. Resch-Genger, U.; Grabolle, M.; Cavaliere-Jaricot, S.; Nitschke, R.; Nann, T. Quantum dots versus organic dyes as fluorescent labels. *Nat. Methods* **2008**, *5*, 763, doi:10.1038/nmeth.1248.

306. Chen, N.; He, Y.; Su, Y.; Li, X.; Huang, Q.; Wang, H.; Zhang, X.; Tai, R.; Fan, C. The cytotoxicity of cadmium-based quantum dots. *Biomaterials* **2012**, *33*, 1238-1244, doi:10.1016/j.biomaterials.2011.10.070.

307. Liu, Z.; Tabakman, S.; Welsher, K.; Dai, H. Carbon nanotubes in biology and medicine: in vitro and in vivo detection, imaging and drug delivery. *Nano Research* **2009**, *2*, 85-120, doi:10.1007/s12274-009-9009-8

308. Kruss, S.; Hilmer, A.J.; Zhang, J.; Reuel, N.F.; Mu, B.; Strano, M.S. Carbon nanotubes as optical biomedical sensors. *Adv. Drug Del. Rev.* **2013**, *65*, 1933-1950, doi:10.1016/j.addr.2013.07.015.

309. Yang, N.; Chen, X.; Ren, T.; Zhang, P.; Yang, D. Carbon nanotube based biosensors. *Sensors Actuators B: Chem.* **2015**, *207*, 690-715, doi:10.1016/j.snb.2014.10.040.

310. O'Connell, M.J.; Bachilo, S.M.; Huffman, C.B.; Moore, V.C.; Strano, M.S.; Haroz, E.H.; Rialon, K.L.; Boul, P.J.; Noon, W.H.; Kittrell, C. Band gap fluorescence from individual single-walled carbon nanotubes. *Science* **2002**, *297*, 593-596, doi:10.1126/science.1072631.

311. Smith, A.M.; Mancini, M.C.; Nie, S. Second window for in vivo imaging. *Nature Nanotechnology* **2009**, *4*, 710-711, doi:10.1038/nnano.2009.326.

312. Hong, G.; Diao, S.; Chang, J.; Antaris, A.L.; Chen, C.; Zhang, B.; Zhao, S.; Atochin, D.N.; Huang, P.L.; Andreasson, K.I., et al. Through-skull fluorescence imaging of the brain in a new near-infrared window. *Nat. Photonics* **2014**, *8*, 723-730, doi:10.1038/nphoton.2014.166.

313. Kruss, S.; Landry, M.P.; Vander Ende, E.; Lima, B.M.; Reuel, N.F.; Zhang, J.; Nelson, J.; Mu, B.; Hilmer, A.; Strano, M. Neurotransmitter detection using corona phase molecular recognition on fluorescent single-walled carbon nanotube sensors. *J. Am. Chem. Soc.* **2014**, *136*, 713-724, doi:10.1021/ja410433b.

314. Beyene, A.G.; Alizadehmojarad, A.A.; Dorlhiac, G.; Goh, N.; Streets, A.M.; Král, P.; Vuković, L.; Landry, M.P. Ultralarge modulation of fluorescence by neuromodulators in carbon nanotubes functionalized with self-assembled oligonucleotide rings. *Nano Lett.* **2018**, *18*, 6995-7003, doi:10.1021/acs.nanolett.8b02937.

315. Mann, F.A.; Herrmann, N.; Meyer, D.; Kruss, S. Tuning selectivity of fluorescent carbon nanotube-based neurotransmitter sensors. *Sensors* **2017**, *17*, 1521, doi:10.3390/s17071521.

316. Wilt, Brian A.; Fitzgerald, James E.; Schnitzer, Mark J. Photon Shot Noise Limits on Optical Detection of Neuronal Spikes and Estimation of Spike Timing. *Biophys. J.* **2013**, *104*, 51-62, doi:https://doi.org/10.1016/j.bpj.2012.07.058.

317. Shen, Y.; Nasu, Y.; Shkolnikov, I.; Kim, A.; Campbell, R.E. Engineering genetically encoded fluorescent indicators for imaging of neuronal activity: Progress and prospects. *Neurosci. Res.* **2020**, *152*, 3-14, doi:10.1016/j.neures.2020.01.011.

318. Shivange, A.V.; Borden, P.M.; Muthusamy, A.K.; Nichols, A.L.; Bera, K.; Bao, H.; Bishara, I.; Jeon, J.; Mulcahy, M.J.; Cohen, B., et al. Determining the pharmacokinetics

of nicotinic drugs in the endoplasmic reticulum using biosensors. *J. Gen. Physiol.* **2019**, *151*, 738-757, doi:10.1085/jgp.201812201.

319. Berzelius, J.J. *Traité de chimie*; Adolphe Wahlen et Cie: 1839; Vol. 1.

320. Plaitakis, A.; Constantakakis, E.; Smith, J. The neuroexcitotoxic amino acids glutamate and aspartate are altered in the spinal cord and brain in amyotrophic lateral sclerosis. *Ann Neurol* **1988**, *24*, 446-449, doi:10.1002/ana.410240314.

321. Müller, A.; León-Kempis, M.d.R.; Dodson, E.; Wilson, K.S.; Wilkinson, A.J.; Kelly, D.J. A bacterial virulence factor with a dual role as an adhesin and a solute-binding protein: the crystal structure at 1.5 Å resolution of the PEB1a protein from the food-borne human pathogen Campylobacter jejuni. *J. Mol. Biol.* **2007**, *372*, 160-171, doi:10.1016/j.jmb.2007.06.041.

322. Meng, E.C.; Pettersen, E.F.; Couch, G.S.; Huang, C.C.; Ferrin, T.E. Tools for integrated sequence-structure analysis with UCSF Chimera. *BMC Bioinform.* **2006**, *7*, 339, doi:10.1186/1471-2105-7-339.

323. Pettersen, E.F.; Goddard, T.D.; Huang, C.C.; Couch, G.S.; Greenblatt, D.M.; Meng, E.C.; Ferrin, T.E. UCSF Chimera--a visualization system for exploratory research and analysis. *J. Comput. Chem.* **2004**, *25*, 1605-1612, doi:10.1002/jcc.20084.

324. Pédelacq, J.-D.; Cabantous, S.; Tran, T.; Terwilliger, T.C.; Waldo, G.S. Engineering and characterization of a superfolder green fluorescent protein. *Nat. Biotechnol.* **2005**, *24*, 79, doi:10.1038/nbt1172.

325. Cadwell, R.C.; Joyce, G.F. Randomization of genes by PCR mutagenesis. *Genome Res.* **1992**, *2*, 28-33, doi:10.1101/gr.2.1.28.

326. Cirino, P.C.; Mayer, K.M.; Umeno, D. Generating Mutant Libraries Using Error-Prone PCR. In *Directed Evolution Library Creation: Methods and Protocols*, Arnold, F.H., Georgiou, G., Eds. Humana Press: Totowa, NJ, 2003; 10.1385/1-59259-395-x:3pp. 3-9.

327. Keeble, A.H.; Turkki, P.; Stokes, S.; Khairil Anuar, I.N.A.; Rahikainen, R.; Hytönen, V.P.; Howarth, M. Approaching infinite affinity through engineering of peptide–protein interaction. *Proc. Natl. Acad. Sci. USA* **2019**, *116*, 26523-26533, doi:10.1073/pnas.1909653116.

328. Ai, H.-w.; Baird, M.A.; Shen, Y.; Davidson, M.W.; Campbell, R.E. Engineering and characterizing monomeric fluorescent proteins for live-cell imaging applications. *Nat. Protoc.* **2014**, *9*, 910, doi:10.1038/nprot.2014.054.

329. Cranfill, P.J.; Sell, B.R.; Baird, M.A.; Allen, J.R.; Lavagnino, Z.; de Gruiter, H.M.; Kremers, G.-J.; Davidson, M.W.; Ustione, A.; Piston, D.W. Quantitative assessment of fluorescent proteins. *Nat. Methods* **2016**, 10.1038/nmeth.3891, doi:10.1038/nmeth.3891.

330. Ward, W.W. Biochemical and physical properties of green fluorescent protein. *Methods Biochem. Anal.* **2006**, *47*, 39-66, doi:10.1002/0471739499.ch3.

331. Zhao, Y.; Araki, S.; Wu, J.; Teramoto, T.; Chang, Y.-F.; Nakano, M.; Abdelfattah, A.S.; Fujiwara, M.; Ishihara, T.; Nagai, T., et al. An Expanded Palette of Genetically Encoded Ca(2+) Indicators. *Science* **2011**, *333*, 1888-1891, doi:10.1126/science.1208592.

332. Marvin, J.S.; Schreiter, E.R.; Echevarría, I.M.; Looger, L.L. A genetically encoded, high-signal-to-noise maltose sensor. *Proteins: Struct. Funct. Bioinform.* **2011**, *79*, 3025-3036.

333. Bennett, B.D.; Kimball, E.H.; Gao, M.; Osterhout, R.; Van Dien, S.J.; Rabinowitz, J.D. Absolute metabolite concentrations and implied enzyme active site occupancy in Escherichia coli. *Nat. Chem. Biol.* **2009**, *5*, 593, doi:10.1038/nchembio.186

334. Brustad, E.M.; Arnold, F.H. Optimizing non-natural protein function with directed evolution. *Curr. Opin. Chem. Biol.* **2011**, *15*, 201-210, doi:10.1016/j.cbpa.2010.11.020.

335. Sachsenhauser, V.; Bardwell, J.C.A. Directed evolution to improve protein folding in vivo. *Curr. Opin. Struct. Biol.* **2018**, *48*, 117-123, doi:10.1016/j.sbi.2017.12.003.

336. Imoto, T.; Yamada, H.; Yasukochi, T.; Yamada, E.; Ito, Y.; Ueda, T.; Nagatani, H.; Miki, T.; Horiuchi, T. Point mutation of alanine (31) to valine prohibits the folding of reduced lysozyme by sulfhydryl-disulfide interchange. *Protein Eng.* **1987**, *1*, 333-338, doi:10.1093/protein/1.4.333.

337. Fan, C.P.; Zhu, D.Y.; Lu, H.X.; Jin, Q.; Wang, D.C. A periplasmic glutamate/aspartate binding protein from Shigella flexneri: Gene cloning, over-expression, purification and preliminary crystallographic studies of the recombinant protein. *Protein Pept. Lett.* **2006**, *13*, 513-516, doi:10.2174/092986606776819646.

338. Quiocho, F.A.; Ledvina, P.S. Atomic structure and specificity of bacterial periplasmic receptors for active transport and chemotaxis: variation of common themes. *Mol. Microbiol.* **1996**, *20*, 17-25, doi:10.1111/j.1365-2958.1996.tb02484.x.

339. De Lorimier, R.M.; Smith, J.J.; Dwyer, M.A.; Looger, L.L.; Sali, K.M.; Paavola, C.D.; Rizk, S.S.; Sadigov, S.; Conrad, D.W.; Loew, L. Construction of a fluorescent biosensor family. *Protein Sci.* **2002**, *11*, 2655-2675, doi:10.1110/ps.021860.

340. Dwyer, M.A.; Hellinga, H.W. Periplasmic binding proteins: a versatile superfamily for protein engineering. *Curr. Opin. Struct. Biol.* **2004**, *14*, 495-504, doi:10.1016/j.sbi.2004.07.004.

341. Karplus, P.A.; Schulz, G.E. Prediction of chain flexibility in proteins. *Naturwissenschaften* **1985**, *72*, 212-213, doi:10.1007/BF01195768.

342. Kalivas, P. Extracellular glutamate: functional compartments operate in different concentration ranges. *Front. Syst. Neurosci.* **2011**, *5*, doi:10.3389/fnsys.2011.00094.

343. Mellman, I.; Fuchs, R.; Helenius, A. Acidification of the endocytic and exocytic pathways. *Annu. Rev. Biochem.* **1986**, *55*, 663-700, doi:10.1146/annurev.bi.55.070186.003311.

344. Zakeri, B.; Fierer, J.O.; Celik, E.; Chittock, E.C.; Schwarz-Linek, U.; Moy, V.T.; Howarth, M. Peptide tag forming a rapid covalent bond to a protein, through engineering a bacterial adhesin. *Proc. Natl. Acad. Sci. USA* **2012**, *109*, E690-E697, doi:10.1073/pnas.1115485109.

345. Patriarchi, T.; Cho, J.R.; Merten, K.; Marley, A.; Broussard, G.J.; Liang, R.; Williams, J.; Nimmerjahn, A.; von Zastrow, M.; Gradinaru, V., et al. Imaging neuromodulators with high spatiotemporal resolution using genetically encoded indicators. *Nat. Protoc.* **2019**, 10.1038/s41596-019-0239-2, doi:10.1038/s41596-019-0239-2.

346. Syková, E.; Nicholson, C. Diffusion in brain extracellular space. *Physiol. Rev.* **2008**, *88*, 1277-1340, doi:10.1152/physrev.00027.2007.

347. Zimmermann, D.R.; Dours-Zimmermann, M.T. Extracellular matrix of the central nervous system: from neglect to challenge. *Histochem. Cell Biol.* **2008**, *130*, 635-653, doi:10.1007/s00418-008-0485-9.

348. Dityatev, A.; Schachner, M. Extracellular matrix molecules and synaptic plasticity. *Nature Reviews Neuroscience* **2003**, *4*, 456, doi:10.1038/nrn1115.

349. Smith, A.C.; Scofield, M.D.; Kalivas, P.W. The tetrapartite synapse: extracellular matrix remodeling contributes to corticoaccumbens plasticity underlying drug addiction. *Brain Res.* **2015**, *1628*, 29-39, doi:10.1016/j.brainres.2015.03.027.

350. Tsien, R.Y. Very long-term memories may be stored in the pattern of holes in the perineuronal net. *Proc. Natl. Acad. Sci. USA* **2013**, *110*, 12456-12461, doi:10.1073/pnas.1310158110.

351. Zhang, H.; Baader, S.L.; Sixt, M.; Kappler, J.; Rauch, U. Neurocan–GFP fusion protein: a new approach to detect hyaluronan on tissue sections and living cells. *J. Histochem. Cytochem.* **2004**, *52*, 915-922, doi:10.1369/jhc.3A6221.2004.

352. Costantini, L.M.; Snapp, E.L. Fluorescent proteins in cellular organelles: serious pitfalls and some solutions. *DNA Cell Biol.* **2013**, *32*, 622-627, doi:10.1089/dna.2013.2172.

353. Costantini, L.M.; Baloban, M.; Markwardt, M.L.; Rizzo, M.; Guo, F.; Verkhusha, V.V.; Snapp, E.L. A palette of fluorescent proteins optimized for diverse cellular environments. *Nat. Commun.* **2015**, *6*, 7670, doi:10.1038/ncomms8670.

354. Ghosh, J.G.; Nguyen, A.A.; Bigelow, C.E.; Poor, S.; Qiu, Y.; Rangaswamy, N.; Ornberg, R.; Jackson, B.; Mak, H.; Ezell, T. Long-acting protein drugs for the treatment of ocular diseases. *Nat. Commun.* **2017**, *8*, 14837, doi:10.1038/ncomms14837.

355. Cruzat, V.; Macedo Rogero, M.; Noel Keane, K.; Curi, R.; Newsholme, P. Glutamine: Metabolism and Immune Function, Supplementation and Clinical Translation. *Nutrients* **2018**, *10*, 1564, doi:10.3390/nu10111564.

356. Wu, G. Amino acids: metabolism, functions, and nutrition. *Amino Acids* **2009**, *37*, 1-17, doi:10.1007/s00726-009-0269-0.

357. Mazat, J.-P.; Ransac, S. The Fate of Glutamine in Human Metabolism. The Interplay with Glucose in Proliferating Cells. *Metabolites* **2019**, *9*, 81, doi:10.3390/metabo9050081.

358. Albrecht, J.; Sonnewald, U.; Waagepetersen, H.S.; Schousboe, A. Glutamine in the central nervous system: function and dysfunction. *Front. Biosci.* **2007**, *12*, e43.

359. Hsiao, C.-D.; Sun, Y.-J.; Rose, J.; Wang, B.-C. The Crystal Structure of Glutamine-binding Protein from Escherichia coli. *J. Mol. Biol.* **1996**, *262*, 225-242, doi:10.1006/jmbi.1996.0509.

360. Sun, Y.-J.; Rose, J.; Wang, B.-C.; Hsiao, C.-D. The structure of glutamine-binding protein complexed with glutamine at 1.94 Å resolution: comparisons with other amino acid binding proteins. *J. Mol. Biol.* **1998**, *278*, 219-229.

361. Disease, S.S.G.C.f.I.; Abendroth, J.; Sankaran, B.; Fairman, J.W.; Staker, B.; Myler, P.; Stewart, L. Crystal structure of a Glutamine-binding periplasmic protein from Burkholderia pseudomallei in complex with glutamine. RCSB Protein Data Bank: 2017; 10.2210/pdb4f3p/pdb.

362. Kille, S.; Acevedo-Rocha, C.G.; Parra, L.P.; Zhang, Z.-G.; Opperman, D.J.; Reetz, M.T.; Acevedo, J.P. Reducing Codon Redundancy and Screening Effort of Combinatorial Protein Libraries Created by Saturation Mutagenesis. *ACS Synth. Biol.* **2013**, *2*, 83-92, doi:10.1021/sb300037w.

363. Schrödinger, L. *The PyMOL Molecular Graphics System, Version 2.0 Schrödinger, LLC (2017)*.

364. Consortium, T.U. UniProt: a worldwide hub of protein knowledge. *Nucleic Acids Res.* **2018**, *47*, D506-D515, doi:10.1093/nar/gky1049.

365. Porcelli, A.M.; Ghelli, A.; Zanna, C.; Pinton, P.; Rizzuto, R.; Rugolo, M. pH difference across the outer mitochondrial membrane measured with a green fluorescent protein mutant. *Biochem. Biophys. Res. Commun.* **2005**, *326*, 799-804, doi:10.1016/j.bbrc.2004.11.105.

366. Scalise, M.; Pochini, L.; Galluccio, M.; Console, L.; Indiveri, C. Glutamine Transport and Mitochondrial Metabolism in Cancer Cell Growth. *Front. Oncol.* **2017**, *7*, 306-306, doi:10.3389/fonc.2017.00306.

367. Berridge, M.J.; Lipp, P.; Bootman, M.D. The versatility and universality of calcium signalling. *Nat. Rev. Mol. Cell Biol.* **2000**, *1*, 11-21, doi:10.1038/35036035.

368. Ghosh, A.; Greenberg, M.E. Calcium signaling in neurons: molecular mechanisms and cellular consequences. *Science* **1995**, *268*, 239-247, doi:10.1126/science.7716515.

369. Nakai, J.; Ohkura, M.; Imoto, K. A high signal-to-noise Ca 2+ probe composed of a single green fluorescent protein. *Nat. Biotechnol.* **2001**, *19*, 137, doi:10.1038/84397.

370. Palmer, A.E.; Tsien, R.Y. Measuring calcium signaling using genetically targetable fluorescent indicators. *Nat. Protoc.* **2006**, *1*, 1057, doi:10.1038/nprot.2006.172.

371. Tian, L.; Hires, S.A.; Looger, L.L. Imaging Neuronal Activity with Genetically Encoded Calcium Indicators. *Cold Spring Harb. Protoc.* **2012**, *2012*, doi:10.1101/pdb.top069609.

372. Lin, M.Z.; Schnitzer, M.J. Genetically encoded indicators of neuronal activity. *Nat. Neurosci.* **2016**, *19*, 1142, doi:10.1038/nn.4359.

373. Akerboom, J.; Carreras Calderon, N.; Tian, L.; Wabnig, S.; Prigge, M.; Tolo, J.; Gordus, A.; Orger, M.B.; Severi, K.E.; Macklin, J.J., et al. Genetically encoded calcium indicators for multi-color neural activity imaging and combination with optogenetics. *Front. Mol. Neurosci.* **2013**, *6*, 2, doi:10.3389/fnmol.2013.00002.

374. Dana, H.; Mohar, B.; Sun, Y.; Narayan, S.; Gordus, A.; Hasseman, J.P.; Tsegaye, G.; Holt, G.T.; Hu, A.; Walpita, D. Sensitive red protein calcium indicators for imaging neural activity. *eLife* **2016**, *5*, doi:10.7554/eLife.12727.

375. Wu, J.; Prole, D.L.; Shen, Y.; Lin, Z.; Gnanasekaran, A.; Liu, Y.; Chen, L.; Zhou, H.; Chen, S.R.W.; Usachev, Y.M., et al. Red fluorescent genetically encoded Ca2+ indicators for use in mitochondria and endoplasmic reticulum. *Biochem. J.* **2014**, *464*, 13-22, doi:10.1042/BJ20140931.

376. Kredel, S.; Oswald, F.; Nienhaus, K.; Deuschle, K.; Röcker, C.; Wolff, M.; Heilker, R.; Nienhaus, G.U.; Wiedenmann, J. mRuby, a Bright Monomeric Red Fluorescent Protein for Labeling of Subcellular Structures. *PLoS ONE* **2009**, *4*, e4391, doi:10.1371/journal.pone.0004391.

377. Bajar, B.T.; Wang, E.S.; Lam, A.J.; Kim, B.B.; Jacobs, C.L.; Howe, E.S.; Davidson, M.W.; Lin, M.Z.; Chu, J. Improving brightness and photostability of green and red fluorescent proteins for live cell imaging and FRET reporting. *Sci. Rep.* **2016**, *6*, doi:10.1038/srep20889.

378. Shen, Y.; Dana, H.; Abdelfattah, A.S.; Patel, R.; Shea, J.; Molina, R.S.; Rawal, B.; Rancic, V.; Chang, Y.-F.; Wu, L., et al. A genetically encoded Ca(2+) indicator based on circularly permutated sea anemone red fluorescent protein eqFP578. *BMC Biol.* **2018**, *16*, doi:10.1186/s12915-018-0480-0.

379. Dana, H.; Sun, Y.; Mohar, B.; Hulse, B.K.; Kerlin, A.M.; Hasseman, J.P.; Tsegaye, G.; Tsang, A.; Wong, A.; Patel, R., et al. High-performance calcium sensors for imaging activity in neuronal populations and microcompartments. *Nat. Methods* **2019**, *16*, 649-657, doi:10.1038/s41592-019-0435-6.

380. Tallini, Y.N.; Ohkura, M.; Choi, B.-R.; Ji, G.; Imoto, K.; Doran, R.; Lee, J.; Plan, P.; Wilson, J.; Xin, H.-B. Imaging cellular signals in the heart in vivo: Cardiac expression of the high-signal Ca2+ indicator GCaMP2. *Proc. Natl. Acad. Sci. USA* **2006**, *103*, 4753-4758, doi:10.1073/pnas.0509378103.

381. Tsien, R.; Pozzan, T. [14] Measurement of cytosolic free Ca2+ with quin2. In *Methods in Enzymology*, Academic Press: 1989; Vol. 172, pp. 230-262.

382. Lam, A.J.; St-Pierre, F.; Gong, Y.; Marshall, J.D.; Cranfill, P.J.; Baird, M.A.; McKeown, M.R.; Wiedenmann, J.; Davidson, M.W.; Schnitzer, M.J., et al. Improving FRET dynamic range with bright green and red fluorescent proteins. *Nat. Methods* **2012**, *9*, 1005, doi:10.1038/nmeth.2171.

383. Inoue, M.; Takeuchi, A.; Horigane, S.-i.; Ohkura, M.; Gengyo-Ando, K.; Fujii, H.; Kamijo, S.; Takemoto-Kimura, S.; Kano, M.; Nakai, J. Rational design of a high-affinity, fast, red calcium indicator R-CaMP2. *Nat. Methods* **2015**, *12*, 64-70, doi:10.1038/nmeth.3185.

384. Inoue, M.; Takeuchi, A.; Manita, S.; Horigane, S.-i.; Sakamoto, M.; Kawakami, R.; Yamaguchi, K.; Otomo, K.; Yokoyama, H.; Kim, R. Rational engineering of XCaMPs, a multicolor GECI suite for in vivo imaging of complex brain circuit dynamics. *Cell* **2019**, *177*, 1346-1360. e1324, doi:10.1016/j.cell.2019.04.007.

385. Suzuki, J.; Kanemaru, K.; Iino, M. Genetically Encoded Fluorescent Indicators for Organellar Calcium Imaging. *Biophys. J.* **2016**, *111*, 1119-1131, doi:10.1016/j.bpj.2016.04.054.

386. Grienberger, C.; Konnerth, A. Imaging Calcium in Neurons. *Neuron* **2012**, *73*, 862-885, doi:10.1016/j.neuron.2012.02.011.

387. Tromberg, B.J.; Shah, N.; Lanning, R.; Cerussi, A.; Espinoza, J.; Pham, T.; Svaasand, L.; Butler, J. Non-invasive in vivo characterization of breast tumors using photon migration spectroscopy. *Neoplasia* **2000**, *2*, 26-40, doi:10.1038/sj.neo.7900082.

388. Lyons, S.K.; Patrick, P.S.; Brindle, K.M. Imaging mouse cancer models in vivo using reporter transgenes. *Cold Spring Harb. Protoc.* **2013**, *2013*, 685-699, doi:10.1101/pdb.top069864.

389. Miller, D.R.; Jarrett, J.W.; Hassan, A.M.; Dunn, A.K. Deep tissue imaging with multiphoton fluorescence microscopy. *Curr. Opin. Biomed. Eng.* **2017**, *4*, 32-39, doi:10.1016/j.cobme.2017.09.004.

390. Shen, Y.; Lai, T.; Campbell, R.E. Red fluorescent proteins (RFPs) and RFP-based biosensors for neuronal imaging applications. *Neurophotonics* **2015**, *2*, 031203, doi:10.1117/1.NPh.2.3.031203.

391. Abbyad, P.; Childs, W.; Shi, X.; Boxer, S.G. Dynamic Stokes shift in green fluorescent protein variants. *Proc. Natl. Acad. Sci. USA* **2007**, *104*, 20189-20194, doi:10.1073/pnas.0706185104.

392. Lin, M.Z.; McKeown, M.R.; Ng, H.-L.; Aguilera, T.A.; Shaner, N.C.; Campbell, R.E.; Adams, S.R.; Gross, L.A.; Ma, W.; Alber, T., et al. Autofluorescent Proteins with Excitation in the Optical Window for Intravital Imaging in Mammals. *Chem. Biol.* **2009**, *16*, 1169-1179, doi:10.1016/j.chembiol.2009.10.009.

393. Strack, R.L.; Hein, B.; Bhattacharyya, D.; Hell, S.W.; Keenan, R.J.; Glick, B.S. A rapidly maturing far-red derivative of DsRed-Express2 for whole-cell labeling. *Biochemistry (Mosc.)* **2009**, *48*, 8279-8281, doi:10.1021/bi900870u.

394. Shen, Y.; Chen, Y.; Wu, J.; Shaner, N.C.; Campbell, R.E. Engineering of mCherry variants with long Stokes shift, red-shifted fluorescence, and low cytotoxicity. *PLoS ONE* **2017**, *12*, e0171257, doi:10.1371/journal.pone.0171257.

395. Shcherbo, D.; Murphy, C.S.; Ermakova, G.V.; Solovieva, E.A.; Chepurnykh, T.V.; Shcheglov, A.S.; Verkhusha, V.V.; Pletnev, V.Z.; Hazelwood, K.L.; Roche, P.M., et al. Far-red fluorescent tags for protein imaging in living tissues. *Biochem. J.* **2009**, *418*, 567-574, doi:10.1042/BJ20081949.

396. Morozova, K.S.; Piatkevich, K.D.; Gould, T.J.; Zhang, J.; Bewersdorf, J.; Verkhusha, V.V. Far-red fluorescent protein excitable with red lasers for flow cytometry and superresolution STED nanoscopy. *Biophys. J.* **2010**, *99*, L13-L15, doi:10.1016/j.bpj.2010.04.025.

397. Chu, J.; Haynes, R.D.; Corbel, S.Y.; Li, P.; González-González, E.; Burg, J.S.; Ataie, N.J.; Lam, A.J.; Cranfill, P.J.; Baird, M.A., et al. Non-invasive intravital imaging of cellular differentiation with a bright red-excitable fluorescent protein. *Nat. Methods* **2014**, *11*, 572-578, doi:10.1038/nmeth.2888.

398. Bajar, B.T.; Lam, A.J.; Badiee, R.K.; Oh, Y.-H.; Chu, J.; Zhou, X.X.; Kim, N.; Kim, B.B.; Chung, M.; Yablonovitch, A.L., et al. Fluorescent indicators for simultaneous reporting of all four cell cycle phases. *Nat. Methods* **2016**, *13*, 993-996, doi:10.1038/nmeth.4045.

399. Hense, A.; Prunsche, B.; Gao, P.; Ishitsuka, Y.; Nienhaus, K.; Nienhaus, G.U. Monomeric Garnet, a far-red fluorescent protein for live-cell STED imaging. *Sci. Rep.* **2015**, *5*, 18006, doi:10.1038/srep18006.

400. Matela, G.; Gao, P.; Guigas, G.; Eckert, A.F.; Nienhaus, K.; Ulrich Nienhaus, G. A far-red emitting fluorescent marker protein, mGarnet2, for microscopy and STED nanoscopy. *Chemical Communications (Cambridge)* **2017**, *53*, 979-982, doi:10.1039/C6CC09081H.

401. Wannier, T.M.; Gillespie, S.K.; Hutchins, N.; McIsaac, R.S.; Wu, S.-Y.; Shen, Y.; Campbell, R.E.; Brown, K.S.; Mayo, S.L. Monomerization of far-red fluorescent proteins. *Proc. Natl. Acad. Sci. USA* **2018**, *115*, E11294-E11301, doi:10.1073/pnas.1807449115.

402. Chen, T.-W.; Wardill, T.J.; Sun, Y.; Pulver, S.R.; Renninger, S.L.; Baohan, A.; Schreiter, E.R.; Kerr, R.A.; Orger, M.B.; Jayaraman, V., et al. Ultrasensitive fluorescent proteins for imaging neuronal activity. *Nature* **2013**, *499*, 295, doi:10.1038/nature12354.

403. Wu, J.; Liu, L.; Matsuda, T.; Zhao, Y.; Rebane, A.; Drobizhev, M.; Chang, Y.-F.; Araki, S.; Arai, Y.; March, K., et al. Improved orange and red Ca2+ indicators and photophysical considerations for optogenetic applications. *ACS Chem. Neurosci.* **2013**, *4*, 963-972, doi:10.1021/cn400012b.

404. Farhi, S.L.; Parot, V.J.; Grama, A.; Yamagata, M.; Abdelfattah, A.S.; Adam, Y.; Lou, S.; Jun Kim, J.; Campbell, R.E.; Cox, D.D., et al. Wide-area all-optical neurophysiology in acute brain slices. *J. Neurosci.* **2019**, 10.1523/JNEUROSCI.0168-19.2019, doi:10.1523/JNEUROSCI.0168-19.2019.

405. Qian, Y.; Piatkevich, K.D.; Mc Larney, B.; Abdelfattah, A.S.; Mehta, S.; Murdock, M.H.; Gottschalk, S.; Molina, R.S.; Zhang, W.; Chen, Y., et al. A genetically encoded near-infrared fluorescent calcium ion indicator. *Nat. Methods* **2019**, *16*, 171-174, doi:10.1038/s41592-018-0294-6.

406. St-Pierre, F.; Marshall, J.D.; Yang, Y.; Gong, Y.; Schnitzer, M.J.; Lin, M.Z. High-fidelity optical reporting of neuronal electrical activity with an ultrafast fluorescent voltage sensor. *Nat. Neurosci.* **2014**, *17*, 884-889, doi:10.1038/nn.3709.

407. Gross, L.A.; Baird, G.S.; Hoffman, R.C.; Baldridge, K.K.; Tsien, R.Y. The structure of the chromophore within DsRed, a red fluorescent protein from coral. *Proc. Natl. Acad. Sci. USA* **2000**, *97*, 11990-11995, doi:10.1073/pnas.97.22.11990.

408. Molina, R.S.; Qian, Y.; Wu, J.; Shen, Y.; Campbell, R.E.; Drobizhev, M.; Hughes, T.E. Understanding the Fluorescence Change in Red Genetically Encoded Calcium Ion Indicators. *Biophys. J.* **2019**, *116*, 1873-1886, doi:10.1016/j.bpj.2019.04.007.

409. Drobizhev, M.; Molina, R.; Hughes, T. Characterizing the Two-photon Absorption Properties of Fluorescent Molecules in the 680-1300 nm Spectral Range. *Bio Protoc.* **2020**, *10*, e3498, doi:10.21769/BioProtoc.3498.

410. Abdelfattah, A.S.; Kawashima, T.; Singh, A.; Novak, O.; Liu, H.; Shuai, Y.; Huang, Y.-C.; Campagnola, L.; Seeman, S.C.; Yu, J., et al. Bright and photostable chemigenetic indicators for extended in vivo voltage imaging. *Science* **2019**, *365*, 699-704, doi:10.1126/science.aav6416.

411. Carlson, H.J.; Campbell, R.E. Mutational analysis of a red fluorescent protein-based calcium ion indicator. *Sensors* **2013**, *13*, 11507-11521.

412. Carlson, H.J.; Campbell, R.E. Circular permutated red fluorescent proteins and calcium ion indicators based on mCherry. *Protein Eng. Des. Sel.* **2013**, *26*, 763-772.

413. Zhang, F.; Gradinaru, V.; Adamantidis, A.R.; Durand, R.; Airan, R.D.; de Lecea, L.; Deisseroth, K. Optogenetic interrogation of neural circuits: technology for probing mammalian brain structures. *Nat. Protoc.* **2010**, *5*, 439-456, doi:10.1038/nprot.2009.226.

414. Molina, R.S.; Tran, T.M.; Campbell, R.E.; Lambert, G.G.; Salih, A.; Shaner, N.C.; Hughes, T.E.; Drobizhev, M. Blue-Shifted Green Fluorescent Protein Homologues Are Brighter than Enhanced Green Fluorescent Protein under Two-Photon Excitation. *The Journal of Physical Chemistry Letters* **2017**, *8*, 2548-2554, doi:10.1021/acs.jpclett.7b00960.

415. Podgorski, K.; Ranganathan, G. Brain heating induced by near-infrared lasers during multiphoton microscopy. *J. Neurophysiol.* **2016**, *116*, 1012-1023, doi:10.1152/jn.00275.2016.

416. Patriarchi, T.; Cho, J.R.; Merten, K.; Howe, M.W.; Marley, A.; Xiong, W.-H.; Folk, R.W.; Broussard, G.J.; Liang, R.; Jang, M.J., et al. Ultrafast neuronal imaging of dopamine dynamics with designed genetically encoded sensors. *Science* **2018**, 10.1126/science.aat4422, doi:10.1126/science.aat4422.

417. Shen, Y.; Wu, S.-Y.; Rancic, V.; Aggarwal, A.; Qian, Y.; Miyashita, S.-I.; Ballanyi, K.; Campbell, R.E.; Dong, M. Genetically encoded fluorescent indicators for imaging intracellular potassium ion concentration. *Commun. Biol.* **2019**, *2*, 18, doi:10.1038/s42003-018-0269-2.

418. Scheepers, G.H.; Lycklama a Nijeholt, J.A.; Poolman, B. An updated structural classification of substrate-binding proteins. *FEBS Lett.* **2016**, *590*, 4393-4401, doi:10.1002/1873-3468.12445.

A. Appendix of DNA sequences

Table A-1 - Primers used for testing different insertion points in PEB1a.

Primer Name	Sequence[a]
LVcpsfGFP-A165PEB1a-R	TCCGCTGTGATATACACATTGTGAGACACCAGCGCATCGAGGGCCGC
LVcpsfGFP-D29PEB1a-R	TCCGCTGTGATATACACATTGTGAGACACCAGATCCAAAAGTGCATAATGAGGAACGT
LVcpsfGFP-D164PEB1a-R	TCCGCTGTGATATACACATTGTGAGACACCAGATCGAGGGCCGCCTTG
LVcpsfGFP-D183PEB1a-R	CGCTGTGATATACACATTGTGAGACACCAGATCAACATAGCCCAGCAGAATTGATTTATC
LVcpsfGFP-D184PEB1a-R	TCCGCTGTGATATACACATTGTGAGACACCAGATCATCAACATAGCCCAGCAGAATTG
LVcpsfGFP-D191PEB1a-R	CGCTGTGATATACACATTGTGAGACACCAGATCAGGAAGAATCTCGGATTTATCATCAAC
LVcpsfGFP-E97PEB1a-R	CTGTGATATACACATTGTGAGACACCAGCTCACTAAAATTGTAGATTCGTTTCCTCTCGG
LVcpsfGFP-E194PEB1a-R	TCCGCTGTGATATACACATTGTGAGACACCAGCTCGAAGGAATCAGGAAGAATCTCGG
LVcpsfGFP-H220PEB1a-R	CTGTGATATACACATTGTGAGACACCAGATGTTCTTTAACGAAGTCGTCAACATACTTCG
LVcpsfGFP-I144PEB1a-R	TCCGCTGTGATATACACATTGTGAGACACCAGTATTTTCTTTGCGGCCTCTCCTATAGC
LVcpsfGFP-K48PEB1a-R	TCCGCTGTGATATACACATTGTGAGACACCAGCTTTGCCAAGAGCTTGGCG
LVcpsfGFP-K55PEB1a-R	TCCGCTGTGATATACACATTGTGAGACACCAGCTTATCATCACCCAGTATGCTCTTTGCC
LVcpsfGFP-K65PEB1a-R	TCCGCTGTGATATACACATTGTGAGACACCAGTTTTGCGTTCACAGCAACCAACTTG
LVcpsfGFP-K90PEB1a-R	CTGTGATATACACATTGTGAGAGACCAGTTTCCTCTCGGGTGTGATCGTAAATG
LVcpsfGFP-K110PEB1a-R	TCCGCTGTGATATACACATTGTGAGACACCAGTTTCAATACAAGAAGTCCGATAGCGTC
LVcpsfGFP-K112PEB1a-R	CGCTGTGATATACACATTGTGAGACACCAGCTTCTCTTTCAATACAAGAAGTCCGATAGC
LVcpsfGFP-K121PEB1a-R	TGTGATATACACATTGTGAGACACCAGTTTCATATCTGCCAAGCTCTTATATTTCTTCTC
LVcpsfGFP-K134PEB1a-R	TCCGCTGTGATATACACATTGTGAGACACCAGCTTCGTGGTTGCGGCCT
LVcpsfGFP-K142PEB1a-R	TCCGCTGTGATATACACATTGTGAGACACCAGCTTTGCGGCCTCTCCTATAGC
LVcpsfGFP-K143PEB1a-R	TCCGCTGTGATATACACATTGTGAGACACCAGTTTCTTTGCGGCCTCTCCTATAGC
LVcpsfGFP-K149PEB1a-R	CGCTGTGATATACACATTGTGAGACACCAGTTTAACGTCTATACCTATTTTCTTTGCGGC
LVcpsfGFP-K166PEB1a-R	TCCGCTGTGATATACACATTGTGAGACACCAGTTTCGCATCGAGGGCCG
LVcpsfGFP-K203PEB1a-R	TCCGCTGTGATATACACATTGTGAGACACCAGCTTGGTAACTATACCGTATGACTGAGGC

LVcpsfGFP-K204PEB1a-R	GCTGTGATATACACATTGTGAGACACCAGTTTCTTGGTAACTATACCGTATGACTGAGGC
LVcpsfGFP-K218PEB1a-R	CCGCTGTGATATACACATTGTGAGACACCAGTTTAACGAAGTCGTCAACATACTTCGCAA
LVcpsfGFP-K221PEB1a-R	GCTGTGATATACACATTGTGAGACACCAGCTTATGTTCTTTAACGAAGTCGTCAACATAC
LVcpsfGFP-N73PEB1a-R	TCCGCTGTGATATACACATTGTGAGACACCAGGTTGTCCAAAAGTGGTCCTCTCG
LVcpsfGFP-N222PEB1a-R	CTGTGATATACACATTGTGAGACACCAGATTCTTATGTTCTTTAACGAAGTCGTCAACAT
LVcpsfGFP-P23PEB1a-R	TCCGCTGTGATATACACATTGTGAGACACCAGAGGAACGTCGTTCTTCACACC
LVcpsfGFP-P87PEB1a-R	TCCGCTGTGATATACACATTGTGAGAGACCAGGGGTGTGATCGTAAATGTCGCG
LVcpsfGFP-P157PEB1a-R	TGTGATATACACATTGTGAGACACCAGTGGATAATCTGGAAATTCGGAAAATTTAACGTC
LVcpsfGFP-P190PEB1a-R	CTGTGATATACACATTGTGAGACACCAGAGGAAGAATCTCGGATTTATCATCAACATAGC
LVcpsfGFP-P207PEB1a-R	TCCGCTGTGATATACACATTGTGAGACACCAGAGGGTCGTCTTTCTTGGTAACTATACC
LVcpsfGFP-Q30PEB1a-R	TCCGCTGTGATATACACATTGTGAGACACCAGCTGATCCAAAAGTGCATAATGAGGAACG
LVcpsfGFP-R91PEB1a-R	CTGTGATATACACATTGTGAGAGACCAGTCGTTTCCTCTCGGGTGTGATC
LVcpsfGFP-S192PEB1a-R	CGCTGTGATATACACATTGTGAGACACCAGGGAATCAGGAAGAATCTCGGATTTATCATC
LVcpsfGFP-V182PEB1a-R	TCCGCTGTGATATACACATTGTGAGACACCAGAACATAGCCCAGCAGAATTGATTTATCG
NPcpsfGFP-A31-PEB1a-F	CATAAATTGGAGTATAACTTTAACAACCCTGCTACGGGCGAAATTAAGGG
NPcpsfGFP-A165PEB1a-F	CATAAGTTGGAGTATAACTTTAACAACCCGGCGAAAAGAGTGGACGCCTTC
NPcpsfGFP-A208PEB1a-F	CATAAGTTGGAGTATAACTTTAACAACCCGGCTTTTGCGAAGTATGTTGACGAC
NPcpsfGFP-D183PEB1a-F	CATAAATTGGAGTATAACTTTAACAACCCTGATGATAAATCCGAGATTCTTCCTGATTCC
NPcpsfGFP-D184PEB1a-F	CATAAATTGGAGTATAACTTTAACAACCCTGATAAATCCGAGATTCTTCCTGATTCCTTC
NPcpsfGFP-D191PEB1a-F	CATAAGTTGGAGTATAACTTTAACAACCCGGATTCCTTCGAGCCTCAGTCATACG
NPcpsfGFP-D205PEB1a-F	CATAAGTTGGAGTATAACTTTAACAACCCGGACGACCCTGCTTTTGCGAAG
NPcpsfGFP-E88PEB1a-F	ATAAGTTGGAGTATAACTTTAACAACCCGGAGAGGAAACGAATCTACAATTTTAGTGAGC
NPcpsfGFP-E111PEB1a-F	CATAAGTTGGAGTATAACTTTAACAACCCGGAGAAGAAATATAAGAGCTTGGCAGATATG
NPcpsfGFP-E219PEB1a-F	CATAAGTTGGAGTATAACTTTAACAACCCGGAACATAAGAATGAAATCGATGCACTGGC
NPcpsfGFP-E223PEB1a-F	CATAAGTTGGAGTATAACTTTAACAACCCGGAAATCGATGCACTGGCCAAAAAATG
NPcpsfGFP-F150PEB1a-F	AGTTGGAGTATAACTTTAACAACCCGTTTTCCGAATTTCCAGATTATCCATCTATCAAGG
NPcpsfGFP-F193PEB1a-F	CATAAGTTGGAGTATAACTTTAACAACCCGTTCGAGCCTCAGTCATACGGTATAG

NPcpsfGFP-G74PEB1a-F	CATAAGTTGGAGTATAACTTTAACAACCCGGGCAGCGTAGATGCCGTTATCG
NPcpsfGFP-G122PEB1a-F	CATAAGTTGGAGTATAACTTTAACAACCCGGGAGCGAATATAGGAGTGGCAC
NPcpsfGFP-G145PEB1a-F	ATAAGTTGGAGTATAACTTTAACAACCCGGGTATAGACGTTAAATTTTCCGAATTTCCAG
NPcpsfGFP-H24PEB1a-F	CATAAATTGGAGTATAACTTTAACAACCCTCATTATGCACTTTTGGATCAGGC
NPcpsfGFP-I92PEB1a-F	ATAAGTTGGAGTATAACTTTAACAACCCGATCTACAATTTTAGTGAGCCTTACTACCAAG
NPcpsfGFP-I144PEB1a-F	AGTTGGAGTATAACTTTAACAACCCGATAGGTATAGACGTTAAATTTTCCGAATTTCCAG
NPcpsfGFP-K56PEB1a-F	CATAAGTTGGAGTATAACTTTAACAACCCGAAAATCAAGTTGGTTGCTGTGAACGC
NPcpsfGFP-K113PEB1a-F	ATAAGTTGGAGTATAACTTTAACAACCCGAAATATAAGAGCTTGGCAGATATGAAAGGAG
NPcpsfGFP-K135PEB1a-F	CATAAGTTGGAGTATAACTTTAACAACCCGAAGGCTATAGGAGAGGCCGC
NPcpsfGFP-K143PEB1a-F	TGGAGTATAACTTTAACAACCCGAAAATAGGTATAGACGTTAAATTTTCCGAATTTCCAG
NPcpsfGFP-K166PEB1a-F	CATAAGTTGGAGTATAACTTTAACAACCCGAAAAGAGTGGACGCCTTCTCCG
NPcpsfGFP-K185PEB1a-F	CATAAGTTGGAGTATAACTTTAACAACCCGAAATCCGAGATTCTTCCTGATTCCTTC
NPcpsfGFP-K204PEB1a-F	CATAAGTTGGAGTATAACTTTAACAACCCGAAAGACGACCCTGCTTTTGCG
NPcpsfGFP-K221PEB1a-F	CATAAGTTGGAGTATAACTTTAACAACCCGAAGAATGAAATCGATGCACTGGCC
NPcpsfGFP-N222PEB1a-F	CATAAGTTGGAGTATAACTTTAACAACCCGAATGAAATCGATGCACTGGCCAA
NPcpsfGFP-P98PEB1a-F	CATAAGTTGGAGTATAACTTTAACAACCCGCCTTACTACCAAGACGCTATCGGAC
NPcpsfGFP-P195PEB1a-F	AGTTGGAGTATAACTTTAACAACCCGCCTCAGTCATACGGTATAGTTACCAAGAAAGACG
NPcpsfGFP-Q30-PEB1a-F	CATAAATTGGAGTATAACTTTAACAACCCTCAGGCTACGGGCGAAATTAAGG
NPcpsfGFP-R91PEB1a-F	ATAAGTTGGAGTATAACTTTAACAACCCGCGAATCTACAATTTTAGTGAGCCTTACTACC
NPcpsfGFP-R167PEB1a-F	CATAAGTTGGAGTATAACTTTAACAACCCGAGAGTGGACGCCTTCTCC
NPcpsfGFP-S49PEB1a-F	AAGTTGGAGTATAACTTTAACAACCCGAGCATACTGGGTGATGATAAGAAAATCAAGTTG
NPcpsfGFP-S158PEB1a-F	CATAAGTTGGAGTATAACTTTAACAACCCGTCTATCAAGGCGGCCCTC
NPcpsfGFP-S192PEB1a-F	CATAAGTTGGAGTATAACTTTAACAACCCGTCCTTCGAGCCTCAGTCATACG
NPcpsfGFP-T66PEB1a-F	CATAAGTTGGAGTATAACTTTAACAACCCGACGAGAGGACCACTTTTGGACAAC
LV(P87K90R91)-cpsfGFP-F	CTGGTCTCTCACAATGTGTATATCACAGCGGACAAG
LVgeneral-cpsfGFP-F	CTGGTGTCTCACAATGTGTATATCACAGCGGACAAGC
NP(A31D183D184)-cpsfGFP-R	AGGGTTGTTAAAGTTATACTCCAATTTATGACCCAGTATATTACCATC

NPgeneral-cpsfGFP-R	CGGGTTGTTAAAGTTATACTCCAACTTATGACC

[a] Sequences in green correspond to cpsfGFP while sequences in black bind to different regions of pBAD-PEB1a. In primers that bind to pBAD-PEB1a, the green sequences are appended for assembly with the cpsfGFP fragment. Differences in the overlap region are silent mutations meant to disrupt hairpin structures.

ATGGGGGGTTCTCATCATCATCATCATCATGGTATGGCTAGCATGACTGGTGGACAGCAAATGGGTCGGGATCTGT
ACGAC*GATGACGATAAGGATCCGAGCTCGAG*AATGGGAAAGCTGGAGTCAATCAAGTCCAAAGGCCAGTTGATCGT
GGGTGTGAAGAACGACGTTCCTCATTATGCACTTTTGGATCAGGCTACGGGCGAAATTAAGGGGTTTGAGGTGGAT
GTCGCCAAGCTCTTGGCAAAGAGCATACTGGGTGATGATAAGAAAATCAAGTTGGTTGCTGTGAACGCAAAAACGA
GAGGACCACTTTTGGACAACGGCAGCGTAGATGCCGTTATCGCGACATTTACGATCACACCCGAGAGGAAACGAAT
CTACAATTTTAGTGAGCCTTACTACCAAGACGCTATCGGACTTCTTGTATTGAAAGAGAAGAAATATAAGAGCTTG
GCAGATATGAAAGGAGCGAATATAGGAGTGGCACAGGCCGCAACCGTTAAGAAGGCTATAGGAGAGGCCGCAAAGA
AAATAGGTATAGACGTTAAATTTTCCGAATTTCCAGATTATCCATCTATCAAGGCGGCCCTCGATGCGAAAAGAGT
GGACGCCTTCTCCACGGATAAATCAATTCTGCTGGGCTATGTTGATGATAAATCCGAGATTCTTCCTGATTCCTTC
GAGCTGGTGTCTCACAATGTGTATATCACAGCGGACAAGCAGAAGAACGGGATAAAAGCGAATTTCAAGATTCGAC
ACAATGTCGAAGATGGGACCGTTCAGCTCGCCGACCATTACCAGCAGAACACACCCATAGGCGATGGACCCGTTTT
GCTTCCTGATAATCACTATTTGTCTACGCAAAGTGTGTTGAGTAAGGATCCAAACGAAAAGCGCGACCATATGGTG
TTGCTGGAATTTGTCACTGCCGCGGGCATTACGCATGGGATGGATGAACTCTACAAAGGGGGAACTGGCGGGTCTA
TGGTGTCCAAAGGGGAAGAACTGTTTACTGGAGTAGTTCCAATCCTTGTGGAACTCGACGGTGATGTAAACGGACA
TAAATTCAGCGTACGAGGTGAGGGAGAGGGAGATGCCACAAACGGCAAACTGACTCTCAAATTTATATGCACTACC
GGCAAACTGCCAGTCCCTTGGCCTACCTTGGTAACCACTTTGACATATGGCGTTCAATGCTTTTCCAGGTACCCTG
ATCACATGAAACGACACGATTTCTTTAAAAGCGCGATGCCAGAAGGGTATGTGCAGGAGCGGACTATAAGTTTTAA
GGACGACGGGACCTATAAAACTAGGGCAGAGGTCAAATTCGAGGGCGATACGCTTGTCAACAGGATAGAGCTCAAG
GGAATAGATTTTAAGGAGGATGGTAATATACTGGGTCATAAGTTGGAGTATAACTTTAACACTCGGCCTCTGTCAT
ACGGTATAGTTACCAAGAAAGACGACCCTGCTTTTGCGAAGTATGTTGGCGACTTCGTTAAAGAACATAAGAATGA
AATCGATGCACTGGCCAAAAAATGGGGACTGTAA*AAGCTTGGCTGTTTTGGCGGATG*

Figure A-1 - DNA sequence for ODIN1a in pBAD/HisB.

DNA sequence for ODIN1a in pBAD/HisB annotated for its features. Sequences in blue are part of the pBAD vector (beginning at the start codon of the reading frame and including its N-terminal tags; bolded sequence indicates the polyhistidine tag). Bases highlighted in yellow indicate the XhoI and HindIII restriction sites. Orange sequence is for PEB1a, green sequence is cpsfGFP, and grey sequences are for the linker regions. Italicized bases

indicate the homologous sequences used for assembly; the complements of these italicized bases were used as the primers to generate linearized vector by PCR.

ATGGGGGGTTCTCATCATCATCATCATCATGGTATGGCTAGCATGACTGGTGGACAGCAAATGGGTCGGGATCTGT
ACGAC*GATGACGATAAGGATCCGAGCTCGAG*AATGGGAAAGCTGGAGTCAATCAAGTCCAAAGGCCAGTTGATCGT
GGGTGTGAAGAACGACGTTCCTCATTATGCACTTTTGGATCAGGCTACGGGCGAAATTAAGGGGTTTGAGGTGGAT
GTCGCCAAGCTCTTGGCAAAGAGCATACTGGGTGATGATAAGAAAATCAAGTTGGTTGCTGTGAACGCAAAAACGA
GAGGACCACTTTTGGACAACGGCAGCGTAGATGCCGTTATCGCGACATTTACGATCACACCCGAGAGGAAACGAAT
CTACAATTTTAGTGAGCCTTACTACCAAGACGCTATCGGACTTCTTGTATTGAAAGAGAAGAAATATAAGAGCTTG
GCAGATATGAAAGGAGCGAATATAGGAGTGGCACAGGCCGCAACCGGGAAGAAGGCTATAGGAGAGGCCGCAAAGA
AAATAGGTATAGACGTTAAATTTTCCGAATTTCCAGATTATCCATCTATCAAGGCGGCCCTCGATGCGAAAAGAGT
GGACGCCTTCTCCACCGATAAATCAATTCTGCTGGGCTATGTTGATGATAAATCCGAGATTCTTCCTGATTCCTTC
GAGCTGGTGTCTCACAATGTGTATATCACAGCGGACAAGCAGAAGAACGGGATAAAAGCGAATTTCAAGATTCGAC
ACAATGTCGAAGATGGGACCGTTCAGCTCGCCGACCATTACCAGCAGAACACACCCATAGGCGATGGACCCGTTTT
GCTTCCTGATAATCACTATTTGTCTACGCAAAGTGTGTTGAGTAAGGATCCAAACGAAAAGCGCGACCATATGGTG
TTGCTGGAATTTGTCACTGCCGCGGGCATTACGCATGGGATGGATGAACTCTACAAAGGGGGAACTGGCGGGTCTA
TGGTGTCCAAAGGGGAAGAACTGTTTACTGGAGTAGTTCCAATCCTTGTGGAACTCGACGGTGATGTAAACGGACA
TAAATTCAGCGTACGAGGTGAGGGAGAGGGAGATGCCACAAACGGCAAACTGACTCTCAAATTTATATGCACTACC
GGCAAACTGCCAGTCCCTTGGCCTACCTTGGTAACCACTTTGACATATGGCGTTCAATGCTTTTCCAGGTACCCTG
ATCACATGAAACGACACGATTTCTTTAAAAGCGCGATGCCAGAAGGGTATGTGCAGGAGCGGACTATAAGTTTTAA
GGACGACGGGACCTATAAAACTAGGGCAGAGGTCAAATTCGAGGGCGATACGCTTGTCAACAGGATAGAGCTCAAG
GGAATAGATTTTAAGGAGGATGGTAATATACTGGGTCATAAGTTGGAGTATAACTTTAACACTCGGCCTCTGTCAT
ACGGTATAGTTACCAAGAAAGACGACCCTGCTTTTGCGAAGTATGTTGGCGACTTCGTTAAAGAACATAAGAATGA
AATCGATGCACTGGCCAAAAAATGGGGACTGTAA*AAGCTTGGCTGTTTTGGCGGATG*

Figure A-2 - DNA sequence for ODIN1b in pBAD/HisB.

DNA sequence for ODIN1b in pBAD/HisB coloured and annotated similar to **Figure A-1**.

ATGGGGGGTTCTCATCATCATCATCATCATGGTATGGCTAGCATGACTGGTGGACAGCAAATGGGTCGGGATCTGT
ACGAC*GATGACGATAAGGATCCGAGCTCGAG*AATGGGAAAGCTGGAGTCAATCAAGTCCAAAGGCCAGTTGATCGT
GGGTGTGAAGAACGACGTTCCTCATTATGCACTTTTGGATCAGGCTACGGGCGAAATTAAGGGGTTTGAGGTGGAT
GTCGCCAAGCTCTTGGCAAAGAGCATACTGGGTGATGATAAGAAAATCAAGTTGGTTGCTGTGAACGCAAAAACGA
GAGGACCACTTTTGGACAACGGCAGCGTAGATGCCGTTATCGCGACATTTACGATCACACCCGAGAGGAAACGAAT
CTACAATTTTAGTGAGCCTTACTACCAAGACGCTATCGGACTTCTTGTATTGAAAGAGAAGAAATATAAGAGCTTG
GCAGATATGAAAGGAGCGAATATAGGAGTGGCACAGGCCGCAACCGGTAAGAAGGCTATAGGAGAGGCCGCAAAGA
AAATAGGTATAGACGTTAAATTTTCCGAATTTCCAGATTATCCATCTATCAAGGCGGCCCTCGATGCGAAAAGAGT
GGACGCCTTCTCCGGGGATAAATCAATTCTGCTGGGCTATGTTGATGATAAATCCGAGATTCTTCCTGATTCCTTC
GAGCTGGTGTCTCACAATGTGTATATCACAGCGGACAAGCAGAAGAACGGGATAAAAGCGAATTTCAAGATTCGAC
ACAATGTCGAAGATGGGACCGTTCAGCTCGCCGACCATTACCAGCAGAACACACCCATAGGCGATGGACCCGTTTT
GCTTCCTGATAATCACTATTTGTCTACGCAAAGTGTGTTGAGTAAGGATCCAAACGAAAAGCGCGACCATATGGTG
TTGCTGGAATTTGTCACTGCCGCGGGCATTACGCATGGGATGGATGAACTCTACAAAGGGGGAACTGGCGGGTCTA
TGGTGTCCAAAGGGGAAGAACTGTTTACTGGAGTAGTTCCAATCCTTGTGGAACTCGACGGTGATGTAAACGGACA
TAAATTCAGCGTACGAGGTGAGGGAGAGGGAGATGCCACAAACGGCAAACTGACTCTCAAATTTATATGCACTACC
GGCAAACTGCCAGTCCCTTGGCCTACCTTGGTAACCACTTTGACATATGGCGTTCAATGCTTTTCCAGGTACCCTG
ATCACATGAAACGACACGATTTCTTTAAAAGCGCGATGCCAGAAGGGTATGTGCAGGAGCGGACTATAAGTTTTAA
GGACGACGGGACCTATAAAACTAGGGCAGAGGTCAAATTCGAGGGCGATACGCTTGTCAACAGGATAGAGCTCAAG
GGAATAGATTTTAAGGAGGATGGTAATATACTGGGTCATAAGTTGGAGTATAACTTTAACACTCGGCCTCTGTCAT
ACGGTATAGTTACCAAGAAAGACGACCCTGCTTTTGCGAAGTATGTTGGCGACTTCGTTAAAGAACATAAGAATGA
AATCGATGCACTGGCCAAAAAATGGGGACTGTAA*AAGCTTGGCTGTTTTGGCGGATG*

Figure A-3 - DNA sequence for ODIN1c in pBAD/HisB.

DNA sequence for ODIN1c in pBAD/HisB coloured and annotated similar to **Figure A-1**.

ATGGAGACAGACACACTCCTGCTATGGGTACTGCTGCTCTGGGTTCCAGGTTCCACTGGTGACATGGGAAAGCT
GGAGTCAATCAAGTCCAAAGGCCAGTTGATCGTGGGTGTGAAGAACGACGTTCCTCATTATGCACTTTT
GGATCAGGCTACGGGCGAAATTAAGGGGTTTGAGGTGGATGTCGCCAAGCTCTTGGCAAAGAGCATACT
GGGTGATGATAAGAAAATCAAGTTGGTTGCTGTGAACGCAAAAACGAGAGGACCACTTTTGGACAACGG
CAGCGTAGATGCCGTTATCGCGACATTTACGATCACACCCGAGAGGAAACGAATCTACAATTTTAGTGA
GCCTTACTACCAAGACGCTATCGGACTTCTTGTATTGAAAGAGAAGAAATATAAGAGCTTGGCAGATAT
GAAAGGAGCGAATATAGGAGTGGCACAGGCCGCAACCGGGAAGAAGGCTATAGGAGAGGCCGCAAAGAA
AATAGGTATAGACGTTAAATTTTCCGAATTTCCAGATTATCCATCTATCAAGGCGGCCCTCGATGCGAA
AAGAGTGGACGCCTTCTCCACCGATAAATCAATTCTGCTGGGCTATGTTGATGATAAATCCGAGATTCT
TCCTGATTCCTTCGAGCTGGTGTCTCACAATGTGTATATCACAGCGGACAAGCAGAAGAACGGGATAAA
AGCGAATTTCAAGATTCGACACAATGTCGAAGATGGGACCGTTCAGCTCGCCGACCATTACCAGCAGAA
CACACCCATAGGCGATGGACCCGTTTTGCTTCCTGATAATCACTATTTGTCTACGCAAAGTGTGTTGAG
TAAGGATCCAAACGAAAAGCGCGACCATATGGTGTTGCTGGAATTTGTCACTGCCGCGGGCATTACGCA
TGGGATGGATGAACTCTACAAAGGGGGAACTGGCGGGTCTATGGTGTCCAAAGGGGAAGAACTGTTTAC
TGGAGTAGTTCCAATCCTTGTGGAACTCGACGGTGATGTAAACGGACATAAATTCAGCGTACGAGGTGA
GGGAGAGGGAGATGCCACAAACGGCAAACTGACTCTCAAATTTATATGCACTACCGGCAAACTGCCAGT
CCCTTGGCCTACCTTGGTAACCACTTTGACATATGGCGTTCAATGCTTTTCCAGGTACCCTGATCACAT
GAAACGACACGATTTCTTTAAAAGCGCGATGCCAGAAGGGTATGTGCAGGAGCGGACTATAAGTTTTAA
GGACGACGGGACCTATAAAACTAGGGCAGAGGTCAAATTCGAGGGCGATACGCTTGTCAACAGGATAGA
GCTCAAGGGAATAGATTTTAAGGAGGATGGTAATATACTGGGTCATAAGTTGGAGTATAACTTTAACAC
TCGGCCTCTGTCATACGGTATAGTTACCAAGAAAGACGACCCTGCTTTTGCGAAGTATGTTGGCGACTT
CGTTAAAGAACATAAGAATGAAATCGATGCACTGGCCAAAAAATGGGGACTGGAACAAAAACTCATCTC
AGAAGAGGATCTGAATGCTGTGGGCCAGGACACGCAGGAGGTCATCGTGGTGCCACACTCCTTGCCCTT
TAAGGTGGTGGTGATCTCAGCCATCCTGGCCCTGGTGGTGCTCACCATCATCTCCCTTATCATCCTCAT
CATGCTTTGGCAGAAGAAGCCACGTTAG

Figure A-4 - pMiniDisplay-ODIN1b sequence.

Annotated DNA sequence for ODIN1b inserted into pMiniDisplay. Sequences in black are part of pMiniDisplay, and the rest is coloured according to **Figure A-1**. For brevity, only the sequence for ODIN1b is shown, but other variants were inserted similarly.

GGGCTAACAGGAGGAATTAACCATGGGGGGTTCTAGCTCGAGA**ATG**GGACGTGGCGTTCCTCATATTGTTATGGTG
GACGCCTACAAACGCTATAAAT*CGGGAGGTGGTTCAGGC*ATGGGAAAGCTGGAGTCAATCAAGTCCAAAGGC
CAGTTGATCGTGGGTGTGAAGAACGACGTTCCTCATTATGCACTTTTGGATCAGGCTACGGGCGAAATT
AAGGGGTTTGAGGTGGATGTCGCCAAGCTCTTGGCAAAGAGCATACTGGGTGATGATAAGAAAATCAAG
TTGGTTGCTGTGAACGCAAAAACGAGAGGACCACTTTTGGACAACGGCAGCGTAGATGCCGTTATCGCG
ACATTTACGATCACACCCGAGAGGAAACGAATCTACAATTTTAGTGAGCCTTACTACCAAGACGCTATC
GGACTTCTTGTATTGAAAGAGAAGAAATATAAGAGCTTGGCAGATATGAAAGGAGCGAATATAGGAGTG
GCACAGGCCGCAACCGGGAAGAAGGCTATAGGAGAGGCCGCAAAGAAAATAGGTATAGACGTTAAATTT
TCCGAATTTCCAGATTATCCATCTATCAAGGCGGCCCTCGATGCGAAAAGAGTGGACGCCTTCTCCACC
GATAAATCAATTCTGCTGGGCTATGTTGATGATAAATCCGAGATTCTTCCTGATTCCTTCGAGCTGGTG
TCTCACAATGTGTATATCACAGCGGACAAGCAGAAGAACGGGATAAAAGCGAATTTCAAGATTCGACAC
AATGTCGAAGATGGGACCGTTCAGCTCGCCGACCATTACCAGCAGAACACACCCATAGGCGATGGACCC
GTTTTGCTTCCTGATAATCACTATTTGTCTACGCAAAGTGTGTTGAGTAAGGATCCAAACGAAAAGCGC
GACCATATGGTGTTGCTGGAATTTGTCACTGCCGCGGGCATTACGCATGGGATGGATGAACTCTACAAA
GGGGGAACTGGCGGGTCTATGGTGTCCAAAGGGGAAGAACTGTTTACTGGAGTAGTTCCAATCCTTGTG
GAACTCGACGGTGATGTAAACGGACATAAATTCAGCGTACGAGGTGAGGGAGAGGGAGATGCCACAAAC
GGCAAACTGACTCTCAAATTTATATGCACTACCGGCAAACTGCCAGTCCCTTGGCCTACCTTGGTAACC
ACTTTGACATATGGCGTTCAATGCTTTTCCAGGTACCCTGATCACATGAAACGACACGATTTCTTTAAA
AGCGCGATGCCAGAAGGGTATGTGCAGGAGCGGACTATAAGTTTTAAGGACGACGGGACCTATAAAACT
AGGGCAGAGGTCAAATTCGAGGGCGATACGCTTGTCAACAGGATAGAGCTCAAGGGAATAGATTTTAAG
GAGGATGGTAATATACTGGGTCATAAGTTGGAGTATAACTTTAACACTCGGCCTCTGTCATACGGTATA
GTTACCAAGAAAGACGACCCTGCTTTTGCGAAGTATGTTGGCGACTTCGTTAAAGAACATAAGAATGAA
ATCGATGCACTGGCCAAAAAATGGGGACTGC*AAGCTT*CCGGC***CATCATCATC*ATCATCAT**TAA

Figure A-5 - DNA sequence for cHis-pBAD-SpyTag003-ODIN1b.

DNA sequence for ODIN1b in cHis-pBAD with SpyTag003 at the N-terminus and annotated for its features. Other ODIN variants were inserted similarly. Sequences in blue are part of the vector (with the polyhistidine tag bolded) while the sequence for SpyTag003 is coloured in red (with the start codon bolded). The rest of the annotation scheme is identical to that in Figure A-1. Italicized bases were appended to the gene encoding ODIN1b by PCR for assembly.

ATGATGGATCAAGCTAGATCAGCATTCTCTAACTTGTTTGGTGGAGAACCATTGTCATGTACCCGGGCCAGCCTGG
CTCGGCAAGTAGATGGCGATAACAGTCATGTGGAGATGAAACTTGCTGTAGATGAAGAAGAAAATGCTGACAATAA
CACAAAGGCCAATGTCACAAAACCAAAAAGGTGTAGTGGAAGTATCTGCTATGGGACTATTGCTGTGATCGTCTTT
TTCTTGATTGGATTTATGATTGGCTACTTGGGCTATGGAAGCGGAGGATCCGGGATGGTGAGCAAGGGCGAGGAGA
ATAACATGGCCATCATCAAGGAGTTCATGCGCTTCAAGGTGCACATGGAGGGCTCCGTGAACGGCCACGAGTTCGA
GATCGAGGGCGAGGGCGAGGGCCGCCCCTACGAGGCCTTTCAGACCGCTAAGCTGAAGGTGACCAAGGGTGGCCCC
CTGCCCTTCGCCTGGGACATCCTGTCCCCTCAGTTCATGTACGGCTCCAAGGTCTACATTAAGCACCCAGCCGACA
TCCCCGACTACTTCAAGCTGTCCTTCCCCGAGGGCTTCAGGTGGGAGCGCGTGATGAACTTCGAGGACGGCGGCAT
TATTCACGTTAACCAGGACTCCTCCCTGCAGGACGGCGTGTTCATCTACAAGGTGAAGCTGCGCGGCACCAACTTC
CCCTCCGACGGCCCCGTAATGCAGAAGAAGACCATGGGCTGGGAGGCCTCCGAGGAGCGGATGTACCCCGAGGACG
GCGCCCTGAAGAGCGAGATCAAGAAGAGGCTGAAGCTGAAGGACGGCGGCCACTACGCCGCCGAGGTCAAGACCAC
CTACAAGGCCAAGAAGCCCGTGCAGCTGCCCGGCGCCTACATCGTCGACATCAAGTTGGACATCGTGTCCCACAAC
GAGGACTACACCATCGTGGAACAGTACGAACGCGCCGAGGGCCGCCACTCCACCGGCGGCATGGACGAGCTGTACA
AGGAACAAAAACTCATCTCAGAAGAGGATCTGGGTTCCGGTGGCTCGGGTGGATCCATGGTGACCACACTGTCCGG
ACTGTCTGGAGAGCAGGGACCATCCGGCGACATGACCACAGAGGAGGATTCTGCCACACACATCAAGTTCAGCAAG
AGGGACGAGGACGGAAGAGAGCTGGCAGGAGCAACCATGGAGCTGAGGGATAGCTCCGGCAAGACCATCAGCACAT
GGATCTCCGACGGCCACGTGAAGGATTTCTACCTGTATCCCGGCAAGTACACCTTTGTGGAGACAGCAGCACCAGA
CGGATATGAGGTGGCAACCCCTATCGAGTTTACAGTGAACGAGGACGGACAGGTGACCGTGGATGGAGAGGCAACA
GAGGGCGATGCACACACCGGATCTAGCGGATCTTAA

Figure A-6 – DNA Sequence of pENTR4-mApple-myc tag-SpyCatcher003.

Underlined sequences are part of the pENTR4-myc tag-SpyCatcher003 backbone from Addgene [327]. The sequence in purple is for the transferrin receptor, the black sequence is for the myc tag and linker region, and the green sequence is for SpyCatcher003. The DNA sequence for mApple is coloured in red.

TAATACGACTCACTATAGGGAGACCCAAGCTGGCTAGCGTGCCGCCACCATGGCCTCGAGCATGAGAGCCTGGATC
TTTTTTCTGCTCTGCCTCGCTGGCAGAGCCCTGGCTGCACCTCTGGGACGAGGAAGC**CATCATCACCA*CCATCAT***G
*GCGGGCTCGCA*ATGGTGAGCAAGGGCGAGGAGCTGTTCACCGGGGTGGTGCCCATCCTGGTCGAGCTGGACGGCGA
CGTAAACGGCCACAAGTTCAGCGTGTCCGGCGAGGGCGAGGGCGATGCCACCTACGGCAAGCTGACCCTGAAGTTC
ATCTGCACCACCGGCAAGCTGCCCGTGCCCTGGCCCACCCTCGTGACCACCCTGACCTACGGCGTGCAGTGCTTCA
GCCGCTACCCCGACCACATGAAGCAGCACGACTTCTTCAAGTCCGCCATGCCCGAAGGCTACGTCCAGGAGCGCAC
CATCTTCTTCAAGGACGACGGCAACTACAAGACCCGCGCCGAGGTGAAGTTCGAGGGCGACACCCTGGTGAACCGC
ATCGAGCTGAAGGGCATCGACTTCAAGGAGGACGGCAACATCCTGGGGCACAAGCTGGAGTACAACTACAACAGCC
ACAACGTCTATATCATGGCCGACAAGCAGAAGAACGGCATCAAGGTGAACTTCAAGATCCGCCACAACATCGAGGA
CGGCAGCGTGCAGCTCGCCGACCACTACCAGCAGAACACCCCCATCGGCGACGGCCCCGTGCTGCTGCCCGACAAC
CACTACCTGAGCACCCAGTCCGCCCTGAGCAAAGACCCCAACGAGAAGCGCGATCACATGGTCCTGCTGGAGTTCG
TGACCGCCGCCGGGATCACTCTCGGCATGGACGAGCTGTACAAG*GGCTCCGGAGGCGCAG*TGTACCACAGAGAAGC
ACGGTCTGGCAAATACAAGCTCACCTACGCAGAAGCTAAGGCGGTGTGTGAATTTGAAGGCGGCCATCTCGCAACT
TACAAGCAGCTAGAGGCAGCCAGAAAAATTGGATTTCATGTCTGTGCTGCTGGATGGATGGCTAAGGGCAGAGTTG
GATACCCCATTGTGAAGCCAGGGCCCAACTGTGGATTTGGAAAAACTGGCATTATTGATTATGGAATCCGTCTCAA
TAGGAGTGAAAGATGGGATGCCTATTGCTACAACCCACACGCAAAGTAAAGCTTAAGTTTAAACCGCTGATCAGC

Figure A-7 – DNA Sequence for EGFP in the secretion construct

DNA sequence for pcDNA3.1m-BM40-EGFP-LINK. The pcDNA3.1m vector backbone sequence is shown in black. The secretion construct consists of BM40 (red), a long linker (purple) with a polyhistidine tag (bolded) after BM40, a shorter linker (purple) after ODIN1b, and the LINK domain (blue). The sequence for EGFP is coloured in green. Italicized sequences were the homologous sequences used for assembly and appended to genes of interest by extension PCR. The complementary sequences were used as primers to linearize the vector and replace the insert. sfGFP and iGluSnFR were amplified by PCR from constructs available in Addgene and inserted to replace EGFP.

ATGGGGGGTTCTCATCATCATCATCATCATGGTATGGCTAGCATGACTGGTGGACAGCAAATGGGTCGGGATCTGT
ACGAC*GATGACGATAAGGATCCGAGCTCGAG*AATGAAGGAACTTGTGGTGGGGACCGATACTAGTTTTATGCCCTT
CGAGTTTAAGCAGGGAGATAAATATGTGGGCTTTGACTTGGATCTCTGGGCGGAGATAGCGAAGGGTGCGGGGTGG
ACGTATAAGATCCAACCCATGGATTTCGCAGGACTCATACCTGCCTTGCAAACACAAAATATAGATGTTGCTCTCA
GTGGAATGACCATAAAGGAAGAACGGCGCAAGGCCATTGATTTTTCTGATCCTTACTATGATAGCGGCCTTGCTGC
TATGGTGCAAGCGAACAATACCACTATTAAATCAATCGACGACTTGAATGGAAAAGTAATTGCCGCGAAAACCGGC
ACAGCAACAATAGATTGGATTAAAGCTCACTTGAAACCGAAAGAGATCCGACAATTCCCGAACATCGATCAGGCGT
ATTTGGCCCTTGAGGCAGGCCGCGTTGATGCTGCAATGCATGATACCCCTAATGTGCTTTTCTTTGTGAATAACGA
GGGTAAAGGCCGAGTCAAAGTGGCTGGCGCTCCTGTTAGCCTGGATGCGCACAATGTGTATATCACAGCGGACAAG
CAGAAGAACGGGATAAAAGCGAATTTCAAGATTCGACACAATGTCGAAGATGGGACCGTTCAGCTCGCCGACCATT
ACCAGCAGAACACACCCATAGGCGATGGACCCGTTTTGCTTCCTGATAATCACTATTTGTCTACGCAAAGTGTGTT
GAGTAAGGATCCAAACGAAAAGCGCGACCATATGGTGTTGCTGGAATTTGTCACTGCCGCGGGCATTACGCATGGG
ATGGATGAACTCTACAAAGGGGGAACTGGCGGGTCTATGGTGTCCAAAGGGGAAGAACTGTTTACTGGAGTAGTTC
CAATCCTTGTGGAACTCGACGGTGATGTAAACGGACATAAATTCAGCGTACGAGGTGAGGGAGAGGGAGATGCCAC
AAACGGCAAACTGACTCTCAAATTTATATGCACTACCGGCAAACTGCCAGTCCCTTGGCCTACCTTGGTAACCACT
TTGACATATGGCGTTCAATGCTTTTCCAGGTACCCTGATCACATGAAACGACACGATTTCTTTAAAAGCGCGATGC
CAGAAGGGTATGTGCAGGAGCGGACTATAAGTTTTAAGGACGACGGGACCTATAAAACTAGGGCAGAGGTCAAATT
CGAGGGCGATACGCTTGTCAACAGGATAGAGCTCAAGGGAATAGATTTTAAGGAGGATGGTAATATACTGGGTCAT
AAGTTGGAGTATAACTTTAACACTCGGAAATACGGTATAGGGTTTCCCAAAGGTAGTCCCCTTGTCGCAAAGGTTA
ATGCAGAACTTGCACGGATGAAGGCGGACGGCCGATATGCAAAGATATATAAGAAGTGGTTCGGGTCAGAACCACC
CAAGAGTCAGTAA*AAGCTT*GGCTGTTTTGGCGGATG

Figure A-8 - DNA sequence of Qigon1 in pBAD/HisB.

DNA sequence for Qigon1 in pBAD/HisB annotated for its features. Sequences in blue are part of the pBAD vector (beginning at the start codon of the reading frame and including its N-terminal tags; bolded sequence indicates the polyhistidine tag). Bases highlighted in yellow indicate the *XhoI* and *HindIII* restriction sites. Orange sequence is for BpQBP, green sequence is cpsfGFP, and grey sequences are for the linker regions. Italicized bases indicate the homologous sequences used for assembly; the complements of these italicized bases were used as the primers to generate linearized vector by PCR.

GGGCTAACAGGAGGAATTAACCATGGGGGGTTCTAGCTCGAGA**ATG**GGACGTGGCGTTCCTCATATTGTTATGGTG
GACGCCTACAAACGCTATAAAT*CGGGAGGTGGTTCAGGC*ATGAAGGAACTTGTGGTGGGGACCGATACTAGTTTTA
TGCCCTTCGAGTTTAAGCAGGGAGATAAATATGTGGGCTTTGACTTGGATCTCTGGGCGGAGATAGCGAAGGGTGC
GGGGTGGACGTATAAGATCCAACCCATGGATTTCGCAGGACTCATACCTGCCTTGCAAACACAAAATATAGATGTT
GCTCTCAGTGGAATGACCATAAAGGAAGAACGGCGCAAGGCCATTGATTTTTCTGATCCTTACTATGATAGCGGCC
TTGCTGCTATGGTGCAAGCGAACAATACCACTATTAAATCAATCGACGACTTGAATGGAAAAGTAATTGCCGCGAA
AACCGGCACAGCAACAATAGATTGGATTAAAGCTCACTTGAAACCGAAAGAGATCCGACAATTCCCGAACATCGAT
CAGGCGTATTTGGCCCTTGAGGCAGGCCGCGTTGATGCTGCAATGCATGATACCCCTAATGTGCTTTTCTTTGTGA
ATAACGAGGGTAAAGGCCGAGTCAAAGTGGCTGGCGCTCCTGTTAGCCTGGATGCGCACAATGTGTATATCACAGC
GGACAAGCAGAAGAACGGGATAAAAGCGAATTTCAAGATTCGACACAATGTCGAAGATGGGACCGTTCAGCTCGCC
GACCATTACCAGCAGAACACACCCATAGGCGATGGACCCGTTTTGCTTCCTGATAATCACTATTTGTCTACGCAAA
GTGTGTTGAGTAAGGATCCAAACGAAAAGCGCGACCATATGGTGTTGCTGGAATTTGTCACTGCCGCGGGCATTAC
GCATGGGATGGATGAACTCTACAAAGGGGGAACTGGCGGGTCTATGGTGTCCAAAGGGGAAGAACTGTTTACTGGA
GTAGTTCCAATCCTTGTGGAACTCGACGGTGATGTAAACGGACATAAATTCAGCGTACGAGGTGAGGGAGAGGGAG
ATGCCACAAACGGCAAACTGACTCTCAAATTTATATGCACTACCGGCAAACTGCCAGTCCCTTGGCCTACCTTGGT
AACCACTTTGACATATGGCGTTCAATGCTTTTCCAGGTACCCTGATCACATGAAACGACACGATTTCTTTAAAAGC
GCGATGCCAGAAGGGTATGTGCAGGAGCGGACTATAAGTTTTAAGGACGACGGGACCTATAAAACTAGGGCAGAGG
TCAAATTCGAGGGCGATACGCTTGTCAACAGGATAGAGCTCAAGGGAATAGATTTTAAGGAGGATGGTAATATACT
GGGTCATAAGTTGGAGTATAACTTTAACACTCGGAAATACGGTATAGGGTTTCCCAAAGGTAGTCCCCTTGTCGCA
AAGGTTAATGCAGAACTTGCACGGATGAAGGCGGACGGCCGATATGCAAAGATATATAAGAAGTGGTTCGGGTCAG
AACCACCCAAGAGTCAG*CAAGCTT*CCGGC***CATCATCATC**ATCATCAT**TAA

Figure A-9 - Sequence of cHis-pBAD-SpyTag003-Qigon1.

DNA sequence for Qigon1 in cHis-pBAD with SpyTag003 at the N-terminus and annotated for its features. Sequences in blue are part of the vector (with the polyhistidine tag bolded) while the sequence for SpyTag003 is coloured in red (with the start codon bolded). The rest of the colour scheme is identical to that in Figure A-8. Italicized bases were appended to the gene encoding Qigon1 by PCR for assembly.

ATGGGGGGTTCT**CATCATCATCATCATCAT**GGTATGGCTAGCATGACTGGTGGACAGCAAATGGGTCGGGATCTGT

ACGAC*GATGACGATAAGGATCCGAG*CTCGAGAATGGTCGACTCATCACGTCGTAAGTGGAATAAGTGGGGTCGCGC

AGTCAGAGCTATAGGTCGGCTGAGCTTAGCGCGTCAGACAGAGATGATGTATCCGGCAGATGGTGGTCTGAGAGGA

TTCACTGACATCGCTCTGAAAGTTGATGGTGGTGGCCAACTGCGCTGCAACTTCGTGACAACTTACAGGTCAAAAA

AGACCGTCGGGAACATCAAGATGCCCGGTGTCCATGCCGTTGATCACCGCCTGGAAAGGATCGAGGAGAATGACGA

TGAAACATACGTAGTGCAACGCGAAGTGGCAGTTGCCAAATACAGCAACCTTGGTGGTGGCGGCGGTACCGGAGGG

AGCATGAACTCTCTGATCAAGGAAGATATGCGTATGAAGGTGGTCATGGAAGGATCGGTCAACGGCCACCAATTCA

AATGCACAGGTGAAGGCGAAGGCAGACCGTATGAGGGAACTCAAACCATGAGGATCAAAGTCATCGAGGGAGGACC

CCTGCCATTTGCCTTTGACATTCTTGCCACGTCGTTCATGTATGGCAGTCGTACTTTTATCAAGTACCCGGCCGAC

ATCCCTGATTTCTTTAAACAGTCCTTTCCTGAGGGTTTTACTTGGGAAAGAGTTACGATATACGAAGATGGTGGAG

TCGTCGCCGTCACGCAGGACACCAGCCTTGAGGATGGCGAGCTCGTCTACAGCGTCAAGGTCAGAGGGGTAAACTT

TCCCTCCAATGGTCCCGTGATGCAGAAGAAGACCAAGGGTTGGGAGCCTATTGTGTCCCAACTGACTGAAGAGCAG

ATCGCAGAATTTAAAGAGGCCTTCTCCCTATTTGACAAGGACGGGGATGGGACAATAACAACCAAGGAGATGGGGA

CGGTGTTGCGGACTCTGGGGCAGAACCCCACAGAAGCAGAGCTGCAGGACATGATCAATGAAGTAGATACCGACGG

TGACGGCACAATCGACTTCCCTGAGTTCCTGATTATGATGGCAGGTAATATGGAATACACAGACAGTGAAGAAGAA

ATTAGAGAAGCGTTCAGCGTGTTTGATAAGGATGGCAATGGCTACATCGGTGCAGCAGAGCTTCGCCACGCGATGA

CAAACCTTGGAGAGAAGTTAACAGATGCTGAGGTTGATGAGTTGATCAGGGAGGCCGATTCCGATGGCGACGGACA

GGTTAACTACGAAGAGTTCGTTCAAATGATGACCGCCAAGTAA*AAGCTT*GGCTGTTTTGGCGGATG

Figure A-10 – RCaMP3 in pBAD/HisB.

DNA sequence for RCaMP3 in pBAD/HisB annotated for its features. Sequences in blue are part of the pBAD vector with the first section encoding the pBAD N-terminal tags (bolded sequence highlights the polyhistidine tag). Bases highlighted in yellow indicate the *XhoI* and *HindIII* restriction sites. The sequence in purple encode for the RS20 peptide, red for cpmRuby3, yellow and highlighted in black for CaM, and grey for the linker regions. Italicized bases indicate the homologous sequences used for assembly; the complements of the italicized sequences were used as the primers to produce linearized vector by PCR.

ATGGGGGGTTCT**CATCATCATCATCATCAT**GGTATGGCTAGCATGACTGGTGGACAGCAAATGGGTCGGGATCTGT

ACGAC*GATGACGATAAGGATCCGAG**CTCGAG***AATGGTAGATTCCTCTAGAAGAAAGTGGAATAAGTGGGGCCATGC

AGTTCGGGCAATAGGTCGCCTGTCTTCTGCAAACAATACTGAGATGATGTACCCAGCCGACGGTGGGTTGCGGGGA

TACACCCACATGGCCTTGAAAGTGGATGGCGGGGGGCACTTGAGTTGTTCCTTCGTTACCACCTATAGGTCTAAGA

AGACTGTAGGGAATATAAAAATGCCTGCTATTCATTACGTCAGTCATCGCCTTGAACGGCTTGAAGAATCCGACAA

CGAAATGTTCGTGGTACAACGCGAGCATGCGGTAGCAAAATTCGTAGGACTTGGCGGGGGCGGAGGGACTGGAGGA

TCTATGAACTCTCTCATAAAAGAGAACATGCGCATGAAGGTTGTCCTTGAAGGGAGCGTAAACGGCCATCAATTCA

AATGTACTGGCGAGGGCGAAGGCAATCCTTATATGGGAACACAGACCATGCGGATAAAGGTAATAGAGGGCGGCCC

TCTTCCATTTGCTTTCGATATTCTGGCAACGAGTTTCATGTACGGCTCTCGGACATTTATCAAATACCCAAAAGGT

ATTCCAGACTTCTTCAAGCAAAGTTTTCCCGAAGGATTCACGTGGGAGAGGGTAACAAGATATGAGGATGGCGGAG

TCATCACCGTAATGCAAGATACGTCACTTGAGGACGGGTGTCTCGTCTATCACGTACAGGTGAGAGGAGTCAACTT

CCCATCCAATGGTGCCGTAATGCAGAAAAAGACTAAAGGTTGGGAGCCAACTGAC**TCCCAATTGACAGAAGAACAG**

ATCGCGGAGTTCAAGGAAGCGTTTTCACTGTTTGACAAAGATGGGGACGGGACGATCACTACTAAGGAGATGGGAA

CAGTCATGAGATCTCTCGGACAAAATCCCACGGAGGCAGAATTGCAAGACATGATAAATGAGGTAGACGCAGATGG

TGACGGGACCATTGATTTTCCCGAGTTTCTGATTATGATGGCAGGCAAAATGAAATATACGGATTCCGAAGAAGAA

ATACGGGAGGCGTTCGGCGTCTTCGATAAAGATGGGAATGGATACATATCAGCGGCTGAGCTCAGGCATGTCATGA

CGAATCTGGGTGAGAAGCTGACCGATGAAGAGGTAGACGAGATGATCAGGGAGGCGGATAGCGACGGAGACGGCCA

GGTCAACTATGAGGAATTTGTACAAATGATGACAGCTAAATAG*AAGCTT**GGCTGTTTTGGCGGATG***

Figure A-11 – jRCaMP1b in pBAD/HisB.

DNA sequence for jRCaMP1b in pBAD/HisB annotated for its features following the scheme described in Figure A-10.

TAATACGACTCACTATAGGGAGACCCAAGCTGGCTAGCGT*GCCGCCACCATGGCCTCGAGC*ATG**CATCATCATCAT**

CATCATGGTATGGCTAGCATGACTGGTGGACAGCAAATGGGTCGGGATCTGTACGACGATGACGATAAGGATCCGA

GCTCGAGAATGGTCGACTCATCACGTCGTAAGTGGAATAAGTGGGGTCGCGCAGTCAGAGCTATAGGTCGGCTGAG

CTTAGCGCGTCAGACAGAGATGATGTATCCGGCAGATGGTGGTCTGAGAGGATTCACTGACATCGCTCTGAAAGTT

GATGGTGGTGGCCAACTGCGCTGCAACTTCGTGACAACTTACAGGTCAAAAAAGACCGTCGGGAACATCAAGATGC

CCGGTGTCCATGCCGTTGATCACCGCCTGGAAAGGATCGAGGAGAATGACGATGAAACATACGTAGTGCAACGCGA

AGTGGCAGTTGCCAAATACAGCAACCTTGGTGGTGGCGGCGGTACCGGAGGGAGCATGAACTCTCTGATCAAGGAA

GATATGCGTATGAAGGTGGTCATGGAAGGATCGGTCAACGGCCACCAATTCAAATGCACAGGTGAAGGCGAAGGCA

GACCGTATGAGGGAACTCAAACCATGAGGATCAAAGTCATCGAGGGAGGACCCCTGCCATTTGCCTTTGACATTCT

TGCCACGTCGTTCATGTATGGCAGTCGTACTTTTATCAAGTACCCGGCCGACATCCCTGATTTCTTTAAACAGTCC

TTTCCTGAGGGTTTTACTTGGGAAAGAGTTACGATATACGAAGATGGTGGAGTCGTCGCCGTCACGCAGGACACCA

GCCTTGAGGATGGCGAGCTCGTCTACAGCGTCAAGGTCAGAGGGGTAAACTTTCCCTCCAATGGTCCCGTGATGCA

GAAGAAGACCAAGGGTTGGGAGCCTATTGTGTCCCAACTGACTGAAGAGCAGATCGCAGAATTTAAAGAGGCCTTC

TCCCTATTTGACAAGGACGGGGATGGGACAATAACAACCAAGGAGATGGGGACGGTGTTGCGGACTCTGGGGCAGA

ACCCCACAGAAGCAGAGCTGCAGGACATGATCAATGAAGTAGATACCGACGGTGACGGCACAATCGACTTCCCTGA

GTTCCTGATTATGATGGCAGGTAATATGGAATACACAGACAGTGAAGAAGAAATTAGAGAAGCGTTCAGCGTGTTT

GATAAGGATGGCAATGGCTACATCGGTGCAGCAGAGCTTCGCCACGCGATGACAAACCTTGGAGAGAAGTTAACAG

ATGCTGAGGTTGATGAGTTGATCAGGGAGGCCGATTCCGATGGCGACGGACAGGTTAACTACGAAGAGTTCGTTCA

AATGATGACCGCCAAGTAA*AGCTTAAGTTTAAACCGCTGATCAGC*

Figure A-12 – DNA sequence for pcDNA3.1m-6His-RCaMP3

DNA sequence for RCaMP3 with the pBAD N-terminal tags in pcDNA3.1m. The sequence is annotated for its features following the scheme described in with the addition of the vector sequence shown in green.

TAATACGACTCACTATAGGGAGACCCAAGCTGGCTAGCGT*GCCGCCACCATGGCCTCGAGC*ATGC**ATCATCATCAT**

CATCATGGTATGGCTAGCATGACTGGTGGACAGCAAATGGGTCGGGATCTGTACGACGATGACGATAAGGATCCGA

GCTCGAGAATGGTAGATTCCTCTAGAAGAAAGTGGAATAAGTGGGGCCATGCAGTTCGGGCAATAGGTCGCCTGTC

TTCTGCAAACAATACTGAGATGATGTACCCAGCCGACGGTGGGTTGCGGGGATACACCCACATGGCCTTGAAAGTG

GATGGCGGGGGGCACTTGAGTTGTTCCTTCGTTACCACCTATAGGTCTAAGAAGACTGTAGGGAATATAAAAATGC

CTGCTATTCATTACGTCAGTCATCGCCTTGAACGGCTTGAAGAATCCGACAACGAAATGTTCGTGGTACAACGCGA

GCATGCGGTAGCAAAATTCGTAGGACTTGGCGGGGGCGGAGGGACTGGAGGATCTATGAACTCTCTCATAAAAGAG

AACATGCGCATGAAGGTTGTCCTTGAAGGGAGCGTAAACGGCCATCAATTCAAATGTACTGGCGAGGGCGAAGGCA

ATCCTTATATGGGAACACAGACCATGCGGATAAAGGTAATAGAGGGCGGCCCTCTTCCATTTGCTTTCGATATTCT

GGCAACGAGTTTCATGTACGGCTCTCGGACATTTATCAAATACCCAAAAGGTATTCCAGACTTCTTCAAGCAAAGT

TTTCCCGAAGGATTCACGTGGGAGAGGGTAACAAGATATGAGGATGGCGGAGTCATCACCGTAATGCAAGATACGT

CACTTGAGGACGGGTGTCTCGTCTATCACGTACAGGTGAGAGGAGTCAACTTCCCATCCAATGGTGCCGTAATGCA

GAAAAAGACTAAAGGTTGGGAGCCAACTGACTCCCAATTGACAGAAGAACAGATCGCGGAGTTCAAGGAAGCGTTT

TCACTGTTTGACAAAGATGGGGACGGGACGATCACTACTAAGGAGATGGGAACAGTCATGAGATCTCTCGGACAAA

ATCCCACGGAGGCAGAATTGCAAGACATGATAAATGAGGTAGACGCAGATGGTGACGGGACCATTGATTTTCCCGA

GTTTCTGATTATGATGGCAGGCAAAATGAAATATACGGATTCCGAAGAAGAAATACGGGAGGCGTTCGGCGTCTTC

GATAAAGATGGGAATGGATACATATCAGCGGCTGAGCTCAGGCATGTCATGACGAATCTGGGTGAGAAGCTGACCG

ATGAAGAGGTAGACGAGATGATCAGGGAGGCGGATAGCGACGGAGACGGCCAGGTCAACTATGAGGAATTTGTACA

AATGATGACAGCTAAATAG*AGCTTAAGTTTAAACCGCTGATCAGC*

Figure A-13 – DNA sequence of pcDNA3.1m-6His-jRCaMP1b.

DNA sequence for jRCaMP1b with the polyhistidine tag in pcDNA3.1m annotated for its features following the scheme described in Figure A-12.

ATGGGGGGTTCT**CATCATCATCATCATCAT**GGTATGGCTAGCATGACTGGTGGACAGCAAATGGGTCGGGATCTGT

ACGAC*GATGACGATAAGGATCCGAG*CTCGAGAATGGGCAGCGTGAAGCAGATCCCTAGCCTGACCACAGTGATCCT

GGTCAAGTCCATGCTGCGGAAGCGGAGCTTCGGCAACCCCTTCGGTTTTCTGACCGAGTACCTGGTGCCTGTGGAC

GGTGGCCTGGCAGGCACATGTGACATGGCCCTGAGACTCGTTGGCGGCGGACACCTGAAGTGCAACCTGAAAACCA

CCTACAGAAGCAAGAAGCCCGCCAAGAACCTGAAGATGCCTGGCGAACACCAGGTGGGCCGGAAGCTGGAAAGAAT

CAAAGAGGCCGACAACGAGACATACGTGGAACAGCACGAAGTGGCCGTGGCCAGATATGTTGGACTTGGCGGAGGC

GGAGGAACAGGCGGATCTGTGTCTGAGCTGATCAAAGAAAACATGCGGATGAAGCTCTACTTGGAAGGGACCGTCG

GCAACCACCACTTCAAGTGTACTGCCGAAGGCGAGGGCAAGCCCTATGAGGGAACACAGACCCAGCGGATCAAGGT

GGTGGAAGGTGGCCCTCTGCCTTTCGCCTTTGACATCCTGGCCACCTGTTTTATGTACGGCAGCAAGACCTTCATC

AACTATCCCCAGGGCATCCCCGATTTCTTCAAGCAGAGCTTCCCCGAGGGCTTCACCTGGGAGAGAGTGACCACAT

ACGAGGATGGCGGCGTGCTGACCGTGACACAGGATACAAGCCTCCAGGACGGCTACCTGATCTACAATGTGAAGCT

GCTGGGCGTGAACTTCCCCAGCGATGGACCCGTGATGCAGAAGAAAACCCTCGGCTGGGTGCCCACCGATGGCACG

CTGACAGAAGAACTGATCGCCGAGTTCAAAGAAGCCTTCAGCCTGTTCGACAAGGACGGCGACGGCACCATCACCA

CCAAAGAACTGGGCTCCGTGATGCGGAGCCTGGGCCAGAATCCAACAGAAGCCGAACTCCAGGACATGATCAACGA

GGTGGACGCCGATGGCGACGGAACCTTCGATTACCCTGAGTTCCTGACCATGATGTCCCGGAAGATGAGCTACAGA

GTGACCGAGGAAGAGATCCGGGAAGCCTTCCAGGTTTTCGATAAGGATGGCAACGGCTACATCGGAGCCGCCGAAC

TGAGACGCGTGATGGCCGATCTGGGCGAGAAGCTGACTGACGAAGAGGTTGACGAGATGATCAGAGTGGCCGACAT

CGACGGCGACGGACAAGTGAACTACGAAGAGTTCGTGCAGATGATGACCGCCAAGTAG*AAGCTT*GGCTGTTTTGGC

GGATG

Figure A-14 – pBAD-FR-GECO1a DNA sequence.

DNA sequence for FR-GECO1a in pBAD/HisB with sequences in blue representing the pBAD/HisB backbone, purple representing the ckkap peptide, grey showing the linkers, red showing the sequence for cpmKelly2, and yellow on black background encoding for CaM. Bases in bold show the polyhistidine tag, while those highlighted in yellow are the *XhoI* and *HindIII* restriction sites. Italicized bases indicate the homologous sequences used

for assembly; the complements of the italicized sequences were used as the primers to produce linearized vector by PCR.

ATGGGGGGTTCT**CATCATCATCATCATCAT**GGTATGGCTAGCATGACTGGTGGACAGCAAATGGGTCGGGATCTGT
ACGAC*GATGACGATAAGGATCCGAG**CTCGAG***AATGGGCAGCGTGAAGCAGATCCCTAGCCTGACCACAGTGATCCT
GGTCAAGTCCATGCTGCGGAAGCGGAGCTTCGGCAACCCCTTCGGTTTTCTGACCGAGACCCTGGTGCCTGTGGAC
GGTGGCCTGGCAGGCACATGTGACATGGCCCTGAGACTCGTTGGCGGCGGACACCTGAAGTGCAACCTGAAAACCA
CCTACAGAAGCAAGAAGCCCGCCAAGAACCTGAAGATGCCTGGCGAACACCAGGTGGGCCGGAAGCTGGAAAGAAT
CAAAGAGGCCGACAACGAGACATACGTGGAACAGCACGAAGTGGCCGTGGCCAGATATGTTGGACTTGGCGGAGGC
GGAGGAACAGGCGGATCTGTGTCTGAGCTGATCAAAGAAAACATGCGGATGAAGCTCTACTTGGAAGGGACCGTCG
GCAACCACCACTTCAAGTGTACTGCCGAAGGCGAGGGCAAGCCCTATGAGGGAACACAGACCCAGCGGATCAAGGT
GGTGGAAGGTGGCCCTCTGCCTTTCGCCTTTGACATCCTGGCCACCTGTTTTATGTACGGCAGCAAGACCTTCATC
AACTATCCCCAGGGCATCCCCGATTTCTTCAAGCAGAGCTTCCCCGAGGGCTTCACCTGGGAGAGAGTGACCACAT
ACGAGGATGGCGGCGTGCTGACCGTGACACAGGATACAAGCCTCCAGGACGGCTACCTGATCTACAATGTGAAGCT
GCTGGGCGTGAACTTCCCCAGCGATGGACCCGTGATGCAGAAGAAAACCCTCGGCTGGGTGCCCACCGATGGCACG
CTGACAGAAGAACTGATCGCCGAGTTCAAAGAAGCCTTCAGCCTGTTCGACAAGGACGGCGACGGCACCATCACCA
CCAAAGAACTGGGCTCCGTGATGCGGAGCCTGGGCCAGAATCCAACAGAAGCCGAACTCCAGGACATGATCAACGA
GGTGGACGCCGATGGCGACGGAACCTTCGATTACCCTGAGTTCCTGACCATGATGTCCCGGAAGATGAGCTACAGA
GTGACCGAGGAAGAGATCCGGGAAGCCTTCCAGGTTTTCGATAAGGATGGCAACGGCTACATCGGAGCCGCCGAAC
TGAGACGCGTGATGGCCGATCTGGGCGAGAAGCTGACTGACGAAGAGGTTGACGAGATGATCAGAGTGGCCGACAT
CGACGGCGACGGACAAGTGAACTACGAAGAGTTCGTGCAGATGATGACCGCCAAGTAG*AAGCTT**GGCTGTTTTGGC*
GGATG

Figure A-15 – pBAD-FR-GECO1c DNA sequence.

DNA sequence for FR-GECO1c in pBAD/HisB with the same annotation scheme as Figure A-14.

TACCACTGAGATCTGCATGCTAGCCGCCACCATGGGCAGCGTGAAGCAGATCCCTAGCCTGACCACAGTGATCCTG
GTCAAGTCCATGCTGCGGAAGCGGAGCTTCGGCAACCCCTTCGGTTTTCTGACCGAGTACCTGGTGCCTGTGGACG
GTGGCCTGGCAGGCACATGTGACATGGCCCTGAGACTCGTTGGCGGCGGACACCTGAAGTGCAACCTGAAAACCAC
CTACAGAAGCAAGAAGCCCGCCAAGAACCTGAAGATGCCTGGCGAACACCAGGTGGGCCGGAAGCTGGAAAGAATC
AAAGAGGCCGACAACGAGACATACGTGGAACAGCACGAAGTGGCCGTGGCCAGATATGTTGGACTTGGCGGAGGCG
GAGGAACAGGCGGATCTGTGTCTGAGCTGATCAAAGAAAACATGCGGATGAAGCTCTACTTGGAAGGGACCGTCGG
CAACCACCACTTCAAGTGTACTGCCGAAGGCGAGGGCAAGCCCTATGAGGGAACACAGACCCAGCGGATCAAGGTG
GTGGAAGGTGGCCCTCTGCCTTTCGCCTTTGACATCCTGGCCACCTGTTTTATGTACGGCAGCAAGACCTTCATCA
ACTATCCCCAGGGCATCCCCGATTTCTTCAAGCAGAGCTTCCCCGAGGGCTTCACCTGGGAGAGAGTGACCACATA
CGAGGATGGCGGCGTGCTGACCGTGACACAGGATACAAGCCTCCAGGACGGCTACCTGATCTACAATGTGAAGCTG
CTGGGCGTGAACTTCCCCAGCGATGGACCCGTGATGCAGAAGAAAACCCTCGGCTGGGTGCCCACCGATGGCACGC
TGACAGAAGAACTGATCGCCGAGTTCAAAGAAGCCTTCAGCCTGTTCGACAAGGACGGCGACGGCACCATCACCAC
CAAAGAACTGGGCTCCGTGATGCGGAGCCTGGGCCAGAATCCAACAGAAGCCGAACTCCAGGACATGATCAACGAG
GTGGACGCCGATGGCGACGGAACCTTCGATTACCCTGAGTTCCTGACCATGATGTCCCGGAAGATGAGCTACAGAG
TGACCGAGGAAGAGATCCGGGAAGCCTTCCAGGTTTTCGATAAGGATGGCAACGGCTACATCGGAGCCGCCGAACT
GAGACGCGTGATGGCCGATCTGGGCGAGAAGCTGACTGACGAAGAGGTTGACGAGATGATCAGAGTGGCCGACATC
GACGGCGACGGACAAGTGAACTACGAAGAGTTCGTGCAGATGATGACCGCCAAGTAGTGAAAGCTTGGTACCGAGC
TCGGATCCACTAGTCCAGTGT

Figure A-16 – pCAG-FR-GECO1a DNA sequence.

DNA sequence for FR-GECO1a in pcDNA3.1/Puro-CAG with the same annotation scheme as Figure A-14 but the vector backbone sequence in green. FR-GECO1c would be inserted similarly.